

UNIVERSITY OF STRATHCLYDE

Department of Biomedical Engineering

# High bandwidth neural interfacing using visible light communication

Gábor Várkonyi



A thesis presented in fulfilment of the requirements for the degree  
of Engineering Doctorate

September 2018

# Declaration of Authorship

This thesis is the result of the author's original research. It has been composed by the author and has not been previously submitted for examination which has led to the award of a degree.

The copyright of this thesis belongs to the author under the terms of the United Kingdom Copyright Acts as qualified by University of Strathclyde Regulation 3.50. Due acknowledgement must always be made of the use of any material contained in, or derived from, this thesis.

Signed:



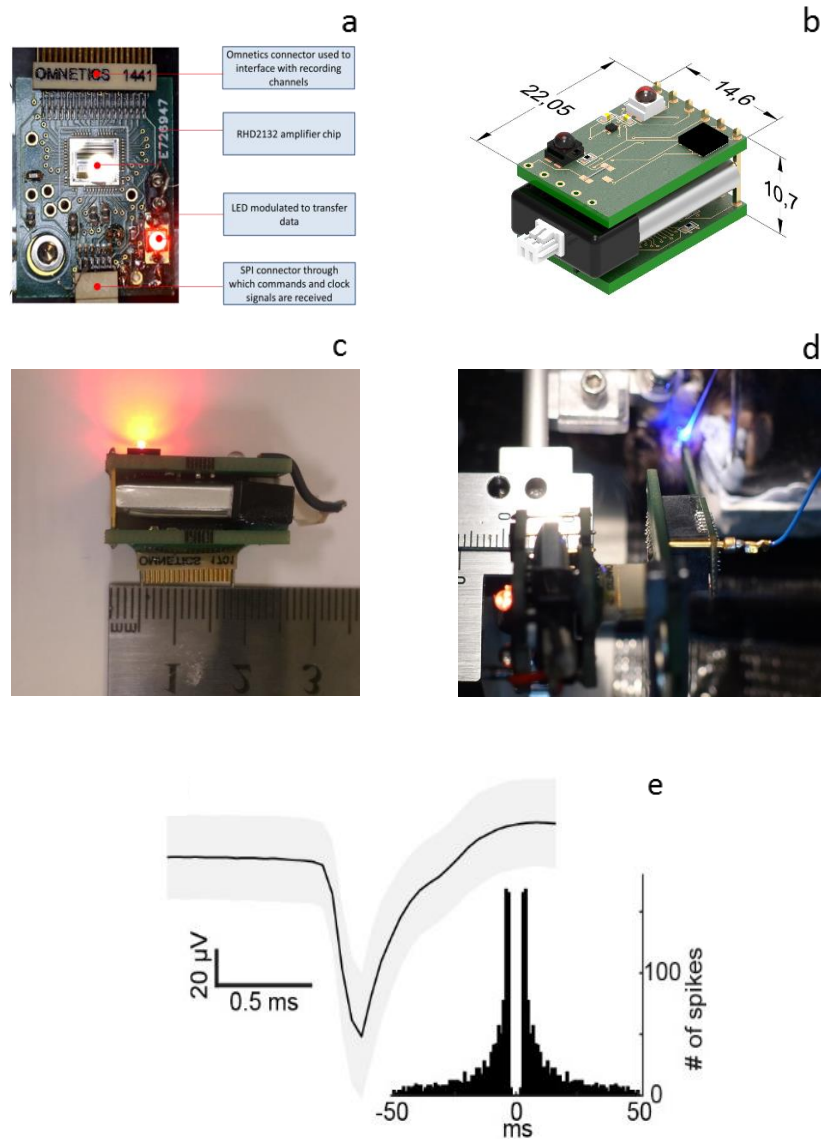
---

Date: 14/10/2019

---



# Frontispiece



(a) The first prototype in vitro device, which was interfaced with a 61-channel array to record spiking activity from retinal tissue (b) Isometric view of the in vivo device. All dimensions in mm. (c) Side view of the in vivo device with the data transmitting LED active (d) In the foreground, the in vivo device can be seen interfacing with an adapter and a 32-channel neural probe, which is inserted into a head-fixed mouse observable in the background. Optogenetic stimulation of the auditory cortex using blue light is also carried out throughout the experiment. (e) A typical averaged neural spike transmitted using the device during an in vivo experiment.

# *Abstract*

The sheer amount of information being processed arising from the high-density network of nerve cells in the brain, imposes severe restrictions with respect to the number of neurons that can be observed simultaneously. Many techniques focus on smaller nerve cell populations, and introduce wired electrode interfaces directly contacting neural tissue. These tethered methods however can lead to a host of detrimental issues, such as movement restriction affecting behaviour, and infections at the interface site. Due to this, devices capable of wirelessly transmitting large amounts of neural data are needed. To correlate neuron activity with behaviour, such devices are inserted into various animal models, preferably *in vivo*. The mouse model is particularly popular because of the familiarity of its genetics, physiology, and low upkeep costs. With the advent of such techniques as optogenetics, which allow increasingly precise light mediated activation of nerve cells, the preference for mice was further reinforced where they are the primary animal of choice. However, the majority of currently available wireless devices are too big and heavy to allow the freely moving behaviour of mice. Most of these use RF based data transmission, and use larger energy storage units to supply the power required for higher data rates. The size limitations also restrict the maximum dimensions for an antenna that can be used, further restricting the maximum available bandwidth. To propose a solution to these issues, the thesis outlines the design of low power devices that use visible light communication (VLC) to transmit neural data. As a pathway towards a fully wireless *in vivo* device we first developed an *in vitro* system, and interfaced with a 61-channel array containing rodent retinal tissue. The device was validated by sending neural data through the optical link, using an off the shelf LED. A fully wireless *in vivo* package was then developed. It was verified with test signals in a simulated environment, and a head fixed mouse at transmission distance of 20 cm. During *in vivo* recording, neural activity was stimulated using optogenetic techniques. The developed wireless system transmits 32 channels of uncompressed data (10.24 Mbps) in a 5g package. Strategies to transition to freely moving experiments and scale up channel count will be discussed. Finally, methods to readily reduce the weight will be outlined.

# Acknowledgements

I would like to thank everyone who has contributed to this work and has helped me realize this extremely exciting project.

Prof. Keith Mathieson for the opportunity, along with the encouragement and support from the very beginning. Also, for being available whenever advice was needed.

Dr. Jonathan McKendry for his invaluable guidance with respect to system design and characterization, and his assistance with system assembly.

Dr. Niall McAllinden for designing the live view software and always being available to assist with general enquiries.

Dr. Shuzo Sakata for his support as second supervisor, and carrying out the *in vivo* analysis, along with detailing the *in vivo* experiment procedures.

Dr. Daniel Lyngholm for arranging the *in vivo* experiments, and allowing the device to be tested.

Johannes for writing the FPGA code enabling the processing of neural data in real time.

The biomedical engineering department for providing the opportunity, and support.

Furthermore, I would like to thank Prof. Martin Dawson and the IoP along with all staff who have made this project possible and working there so enjoyable.

I would also like to thank Ruaridh, Antoine, Yunzhou along with family and friends who have shown interest and supported me throughout the entire project.

Thank you all!

# Table of Contents

Declaration of Authorship.....	i
Frontispiece.....	ii
Abstract.....	iii
Acknowledgements.....	iv
Table of Contents.....	v
List of Figures.....	ix
List of Tables.....	xiii
Abbreviations.....	xiv

## I Introduction

1.1 Motivation.....	1
1.2 Thesis outline.....	4

## II Background

2.1 The Nervous System.....	6
2.2 Techniques for studying the nervous system.....	8
2.3 Electrodes and Wired Methods.....	10
2.4 RF Based Wireless Methods.....	12
2.5 Optical based neural data transmission.....	19
2.6 Visible Light Communication.....	21
2.7 Powering solutions.....	25
2.8 Stimulating techniques.....	28
2.8.1 Electrical stimulation.....	28
2.8.2 Optogenetic stimulation.....	28
2.9 Device target specification.....	31
2.10 Conclusion.....	31

### III *In vitro* device setup

3.1 Introduction .....	48
3.2 Data acquisition system .....	50
3.2.1 Evaluation board .....	51
3.2.2 Amplifier chip .....	54
3.3 LEDs and photodetectors.....	59
3.3.1 LEDs.....	59
3.3.2 Photodetectors.....	63
3.4 Transmitter end device design .....	68
3.5 DAQ using an oscilloscope .....	69
3.6 DAQ with live streaming using Intan GUI.....	73
3.6.1 Break-out boards .....	75
3.6.2 Digitizing circuitry.....	76
3.6.3 Results .....	77
3.7 Conclusion.....	80

### IV *In vivo* device setup

4.1 Introduction .....	84
4.2 Head mountable device .....	86
4.2.1 Device overview .....	86
4.2.1 The PCBs – lower module.....	88
4.2.2 The PCBs –top module .....	89
4.2.3 MCU .....	89
4.2.4 Battery, charging and voltage regulation.....	93
4.2.5 IR receiver .....	94
4.2.6 Adapter board and probes .....	95
4.2.7 LEDs.....	96

4.2.8 Device Summary .....	99
4.3 The receivers .....	101
4.3.1 SensL photodetectors .....	101
4.3.2 Digitizing circuitry .....	102
4.3.3 Pulse digitization .....	102
4.3.4 FPGA .....	103
4.3.5 LabVIEW VI .....	106
4.3.6 Saleae Matlab code .....	107
4.4 The Experimental setups .....	108
4.4.1 The dummy data setup .....	108
4.4.2 The <i>in vivo</i> setup .....	112
4.5 Results .....	114
4.5.1 Distance measurements .....	115
4.5.2 Angle measurements .....	115
4.5.3 Eye diagrams .....	116
4.5.4 Performance modelling comparison .....	118
4.5.5 Power measurements .....	119
4.5.6 Noise measurements .....	121
4.5.7 <i>In vivo</i> results .....	122
4.6 Conclusion .....	123

## V Conclusion and Future Work

5.1 Overall summary .....	125
5.2 Detector placement .....	128
5.3 Receiving end circuitry modifications .....	135
5.4 Alternative powering solutions .....	136
5.5 Weight reduction .....	139

5.6 Alternative LED solutions.....	141
5.7 Manchester encoding.....	143
5.8 Further data encoding techniques.....	144
5.9 Multiple chip systems.....	146
5.10 Bidirectional probes and stimulating.....	147
5.11 Auxiliary improvements.....	147
5.12 Transfer printing.....	148
5.13 Concluding remarks.....	149

## **Appendix**

Appendix Chapter III.....	154
Appendix Chapter IV.....	160
Appendix Chapter V.....	182
Publications and Projects Arising from This Work.....	184

## List of Figures

2.1	Structure of a typical neuron.....	6
2.2	Typical ion channel .....	7
2.3	Action potential of a neuron.....	7
2.4	(a) A tetrode fiber made wires inserted into neural tissue. (b) Extracellular spiking activity around a firing pyramidal cell, showing the effect of an action potential on the local field potential.....	9
2.5	High channel probe configurations A.....	11
2.6	High channel probe configurations B.....	11
2.7	Channel count to weight ratio in currently available devices.....	15
2.8	Sub 20g devices from the graph in figure 2.7.....	15
2.9	“Neural Dust” device overview.....	17
2.10	Summary of wireless devices.....	18
2.11	The dispersion profile of LEDs vs VCSELs.....	20
2.12	A VCSEL based neural recording device.....	20
2.13	The electromagnetic spectrum.....	24
2.14	The steps outlining the optogenetic transfection and stimulating procedure .....	29
3.1	Block diagram of the Intan setup.....	50
3.2	The Intan evaluation board.....	51
3.3	Intan timing diagram for a single sample.....	53
3.4	Block diagram of the Xilinx Spartan-6 FPGA .....	54
3.5	Block diagram of the Intan RHD2132 amplifier chip .....	55
3.6	Timing diagram of the of the SPI communication implemented between the evaluation board (master) and the RHD2132 amplifier chip (slave).....	56
3.7	Block diagram outlining the command cycle of the Intan system.....	57
3.8	A comparison of CMOS signalling and LVDS signalling.....	59



3.9	Electrical characteristics and physical dimensions of the Avago HLMP-Q156 LED.....	61
3.10	Electrical characteristics and physical dimensions of the Kingbright APETD3528SEC/J3-PRV.....	63
3.11	First Sensor AD800-11 APD photodetector.....	63
3.12	SensL C-series 10020 photodetector.....	64
3.13	(a) Circuit schematic of the SensL SiPM showing each microcell. (b) Breakdown, quench and reset cycle of a SPAD working in Geiger mode.....	65
3.14	Plan view of the <i>in vitro</i> device showing the main components.....	68
3.15	Block diagram showing the initial VLC setup, using an oscilloscope.....	69
3.16	Illustration of how the data is processed on the bit level.....	71
3.17	(a) The PCB with the central aperture into which the 61-channel array is inserted into. (b) The 61-channel array with tracks leading to the edge of the glass substrate (c) Electrode layout of the array arranged in a hexagonal fashion (d) Illustration of the cross section of retinal tissue on.....	72
3.18	The block diagram of the final setup with the digitizing boards and the break-out boards present.....	73
3.19	(a) Top down view of the 61-channel array. (b) The updated device and its main components.....	74
3.20	The front end of the setup showing the device interfacing with the 61-channel array and the PCB.....	75
3.21	Board layout of the break-out boards.....	76
3.22	(a) Schematic of the digitising circuit (b) Diagram of a typical low pass-filter..	77
3.23	(a) Electrical trace from the digital output of the Intan ASIC while recording neural data from retinal tissue (b) Received optical trace corresponding to trace in (a).....	79
3.24	(a) Pseudo-neural signals recorded using the Intan software through the SPI cable while the system was running live (b) through optical link displayed using the Intan GUI.....	79

3.25	Results from an in vitro experiment of a mouse retina .....	80
4.1	Simplified block diagram for <i>in vivo</i> system.....	85
4.2	View and dimensions of the <i>in vivo</i> device.....	86
4.3	Exploded view of the device showing all the sub components.....	87
4.4	Exploded view of the device coupled with the schematic for the different layers .....	87
4.5	Bottom PCB.....	88
4.6	Top PCB.....	90
4.7	Block diagram for data transmission using DMA.....	91
4.8	(a) Ares 50 mAh LiPo battery used to power the device. (b) USB based battery charger used to charge the battery.....	94
4.9	Exploded view of the device connecting to an adapter board required to interface with the 32 channel A32 Neuronexus recording probe.....	96
4.10	Electrical characteristics and physical dimensions of the OSRAM OSLON® Black SFH 4715AS .....	97
4.11	Emission spectra of the Kingbright and OSRAM IR LEDs, showing filter cut-off .....	97
4.12	LED spectra and SensL receiver spectral range comparison.....	98
4.13	LED spectra and filter cut-off wavelengths .....	101
4.14	Schematic for the digitizing circuit.....	103
4.15	Digitized optical pulse oscilloscope traces recorded at 0-40 cm.....	104-105
4.16	FPGA used to convert the processed digital signals.....	106
4.17	Data traces recorded using the Saleae logic analyser.....	108
4.18	A zoomed in view of the A32 Neuronexus probe.....	109
4.19	A schematic of the system used for the experiments.....	110
4.20	Data flow for the setup used for generating dummy spikes.....	110
4.21	Snapshot of 32 channels worth of dummy neural data being transmitted from a distance of 10 cm .....	111

4.22	A running <i>in vivo</i> experiment with the device inserted into the brain of a head-fixed mouse .....	114
4.23	Eye diagrams for a range of angles and distances .....	117
4.24	Eye diagrams for a range of data rates.....	118
4.25	Modelled BER vs distance performance .....	119
4.26	Graph showing how the battery voltage changes with respect to time as the device is running .....	120
4.27	The power consumption at various sampling rates and theoretically scaled up channel counts.....	120
4.28	(a) Noise from all channels superimposed on one another. (b) Noise recorded from a single channel .....	121
4.29	<i>In vivo</i> neural recording .....	122
5.1	A possible photodetector placement strategy for a 20 cm x 20 cm cage.....	129
5.2	Photodetectors placed flush against the container, and angles from different light source points .....	130
5.3	Photodetectors 20 cm away from container wall.....	131
5.4	Side view of the proposed detector system (20 cm x 20 cm).....	132
5.5	Photodetector placement for a 20 cm x 30 cm cage.....	132
5.6	Top view of the 20 cm 30 cm cage.....	133
5.7	Side view of the 20 cm x 30 cm cage.....	133
5.8	Ferro Solutions devices .....	138
5.9	Ossia Cota devices.....	138
5.10	Device interfacing with the Neuronexus CM32 probe .....	141
5.11	Three different LEDs proposed to transmit data .....	141
5.12	Manchester encoding combining CS and MISO.....	144
5.13	Manchester encoding combining SCLK and MISO.....	145
5.14	Transfer printing fabrication steps .....	148

## List of Tables

2.1 Recording only wireless devices.....	33
2.2 Commercial recording only wireless devices.....	34
2.3 Neural stimulating only devices .....	34
2.4 Neural recording and stimulating devices .....	35
2.5 Neural recording chips.....	35
3.1 Summary of results for random noise that was transmitted optically.....	79
4.1 The weight of the different components making up the device.....	99
4.2 The current draw of the different components.....	99
4.3 The current draw of the different parts of the amplifier chip as listed in the Intan datasheet .....	100
4.4 A summary of the fundamental characteristics of the device.....	100
4.5 BER measurements at distances from 0 to 60 cm.....	115
4.6 BER measurements at various distances and angles.....	116
4.7 Channel RMS noise.....	121
5.1 The weight of the main components in the default configuration.....	140
5.2 The weight of the main components using thin PCBs.....	140
5.3 The weight of the main components using thin flexible PCBs.....	140
5.4 The weight of the main components using thin flexible PCBs, and the inductively powered 3D coil.....	140
5.5 Manchester values tabulated depending on the input bit and clock values going through an XOR gate.....	144

## Abbreviations

AC	Auditory cortex
ADC	Analogue-to-digital converter
AHB	Advanced high-performance bus
APD	Avalanche photodiode
APB	Advanced peripheral bus
API	Application programming interface
BER	Bit-error rate
ChR2	Channelrhodopsin2
CMOS	Complementary metal-oxide semiconductor
CS	Chip select
DAQ	Data acquisition
DMA	Direct memory access
EEG	Electroencephalography
ENG	Electroneurogram
EMG	Electromyogram
FEC	Forward-error correction
FPGA	Field programmable gate array
GND	Ground
GPIO	General-purpose input output
GUI	Graphical user interface
IC	Integrated Circuit
IR	Infrared
LL	Low layer
LED	Light-emitting diode
LFP	Local field potential
LiPo	Lithium polymer
LVDS	Low voltage differential signalling
MCU	Microcontroller unit
MEA	Micro-electrode array
MRI	Magnetic resonance imaging
MISO	Master in slave out
MOSI	Master out slave in

<b>MUA</b>	Multiunit activities
<b>NIRS</b>	Near-infrared spectroscopy
<b>OCT</b>	Optical coherence tomography
<b>OFDM</b>	Orthogonal frequency-division multiplexing
<b>OOK</b>	On-off keying
<b>PAM</b>	Pulse-amplitude modulation
<b>PPM</b>	Pulse-position modulation
<b>PV</b>	Parvalbumin
<b>QFN</b>	Quad flat no-leads
<b>RF</b>	Radio frequency
<b>RGC</b>	Retinal ganglion cell
<b>SCLK</b>	Serial Clock
<b>SiPM</b>	Silicon photomultiplier
<b>SMA</b>	SubMiniature version A
<b>SNR</b>	Signal to noise ratios
<b>SOM</b>	Somatostatin
<b>SPAD</b>	Single photon avalanche diode
<b>SPI</b>	Serial peripheral interface cable
<b>SWCLK</b>	Serial wire clock
<b>SWD</b>	Serial wire debug
<b>ToF</b>	Time of flight

## Chapter I - Introduction

### 1.1 Motivation

It is fascinating to realize that a roughly 1.4 kg piece of tissue: the brain, is the repository for all our experiences and memories, while also holding the key to understanding how exactly our behaviour, thoughts and emotions are manifested. Despite its importance, very little is known about its exact operation, even with the strides that have been made in neural research in the last couple of decades. Neurodegenerative diseases also account for a large amount of healthcare expenditure with €134 billion[1] being spent per annum in the UK alone. Diseases like Alzheimer's and Parkinson's are ubiquitously present irrespective of geographical locations, and can severely decrease the quality of life for elderly patients while simultaneously affecting the lives of close relatives as well. It is not just the aging population that is at risk, however, as disorders such as epilepsy, anxiety, and depression can develop in anyone, regardless of age. Other conditions such as traumatic brain or spinal cord injuries leading to paralysis, and limb loss, are also prevalent and can drastically change the lifestyle of those suffering from it. The inherent complexity of the brain presents a number of difficult tasks that have long challenged neuroscientists, largely stemming from the sheer amount of information processed in the brain. The issue of monitoring and recording all this information, while simultaneously understanding the correlation between neural activity and behaviour, presents significant challenges. An average human brain is made up from 85 billion neurons, with the total number of synapses reaching a 100 trillion [2]. Like the notes in a musical symphony, the neural cells have to be in harmony to facilitate healthy signal transmission. Out of synch

firings with incorrect timings, or neural spike amplitudes that are lower or higher than what they should be are often the underlying causes for many neural ailments. Just reading this paragraph alone requires the combined processing power of this vast network, in many ways outperforming even the most advanced of super computers available today. While the basic structures of neurons are the same for each individual, the unique way in which they are networked, and the patterns with which they are activated produce the nuanced characteristics representative of each person. Using the current techniques available, it is impossible to observe all of these neural circuitries in the brain simultaneously. Due to this, most cellular level techniques focus on localized microcircuits made up from smaller populations of neurons. Several large scale enterprises have been established to enable the observation and study of larger population of neurons, such as the European Union commissioned Human Brain Project[3] and United States launched BRAIN (Brain Research through Advancing Innovative Neuro technologies) 2025[4] initiative. While understanding the human brain is the primary goal, it is important to develop experiments for simpler nervous systems present in animal models. These types of trials have less restrictions, and can be rapidly facilitated due to reduced costs, and less rigorous approval requirements. They allow us to draw conclusions about how the neural activity detected in lesser nervous systems can be correlated to our own. Although alike in many aspects, care must be taken to pinpoint the distinctions observed in animals, and to meticulously examine which findings may be relevant to humans. Despite the differences, there is large amounts of evidence showing how similarities exist between the nervous systems of different organisms, and how several important characteristics and structures are preserved throughout the evolutionary spectrum, all the way from simpler to more complex animals. By identifying key neural circuits, and deciphering their exact roles in animal models such as mice and rats, connection can be discovered that may just as well apply to our own nervous system.



Currently available advanced solutions can wirelessly record  $<16$  channels worth of data from mice, providing a very limited view of the total activity of the  $\sim 8 \times 10^7$  neurons present. To gain a more comprehensive picture, it is imperative to scale up recording capabilities to a level where thousands of neurons can be interrogated from numerous brain structures simultaneously. The current method of carrying out numerous independent recordings for different brain regions of interest introduces uncertainties, as the animal may exhibit various behavioural and physiological states throughout the separate recording sessions. This makes it progressively difficult to decode which behaviour is associated with what neural activity for data sets created from an increasingly large number of experiments. Having the capability to carry out high spatial resolution recording from several brain structures simultaneously would significantly improve data integrity. Furthermore, by increasing the channel count, drug interactions across multiple areas could be synchronously observed for pharmaceutical research, while connections between different brain areas may also be better understood. Existing wireless neural recording systems for freely moving animals are primarily based on RF technologies which typically have a trade-off between power consumption, size, and data rate. Ideally all three of these requirements should be satisfied, however, due to the relationship between increased data rates requiring more power from larger and heavier energy sources, this is currently impossible. By using visible light communication (VLC) in a neuroscience context, a novel solution characterized by low power high data transmission capabilities is presented to address these issues. Previous optical based methods were either very limited in data transmitting capability, or extremely sensitive to alignment. Here we demonstrate a system capable of high bandwidth neural information with the option to scale up even further, and plans to translate to a freely moving setup. The system presented in this work offers a solution that satisfies the core requirements. It is light weight (5g) with a view to reduce even further to  $<3g$  with simple modifications, low power enough to operate for several hours, has the

capability to transmit large amounts of neural data, and the potential to scale up to many thousands of recording channels.

## 1.2 Thesis Outline

Chapter II will introduce the background discussing how neurons work, and the microelectronic techniques used to study them. It will also delve into state of the art devices currently available and explore the limitations of current solutions. Wireless data transmission methods, such as ultra-wide bandwidth and regular radio frequency modulation schemes, will be briefly discussed, while outlining the physical restrictions for applying them in low weight devices. The basics of visible light communication are introduced while emphasizing the potential benefits of using it in neuroscience experiments involving small animals. Finally stimulating procedures such traditional electrical excitation, and newer optogenetic methods developed for mice will also be discussed. To initially test the central concept, an *in vitro* quasi wireless VLC device was developed and is outlined in Chapter III. While the neural data was relayed wirelessly, the synchronizing clocks and power were still received through a wire at this stage. The complete system involved a custom developed PCB incorporating an Intan amplifier chip and data transmitting LED, which was interfaced with a 61-channel electrode array containing mouse retinal tissue. The neural data was then received by a photodetector. Clock signals and the received optical signal were then recorded using an oscilloscope to carry out bit error ratio (BER) measurements. A further developed system allowed the neural data to be displayed in real-time using a graphical user interface. Chapter IV demonstrates a fully wireless device that includes its own power source and Microcontroller Unit (MCU) for providing the necessary clock signals and commands. Additionally to the data stream, a clock signal was also sent optically for data reconstruction and synchronization purposes on the receiving end. The two optical streams were different in wavelength and separated by appropriate filters. The device was initially tested by placing a connected neural probe

in saline solution where dummy neural spikes were introduced. It was then characterized at various emitter-detector angles and distances by calculating the BER at given locations. Other parameters of the system, such as reference noise, operating time and power consumption, were also measured. Lastly, an *in vivo* experiment was carried out, with the device being implanted in a head-fixed awake mouse. Chapter V concludes with discussing the overall parameters and performance of the device, and outlines further developments that may be pursued. The integration of custom made LEDs for data transmission, to allow even higher data rates, will be discussed. Other powering solutions to replace the battery, such as inductive methods and other upcoming novel methods are analysed. Weight reduction strategies such as using different PCBs and different components will also be deliberated. The possibilities for transitioning to a system where the animal could move freely are also outlined, with potential photodetector and observational area arrangements demonstrated.

## References

- [1] N. A. Fineberg *et al.*, “The size, burden and cost of disorders of the brain in the UK,” *J. Psychopharmacol.*, vol. 27, no. 9, pp. 761–770, 2013.
- [2] A. P. Alivisatos *et al.*, “Nanotools for neuroscience and brain activity mapping,” *ACS Nano*, vol. 7, no. 3, pp. 1850–1866, 2013.
- [3] “Human Brain Project Home.” [Online]. Available: <https://www.humanbrainproject.eu/en/>. [Accessed: 01-Jul-2017].
- [4] “BRAIN 2025: A Scientific Vision,” 2014. [Online]. Available: [https://www.braininitiative.nih.gov/pdf/BRAIN2025\\_508C.pdf](https://www.braininitiative.nih.gov/pdf/BRAIN2025_508C.pdf). [Accessed: 01-Jul-2017].

## Chapter II - Background

### 2.1 The Nervous System

The building blocks of the nervous system are neurons (Figure 2.1), which communicate using signals that are generated by the rapid electrical depolarizations and repolarizations across their membranes. The method of transmission for spiking neurons is binary, that is, they either fire or they do not. The frequency of the firing rate and pattern of spikes determine the information encoded in the signal being relayed. The local electrical fields within and outside the neuron are due to the different concentration of positively and negatively charged ions present in neural tissue.

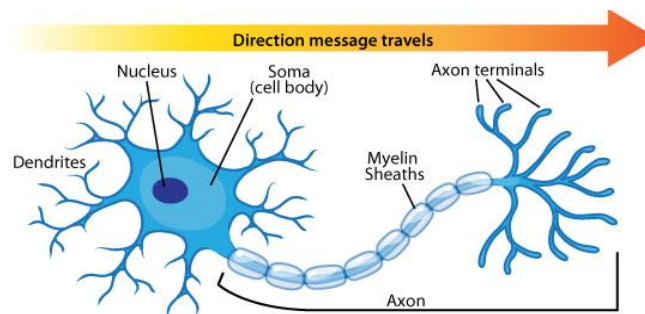


FIGURE 2.1: Structure of a typical neuron. The signal cascades towards the axon terminals along the axon. Image from [1]

The primary ions present are calcium, sodium, potassium and chloride, with their concentrations being regulated by voltage gated ion channels (Figure 2.2). The resting potential of a typical neuron is typically in the range of  $-85$  mV to  $-60$  mV [2]. However, this can rapidly increase if an outside stimulus results in the voltage passing a threshold value of typically around  $-55$  mV. What follows is a series of depolarizations and repolarizations, or action potentials (Figure 2.3) cascading down

the axon of the neuron all the way to its terminal, where communication can continue with neighbouring neurons across the synapses. Synapses can come in the form of electrical and chemical varieties, with each type serving a specific purpose. Electrical synapses are quicker, and usually activate most of their neighbouring neurons through the gap junctions, while chemical synapses allow more control by being capable by individually activating specific neurons.

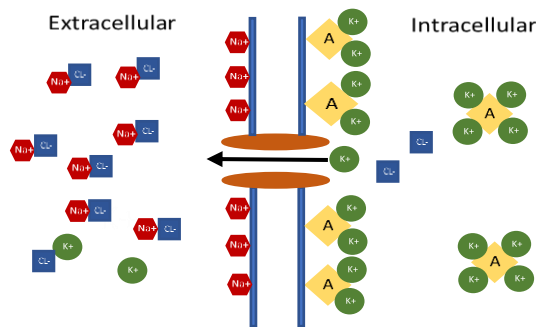


FIGURE 2.2: Typical ion channel, controlling the concentration of ions across the membrane of the neuron. The selective pumping of potassium ions out of the cell creates a net negative charge in the intracellular region, while creating a net positive charge in the extracellular region. This leads to the aligning of the positive sodium ions on the outside of the membrane and negative anions on the inside of the membrane resulting in the resting potential. Chlorine and membrane impermeable anions indicated with “A” also contribute to the overall charge distribution around the membrane.

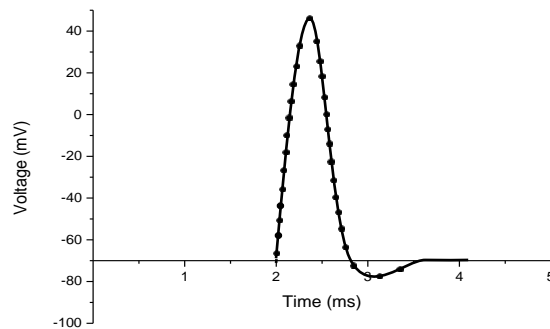


FIGURE 2.3: Action potential of a neuron. If a stimulus exceeds a certain threshold, the selective transport of sodium ions into the cell repolarizes the membrane leading to a rise in its potential. Once the peak is reached voltage gated potassium channels open, allowing potassium to exit the intracellular area leading to the depolarization of the membrane.

## 2.2 Techniques for studying the nervous system

There are large number of fields that have been developed to study the nervous system by either observing, stimulating, recording or imaging neural tissue or activity. Each of these methods encompass several sub fields that are out of the scope of this work to cover in full detail. The following section will give a brief overview about some of these techniques, with references provided for more in-depth explanations and studies. Non-invasive techniques such as electroencephalography (EEG) and magnetic resonance imaging (MRI) provide information about what happens in the brain on a global level, but are not capable of giving insight into what transpires on a local cellular level. EEG detects information from electrodes placed on the scalp, and records the local summation of electrical activity from thousands of neurons[3]–[5]. It is characterized by poor spatial resolution, and and superior timing characteristics compared to MRI, with optimum sampling at 0.5 kHz[6]. MRI creates a strong magnetic field around the tissue, which excites the hydrogen atoms present that then generate a measurable radio frequency signal, which is then detected by a receiving coil[7]. The rate at which the excited atoms return to their equilibrium can then be used to visualize the tissue. In contrast to EEG, the spatial resolution is superior, however, the temporal resolution is significantly lower (20-50 ms)[8]. Near-infrared spectroscopy (NRIS) is a non-invasive technique, which involves applying IR light in the range of 650-950 nm. At this wavelength, light passes through neural tissue with ease, with oxy-(O<sub>2</sub>Hb) and deoxy-hemoglobin (HHb) being the main absorbers. By interrogating the reflected light, blood flow behaviour can be deduced, giving an indirect quantification of neural activity [9]. The non-invasive nature of EEG, MRI and NRIS allow them to be readily applied to humans as well. This makes them some of the only practices that enables direct insight into a how a human brain might work *in vivo*. Imaging technologies such as confocal, two photon and multi-photon spectroscopy are methods where light is directed onto fluorescent containing molecules injected into the target tissue[10], [11], and can give insight on a single neuron level.

The energy transferred from the light to the tissue excites the fluorescent particles, allowing visualisation using scanning methods. This allows neural tissue volumes to be imaged in a 3-D fashion up to depths of a  $\sim 100$  microns [12], with sub-micron resolutions. The requirement for large scale equipment to precisely target the tissue of interest with focused beams of light constrains the technique to *in vitro* or fixed *in vivo* imaging. Optical coherence tomography (OCT) involves interferometry techniques using long wavelength light usually in the IR range to allow deeper tissue penetration [13]–[15] ( $\sim 1\text{--}2\text{mm}$  depending on the light source). By manipulating the light sources to different depths, image slices are created that are then imposed on top of each other to create a 3D image [16]. This allows larger volumes of tissue to be visualized compared to spectroscopy, however the lateral resolutions are also lower [17]. Similarly to spectroscopy, the need for complex apparatus and time consuming setups make OCT constrained to specific types of experiments, and not suitable for freely moving animals.

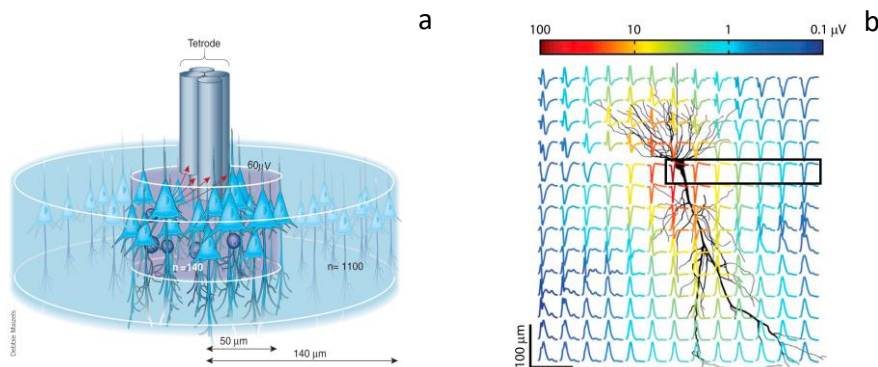


FIGURE 2.4: (a) A tetra electrode fiber made from four small electrode wires inserted into neural tissue. Using these type of multisite recordings, techniques such as clustering and triangulation can be used to estimate the position of neurons. The red arrows indicate the distance of neurons from the electrode, while the cylinder with a radius of 50 microns contains  $\sim 140$  neurons with spike amplitudes of  $>60 \mu\text{V}$ . The larger cylinder with a radius of 140 microns contains  $\sim 1100$  neurons. Image from [18] (b) Extracellular spiking activity around a firing pyramidal cell, showing the effect of an action potential on the local field potential. The signal is strongest at the soma of the cell, with attenuation taking effect away from the cell body. The spikes are normalized, with the colour coded bar on the top indicating their peak to peak magnitude. Image from [19]

## 2.3 Electrodes and Wired Methods

Invasive recording techniques concentrate on detecting the electrical activity such as voltage changes, when neurons are firing [20]. Materials that are sensitive to the potential differences present in neural tissue are fabricated into fibres, neural probes and arrays and inserted into intra-cellular space to sense the neuronal activity (Figure 2.4). The electrodes must be capable of penetrating the tissue, and are shaped in way to have micro scale sharp tips. Different configurations have been fabricated with varying number of shanks and recording sites, with devices containing a 1000 channels already being demonstrated as shown in Figure 2.5 and 2.6. The neural probes are usually interfaced with recording devices through regular wired connections as they are the most prevalent and easy to implement. The tension present in the cable connecting the animal to the data capturing apparatus, inevitable constraints movement, making the observation of authentic freely moving behaviour difficult[21]. Additionally, infection and injury are also more likely to occur as the irritation and chafing present at the site of insertion can quickly damage tissue[22][23]. Because of this, minimally invasive high channel recording wireless solutions are required that allow the observations of many neurons at different locations simultaneously. To study animals in a way that they maintain their authentic behaviour, it is desirable to design devices that are minimally intrusive, and would allow the subjects to move untethered. Additionally, due to the fast firing rates of certain neurons (up 611 Hz instantaneous frequency[24]), high sampling rates and bit resolutions are required to allow the data to be recorded with sufficient detail. The Nyquist rate imposes restrictions with respect to what this minimum rate can be. Since spikes can show frequency components up to 10 Khz, sampling rates of  $\geq 20$  Khz are required to capture the fine details of the spikes sufficiently [25]. Other techniques such as patch clamp methods enable the potentials to be recorded from inside the cell.



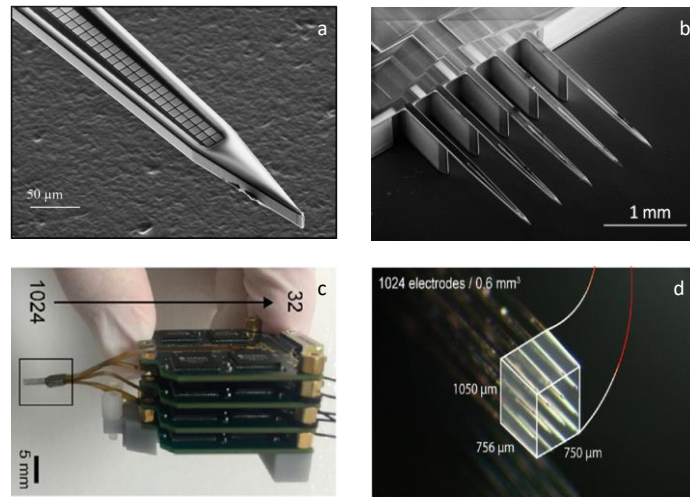


FIGURE 2.5: (a) Neural shank containing 200 electrodes[26] (b) 5 shank version containing a total of a 1000 recording sites[26] (c) Head-front stage for all the IC required to process the incoming neural data for probes shown in (c)[27] (d) 3-D probe array containing a total of 1024 electrodes[27]

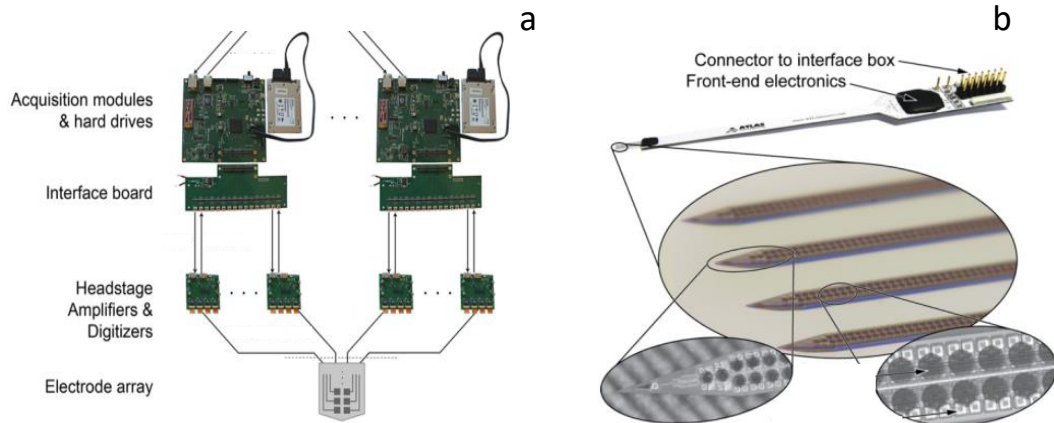


FIGURE 2.6: (a) Recording apparatus for a 1000 channel data acquisition system consisting of an electrode array, headstage amplifiers and digitizers, interface boards and acquisition modules and hard drives[28] (b) Recording probe with four shanks and 257 recording sites. However, not all sites are simultaneously accessible. Using electronic depth control (EDC) groups of sites can be activated along the shank to allow depth specific recording[29]

## 2.4 RF Based Wireless Methods

The primary mode of data transmission for most wireless neural recording is based on radio frequency (RF) protocols. Table 2.1 at the end of the chapter summarizes the currently available devices, where a correlation between the amount of data that can be transmitted with respect to size can be seen, with larger devices reaching speeds of 48 Mbit/s[30]. At a weight of 46.1g this is suitable for larger animals like primates, but not for rodents, which are an important primary animal used in neuroscience experiments[31], [32], and are often used to validate experimental protocols before moving to larger animals. Due to their small size, there are severe size and weight limitations that have to be adhered to. While there is no weight limit that can be allowed for head mountable devices, it is desirable to keep it as low as possible, and to not exceed 10% of the total body mass of the animal[19][33] (3.5g for an adult male mouse). This limits the possible size and weight of the power supplying component of the device, and the energy available for RF transmission. It makes most protocols, consuming 10s of mAs, too power hungry[34] to allow sustained recordings at the scale of hours. It also imposes a boundary on the size of the antennas, and consequently the maximum data transmission that can be carried out according to the Shannon-Hartley theorem and the Chu-Harrington limit[35]–[37].

The Shannon-Hartley theorem is defined as:

$$C = B \log_2 \left( 1 + \frac{S}{N} \right) \quad (1.1)$$

and expresses the theoretical upper bound for data rates for a given channel,

where:

$C$  = Capacity in bps

$B$  = Bandwidth in Hz

$S$  = Received signal power in W

$N$  = Average power of noise and interference in W

This equation shows that the capacity can be increased in the following ways: Increasing the bandwidth, increasing signal strength, and reducing the noise. The signal strength is defined by the electromagnetic field strength of the source and distance from it, while noise levels are often intrinsic to the environment. In a real-world application, the S/N ratio will always be limited. Given optimum conditions however, different modulation techniques, such as quadrature amplitude modulation QAM can be applied. Using these techniques, the amplitude can be resolved into more discrete levels that correlate to fundamental units of information, thus increasing the throughput per radio wave. The bandwidth is also influenced by the Q-factor of the antenna and is defined by the following equation developed by Chu-Harrington:

$$Q \geq \frac{1}{k^3 a^3} + \frac{1}{ka} \quad (1.2)$$

Where:

$a$  = radius of the smallest sphere the antenna can fit in

$Q$  = Q-factor

$$k = \frac{2\pi}{\lambda} \quad (1.3)$$

$$\lambda = \frac{c_0}{f}, \text{ where } c_0 = \text{speed of light} \quad (1.4)$$

The  $Q$  factor can also generally be expressed for a resonant system as:

$$Q = \frac{f_c}{f_2 - f_1}, f_2 - f_1 = \frac{f_c}{Q} \quad (1.5)$$

Where:

$f_c$  = centre frequency

$f_2$  = upper frequency band limit

$f_1$  = lower frequency band limit

and defines how underdamped an oscillator such as an antenna is, and influences the maximum bit rate, energy required to operate at a given frequency, and the range at

which it can operate. Higher  $Q$  values are associated with lower bandwidths, resulting in lower  $Q$  values being desirable for high throughput broadband applications. (1.5) shows that the bandwidth  $f_2 - f_1$ , can be increased by either increasing  $f_c$  or decreasing  $Q$ . As  $f_c$  is increased,  $\lambda$  decreases, requiring a smaller antenna size for efficient coupling. However, (1.2) shows that as the antenna size  $a$  decreases,  $Q$  increases, resulting in a trade-off that needs to be considered when deciding the optimum antenna design.

Additionally to the fundamental physical limitations outlined above, centre frequencies and accompanying frequency bands are also strictly regulated by Ofcom in the UK and put further restraints on RF links. These combined factors lead to the limited capacities at which small head mountable RF devices can operate.

Attempts have been made to condense the detected information as well to allow the sending of more data from a single recording device[23][38]. While these compression techniques are suitable for preserving the crucial characteristics of the neural behaviour, they often omit information that is required for certain tests: such as sleep wake experiments, where long times of neuronal inactivity are also of interest. A large number promising devices also have never left the bench, and were tested with restricted conditions making assessment of its applicability in live animals difficult[39]–[42]. Commercial devices are also limited due to the constraints intrinsic to wireless applications, with devices either being too heavy[43], or having too few recording channels[44].

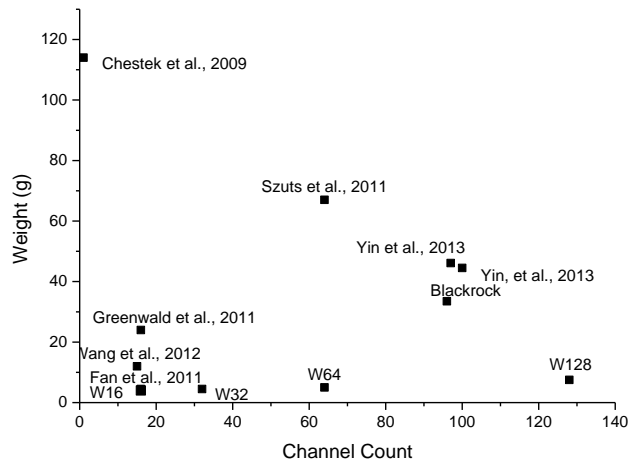


FIGURE 2.7: Channel count to weight ratio in currently available devices. Only devices that were tested *in vivo* utilising all channels simultaneously without doing any spike sorting or compression were included.

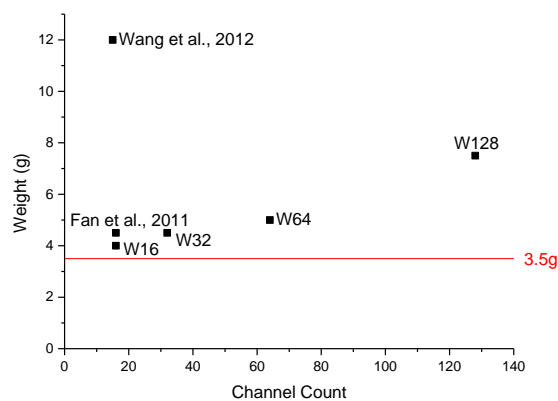


FIGURE 2.8: (a) Sub 20g devices from the graph in figure 2.7. The red line indicates the 10% of total body weight limit that could be head mounted on a mouse (assuming a body mass of 35g).

Tables 2.1-2.5 at the end of this chapter and figure 2.10 summarize the different wireless devices that have been made. A substantial number of these devices are aimed at larger animals from rats, through to primates. Very few are specifically designed for mice, and even less have been verified in freely moving mice, most likely due to the fact that they have weights that are still too heavy for the animal to sustain for longer periods (Figure 2.7 and 2.8). The W-series Triangle Biosystems range of devices are advertised for mice for up to 32-channels with a weight of

4.5g[45]. They use two dipole antennas to transmit the data using RF transmission, centred around a carrier frequency of 3.05 GHz, and bandwidth of 50 MHz. The analogue signal from the different channels is amplified, multiplexed, and sampled at 50 KHz. Using a voltage controlled oscillator, frequency modulation is carried out to transmit the signal. Since no analogue to digital conversion is carried out on the head stage (processed on the receiving end), direct comparison of equivalent transmitted digital data is not straightforward. Based on the number of channels that are transmitted, however, estimations can be made. Taking into account that a sampling rate of 20 KHz at 12 bit resolution is sufficient per sample to maintain spike characteristics, for the 32 channel 4.5g system, we get  $\sim 7.68$  Mbps. Newer devices such as the Taini[46] manage to reduce the weight to sub 3g levels, but are still constrained by the data limitations imposed by RF links, and do not demonstrate the transmission of more than 16 channels of data in a small package. Turcotte [38] also demonstrate a 32 channel wireless recording system for mice with a weight of 4.9g. However, the device was only tested with mice in head fixed conditions with the data transmission being lossy due to the compression technique involved.

Other approaches incorporate the use of ultrasonic modulation techniques (Figure 2.9) for both powering the device, and receiving the data through backscatter analysis[47]–[50]. The core of this technology involves exploiting the bidirectional nature of piezo electric materials. Sound waves are used to resonate piezo electric receivers that generate energy to power on-board circuitry. The detection of neural signals involves analysis of backscattered ultrasonic waves from the receiver, which will also resonate and generate an electrical signal in accordance with the detected neural activity. This allows devices to operate without any energy source or IC components required for data transmission, making them extremely lightweight and small with near sub mm dimensions already being reached. They suffer from high ground floor noise levels (180  $\mu$ V). However, with research being conducted into transducers with improved drive electronics, lower noise, and higher power densities at the focal points, this is a promising area. While suitable for electroneurogram (ENG) and electromyogram

(EMG) measurements, the large base noise does not allow the recording of smaller neural spikes especially prevalent in the central nervous system, which require better signal to noise ratios (SNR). Their data rates are also in the lower range at 0.5-1 Mbps per implant. This is acceptable since due to their small size, numerous devices could simultaneously be inserted, each monitoring a group of neurons at a given location. The downside, however, is that as of now the devices are very alignment sensitive, and there are no methods that allow the individual addressing of separate implants, with research ongoing into creating transducers that can use beam steering to selectively activate implants. This could potentially be solved by the further miniaturization of the transducer allowing mounting on the back of the animal. While more applicable to implants than head mountable devices, sound waves have the benefit of scattering significantly less within tissue, allowing higher power levels to be transmitted and increasing source-detector distances. FCC and FDA regulations limit the energy that can be propagated within tissue, correlated to the amount that would result in the heating of it by 1 C°. This translates to 10 mW/cm<sup>2</sup>[51] and 720 mW/cm<sup>2</sup>[52] power densities being specified as the upper limits in EM and ultrasound based transmissions respectively. As outlined above the approach in its current state is not without its limitations, however, its small weight and size coupled with the high energy densities that can be transmitted using ultrasound make it an attractive option worth exploring.

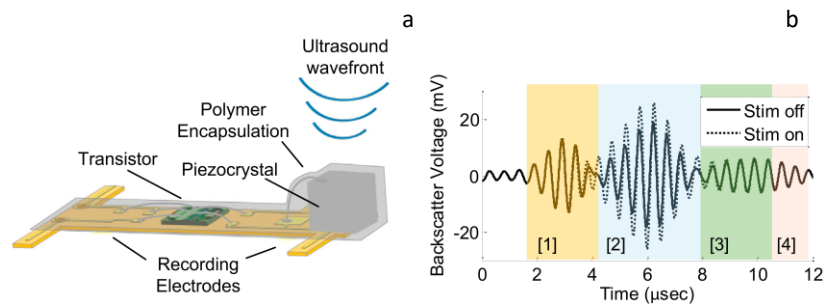


FIGURE 2.9: (a) Layout of the implant (0.8 x 3 x 1mm) with the electrodes connected to the transistor and the piezoelectric component. Image from [46] (b) Reflected backscatter used to identify the different boundaries of the implant. [2] is correlated to the piezoelectric component, which resonates depending on the electrophysiological activity. Image from [49].

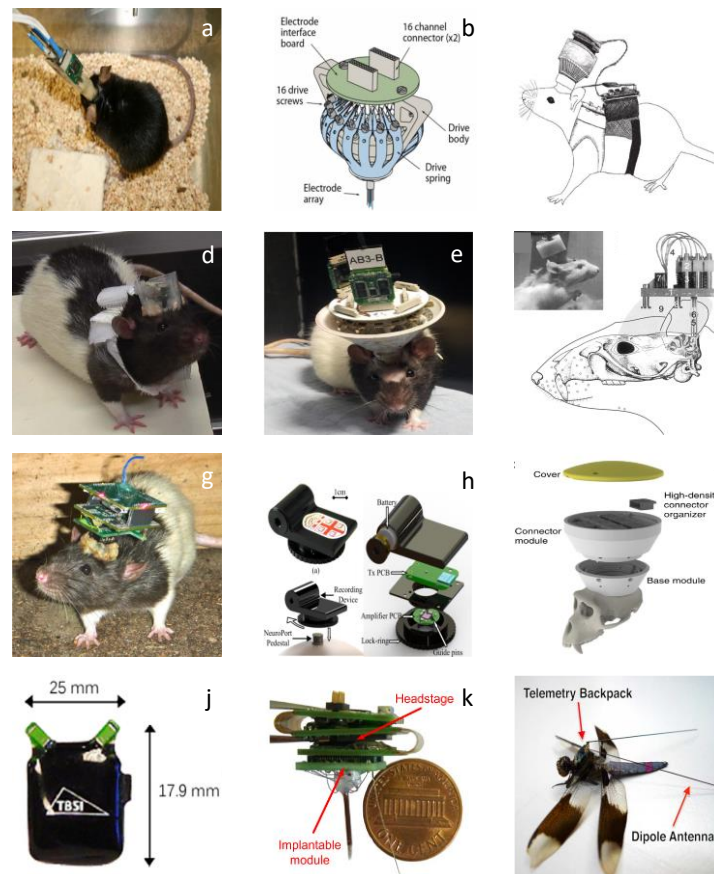


FIGURE 2.10 **Summary of wireless devices:** (a) A wired system containing an accelerometer and neural processing headstage mounted on the head of a mouse. The large cables protruding can severely restrict movement[53] (b) Flexdrive head mountable wired device with microdrives allowing depth control of 32-64 recording electrodes. The device is light at 2g but requires wires to connect through the 16 channel connectors[54] (c) Recording system for rats with a backpack. The entire systems weighs 67g[33] (d) A wireless device mounted on a rat with precision microdrives. The device weighs over 16g[55] (e) A wired headstage for rats with microdrives[56] (f) Side view of a typical headmounted device with its electrodes inserted into the brain of a rat[57] (g) RoSco, another headmountable device for rats, weighing 22g[58] (h) A wireless neural recording device, designed for primates, weighing 46.1g and capable of transmitting data at 48 Mbps. This makes it one of the fastest demonstrated wireless devices for freely moving animals[30] (i) Exploded view of a 512-channel wireless recording system for primates. The system carries out spike detection and sorting by compressing the data down into a 8 Mbps streamline[23] (j) 32 channel commercially available wireless headstage from TBSI. Although advertised for mice, its weight of 4.5g likely makes movement difficult for the animal[45] (k) A dual-purpose device capable of recording and stimulating 32 channels. The device weighs 4.9g with the battery making it heavy for freely moving mice. The device was tested on *in vivo* head fixed mice with one optogenetic stimulating fiber coupled to an LED, and 8 electrodes detecting neural spikes. The device compresses the data to allow transmission across a 1.4 Mbps RF link[38] (l) A wireless device designed for dragonflies. Insects impose even greater size and weight restrictions than mice, making design particularly challenging. The device is capable of recording 10 neural channels, and transmitting 5 Mbps of data through its RF link, and was bench tested using simulated conditions[42]



## 2.5 Optical based neural data transmission

The transmission of biological data using optical signals has been attempted by Donati et al., [59]–[61]. These initiatives, however, were limited with respect to the amount of data they could handle due to the restrictions of numerous key technologies at the time, and were used to detect slower neural spiking along with polygraphy measurements. The lack of digitizing circuitry on the device also makes the processing of recorded data, and interfacing with computer systems difficult. A number of coherent light based techniques have been developed to send neural data[62], [63] with data rates of  $\sim 5$  Mbps being reached. Nurmikko et al.[64], [65] have used an IR vertical-cavity surface-emitting lasers (VCSEL) (Figure 2.12). VCSELs are fabricated by sandwiching a laser cavity between two mirror layers. The cavity contains quantum wells that are provided with current through an injection site. Photons are generated, which get pumped and reflected between the mirror layers, producing a narrow beam transmitted through an opening on the device. They can provide high data rates in the Gbps range with low bias current consumptions of  $<10$  mA[66]. The narrow beam and opening, however, means that VCSEL based systems are also very sensitive to alignment, where a small mismatch on the order of mm between the transmitter and receiver can break the link[52], making it difficult to implement with freely moving animals. While the wide-angle dispersion of other light emitting devices such as LEDs may be considered as a disadvantage for certain applications, such as coupling into a fibre, it is indeed beneficial for cases such as being a data transmitter for freely moving animals. The large dispersion angle enables coupling between the transmitter and receiver at a wide range of alignments possible with an unpredictably moving source such as freely moving animal. Figure 2.11 illustrates how the beam dispersion differs for different light sources.

The VCSEL based system in figure 2.12 received its power and necessary clock signals through an inductive coil. This method, however, can further restrict operating

distances, limiting it to  $<5\text{mm}$ . Thus again make it difficult to apply to freely moving animals.

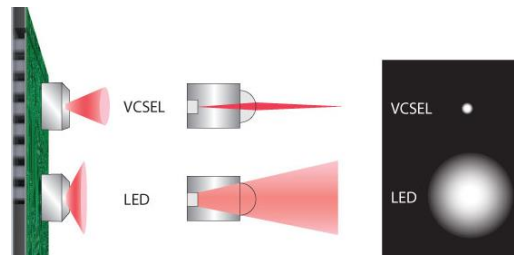


FIGURE 2.11: The dispersion profile of LEDs vs VCSELs. The VCSEL produces a much narrower beam of emission, which is not suitable as an unpredictable freely moving transmission source. The LED on the other hand produces a much wider profile, making it suitable for a much broader range of detector transmitter arrangements. Illustration from [67]

The device was tested in anesthetized rats and head fixed primates, with the total weight of the device being unspecified. The distance of transmission was 3 mm, with no indication of how the clock and power delivery would scale with further separation. While not directly stated, the inferred data transmission rates that were performed during the *in vivo* experiments were 6.52-7.68 Mbps.

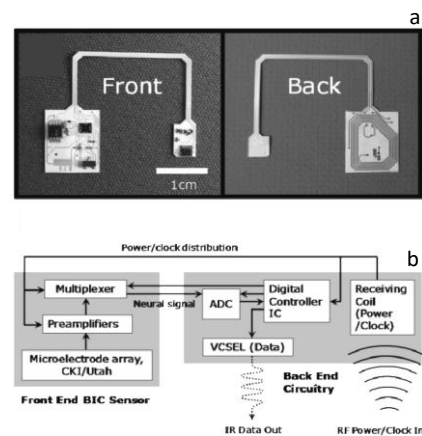


FIGURE 2.12: A VCSEL based neural recording device, tested in head fixed primates, and anesthetised rats (a) Photographic images showing an implantable 16-channel microsystem with a dual-panel liquid crystal polymer substrate. A spiral pattern of RF power receiving coil is clearly visible in the backside image. Image from [64] (b) Block diagram of the dual-panel microsystem showing neural signal and power/clock flows among various micro- and optoelectronic components. Image from [64]

## 2.6 Visible Light Communication

The growing drive for increased wireless data transmission, coupled with the progressive congestion of RF bands available for sending information, has led to alternative wireless techniques to be explored. Visible light communication (VLC) is emerging as one of the most promising solutions, with the potential for increased data rates across a high bandwidth range available ( $>300$  THz). So far most of the VLC research has focused on providing solutions for general communications problems such as complementing and extending the capabilities of global wireless networks such as 5G and beyond. However, the low power, energy efficient high-data rate nature of the technology gives it the potential to make it suitable for biomedical applications, such as small-scale neural interfaces with the ability to transmit vast amounts of information. The device demonstrated in this work outlines a system where VLC is applied in such a framework, with the view to developing a light weight device with the capability to record from thousands of channels and beyond. VLC is a technique that allows information to be transmitted using light (Figure 2.13). Signal transmission by diffuse radiation has been explored as far back as the 1980s[68], however, a more comprehensive overview outlining the more recent advances can be found in [69]. A source such as a light emitting diode (LED) is modulated at high frequencies, with each on or off state being analogous to a digital one and zero. This is referred to as on-off keying (OOK), and is the simplest form of modulation techniques, yielding the lowest data rates and spectral efficiency ( $1 \text{ bits s}^{-1} \text{ Hz}^{-1}$ ). For the device presented in this work OOK was used, as it allows data transmission with the least amount of complexity, while also maintaining low power requirements. Higher bandwidth data transmission protocols are available such as Pulse-Amplitude Modulation (PAM), wavelength division multiplexing (WDM), and orthogonal frequency-division multiplexing (OFDM) [69]. These require additional circuitry and components, thus further increasing the total size, weight and power consumption. Connecting the data transmitting LEDs to the digital lines allows them to be driven

directly, with minimal additional power required to operate them, while still maintaining a small overall footprint. The photons emitted by the LED are detected by a photodetector that can then relay the information for processing. Depending on the rise and fall times of the LED, speeds up to 10 Gbit/s can be achieved using a single transmission source with OFDM[70]. Additionally, using parallel light sources transmission rates in excess of 100 GBit/s have been reached[71]. A wide number of different types of light emitters have been explored for data transmission purposes such as organic LEDs, RCLEDs, laser diodes, VCSELs and GaN LEDs. Through the careful selection of appropriate materials, p-n doping percentages, and structure dimensions, LED characteristics such as colour/wavelength and timing responses can be engineered to suit link requirements. A key factor that determines the timing, and consequently maximum data rate capability of the LEDs is the charge carrier lifetime within the quantum wells, which decreases with increased carrier densities associated with larger injected currents per unit area. Because of this, small area micro area LEDs typically operate with larger current densities and higher bandwidths, and have been demonstrated to reach rates of Gbit/s and beyond [69], [70]. For the device presented in the thesis however, generic off-the shelf LEDs were used (section 3.3.1 and section 4.2.7), as they offered improved performance compared to standard RF methods (<5 Mbps in <3g devices) and are easier to interface than custom fabricated micro LEDs.

The data link between the transmitter and receiver can either be line of sight (LOS) based, or diffused. LOS methods typically involve a narrow beam of light, such as one emitted by a laser diode, or VCSEL. Due to their low divergence angles [72], and sensitivity to blocking, these light sources are typically not suitable for freely moving animals. As discussed in section 2.5, VCSELS have been demonstrated to reach high data rates using low currents [73]. Most research that explored their use in VLC applications however, employed fixed, point to point data transmissions using optics placed in front of the transmitter and receiver [66], [74]; a scenario not practical with live animals. Recently, commercial VCSELs with diffusers mounted on them have

been introduced and developed for time of flight (ToF) applications[75][76]. While this does increase their viewing angle, the added complexity and weight to the system imposes a negative trade-off compared to readily available high angle LEDs specifically designed for wide area emissions. Furthermore, at low currents and voltages their optical output characteristics (on the scale of  $\mu\text{Ws}$ ) [77] [72] don't compare favourably to LEDs (on the scale of mW) [78], [79], thus making them less suitable for low-power systems. The device presented in the paper is capable of driving through its amplifier chip at a maximum potential of 3.3V and 2 mA, thus severely limiting the optical power that VCSELS could provide.

A much more feasible solution is using diffused light sources such as wide-angle LEDs, which offer increased coverage and mobility at the cost of increased path loss. Bare LED chips without any optics on them typically emit light in Lambertian pattern. The radiation pattern is modelled for a number of commercially available LEDs in [80], demonstrating the high viewing angles ( $>100^\circ$ ) that are achievable. The main source of light loss, which arises from the refractive index difference between the ambient medium and semiconductor, can be mitigated by the use of integrated reflectors and incorporating various optics into the packaging [81], [82]. While there are higher angle LEDs than the one used on the device (section 3.3.1 and section 4.2.7); there is typically a trade-off between irradiance and viewing angles. High irradiance LEDs typically have narrower beam profiles and will have favourable performance when directly facing the photodetector. However, they will have sub optimum characteristics when the angle between an LED and photodetector becomes larger, making them difficult to implement without using a large number of detectors for freely moving animals. Diffused LEDs on the other hand have reduced intensities when aligned with a receiver, but have more uniform responses across a wider range of orientations. Typical off-the-shelf LEDs have viewing angles ranging from  $10^\circ$  -  $180^\circ$ . A number of potential alternative LEDs with wider viewing angles are listed in appendix 5.1.

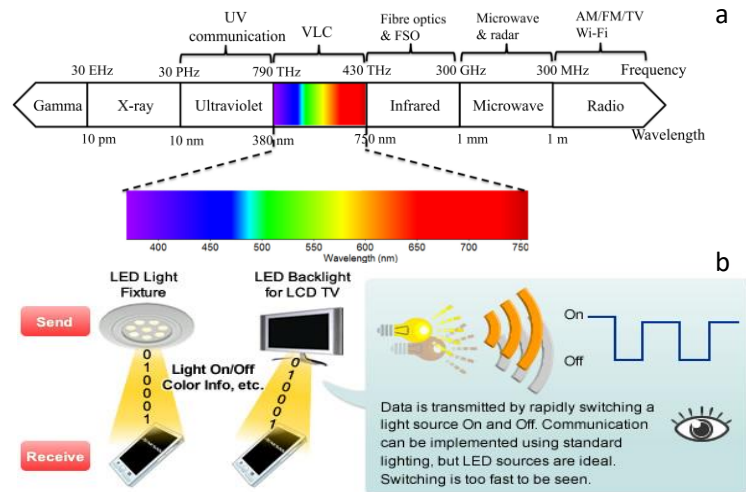


FIGURE 2.13: (a) The electromagnetic spectrum, indicating the visible light wavelengths [69] (b) The basic principles of VLC. A light source is modulated at high frequencies with each state being analogous to a digital 1 or 0. Image from [83]

Optical to electrical converters such as photodetectors or optical receivers are required to transform incident light into electrical signals that can be digitized for further processing. These include photomultiplier tubes (PMT) which generally have low quantum efficiencies (25% at 4° nm) and require high voltages to operate (1-2 KV). This coupled with their delicate and fragile nature make them impractical and expensive to implement in most animal laboratories.

PN diodes are intrinsically photosensitive however are generally inefficient due to the limited depletion region that they naturally possess. PIN diodes are more improved in this regard and have superior photosensitivity with the added intrinsic layer introducing additional charge carriers thus improving performance. Their main disadvantage however is that they completely lack any internal gain making them less sensitive to low irradiance light sources such as those present on the neural data transmitting head mountable device. APDs operate at voltages beyond breakdown, resulting in impact ionization, and much improved gain (~100) and sensitivity to incident photons. However, they require high bias voltages (100-200V) and have significant associated noise. Furthermore, the larger the detector becomes the higher its capacitance and associated noise, while the increased thickness also restricts the

timing characteristic of the devices. SiPMs on the other hand maintain the characteristics of small APDs, and are made up from several thousands of microcell SPADs that have low capacitances and fast timing characteristics coupled with the increased sensitivity at low operating voltages ( $\sim 30\text{V}$ ).

## 2.7 Powering solutions

Powering of the implanted devices also presents significant challenges. The processing of neural signals requires a series of operations before it can be interfaced with recording apparatus. Since neural impulses are on the  $\mu\text{V}$  scale, an integrated circuit capable of amplifying these signals is required. The signal then has to then go through an analogue-to-digital conversion (ADC), while multiplexing several channels of data into a single stream for transmission. All of these processes require significant amount of power, and are constrained by fundamental hard limits dictated by the unit energy required to process a bit[25].

Designing a device from commercially available components leaves the user with not many options for neural amplifier chips, with Intan Technologies[84] being the primary provider of such devices. However, several research groups have demonstrated that a further decrease of power for amplifying ICs is possible (Table 2.5), with values as low as  $48.2\text{ pJ}$  per bit being reached[85]. While custom designed low power ICs could decrease the total power requirements, they are not within the scope of this thesis. Probes incorporating CMOS circuitry that carry out ADC and amplification have also been designed[86]. By integrating several of the key components onto a single device a severe reduction in size and power consumption can be reached, and will be further discussed in the future work chapter.

The powering solutions available for embedded devices can generally be divided into two major categories. Those that perpetually supply the system with power e.g. RF harvesting, and those that offer fixed capacity stored energy i.e. batteries. Both approaches have their pros and cons with the feasibility of their application being

highly dependent on the specific requirements needed for the experiment. Perpetual powering solutions have the advantage of infinitely supplying the device with energy as long as it is within the range of the transmitter. They also tend to have lower weights, with several receivers being in the mg range[87], [88]. The primary disadvantages, however, are that using small coils that would be feasible for mice, the operating distances are short, with working conditions usually requiring  $<5\text{cm}$  distances[65], [89], and the power supplied being insufficient to power more complex devices. Magnetic induction is one of the more widely used techniques used to provide wireless energy, but is limited.

Loops of the receiving coil are placed close to a transmitter. The field lines of the transmitting coil transect the loops of the receiving coil, and generate a current. The distance at which power can be efficiently transmitted is proportional to the coil loop size. To achieve sufficient power transmission efficiencies, either very large loop sizes, or very close distances are required, as the effectiveness of energy transfer decreases with the inverse square root of the distance from the transmitter. Higher efficiencies can be achieved by using resonant frequency based methods. The principle behind this technique lies in creating a transmission circuit that resonates at the same fundamental frequency as the receiving circuit, thus allowing coupling hence more efficient energy transfer between them. Despite the improved efficiency, the power provided is still insufficient for supplying most systems at distances over several cm. Commercial solutions as those provided by Ferro Solutions can supply up to 200 mW at 8cm[90], but are expensive, and still limited with respect to operating distances.

RF harvesting is another form of perpetual powering solution, where energy is collected from ambient sources derived from the multitude of wireless devices ubiquitously transmitting nearly everywhere. Similarly to induction based powering methods, the received energy is minimal and in the  $\mu\text{W}$  range, not nearly enough to power more energy hungry ICs such as amplifier chips. Solutions such as those developed by Powercast[91] involve specifically developed receivers and transmitters



that are suitable for low power sensors but lack the power to supply high channel recording systems. Photo-voltaic systems have also been developed[92] but again suffer from the same drawbacks as outlined before, and lack the capability to provide enough power to continuously run more complex devices.

Other wireless power techniques are also emerging, such as Ossia's Cota technology[93] or Energous's WattUp[94]. They use a transmitting unit made up from hundreds of miniature antennas, which are tuned and directed on the fly depending on the location of the device containing a receiver, pinging its position a hundreds of times per second. They are not yet commercially available, and will be further discussed in the future work chapter. While other data transmission methods will no doubt benefit from novel wireless powering methods as well, the fundamental limitation pertaining to RF bandwidth limits will still persist.

Fixed capacity energy storage units such as batteries, on the other hand are usually heavier, and eventually require either changing or charging. They can, however, supply much higher currents, giving them fewer limitations with respect to the possible components they can be integrated with. Due to the size and weight constraints imposed by what a mouse can tolerate, however, most batteries are unsuitable. The two main types that conform to the requirements are Lithium based batteries and coin cell batteries. Both types come in many different chemistries, providing different voltages. While coin cells are small, low in weight, and have high energy densities, they usually have low nominal voltages of about 1.5V that require step-up, and also have low continuous current limits in the  $<5$  mA range. High power zinc-air batteries can provide currents up to 30 mA at 1.2V, or  $\sim 8$  mA at 3.3V after using a high efficiency step-up IC. While this might be enough for lower power systems with fewer channels, it is insufficient for the data processing required for high bandwidth data transmissions.

## 2.8 Stimulating techniques

### 2.8.1 Electrical Stimulation

To properly understand the brain, it is important to not just observe nerve cells *in vivo*, but to activate them in a targeted manner as well. This way their exact function can be mapped to specific behaviour, and their electrophysiological activity along with the way they are connected to neighbouring cells can also be observed. As far back as the 18<sup>th</sup> century, it was discovered that electrical stimulation can induce involuntary muscle movement even in non-living animals. Galvani[95] demonstrated that applying electricity to the sciatic nerve of skinned frogs triggered movement in the hind legs. The introduced current initiates a response by exceeding the threshold required for neuron to generate an action potential. This was the primary method used for neural stimulation, and is still used to this day. The technique was refined over the years, with increasingly fine wires and electrodes being introduced thus enabling the perturbation of increasingly small tissue volumes. Neural probes even further improved spatial resolution allowing electrodes to be on the micron scale. The main trade-off for using electricity however is that it indiscriminately activates all neurons within a given region. This poses difficulties, as several different types of neurons are often tightly intertwined within a volume of neural tissue, making it difficult to decipher which type of neuron is responsible for which response exactly. To gain a more accurate understanding of how neurons are connected and what their exact role is, increasingly precise methods had to be developed, such as optogenetics.

### 2.8.2 Optogenetics

Further techniques such as optogenetics have allowed the increasingly precise light mediated activation of nerve cells. Using this method, neurons can be activated and deactivated using light at certain wavelengths (activated using blue 450 nm for channelrhodopsin), and inhibited using 520 nm yellow for halorhodopsin. Light sensitive opsins from algae are extracted and using viral vectors transfected into target

cells (Figure 2.14). The simultaneous stimulation and recording of neurons of interest can allow a more accurate mapping of brain structures, where stimulation of specific nerve population can quickly be correlated with behaviour, and simultaneously be linked with high channel count neural recordings. Probes with a large number of  $\mu$ LEDs have been developed allowing the control of neurons at several points within neural tissue[96]. Devices containing both stimulating  $\mu$ LEDs and recording sites have also been developed[97] with future research going into reducing the cross talk between recording and stimulating channels, while improving fabrication processes to ensure reliable electrode operation.

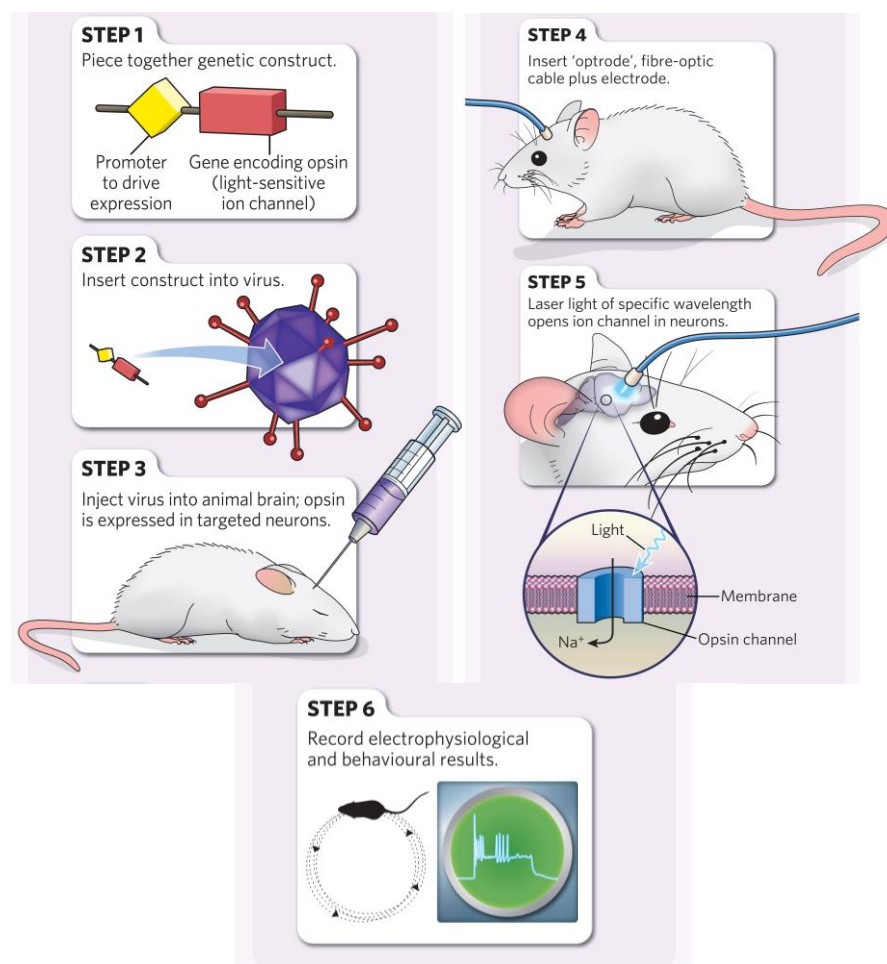


FIGURE 2.14: (a) The steps outlining the procedure to transfect target nerve cells, and activating them using blue light. Image from [98].

When these probes are combined with high channel count neural recordings, it allows the control and observation of neurons at levels and depths much more accurate than conventional electrical stimulation techniques have previously allowed. By adjusting the brightness of the  $\mu$ LEDs, the neural tissue volume being excited can be accurately controlled. As outlined before, to maintain authentic behaviour it is important to make these systems as non-intrusive and lightweight as possible. Since most of the genetics allowing the light based control of neurons has been developed for mice[87], [88], [99]–[102], it's important to create the high channel count recording systems that conform to the limitations imposed by their small size as outlined before.

ICs such as those developed by Hottowy et al.[103]–[105] allow two way operations of the ICs, capable of both recording and stimulating 64 channels. This allows the creation of more streamlined devices that can be designed around a single component, without the use of separate parts for recording and stimulation. Furthermore the stimulating component of the IC permits the very accurate current control of LEDs, while keeping the voltage steady required for optogenetic neural probes. The output is not digitized, however, making it difficult to interface with LEDs for VLC. The recently introduced RHS range amplifier/stimulator chip[106] from Intan Technologies is also capable of recording, and stimulating 16 channels while also digitizing the recorded data. The channel count is relatively low nonetheless, although stacking of chips would allow higher channel counts to be achieved. Additionally, different type of chips could be stacked, with RHS chips used for stimulating only, while higher channel count recording only RHD chips can be used to scale up the recording sites. While this would increase the complexity of the system, the dual function capability with accurate LED control would still be maintained.

## 2.9 Device target specifications

Summarizing and further expanding on the requirements outlined in the previous sections, an ideal neural recording interface should have the following characteristics: Wireless recording capability in a low weight package to allow freely moving authentic behaviour to be observed. Since the primary target animals are mice, this limits the total weight of such devices to  $<3\text{g}$  before it starts to affect behaviour. The device should also operate on a single charge long enough to record  $>1$  hour of neural information. It should be capable of sampling fast enough ( $\geq 20$  KS/s at 10-bit resolution) to capture the fine details of fast firing neural spikes. Typical enclosure sizes for mice are  $20 \times 20$  cm or  $30 \times 30$  cm, so the system should be able to receive data from distances correlating to such dimensions with minimal number of errors (BER  $>10^{-3}$ ) in all orientations between the transmitting device and receivers. Cost of such systems are typically linear with the channel count, with a 32-channel setup from market leader Triangle Biosystems costing  $\sim\pounds 28,000$ . Material costs for the system proposed in the thesis are approximately  $\sim\pounds 1,500$  allowing significant profit to be generated if priced competitively with current solutions, even if including assembly, packaging and shipping costs.

## 2.10 Conclusion

This chapter explained the basics of neurons, and how they generate electrical signals to communicate. It also detailed what techniques are currently available to study the nervous system, and what their disadvantages are. The importance of high channel recordings in mice is explained and the limitations of wired methods are outlined. State-of-the-art wireless devices are presented, with focus on their weight and data transmission rates. The restrictions associated with small RF based devices are discussed, and the advantages of optical based systems are presented. Power requirements are also deliberated, and different modes of energy supply methods are

defined. The emerging field of optogenetics is introduced, and the benefits of interfacing such techniques with high channel count neural recording for freely moving mice are discussed.

TABLE 2.1  
COMPARISON OF WIRELESS NEURAL RECORDING DEVICES

Research Group	Channel Count	Weight (g)	Data Rate (Mbps)	Testing Method	Power Consumption(mW)	Animal Model	Operating Distance (m)	Operating Time (Hrs)
Donati 1990 [59]	-	-	0.001	Freely Moving	-	Rat	-	15
Guillory 2004 [107]	-	-	40	Bench	20-120	-	<5mm	Inductive
Rizk 2007 [108]	96	17	1	In vivo -	100	Owl Monkey	2	Inductive
Parmentier 2008 [62]	-	-	16	Bench	10	-	<5mm	-
Rizk 2009 [109]	96	-	-	Anesthetised	100	Sheep	2	Inductive
Song 2009 [64]	16	-	6.528 - 7.680	Anesthetised	12	Rat, Monkey	0.003	Inductive
Sodagar 2009 [40]	64	0.275	2	Bench	14.4	-	0.01	Inductive
Wei 2009 [110]	16	-	-	In vitro	-	-	<5mm	-
Chestek 2009 [111]	1	114	0.3456	Freely Moving	63.2	Rhesus Monkey	4	144
Miranda H. 2010 [112]	32	-	24	Restricted	142	Primate	1	33
Greenwald 2011 [113]	16	24	1	Freely Moving	4.8 mAh	Rat	3	40
Szuts 2011 [33]	64	67	12	Freely Moving	645	Rat	60	6
Fan D. 2011 [114]	16	4.5	Analog	Freely Moving	-	Mouse	4	6
Sharma 2011 [41]	-	-	-	Bench	-	-	-	Inductive
Thomas 2012 [42]	10	0.038	5	Bench	1.23	-	1.5	RF Harvesting
Rush 2012 [115]	16	-	3	Bench	4.2	-	20	Inductive
Liu 2012 [63]	-	-	50	Bench	5.5	-	<5mm	-
Roy 2012 [116]	15	12	Analog	Freely Moving	-	Marmoset	3	5
Yin 2013 [30]	100	44.5	48	Freely Moving	90.6	Rhesus monkey	1	6.6
Yin 2013 [117]	97	46.1	48	Restricted	51	Primate	1-2	48
Schwarz 2014 [23]	512 C	-	8*	Freely Moving	264	Rhesus Monkey	-	30
Liu 2014 [118]	-	-	100	Anesthetised	2.1	Sheep	<5mm	-
Pinnel 2015 [119]	4	8.5	-	Freely Moving	20 mAh	Rat	03-May	6-8
Hasegawa 2015 [55]	3	16<	0.2	Freely Moving	200	Rat	5	4
Kuan 2015 [120]	-	-	6000	Bench	12.5	-	0.06	-
Turcotte 2016 [38]	32 C	4.9	1.4	Head-Fixed	175	Mouse	-	1.16
Lin 2016 [121]	8	-	2	Anesthetised	-	Rat	<5mm	Inductive
Lu 2017 [122]	1	0.5	0.000336	Freely Moving	-	Mouse	-	2
Intsy 2018 [123]	64	40	0.056	-	-	Pig	5	-
This Work	32	5.045	10.24	Head-Fixed	45	Mouse	0.2	3.5-4

Devices marked with “C” compress the neural recording, resulting in data loss

TABLE 2.2  
COMPARISON OF COMMERCIALY AVAILABLE WIRELESS NEURAL RECORDING DEVICES

Company/Device Name	Channel Count	Weight (g)	Data Rate (Mbps)	Testing Method	Power Consumption(mW)	Animal Model	Operating Distance (m)	Operating Time (Hrs)
Blackrock Cereplex W [43]	96	33.5	-	Freely Moving	-	Primate	2	3.5
Blackrock Cereplex Exilis [124]	96	9.87	-	Freely Moving	-	Rat	1	2.5
TBSI W5 [44]	5	2.8	Analog	Freely Moving	13-24 mAh	Mouse	4	3.5-4.2
TBSI W16 [125]	16	4	Analog	Freely Moving	13-24 mAh	Mouse	3	3.5-4.2
TBSI W32 [45]	32	4.5	Analog	Freely Moving	13-24 mAh	Mouse	4	3.5-4.2
TBSI W64 [126]	64	5	Analog	Freely Moving	13-24 mAh	Rat	4	3.5-4.2
TBSI W128 [127]	128	12	Analog	Freely Moving	13-24 mAh	Rat	4	1-3
TBSI W256 [128]	256	9	Analog	Freely Moving	66 mA	Rat	10	1-3
Taini [46]	16	1.5	-	Freely Moving	2.8	Mouse	2.5	72
Neuralynx Cube2 [129]	64	21.3	-	Freely Moving	-	Rat	10	0.5-24
Deuteron Mouselog-16 [130]	16 DL	2.8	7.5	Freely Moving	140	Mouse	200	0.6
Deuteron Ratlogger [131]	64 DL	6.58	30	Freely Moving	275	Rat	200	2
Doric [132]	4	2.8	0.915	Freely Moving	-	Mouse	5	1.5
Spike Gadgets [133]	128 DL	9.2	61.44	Freely Moving	-	Rat	-	2.25
Jaga Penny [134]	16	2.8	0.125	Freely Moving	-	Mouse	-	1.5
Jaga 16 [134]	16	11.2	3.584	Freely Moving	-	Rat	-	1

TABLE 2.3  
NEURAL STIMULATING ONLY DEVICES

Research Group	Stimulating Channels	Weight (g)	Dimensions (mm)	Testing Method	Animal Model	Operating Distance (m)	Operating Time (Hrs)	Stimulation Method
Iwai et al., 2011[135]	1	3.1	-	In vivo - Freely Moving	Mouse	2	-	Optogenetic
Wentz et al., 2011[99]	up to 16	43161	-	In vivo - Freely Moving	Mouse	several cm	Inductive	Optogenetic
Hashimoto et al., 2014[102]	3	2.4	10 x 14 x 14	Bench	-	15	-	Optogenetic
Park et al., 2015[92]	1	0.07	-	In vivo - Freely Moving	Mouse	1.6	PV, RF Harvesting	Optogenetic
Montgomery et al., 2015[136]	1	0.02-0.05	10–25 mm <sup>3</sup>	In vivo - Freely Moving	Mouse	0.03	Inductive	Optogenetic
Rossi et al., 2015[100]	2	2.9	5 x 14 x 17	In vivo - Freely Moving	Mouse	4	2	Optogenetic
Lee et al., 2015[137]	1	-	-	In vivo - Freely Moving	Mouse	-	-	Optogenetic
Park et al., 2016[88]	2	0.033	0.7 x 4.3 x 8	In vivo - Freely Moving	Mouse	-	RF harvesting	Optogenetic
Shin et al., 2017[87]	2	0.03	9.9 dia x 1.3	In vivo - Freely Moving	Mouse	0.12	Inductive	Optogenetic
Commercial TBSI S-series[138]	2	3.6	10.5 x 17.8 x 19.6	In vivo - Freely Moving	Mouse	-	5.5	Electrical
Commercial TBSI S-series[138]	2	2.9	10.5 x 17.8 x 19.6	In vivo - Freely Moving	Mouse	-	5.5	Optogenetic
Turcotte, et al. 2017[139]	1	-	-	-	Mouse	-	-	Optogenetic

Devices marked with “C” compress the neural recording resulting in data loss



TABLE 2.4  
NEURAL RECORDING AND STIMULATING DEVICES

Research Group	Recording Channels	Stimulating Channels	Weight (g)	DR (Mbps)	Sampling Rate (kS/s/channel)	Power Consumption (mW)	Animal Model	Operating Distance (m)	Operating Time (Hrs)	Stimulation Method
Ativanichayaphong et al., 2008[140]	1	1	-	-	10	-	Rat	-	6	Electrical
Kim et al., 2013[141]	1	4	0.7-2	-	-	4	Mouse	1	RF Harvesting	Optogenetic
R C Pinnell, et al. 2015[119]	4	2	8.5	-	0.5	20 mAh	Rat	3-5	3-5	Electrical
Kwon et al., 2015[142]	up to 32 C	up to 32	4.9	1.4	20	175	Mouse	-	1.16	Optogenetic
Turcotte, et al. 2016[38]	32C	32	-	-	-	-	Rat	-	Inductive	Optogenetic

\*Assuming CMOS signalling mode and 20 kS/s sampling rate, \*\* Assuming CMOS signalling mode, 20 kS/s sampling rate and a total stimulating current of 1.16 mA

† 30 mW when the stimulation is disabled on all channels and increases by 1.1–1.7 mW for each enabled channel depending on the defined stimulation mode and the range of the output signal

TABLE 2.5  
NEURAL RECORDING AND STIMULATING CHIPS

Research Group	Voltage (V)	Data Rate (Mbps)	Sampling Rate (KS/s)	Recording Channels	Stimulating Channels	Bare Die Size (mm)	Resolution (bit)	Power Consumption (mW)	Energy Consumption/Bit (pJ)
Chae et al., 2008[143]	3.3	90	40	128	-	7.2 x 8.8	9	6	67
Bonfanti et al., 2010[144]	3	1.25	-	64	-	2.7 x 3.1	8	16.6	11400
Hottowy et al., 2012[79]	±2.5	Analogue	Analogue	64	64	2.8 x 6.4	Analogue	30 mW†	Analogue
Abdelhalim et al., 2013[145]	1.2	1.5	7.1	64	-	3 x 4	8	5.03	3350
Tan et al., 2014[146]	0.5	1/5/8	25	8	-	2.09 x 2.59	8	3.66	3700/730/460
Muller et al., 2014[147]	0.5	1	-	64	-	2.4 x 2.4	15	0.225	225
Brenna et al., 2016[85]	0.5	20	31.25	64	-	5 x 5	10	0.965	48.2
Commercial Intan RHD2132[72]	3.3	16.8	30	32	-	4.1 x 4.8	16	18.48*	1650*
Commercial Intan RHS2116 [106]	3.3	10.24	40	16	16	4.7 x 4.9	16	25.13**	4908**

## References

- [1] “Neuron Diagram & Types | ASU - Ask A Biologist.” [Online]. Available: <https://askbiologist.asu.edu/neuron-anatomy>. [Accessed: 21-May-2017].
- [2] B. P. Bean, “The action potential in mammalian central neurons,” *Nat. Rev. Neurosci.*, vol. 8, no. 6, pp. 451–465, Jun. 2007.
- [3] W. Klimesch, “EEG alpha and theta oscillations reflect cognitive and memory performance: A review and analysis,” *Brain Res. Rev.*, vol. 29, no. 2–3, pp. 169–195, 1999.
- [4] J. S. Kumar and P. Bhuvaneswari, “Analysis of electroencephalography (EEG) signals and its categorization - A study,” *Procedia Eng.*, vol. 38, pp. 2525–2536, 2012.
- [5] R. Sharp, N. R. Swerdlow, and D. L. Braff, *EEG and ERPs*, no. 619. 2011.
- [6] H. Jing and M. Takigawa, “Low sampling rate induces high correlation dimension on electroencephalograms from healthy subjects,” *Psychiatry Clin. Neurosci.*, vol. 54, no. 4, pp. 407–412, 2000.
- [7] V. P. B. Grover, J. M. Tognarelli, M. M. E. Crossey, I. J. Cox, S. D. Taylor-Robinson, and M. J. W. McPhail, “Magnetic Resonance Imaging: Principles and Techniques: Lessons for Clinicians,” *J. Clin. Exp. Hepatol.*, vol. 5, no. 3, pp. 246–255, 2015.
- [8] A. A. Eugene Lin, “What are the basic concepts of temporal, contrast, and spatial resolution in cardiac CT?,” *J. Cardiovasc. Comput. Tomogr.*, vol. 3, no. 6, pp. 403–408, 2009.
- [9] I. M. Kopton and P. Kenning, “Near-infrared spectroscopy (NIRS) as a new tool for neuroeconomic research,” *Front. Hum. Neurosci.*, vol. 8, no. August, pp. 1–13, 2014.
- [10] K. Svoboda and R. Yasuda, “Principles of Two-Photon Excitation Microscopy and Its Applications to Neuroscience,” *Neuron*, vol. 50, no. 6, pp. 823–839, 2006.
- [11] A. Ustione and D. W. Piston, “A simple introduction to multiphoton microscopy,” *J. Microsc.*, vol. 243, no. 3, pp. 221–226, 2011.
- [12] M. R. Warden, J. A. Cardin, and K. Deisseroth, “Optical Neural Interfaces,” *Annu. Rev. Biomed. Eng.*, vol. 16, pp. 103–29, 2014.
- [13] J. Fujimoto and D. Huang, “Foreword: 25 Years of Optical Coherence Tomography,” *Investig. Ophthalmology Vis. Sci.*, vol. 57, no. 9, p. OCTi, 2016.
- [14] M. Wojtkowski, “High-speed optical coherence tomography: basics and

- applications,” *Appl. Opt.*, vol. 49, no. 16, p. D30, 2010.
- [15] D. P. Popescu *et al.*, “Optical coherence tomography: Fundamental principles, instrumental designs and biomedical applications,” *Biophys. Rev.*, vol. 3, no. 3, pp. 155–169, 2011.
- [16] M. L. Gabriele *et al.*, “Optical coherence tomography: history, current status, and laboratory work.,” *Invest. Ophthalmol. Vis. Sci.*, vol. 52, no. 5, pp. 2425–36, Apr. 2011.
- [17] L. Pantanowitz, Y. Chen, C.-P. Liang, Y. Liu, A. Fischer, and A. Parwani, “Review of advanced imaging techniques,” *J. Pathol. Inform.*, vol. 3, no. 1, p. 22, 2012.
- [18] G. Buzsáki, “Large-scale recording of neuronal ensembles,” *Nat. Neurosci.*, vol. 7, no. 5, pp. 446–451, 2004.
- [19] G. Buzsáki *et al.*, “Tools for probing local circuits: High-density silicon probes combined with optogenetics,” *Neuron*, vol. 86, no. 1, pp. 92–105, 2015.
- [20] V. Marx, “Neurobiology: rethinking the electrode,” *Nat. Methods*, vol. 11, no. 11, pp. 1099–1103, 2014.
- [21] E. Stark, T. Koos, and G. Buzsáki, “Diode probes for spatiotemporal optical control of multiple neurons in freely moving animals.,” *J. Neurophysiol.*, vol. 108, no. 1, pp. 349–63, 2012.
- [22] M. A. Lebedev and M. A. L. Nicolelis, “Brain-machine interfaces: past, present and future,” *Trends Neurosci.*, vol. 29, no. 9, pp. 536–546, 2006.
- [23] D. A. Schwarz *et al.*, “Chronic, wireless recordings of large-scale brain activity in freely moving rhesus monkeys,” *Nat. Methods*, vol. 11, no. 6, pp. 670–676, 2014.
- [24] B. Wang *et al.*, “Firing Frequency Maxima of Fast-Spiking Neurons in Human, Monkey, and Mouse Neocortex,” *Front. Cell. Neurosci.*, vol. 10, no. October, pp. 1–13, 2016.
- [25] A. H. Marblestone *et al.*, “Physical principles for scalable neural recording.,” *Front. Comput. Neurosci.*, vol. 7, no. October, p. 137, 2013.
- [26] J. Scholvin *et al.*, “Close-packed silicon microelectrodes for scalable spatially oversampled neural recording,” *IEEE Trans. Biomed. Eng.*, vol. 63, no. 1, pp. 120–130, 2016.
- [27] A. G. Siapas, “Nanofabricated Neural Probes for Dense 3 - D Recordings of Brain Activity,” pp. 6–11, 2016.
- [28] J. P. Kinney *et al.*, “A direct-to-drive neural data acquisition system,” *Front. Neural Circuits*, vol. 9, no. September, pp. 1–8, 2015.

- [29] R. Fiáth *et al.*, “Large-scale recording of thalamocortical circuits: in vivo electrophysiology with the two-dimensional electronic depth control silicon probe,” *J. Neurophysiol.*, p. jn.00318.2016, 2016.
- [30] A. Manuscript, C. Wireless, and N. Applications, “A 100-Channel Hermetically Sealed Implantable Device for Chronic Wireless Neurosensing Applications,” vol. 7, no. 2, pp. 115–128, 2014.
- [31] B. Ellenbroek and J. Youn, “Rodent models in neuroscience research: is it a rat race?,” *Dis. Model. Mech.*, vol. 9, no. 10, pp. 1079–1087, 2016.
- [32] A. Shuster, “The Best-Laid Schemes of Mice and Men | Neurosciences Institute.” [Online]. Available: <https://neuroscience.stanford.edu/news/best-laid-schemes-mice-and-men>. [Accessed: 05-Sep-2017].
- [33] T. A. Szuts *et al.*, “A wireless multi-channel neural amplifier for freely moving animals,” *Nat. Neurosci.*, vol. 14, no. 2, pp. 263–269, 2011.
- [34] M. S. Mahmoud and A. A. H. Mohamad, “A Study of Efficient Power Consumption Wireless Communication Techniques/ Modules for Internet of Things (IoT) Applications,” *Adv. Internet Things*, vol. 06, no. 02, pp. 19–29, 2016.
- [35] R. F. Harrington, “Effect of antenna size on gain, bandwidth, and efficiency,” *J. Res. Natl. Bur. Stand. Sect. D Radio Propag.*, vol. 64D, no. 1, p. 1, 1960.
- [36] J. S. McLean, “A re-examination of the fundamental limits on the radiation Q of electrically small antennas,” *IEEE Trans. Antennas Propag.*, vol. 44, no. 5, pp. 3–7, 1996.
- [37] C. Pfeiffer, “Fundamental Efficiency Limits for Small Metallic Antennas,” 2016.
- [38] G. Gagnon-Turcotte, Y. LeChasseur, C. Bories, Y. Messaddeq, Y. De Koninck, and B. Gosselin, “A Wireless Headstage for Combined Optogenetics and Multichannel Electrophysiological Recording,” *IEEE Trans. Biomed. Circuits Syst.*, pp. 1–14, 2016.
- [39] M. Chae *et al.*, “A 128-channel 6mW wireless neural recording IC with on-the-fly spike sorting and UWB Transmitter,” *Dig. Tech. Pap. - IEEE Int. Solid-State Circuits Conf.*, vol. 51, pp. 146–148, 2008.
- [40] A. M. Sodagar, G. E. Perlin, Y. Yao, K. Najafi, and K. D. Wise, “An implantable 64-channel wireless microsystem for single-unit neural recording,” *IEEE J. Solid-State Circuits*, vol. 44, no. 9, pp. 2591–2604, 2009.
- [41] A. Sharma *et al.*, “Long term in vitro functional stability and recording longevity of fully integrated wireless neural interfaces based on the Utah Slant Electrode Array,” *J. Neural Eng.*, vol. 8, no. 4, p. 45004, 2011.

- [42] S. J. Thomas, S. Member, R. R. Harrison, A. Leonardo, M. S. Reynolds, and S. Member, “A Battery-Free Multichannel Digital Neural / EMG Telemetry System for Flying Insects,” vol. 6, no. 5, pp. 424–436, 2012.
- [43] “Blackrock CerePlex.” [Online]. Available: <http://blackrockmicro.com/wp-content/uploads/2016/08/LB-0805-1.00-CerePlex-W-IFU.pdf>. [Accessed: 31-May-2017].
- [44] “TBSI W5 System Manual Version 3.0 W5 System User’s Manual,” *Office*, no. 919, pp. 361–2663.
- [45] “TBSI W32 System Manual Version 3.0 W32 System User’s Manual.”
- [46] Z. Jiang *et al.*, “TaiNi: Maximizing research output whilst improving animals’ welfare in neurophysiology experiments,” pp. 1–12, 2017.
- [47] J. Charthad, M. J. Weber, T. C. Chang, and A. Arbabian, “A mm-Sized Implantable Medical Device (IMD) With Ultrasonic Power Transfer and a Hybrid Bi-Directional Data Link,” *IEEE J. Solid-State Circuits*, vol. 50, no. 8, pp. 1741–1753, 2015.
- [48] D. Seo, J. M. Carmena, J. M. Rabaey, M. M. Maharbiz, and E. Alon, “Model validation of untethered, ultrasonic neural dust motes for cortical recording,” *J. Neurosci. Methods*, vol. 244, pp. 114–122, 2015.
- [49] D. Seo *et al.*, “Wireless Recording in the Peripheral Nervous System with Ultrasonic Neural Dust,” *Neuron*, vol. 91, no. 3, pp. 529–539, 2016.
- [50] D. Seo, J. M. Carmena, J. M. Rabaey, E. Alon, and M. M. Maharbiz, “Neural Dust: An Ultrasonic, Low Power Solution for Chronic Brain-Machine Interfaces,” no. April, 2013.
- [51] A. F. Robert Cleveland and J. L. Jerry Ulcek, “Questions and Answers about Biological Effects and Potential Hazards of Radiofrequency Electromagnetic Fields Questions and Answers about Biological Effects and Potential Hazards of Radiofrequency Electromagnetic Fields OET BULLETIN 56,” 1999.
- [52] “Guidance for Industry and FDA Staff Information for Manufacturers Seeking Marketing Clearance of Diagnostic Ultrasound Systems and Transducers Preface Public Comment Additional Copies,” 2008.
- [53] S. Venkatraman, X. Jin, R. M. Costa, and J. M. Carmena, “Investigating Neural Correlates of Behavior in Freely Behaving Rodents Using Inertial Sensors,” *J. Neurophysiol.*, vol. 104, no. 1, pp. 569–575, 2010.
- [54] J. Voigts, J. H. Siegle, D. L. Pritchett, and C. I. Moore, “The flexDrive: an ultra-light implant for optical control and highly parallel chronic recording of neuronal ensembles in freely moving mice.,” *Front. Syst. Neurosci.*, vol. 7, no. May, p. 8, 2013.

- [55] T. Hasegawa, H. Fujimoto, K. Tashiro, M. Nonomura, A. Tsuchiya, and D. Watanabe, “A wireless neural recording system with a precision motorized microdrive for freely behaving animals,” *Sci. Rep.*, vol. 5, p. 7853, 2015.
- [56] F. Michon *et al.*, “Integration of silicon-based neural probes and micro-drive arrays for chronic recording of large populations of neurons in behaving animals,” *J. Neural Eng.*, vol. 13, no. 4, p. 046018, 2016.
- [57] B. P. Vos, M. Wijnants, S. Taeymans, and E. De Schutter, “Miniature carrier with six independently moveable electrodes for recording of multiple single-units in the cerebellar cortex of awake rats,” *J. Neurosci. Methods*, vol. 94, no. 1, pp. 19–26, 1999.
- [58] D. Ball *et al.*, “Rodent scope: A user-configurable digital wireless telemetry system for freely behaving animals,” *PLoS One*, vol. 9, no. 2, pp. 1–10, 2014.
- [59] S. Donati and V. Annovazzi-Lodi, “Optoelectronic Telemetry for Electrophysiological Signals.” 1990.
- [60] S. Donati and V. Annovazzi-Lodi, “Simultaneous Polarographic and Electrophysiological In Vivo Measurements Through Optoelectronic Interconnection.” 1991.
- [61] S. Donati and V. Annovazzi-Lodi, “An Optoelectronic Interconnection for Bidirectional Transmission of Biological Signals.” 1988.
- [62] S. Parmentier, R. Fontaine, and Y. Roy, “Laser diode used in 16 Mb/s, 10 mW optical transcutaneous telemetry system,” *2008 IEEE-BIOCAS Biomed. Circuits Syst. Conf. BIOCAS 2008*, pp. 377–380, 2008.
- [63] T. Liu, U. Bihl, S. M. Anis, and M. Ortmanns, “Optical transcutaneous link for low power, high data rate telemetry,” *Proc. Annu. Int. Conf. IEEE Eng. Med. Biol. Soc. EMBS*, pp. 3535–3538, 2012.
- [64] Y.-K. Song *et al.*, “Active microelectronic neurosensor arrays for implantable brain communication interfaces,” *IEEE Trans. Neural Syst. Rehabil. Eng.*, vol. 17, no. 4, pp. 339–45, 2009.
- [65] Y. K. Song *et al.*, “A brain implantable microsystem with hybrid RF/IR telemetry for advanced neuroengineering applications,” *Annu. Int. Conf. IEEE Eng. Med. Biol. - Proc.*, pp. 445–448, 2007.
- [66] I. C. Lu, C. H. Yeh, D. Z. Hsu, and C. W. Chow, “Utilization of 1-GHz VCSEL for 11.1-Gbps OFDM VLC Wireless Communication,” *IEEE Photonics J.*, vol. 8, no. 3, pp. 3–9, 2016.
- [67] Finisar, “Designing With VCSELs | VCSEL.” [Online]. Available: <http://myvcSEL.com/designing-with-vcSels/>. [Accessed: 12-Oct-2017].

- [68] S. Donati, G. Martini, and C. Cignoli, "Optoelectronic Signal Transmission by Diffuse Radiation: Design and Performances," *Laser Electro-Optik*, vol. 13, no. 2, pp. 70–72, 1981.
- [69] S. Rajbhandari *et al.*, "A review of gallium nitride LEDs for multi-gigabit-per-second visible light data communications," *Semicond. Sci. Technol.*, vol. 32, no. 2, p. 023001, 2017.
- [70] M. S. Islim *et al.*, "Towards 10 Gb/s orthogonal frequency division multiplexing-based visible light communication using a GaN violet micro-LED," *Photonics Res.*, vol. 5, no. 2, p. A35, 2017.
- [71] A. Gomez *et al.*, "Beyond 100-Gb/s indoor wide field-of-view optical wireless communications," *IEEE Photonics Technol. Lett.*, vol. 27, no. 4, pp. 367–370, 2015.
- [72] T. Takeuchi, S. Kamiyama, M. Iwaya, and I. Akasaki, "GaN-based vertical-cavity surface-emitting lasers with AlInN/GaN distributed Bragg reflectors," *Reports Prog. Phys.*, vol. 82, no. 1, pp. 12–14, 2019.
- [73] I. C. Lu, C. H. Yeh, D. Z. Hsu, and C. W. Chow, "Utilization of 1-GHz VCSEL for 11.1-Gbps OFDM VLC Wireless Communication," *IEEE Photonics J.*, vol. 8, no. 3, pp. 1–6, 2016.
- [74] C.-H. Yeh and I.-C. Lu, "sharing VLC transmission by using VCSEL laser," vol. 24, no. 18, pp. 21113–21118, 2016.
- [75] "VCSELs arrays with diffusers mounted on top to change divergence angle for 3D Imaging applications - Laser Diodes, High Power VCSELs, VCSEL Arrays, Diode Lasers." [Online]. Available: <http://www.princetonoptronics.com/vcsels-arrays-with-diffusers-mounted-on-top-to-change-divergence-angle-for-3d-imaging-applications/>. [Accessed: 12-Oct-2017].
- [76] "940nm High Power VCSEL Die in Ceramic Package with Diffuser | Finisar Corporation." [Online]. Available: <https://www.finisar.com/sensing-components/hvs7000-004>. [Accessed: 25-Jun-2019].
- [77] Y. Mei *et al.*, "Quantum dot vertical-cavity surface-emitting lasers covering the 'green gap,'" *Light Sci. Appl.*, vol. 6, no. 1, 2017.
- [78] E. Xie *et al.*, "High-Speed Visible Light Communication Based on a III-Nitride Series-Biased Micro-LED Array," *J. Light. Technol.*, vol. 37, no. 4, pp. 1180–1186, 2019.
- [79] Z. Lu *et al.*, "Active tracking system for visible light communication using a GaN-based micro-LED and NRZ-OOK," *Opt. Express*, vol. 25, no. 15, p. 17971, 2017.
- [80] I. Moreno and C.-C. Sun, "Modeling the radiation pattern of LEDs," *Opt.*

- Express*, vol. 16, no. 3, p. 1808, 2008.
- [81] C. Wiesmann, *Nano-structured LEDs – Light extraction mechanisms and applications*. Regensburg: University of Regensburg, 2010, 11-13.
- [82] H. Morkoç, *Nitride Semiconductor Devices*. Springer-Verlag Berlin Heidelberg, vol. 3. 2013, 7-10.
- [83] “Renesas Solutions for Wireless Sensor Networks–Part 4: Visible Light Communication (VLC) |.” [Online]. Available: <https://www.renesas.com/zh-tw/about/web-magazine/edge/solution/10-visible-light-communication.html>. [Accessed: 31-May-2017].
- [84] Intan Technologies, “RHD2000 Series Digital Electrophysiology Interface Chips,” RHD2216 RHD2132 datasheet, Dec. 2012. [Revised Sept. 2013].
- [85] S. Brenna, F. Padovan, A. Neviani, A. Bevilacqua, A. Bonfanti, and A. L. Lacaita, “A 64-Channel 965  $\mu$ W Neural Recording SoC with UWB Wireless Transmission in 130-nm CMOS,” *IEEE Trans. Circuits Syst. II Express Briefs*, vol. 63, no. 6, pp. 528–532, 2016.
- [86] C. Mora Lopez *et al.*, “A Neural Probe With Up to 966 Electrodes and Up to 384 Configurable Channels in 0.13  $\mu$ m SOI CMOS,” *IEEE Trans. Biomed. Circuits Syst.*, no. April, 2017.
- [87] G. Shin *et al.*, “Flexible Near-Field Wireless Optoelectronics as Subdermal Implants for Broad Applications in Optogenetics,” *Neuron*, pp. 1–13, 2017.
- [88] S. Il Park *et al.*, “Stretchable multichannel antennas in soft wireless optoelectronic implants for optogenetics,” *Proc. Natl. Acad. Sci.*, p. 201611769, 2016.
- [89] R. R. Harrison *et al.*, “A wireless neural interface for chronic recording,” *2008 IEEE-BIOCAS Biomed. Circuits Syst. Conf. BIOCAS 2008*, pp. 125–128, 2008.
- [90] “Ferro Solutions Transmitter Manual.” [Online]. Available: [http://www.ferrosi.com/pdf/FS\\_WPT-05\\_data\\_sheet.pdf](http://www.ferrosi.com/pdf/FS_WPT-05_data_sheet.pdf). [Accessed: 01-Jun-2017].
- [91] “Wireless Power Products - Powercast Co.” [Online]. Available: <http://www.powercastco.com/>. [Accessed: 01-Jun-2017].
- [92] S. Il Park *et al.*, “Ultraminaturized photovoltaic and radio frequency powered optoelectronic systems for wireless optogenetics,” *J. Neural Eng.*, vol. 12, no. 5, p. 056002, 2015.
- [93] “Ossia Cota.” [Online]. Available: <http://www.ossia.com/cota/>. [Accessed: 01-Jun-2017].
- [94] “Energous – WattUp® Wire-Free Charging Technology.” [Online]. Available:



- <http://energous.com/>. [Accessed: 01-Jun-2017].
- [95] M. Bresadola, "Medicine and science in the life of Luigi Galvani (1737–1798)," *Brain Res. Bull.*, vol. 46, no. 5, pp. 367–380, 1998.
- [96] R. Scharf, T. Tsunematsu, N. McAlinden, M. D. Dawson, S. Sakata, and K. Mathieson, "Depth-specific optogenetic control in vivo with a scalable, high-density  $\mu$ LED neural probe," *Sci. Rep.*, vol. 6, no. 1, p. 28381, 2016.
- [97] F. Wu, E. Stark, P. C. Ku, K. D. Wise, G. Buzsáki, and E. Yoon, "Monolithically Integrated  $\mu$ LEDs on Silicon Neural Probes for High-Resolution Optogenetic Studies in Behaving Animals," *Neuron*, vol. 88, no. 6, pp. 1136–1148, 2015.
- [98] L. Buchen, "Neuroscience: Illuminating the brain," *Nature*, vol. 465, no. 7294, pp. 26–28, 2010.
- [99] C. T. Wentz, J. G. Bernstein, P. Monahan, A. Guerra, A. Rodriguez, and E. S. Boyden, "A wirelessly powered and controlled device for optical neural control of freely-behaving animals," *J. Neural Eng.*, vol. 8, no. 4, p. 046021, 2011.
- [100] M. A. Rossi, V. Go, T. Murphy, Q. Fu, J. Morizio, and H. H. Yin, "A wirelessly controlled implantable LED system for deep brain optogenetic stimulation," *Front. Integr. Neurosci.*, vol. 9, no. February, p. 8, 2015.
- [101] J. G. McCall *et al.*, "Preparation and implementation of optofluidic neural probes for in vivo wireless pharmacology and optogenetics," *Nat. Protoc.*, vol. 12, no. 2, pp. 219–237, 2017.
- [102] M. Hashimoto, A. Hata, T. Miyata, and H. Hirase, "Programmable wireless light-emitting diode stimulator for chronic stimulation of optogenetic molecules in freely moving mice," *Neurophotonics*, vol. 1, no. 1, p. 011002, 2014.
- [103] P. Hottowy, W. Dabrowski, A. Skoczeń, and P. Wiacek, "An integrated multichannel waveform generator for large-scale spatio-temporal stimulation of neural tissue," *Analog Integr. Circuits Signal Process.*, vol. 55, no. 3, pp. 239–248, 2008.
- [104] P. Hottowy *et al.*, "512-electrode MEA System For Spatio-Temporal Distributed Stimulation and Recording of Neural Activity," *MEA Meet. 2010 7th Int. Meet. Substrate-integrated microelectrode arrays*, pp. 5–8, 2010.
- [105] P. Hottowy *et al.*, "Properties and application of a multichannel integrated circuit for low-artifact, patterned electrical stimulation of neural tissue," *J. Neural Eng.*, vol. 9, no. 6, p. 066005, 2012.
- [106] Intan Technologies, "Digital Electrophysiology Stimulator/Amplifier Chip," RHS2116 datasheet, Jan. 2016. [Revised March. 2017].

- [107] K. Guillory, a Misener, and a Pungor, “Hybrid RF/IR transcutaneous telemetry for power and high-bandwidth data.,” *Conf. Proc. IEEE Eng. Med. Biol. Soc.*, vol. 6, pp. 4338–4340, 2004.
- [108] M. Rizk, I. Obeid, S. H. Callender, and P. D. Wolf, “A single-chip signal processing and telemetry engine for an implantable 96-channel neural data acquisition system,” *J. Neural Eng.*, vol. 4, no. 3, pp. 309–321, 2007.
- [109] M. Rizk *et al.*, “A Fully Implantable 96-channel Neural Data Acquisition System,” *System*, vol. 6, no. 2, pp. 1–26, 2010.
- [110] P. Wei and B. Ziaie, “An optical microsystem for wireless neural recording,” *Proc. 31st Annu. Int. Conf. IEEE Eng. Med. Biol. Soc. Eng. Futur. Biomed. EMBC 2009*, pp. 5522–5524, 2009.
- [111] C. A. Chestek *et al.*, “HermesC: Low-Power Wireless Neural Recording System for Freely Moving Primates,” *330 Ieee Trans. Neural Syst. Rehabil. Eng.*, vol. 17, no. 4, pp. 330–338, 2009.
- [112] H. Miranda, V. Gilja, C. A. Chestek, K. V. Shenoy, and T. H. Meng, “HermesD: A high-rate long-range wireless transmission system for simultaneous multichannel neural recording applications,” in *IEEE Transactions on Biomedical Circuits and Systems*, 2010, vol. 4, no. 3, pp. 181–191.
- [113] E. Greenwald, M. Mollazadeh, C. Hu, W. Tang, E. Culurciello, and N. Thakor, “A VLSI neural monitoring system with ultra-wideband telemetry for awake behaving subjects,” *IEEE Trans. Biomed. Circuits Syst.*, vol. 5, no. 2, pp. 112–119, 2011.
- [114] D. Fan *et al.*, “A wireless multi-channel recording system for freely behaving mice and rats,” *PLoS One*, vol. 6, no. 7, 2011.
- [115] A. D. Rush and P. R. Troyk, “A power and data link for a wireless-implanted neural recording system,” *IEEE Trans. Biomed. Eng.*, vol. 59, no. 12 PART2, pp. 3255–3262, 2012.
- [116] S. Roy and X. Wang, “Wireless multi-channel single unit recording in freely moving and vocalizing primates,” *J. Neurosci. Methods*, vol. 203, no. 1, pp. 28–40, 2012.
- [117] M. Yin *et al.*, “An externally head-mounted wireless neural recording device for laboratory animal research and possible human clinical use,” *Conf. Proc. ... Annu. Int. Conf. IEEE Eng. Med. Biol. Soc. IEEE Eng. Med. Biol. Soc. Annu. Conf.*, vol. 2013, pp. 3109–3114, 2013.
- [118] T. Liu, U. Bihl, J. Becker, J. Anders, and M. Ortmanns, “In vivo verification of a 100 Mbps transcutaneous optical telemetric link,” *IEEE 2014 Biomed.*

- Circuits Syst. Conf. BioCAS 2014 - Proc.*, pp. 580–583, 2014.
- [119] R. C. Pinnell, J. Dempster, and J. Pratt, “Miniature wireless recording and stimulation system for rodent behavioural testing,” *J. Neural Eng.*, vol. 12, no. 6, p. 066015, 2015.
- [120] Y. C. Kuan, Y. K. Lo, Y. Kim, M. C. F. Chang, and W. Liu, “Wireless gigabit data telemetry for large-scale neural recording,” *IEEE J. Biomed. Heal. Informatics*, vol. 19, no. 3, pp. 949–957, 2015.
- [121] Y. P. Lin *et al.*, “A Battery-Less, Implantable Neuro-Electronic Interface for Studying the Mechanisms of Deep Brain Stimulation in Rat Models,” *IEEE Trans. Biomed. Circuits Syst.*, vol. 10, no. 1, pp. 98–112, 2016.
- [122] L. Lu *et al.*, “Wireless optoelectronic photometers for monitoring neuronal dynamics in the deep brain,” *Proc. Natl. Acad. Sci. U. S. A.*, vol. 115, no. 7, pp. E1374–E1383, Feb. 2018.
- [123] J. C. Erickson, J. A. Hayes, M. Bustamante, R. Joshi, and A. Rwagaju, “bioamplifier system,” 2018.
- [124] Blackrock Microsystems, “CerePlex Exilis,” LB-0889 datasheet, 2018.
- [125] Triangle Biosystems International, “TBSI W16 System Manual,” datasheet, July. 2015.
- [126] Triangle Biosystems International, “TBSI W64 System Manual,” datasheet, Jan. 2014.
- [127] Triangle Biosystems International, “TBSI W128 System Manual” datasheet, March. 2014.
- [128] Triangle Biosystems International, “TBSI W256 System Manual,” datasheet, Sept. 2017
- [129] “Cube2 . Neuralynx.” [Online]. Available: <https://neuralynx.com/hardware/cube2>. [Accessed: 28-May-2018].
- [130] Deuteron Technologies Ltd, “MouseLog-16.” datasheet.
- [131] Deuteron Technologies Ltd, “RatLog-64.” datasheet.
- [132] “Fiberless & Wireless Headstage - Doric Lenses.” [Online]. Available: <http://doriclenses.com/life-sciences/ose-components/920-fiberless-wireless-headstage.html>. [Accessed: 28-May-2018].
- [133] “SpikeGadgets|Hardware|HH128.” [Online]. Available: <http://www.spikegadgets.com/hardware/hh128.html>. [Accessed: 28-May-2018].
- [134] “JAGA Penny.” [Online]. Available: <https://www.jinga-hi.com/hardware>. [Accessed: 28-May-2018].

- [135] Y. Iwai, S. Honda, H. Ozeki, M. Hashimoto, and H. Hirase, “A simple head-mountable LED device for chronic stimulation of optogenetic molecules in freely moving mice,” *Neurosci. Res.*, vol. 70, no. 1, pp. 124–127, 2011.
- [136] K. L. Montgomery *et al.*, “Wirelessly powered , fully internal optogenetics for brain , spinal and peripheral circuits in mice,” *Nat. Methods*, no. august, pp. 3–5, 2015.
- [137] J. Lee, I. Ozden, Y.-K. Song, and A. V Nurmikko, “Transparent intracortical microprobe array for simultaneous spatiotemporal optical stimulation and multichannel electrical recording,” *Nat. Methods*, vol. 12, no. October, pp. 1–8, 2015.
- [138] Triangle Biosystems International, “Opto Stim Ware, Wireless Optical Stimulation,” S-series datasheet, March., 2015.
- [139] G. Gagnon-Turcotte, L. L. Gagnon, G. Bilodeau, and B. Gosselin, “Wireless brain computer interfaces enabling synchronized optogenetics and electrophysiology,” *Proc. - IEEE Int. Symp. Circuits Syst.*, pp. 8–11, 2017.
- [140] T. Ativanichayaphong, J. W. He, C. E. Hagains, Y. B. Peng, and J. C. Chiao, “A combined wireless neural stimulating and recording system for study of pain processing,” *J. Neurosci. Methods*, vol. 170, no. 1, pp. 25–34, 2008.
- [141] T. Il Kim *et al.*, “Injectable, cellular-scale optoelectronics with applications for wireless optogenetics,” *Science (80-. )*, vol. 340, no. 6129, pp. 211–216, 2013.
- [142] K. Y. Kwon, H.-M. Lee, M. Ghovanloo, A. Weber, and W. Li, “Design, fabrication, and packaging of an integrated, wirelessly-powered optrode array for optogenetics application,” *Front. Syst. Neurosci.*, vol. 9, no. May, pp. 1–12, 2015.
- [143] M. S. Chae, Z. Yang, M. R. Yuce, L. Hoang, W. Liu, and S. Member, “A 128-Channel 6 mW Wireless Neural Recording IC With Spike Feature Extraction and UWB Transmitter,” vol. 17, no. 4, pp. 312–321, 2009.
- [144] A. Bonfanti *et al.*, “A multi-channel low-power IC for neural spike recording with data compression and narrowband 400-MHz MC-FSK wireless transmission,” *ESSCIRC 2010 - 36th Eur. Solid State Circuits Conf.*, pp. 330–333, 2010.
- [145] K. Abdelhalim, L. Kokarovtseva, J. L. Perez Velazquez, and R. Genov, “915-MHz FSK/OOK wireless neural recording soc with 64 mixed-signal fir filters,” *IEEE J. Solid-State Circuits*, vol. 48, no. 10, pp. 2478–2493, 2013.
- [146] J. Tan, W. S. Liew, C. H. Heng, and Y. Lian, “A 2.4 GHz ULP reconfigurable asymmetric transceiver for single-chip wireless neural recording IC,” *IEEE Trans. Biomed. Circuits Syst.*, vol. 8, no. 4, pp. 497–509, 2014.

- [147] R. Muller *et al.*, “A Minimally Invasive 64-Channel Wireless  $\gamma$ eCoG Implant,” *IEEE J. Solid-State Circuits*, vol. 50, no. 1, pp. 344–359, 2014.

## Chapter III – *In vitro* device setup

### 3.1 Introduction

The previous chapter outlined the potential for VLC to send large amounts of data[1]–[4]. To verify the feasibility of using the technique for transmitting neural information, a tethered *in vitro* test setup was created. A staged approach creating two prototypes was adopted; were the first test device incorporated a neural amplifier chip and data transmitting LED, but still received its power and command signals through a wire. By keeping the focus on the optical link, the fundamental question of feasibility for LEDs to transmit neural signals was substantiated and quantified in the form of bit error ratio (BER) measurements. This was required before seriously investing into the development of the auxiliary components such as control circuits and powering scheme needed for a completely wireless device. The purpose of this stage wasn't to completely characterize a device, but to create a platform which: demonstrates the fundamental transmission requirements, and serves as a basis for the complete device. The further developed fully tetherless version of the device is described in more detail in Chapter IV.

A setup was created that recorded nerve signals that were relayed to an amplifier chip, which had a red-emitting AlGaAs LED connected to its multiplexed digital output driven at 3.3V and 2 mA, with a peak wavelength of 654 nm and radiant intensity of  $\sim 0.25$  mW/sr. The LED is modulated in accordance with the output of the amplifier chip, and transmits the neural information to a receiver. The heart of the device is a printed circuit board (PCB) consisting of a 32 channel wire-bonded Intan amplifier chip (RHD 2132), and all the complementary surface mount devices

soldered onto it using standard heat reflow techniques. The PCB was designed in-house and it consists of four layers with the inner two being a ground and power plane. Pads for LEDs are placed in the lower right corner of the device with the anode pin connected to the neural data digital output Master In Slave Out (MISO) pad of the chip, and the cathode pad connected to ground. The serial clock in (SCLK) signal, and the power to run the chip were received from the evaluation board connected to a laptop, which was used to send input commands to the device (Figure 3.1). Since the digital output of the amplifier chip was not designed for the modulation of an LED, its current output was limited to an average 2 mA with the use of a 200 $\Omega$  resistor connected in series, in accordance with the guidelines provided by the manufacturer. Two, off-the-shelf, LEDs (Avago HLMP-Q156, Kingbright APETD3528SEC/J3-PRV) were used for the experiments, as they fulfilled the criteria for providing the required radiant intensity at the supplied current levels ( $\sim 0.25$  mW/sr for the Avago and 3.2 mW/sr for the Kingbright), and have a response time ( $< 90$  ns) that can accommodate the data rate (10.24 Mbps).

Two types of photodetectors were used; an avalanche photo diode (APD) by First Sensor and a C-series silicon photomultiplier (SiPM) by SensL. These were placed vertically above the device's light source at various distances and the optical signal from the LED was recorded using a 1GHz bandwidth digital sampling oscilloscope (Tektronix MDO4104C). SCLK and the digitized data input to the LED were simultaneously recorded using voltage probes allowing the data input to the LED to be compared to the received optical signal from the LED. This data was processed offline in MATLAB to estimate the bit-error ratio (BER) for each measurement. When signal degradation reached a level where the error rate was high, i.e.  $> 2 \times 10^{-3}$  [1], a commonly used threshold for the use of forward-error correction (FEC) codes, a 50 mm diameter lens with 10 cm focal length was used to improve the conditions and focus the light onto the photodetector. The device was initially tested with its input pins left floating and picked up random noise from the surrounding environment. These random samples were read by the Intan chip and sent to the LED via the

MISO output. Biological experiments were carried out by interfacing the device with a 61-channel microelectrode recording from a rat whole-mount retinal preparation. A break-out board system was also developed that allowed the introduction of the optically received stream to the evaluation board and enable live viewing of the neural data using the Intan provided GUI

### 3.2 Data acquisition system

The setup was built around an Intan neural data acquisition system, consisting of an evaluation board (Figure 3.2) and 32 channel amplifier chip (Figure 3.5) communicating with each other through a 3-wire serial peripheral interface cable (SPI). The evaluation board acts as the master device, while the amplifier chip connected to the system acts as the slave.

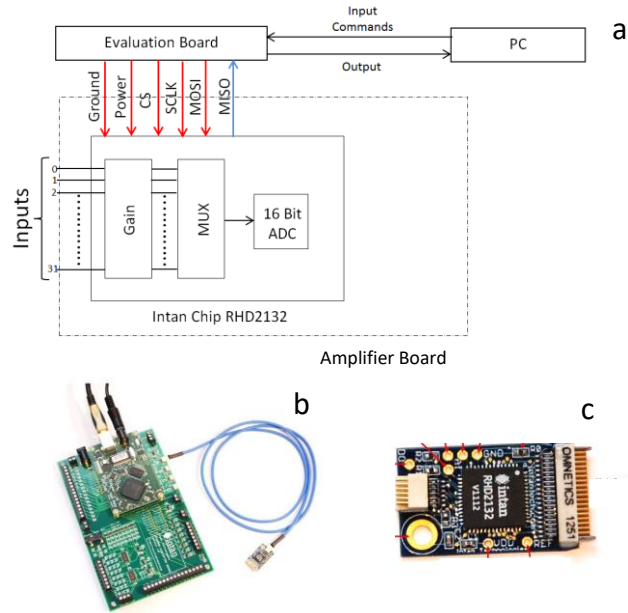


FIGURE 3.1: (a) Block diagram of the Intan setup showing the flow of clock signals and commands (CS, SCLK, MOSI) and output data (MISO) between the amplifier board and evaluation board. (b) The Intan Evaluation board with an amplifier board connected to it through a blue SPI cable. Image from [5](c) An Intan RHD2132 amplifier board with the amplifier chip located in the middle. The small connector on the left side is used to interface to the evaluation board with an SPI cable. The larger Omnetics connector on the right is used to attach neural probes. Image from [5].

The block diagram in Figure 3.1 shows the default Intan setup that was modified to accommodate the VLC device (Section 3.6). The evaluation board is connected to a



PC, which receives the user commands through a graphical user interface (GUI) provided by Intan. Through this GUI different parameters are set such as sampling rate, lower/higher bandwidth cut-off points and noise rejection filters. The command signals are sent from the evaluation board to the amplifier chip to initialize it, after which the amplification and (analogue to digital conversion) ADC begins. The 32 inputs of the chip are connected through an Omnetics NSD-36-AA-GS connector to the observed signal/tissue. The chip then carries out the amplification and multiplexing of the data into a single stream, which is then digitized through a 16-bit analogue to digital converter. The neural data is then sent through the (Master In Slave Out) MISO line to the evaluation board, which then processes the 16-bit samples and converts them into voltage readings. The results can then be displayed in real-time using Intan's GUI, while also saving the data to a hard disk to enable long term recording.

### 3.2.1 Evaluation Board

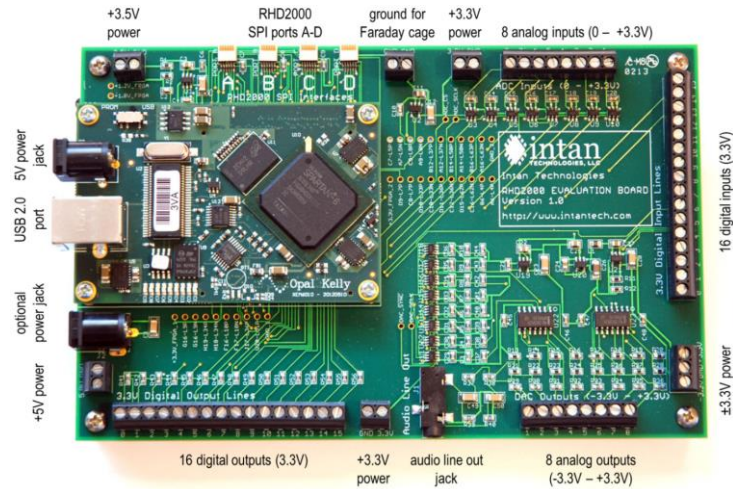


FIGURE 3.2: The Intan evaluation board with the Opal Kelly daughter board on top containing the Xilinx Spartan-3 (Field Programmable Gate Array) FPGA. The four SPI ports can be seen at the top left, which can each interface with up to two 32 channel amplifier boards. Additionally, various analogue and digital inputs and outputs are present, which can be used to conveniently record or easily introduce outside signals. Image from Intan manual[5]

To process the incoming neural bit stream from the amplifier chip in real time, circuitry is required to read the data and convert it to voltage recordings on the fly. This was carried out by the Intan system evaluation board (Figure 3.2), which provided the necessary clock signals for synchronisation and executed the conversion of the 16-bit samples to voltage readings. The evaluation board interfaced to a PC through a USB 2.0 port. The evaluation board comprised of an Opal Kelly daughter board containing a Xilinx Spartan-6 FPGA (Figure 3.4) with thousands of logic gates and flip-flops. These are set through a user definable bit file that was provided by the manufacturer, and automatically uploaded upon power up. The daughter board slots into the bottom larger board containing all the digital and analog outputs, along with four SPI ports required to interface with the Intan amplifier chips. Each port is capable of handling dual lines, enabling the reading of the data from two chips simultaneously, or a total of 64 channels. This amounts to a total of 256 channels that the evaluation board can process simultaneously. For the purposes of both the *in vitro* and the *in vivo* experiments, however only a single line of 32 channels was used. The FPGA is configured to run with a 100 MHz clock source, enabling a programmable clock generator to set the internal clock frequency depending on the sampling rate. The internal clock frequency is set by the equation:

$$f_s = 100 \text{ MHz} \times \frac{M/D}{2} \quad (2.1)$$

Where  $M$  is a multiplier integer and  $D$  is a divider that can be adjusted to set the internal clock frequency to a maximum of 84 MHz or 30 kS/s for each channel. The FPGA is based on a finite machine state code that repeats every 80 states as illustrated in Figure 3.3. These 80 states define the timing relation for the necessary SPI commands, and serve as a basis for the digital lines. Each period of the SCLK is made up from 4 states that is repeated 16 times. The rising edges of these pulses indicate where the bit values constituting the 16 bit samples should be defined. In the case of commands sent to the chip, the samples are sent on the Master Out Slave In (MOSI) line, while the output data of the chip is sent on MISO line. After the falling



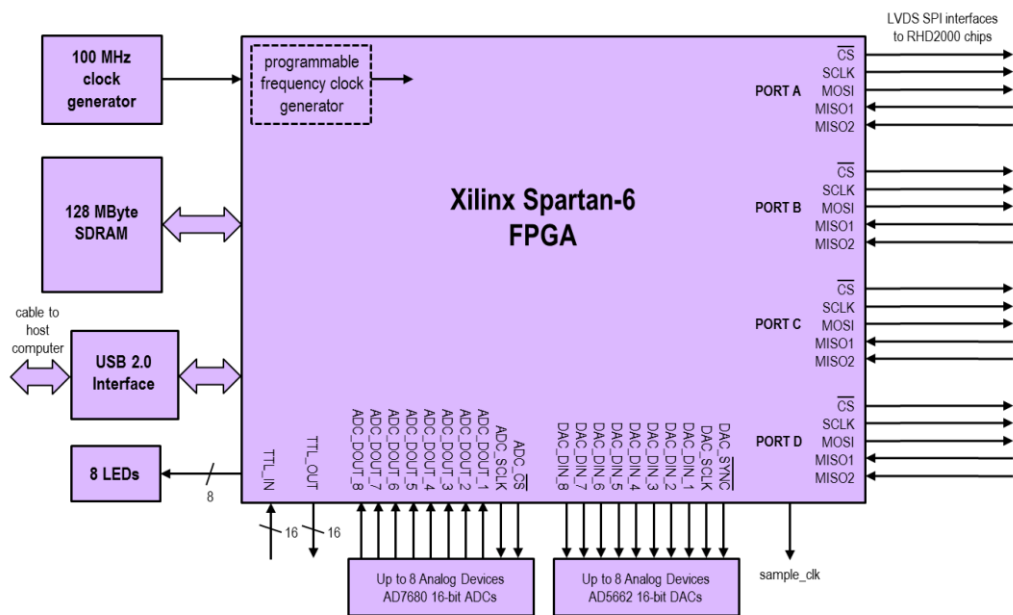


FIGURE 3.4: A block diagram of the Xilinx Spartan-6 FPGA outlining the core sections of its architecture. A 100 MHz clock source is used to set a programmable clock based on the required sampling rate. The four SPI ports and associated digital lines are shown on the right side, and can each interface with two amplifier chips (MISO1, MISO2). The USB host interface allows connection to a computer, which it can communicate with, while a 128 Mbyte of SDRAM is also present to store the necessary files configuring the setting required for its operation. Image from Intan manual[6]

### 3.2.2 Amplifier chip

The RHD family of amplifier chips amplify, multiplex and digitize biopotential signals (Figure 3.5). They interface with the evaluation board through a 3-wire SPI link, from which they receive the clock signals chip select (CS) and serial clock (SCLK), along with the commands from the MOSI line to control the chip (Figure 3.6 and 3.7). The ADC results are sent to the evaluation board for further processing over the MISO line. The clock signals are required to synchronize the data with the falling edge of the CS clock indicating the beginning of a sample, while the rising edge designates the end. SCLK is active and toggled 16 times when CS is low, with each rising edge correlating to a point in time when MOSI or MISO should be sampled to determine the bit values making up the 16 bit samples. In default operation the Intan chip is set up to cycle through the 32 input channels, and the 3 auxiliary channels in a round

robin fashion, while relaying back the results down the MISO line in a pipelined protocol. This is done by sending the CONVERT(63) command, which sends the decimal value 63 in binary format on the MOSI line, and instructs the chip to sequentially sample through all channels.

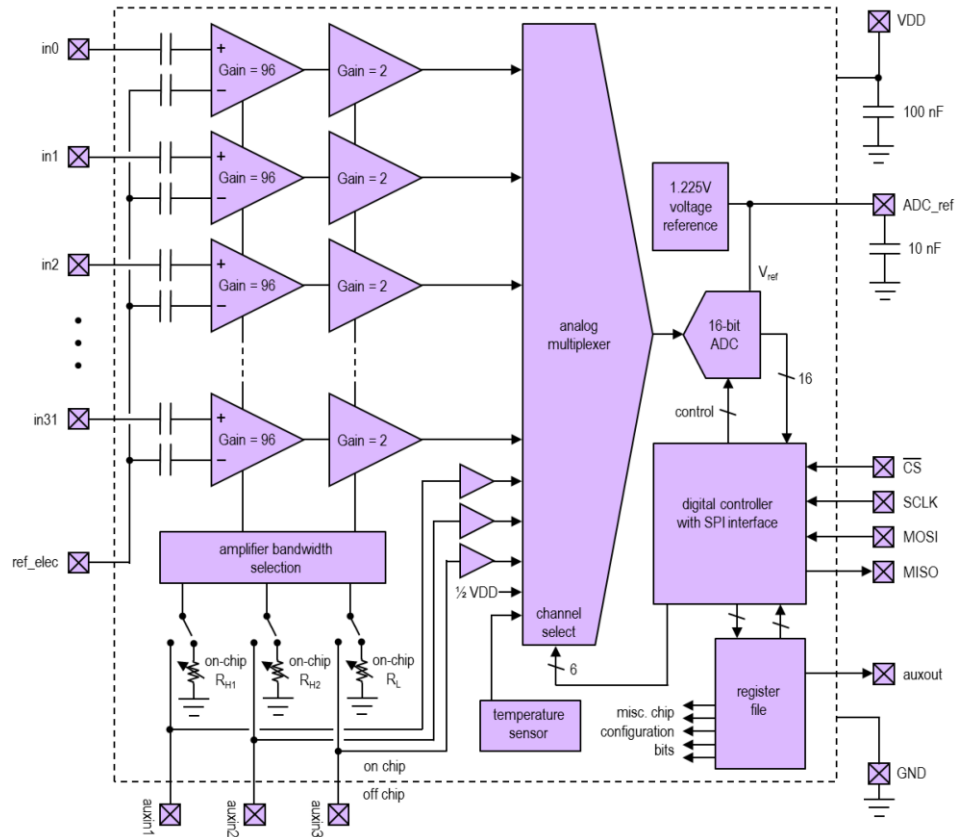


FIGURE 3.5: Block diagram of the Intan RHD2132 amplifier chip. The differential inputs go through a two stage amplification with a gain of 96 and 2, and have a common reference electrode connected through the negative inputs through a capacitor in series. After the gain stage the signals are passed through a 32:1 analogue multiplexer and sent through an ADC stage. This has its voltage set by an internal reference set at 1.225V and connected to an external 10 nF capacitor. The ADC block is also connected to a digital controller with an SPI interface, which is used to set the requested sampling rate for the chip, while also providing the necessary commands. The registers configuring the chip are also set through this block and written into the register file block. Image from Intan manual[7]

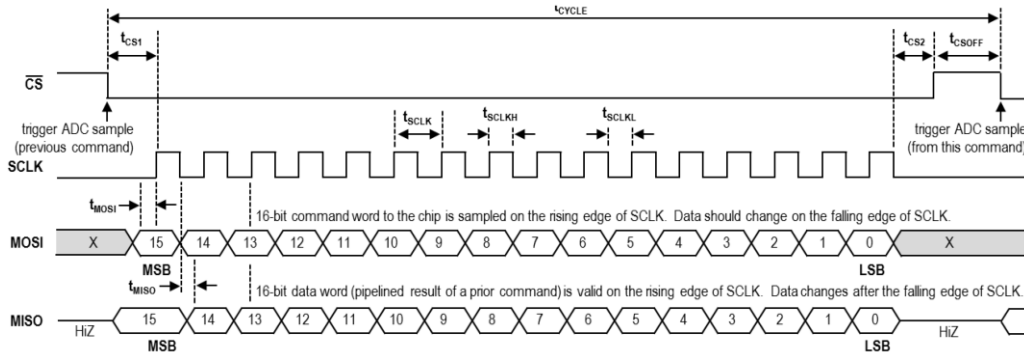


FIGURE 3.6: Timing diagram of the of the SPI communication implemented between the evaluation board (master) and the RHD2132 amplifier chip (slave). When CS goes low SCLK is toggled 16 times to define the bits at its rising edges for the MISO and MOSI lines. Image from Intan manual[7]

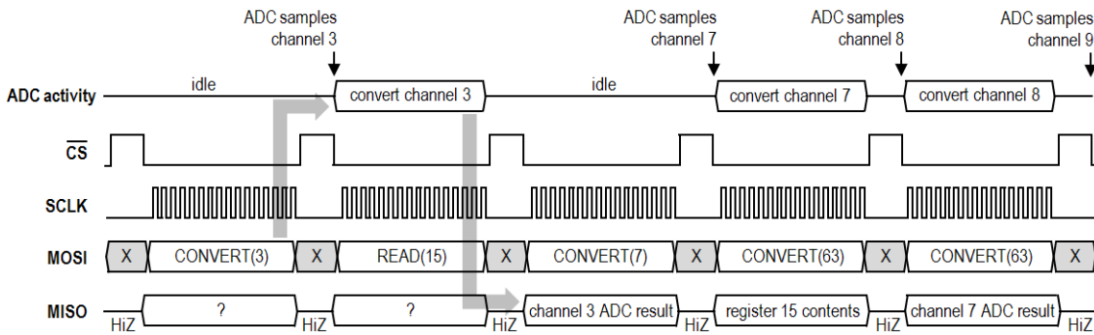


FIGURE 3.7: Block diagram outlining the command cycle for the system. When a command is sent on the MOSI line e.g. CONVERT(3) it takes up one samples worth of time to send it. The instruction of the command takes a further one sample’s worth of time to execute, while the results are sent on the MISO line in the next sample time block. Essentially the results are relayed back to the evaluation board two sample blocks after a command is initially sent. Image from Intan manual[7]

Upon power up, the evaluation board sends the appropriate commands to setup the chip for data processing. These are relayed through the MOSI digital line. Depending on the specific parameter, bit banks in the registers can be modified to enable/disable certain features of the chip: These commands are applied through writing to 17 of the 64 8-bit registers the chip contains, and will be outlined in the following section to give an overview about how the chip is initialized. For the fully wireless system these commands will be sent by an MCU, which will be discussed in more detail in chapter IV.

**Register 0** can be used to set the *ADC reference bandwidth*, which according to the data sheet should always be set to 3, and controls the bandwidth of an internal ADC reference generator feedback circuit. The *amp fast settle* function is normally set to 0 and can be used to activate a switch to close all the amplifiers, and settle their voltage. This can be used to overcome large transient responses, and is not set by default. The *reference voltage* is also set here, and is normally activated on power up. There is the option however to switch this off in case the amplifiers are not used to conserve power. The *ADC comparator bias* setting should always be set to 3, and sets the bias current for the comparator. Using the comparator select option, 4 different comparators can be selected, and by default should be set to 2.

**Register 1** controls the voltage sensor, which is on by default and can be turned off for power saving purposes. The ADC buffer bias can also be set here and is adjusted depending on the sampling rate. According to the data sheet, if it is  $>700$  MS/s an ADC buffer bias of 40 needs to be input. As the sampling used for the experiments exceeds this, this is the value that is used.

**Register 2** configures the multiplexer bias current, and is again set with respect to the sampling rate. For the sampling rate that is required at 20 KS/channel, a value of 4 needs to be set according to the data sheet.

**Register 3** sets the *MUX load*, and can be used to control the total capacitance at the input of the ADC, and should always be set to 0. This register also controls the activation and control of the temperature sensors as well as the digital output pin, which may be used to control external circuits. These were turned off by default.

**Register 4** is used to set *weak MISO*. This setting can be used to enable high impedance when CS is pulled high, allowing more than one chip to share the line (as long as only one of the chip's CS line is active at any time). If only one chip is connected to the line this may be set to one, which can prevent the line from drifting from values between logic low and high. The *sign of the bits* is also set in this register, and can be used to either assign negative values if they are below a reference value or

have all values measured from a baseline level of 1000000000000000. *Absolute value mode* may also be enabled, which sends the incoming results through an absolute value function, and carries out full wave rectification. This can be useful when symmetric negative/positive thresholds are needed or envelope estimation algorithms are to be implemented.

**Register 5-8** can be used to set the parameters for the generation of a waveform used for impedance measurements. Additionally, they are also used to enable the option of connecting all the inputs to a common reference electrode, which can be connected to a DC voltage for electroplating purposes.

**Registers 9-13** are required to configure the lower and upper cut-off frequencies. This can be controlled either on chip or externally by resistors. For the experiments on chip control was used with the lower and upper cut-off frequencies being set to 50 Hz and 10000 Khz respectively. These registers also control the 3 auxiliary inputs, which were left on by default.

**Registers 14-17** are used to individually set and power up the 32 amplifiers. These were all turned on.

Once writing to the registers is completed, an ADC calibration command is sent which can take many cycles to execute. Because of this, nine dummy commands are transmitted to give time for the calibration to be fully carried out.

The Intan chip can function in two modes (Figure 3.8): Complementary metal–oxide–semiconductor (CMOS) or Low Voltage Differential Signalling (LVDS) mode. LVDS involves two lines being used for each digital signal. These two lines are terminated with a 100 Ohm resistor, while a current of 3.5 mA is forced through them with an alternating direction. A voltage of 1.25V is applied to the wires, which acts as a baseline around which the data is modulated at logic levels of  $\pm 350$  mV. The termination resistors reduce reflections, which combined with the smaller voltage levels, and nearly constant current greatly alleviate noise levels. For the device



however, CMOS signalling was used. This was required as the voltage provided by LVDS signalling was too low to reach the turn on voltage of most LEDs. Using CMOS signalling, a voltage swing of 3.3V is used, enough to activate all wavelength LEDs while also reducing the total current consumption to 5.6 mA from 10.4 mA. The trade-off however is that using CMOS signalling imparts a higher noise level propagating through the system as the bursts of current drawn from the power supply introduce high-frequency noise to the chip power supply.

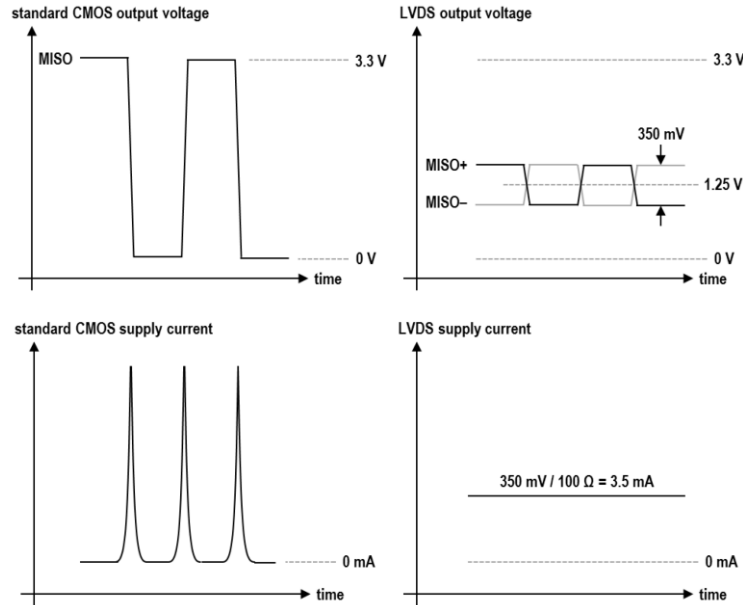


FIGURE 3.8: A comparison of CMOS signalling and LVDS signalling from the Intan documentation showing how the current and voltage characteristics of the two configurations differ. CMOS signalling results in large supply current spikes resulting in noise, but operate with a larger voltage swing ideal for driving an LED. Image from Intan manual.[7]

## 3.3 LEDs and photodetectors

### 3.3.1 LEDs

The LED on the device has three functions. Its primary one was to transmit the neural data, which was received by a photodetector. Secondly it served as an indicator showing if the device is on or off, and finally it will also serve as a tracking

LED to follow the motion of animals in future freely moving experiments. For initial tests the Avago HLMP-Q156 LED was selected as it possessed a number of key characteristics that made it suitable for the system. It had a small volume and weight (Fig. 3.9a, 3.9b), and had a fast enough response time of 45 ns. While even smaller LEDs are available in 0402, and 0603 packages, the weight reduction achieved by implementing one would be negligible, as the dominant source of weight are the battery and PCBs. It had a deep red colour with a dominant wavelength of 644 nm (peak of 654 nm), thus operated in a spectrum that has been reported to not be observable by mice [8]. While there is no uncertainty about rodents being significantly less sensitive to red light than humans, some studies have shown that  $>600$  nm wavelengths can in some cases trigger a response[9], [10] (further explored in section 5.6). The turn on voltage was low at 1.5V, leaving the CMOS digital output driven at 3.3V sufficient enough to fully turn on the LED at the currents it was limited to. The system ran fine without any current limiting measures being implemented, and the LED drawing the maximum current the chip pin could provide ( $\sim 7$  mA). However, as recommended by Intan Technologies, the current was limited to 2 mA to avoid any excessive thermal stress on the pin for the sake of maximizing the operational lifetime of the chip. The output of the chip acted as a voltage source with the current draw being purely determined by the load, which was reduced with a  $200\Omega$  resistor in series, thus dropping the current draw to 2 mA. While not the most efficient way to reduce current as energy is lost across the resistor in the form of heat, it is the simplest, requiring the least amount of components and smallest footprint. The limiting resistor value was picked using Ohm's law:

$$V = IR \tag{2.2}$$

$$R = \frac{V}{I} \tag{2.3}$$

From Figure 3.9 (c), it can be seen that the voltage is 1.6V at 2 mA current draw for the LED. Using these values we get  $800\Omega$  for R. The duty cycle of the average outgoing digital stream correlated to random neural data with the data gaps required

for sample separation is  $\sim 30\%$ . Taking this into account, a resistor that is  $\sim 30\%$  of  $800\Omega$  ( $240\Omega$  or  $200\Omega$ ) was selected. Lastly the LED had a speed of response time constant of  $45\text{ ns}$ , making it fast enough to transmit data at the required data rates ( $16\text{ bit resolution} \times 32\text{ channels} \times 20000\text{ KS/s sampling rate} = 10.24\text{ Mbps}$ ).

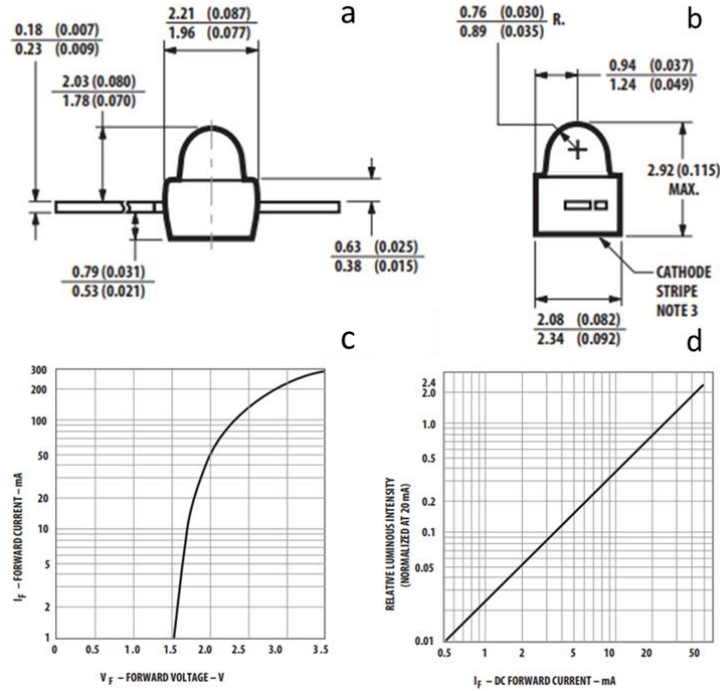


FIGURE 3.9: (a)(b) Physical dimensions of the Avago HLMP-Q156 LED. (c) IV graph for LED (d) Luminous intensity vs forward current. Images from Avago data sheet[11]

For later experiments (section 4.4, chapter IV) the Kingbright APETD3528SEC/J3-PRV (Figure 3.10) was used, as it had superior luminous intensity characteristics for the same currents ( $\sim 3.2\text{ mW/sr}$  vs  $\sim 0.25\text{ mW/sr}$  at  $2\text{ mA}$ ). Since for the irradiance for the LEDs was given in photometric units the following calculations were used to convert it to radiometric units. From [12], [13] the below equations outline the relationship between photometric and radiometric functions where  $\Phi_v$  is the photometric quantity in lumens and was applied to calculate and estimate the irradiance in  $\text{mW/sr}$  for the LEDs used, by using numerical integration methods.

$$\Phi_v = K_m \int_{\lambda_1}^{\lambda_2} \Phi_E(\lambda) v(\lambda) \delta\lambda \quad (3.3)$$

$\Phi_v$  = luminous flux in lumens

$K_m$  = scaling factor equal to 683 lumens per watt

$\Phi_E(\lambda)$  = spectral power in watts per nanometer

$v(\lambda)$  = photopic spectral luminous efficiency function

$I_v$  = luminous intensity in millicandela

$I$  = radiometric intensity in mW/sr

$f(\lambda)$  = dimensionless spectral distribution function for LED

$$I_v = 683I \int_{\lambda=595}^{\lambda=675} f(\lambda)v(\lambda)\delta\lambda \approx 683I \frac{\sum_i f_i v_i}{\sum_i f_i} \quad (\text{Kingbright}) \quad (3.4)$$

$$I_v = 683I \int_{\lambda=580}^{\lambda=700} f(\lambda)v(\lambda)\delta\lambda \approx 683I \frac{\sum_i f_i v_i}{\sum_i f_i} \quad (\text{Avago}) \quad (3.5)$$

$$I = \frac{I_v \sum_i f_i}{683 \sum_i f_i v_i} \quad (3.6)$$

$$I = 0.25 \text{ mW/sr} \quad (\text{Avago})$$

$$I = 3.2 \text{ mW/sr} \quad (\text{Kingbright})$$

Additionally, the Kingbright LED also had a larger viewing angle ( $60^\circ$  vs  $15^\circ$ ) compared to the Avago Q156. While the response time was not listed in the datasheet, it proved to be capable of transmitting data at the required rates (10.24 Mbps). As this was the LED that was incorporated into the fully wireless device, a more thorough analysis of its characteristics and limitations will be described in chapter IV.

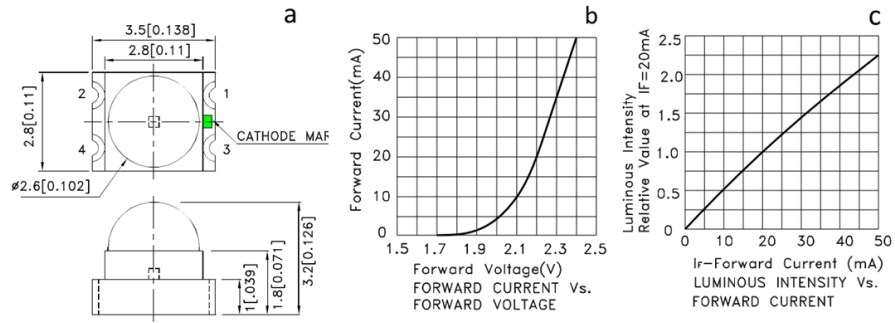


FIGURE 3.10: (a) Physical dimensions of the Kingbright APETD3528SEC/J3-PRV (b) IV graph for LED (c) Luminous intensity vs forward current. Images from Kingbright data sheet[14]

### 3.3.2 Photodetectors

Two photodetectors were used to receive the optical data. Initially the First Sensor AD800-11 (Figure 3.11) avalanche photo diode (APD) was implemented, as it had a more than fast enough rise time (1 ns) to handle the transmitted bit stream. Detectors with higher response times than required for the target data rate (10.24 Mbps) were selected, to enable future scaling up options for higher data rates. The detector had an area of  $0.5 \text{ mm}^2$ , and peak spectral response of 600 nm which was sufficiently close to the LEDs dominant wavelength of 644 nm. This resulted in a high enough sensitivity to receive data at practical distances ( $>10 \text{ cm}$ ). A high voltage of 220V from two Yokogawa GS610 power supplies tied in series was applied to the detector to operate it around its breakdown voltage, and facilitate impact ionization.

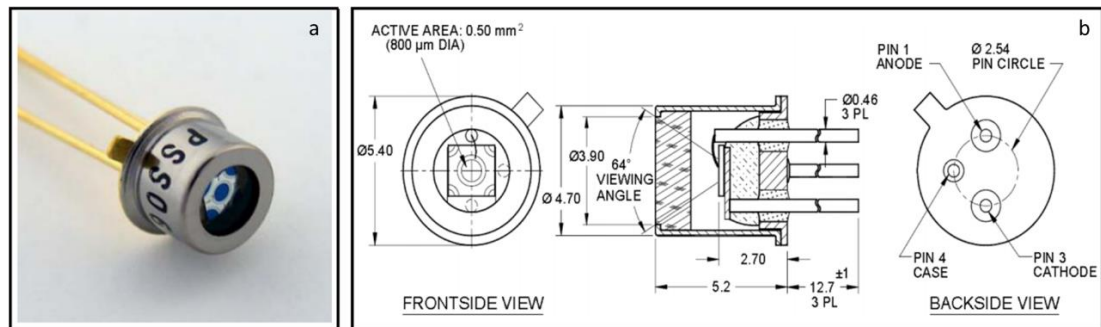


FIGURE 3.11: (a) The First Sensor AD800-11 APD photodetector with a  $0.5 \text{ mm}^2$  detector area. (b) Physical dimensions of the First Sensor AD800-11 APD photodetector. Images from First Sensor data sheet[15]

Eventually the First Sensor AD800-11 was replaced by the SensL C-series 10020 Silicon Photomultiplier (SiPM), (Figure 3.12) as it proved to be more suitable for a number of requirements. SiPMs combine an array of Single Photon Avalanche Diodes (SPAD), which in contrast to APDs operate at voltages well above the breakdown potential, resulting in electrons to accelerate with a much greater force. Similarly to APDs, this results in an avalanche effect referred to as impact ionization where the newly dislodged electrons transfer kinetic energy to further electrons, resulting in a large current flow. In this case however, the collisions are at such a magnitude and rate, that a single photon can trigger a significant current output. When a photodetector is operating in such a fashion, it is referred to be in Geiger mode. Each of the SPADs are referred to as microcells, and are biased to operate in the above described fashion. A photon detected by a microcell has no effect on the neighbouring cells, and allows them to operate in a completely independent manner. By summing the outputs from all the microcells, a virtually analog detection scheme is achieved, where the output is proportional to the number of detected photons. As long as the voltage is applied, the diode remains conductive. To avoid this, quenching is carried out, which reduces the current drawn by the diode, and resets it to a state where it is ready to detect photons again. This can be done passively by a resistor, which lowers the current consumption, and consequently the reverse voltage seen by the diode to a value below the breakdown voltage (Fig. 3.13b). The main advantages of the detector included its larger photodetector area ( $1 \text{ mm}^2$ ) and improved sensitivity that resulted in enhanced SNR ratio while reducing BER, which is expanded on in section 3.6.3. The breakdown voltage ( $V_{br}$ ) was also significantly lower at 24.7V than for the APD, allowing a single small power source (RS Pro IPS 4303S) to be used for the system instead. As outlined in the data sheet, a voltage of  $V_{br} + 5V$  was applied to the device to reach optimum performance. The response time of the SiPM was less favourable compared to the APD, and was limited by the microcell recharge time constant which for this particular model was 23 ns. The limiting factor of the optical link however

was still the transmitting LED, as it had a speed of response time constant of 45 ns, which was likely higher due to the limited current driving it.

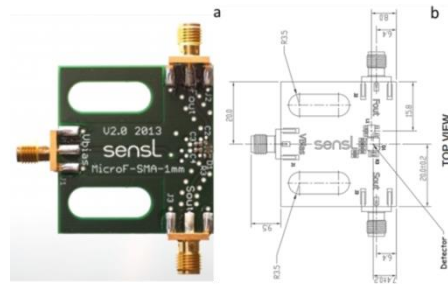


FIGURE 3.12: (a) The SensL C-series 10020 SiPM with a 1 mm<sup>2</sup> detector area, and 20 micron SPAD detector cells. Image from SensL website [16] (b) The dimensions of the photodetector. Image from SensL data sheet[17]

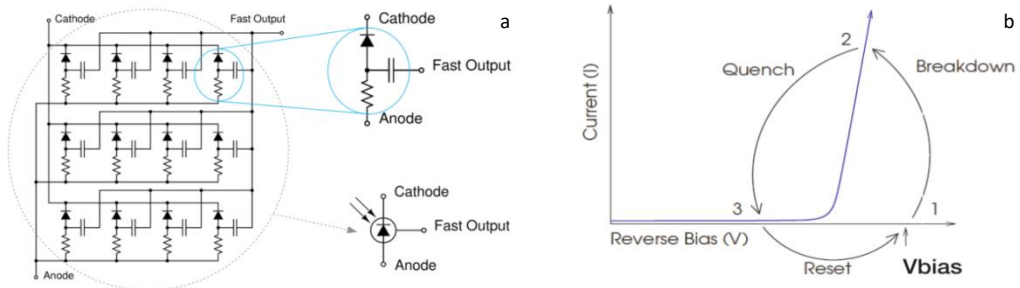


FIGURE 3.13: (a) Simplified circuit schematic of the SensL SiPM (left) showing each microcell which is composed of the SPAD, quench resistor and fast output capacitor (top right). Image from SensL data sheet [18](b) Breakdown, quench and reset cycle of a SPAD working in Geiger mode. Image from SensL manual[19]

Sources of noise for SiPMs include shot noise, which is the random firing of electrons due to the discretised nature of photons independently hitting the photodetector characterised by a Poisson distribution. At very low optical intensities it can become a significant factor, however the dominant source of noise for SiPM photodetectors is ambient light and dark current due to the intrinsic thermal electrons present in the active region. Dark noise increases linearly with the detector size so a 9 mm<sup>2</sup> device will have ~9 times the dark current as 1 mm<sup>2</sup> and is also directly correlated to overvoltage.

Triggered microcells can also initiate additional avalanches in neighbouring cells through photons emitted by the accelerated carriers. These can travel to the neighbouring microcells through a number of paths such as being reflected from the epoxy or glass on the top of the photodetector, reflected from the bottom of the substrate or transitioning parallel along the p-n junction. The number and size of microcells will determine the cross talk percentage. Similarly to other sources of noise, it is a function of overvoltage, increasing linearly with larger potentials. The cross talk percentage for the C10020 is 5% while for the J30035 (used in chapter IV) it is 25% [18], [20]. Due to defects in the silicon, charge carriers can become trapped. After a short delay on the order of a couple of ns they can escape however, and trigger additional avalanches. The probability of this occurring is correlated to the overvoltage. The photodetectors used in the experiments however have very low afterpulse probabilities (0.4% for C10020 and 5% for J30035 at 5.0V overvoltage), making their noise contribution negligible. To maintain electrical and optical isolation, gaps are required between neighbouring microcells, along with space for quenching resistors to bring back the detectors to a receptive non-firing state. These structures on the detector are referred to as dead space, an area across which the detector is not receptive to light. The fill factor obtained from the data sheet determines what percentage of the detector surface area is sensitive to incident photons. For the C-series 10020 photodetector this is 48% (0.48 mm<sup>2</sup>), while for the J-series 30035 it is 64% (5.76 mm<sup>2</sup>). The smaller the microcells, and the larger the total photodetector area, the lower the fill rate will be due to the increased number of microcells with associated dead areas.

Peak sensitivity of the C-series 10020 photodetector is at a wavelength of 420 nm with a PDE of 31%, and decreasing to ~9% at around 640 nm [18], the dominant wavelength for the data transmitting LED. While these two didn't align, the high gain factor along with the fast recovery time allowed the required data amount (10.24 Mbps) to be transmitted over large enough distances (>20 cm). For future improvements, the J-series offer packages with larger detector areas (3x3 mm) with



similarly sized faster microcells could prove as a viable upgrade. Other detectors such as the SensL R-series are optimized for the  $>600$  nm wavelength range but are not available in packages with larger photodetector areas ( $>1$  mm<sup>2</sup>). While they have better photodetector efficiencies in the red spectrum (PDE of 35% vs 12.5% at 650 nm) the total light sensitive area is decreased by almost a magnitude (0.63 mm<sup>2</sup> vs 4.32 mm<sup>2</sup>) compared to alternatives such as the J-series 30020 photodetector available with 20 micron cells while having improved timing characteristics (15 ns vs 21 ns). The rise and fall times were calculated as follows based on the SenL application notes [21].

$$\tau = C_{\mu cell}(R_Q + NR_L) \quad (3.1)$$

$$T_{90\%-10\%} = 2.2\tau_R \quad (3.2)$$

$\tau$  = microcell recharge time constant (recovery time)

$C_{\mu cell}$  = microcell capacitance

$R_Q$  = quench resistance

$N$  = number of microcells

$R_L$  = series or termination resistance

$T$  = 90% to 10% recovery time

For the C-series 10020 photodetector from the above variables from the manufacturer datasheet are:

$$C_{\mu cell} = \frac{90 \text{ pF}}{1296} = \sim 69 \text{ fF}$$

$$R_Q = 290 \text{ k}\Omega$$

$$N = 1296$$

$$R_L = 50\Omega$$

Using the above values in equation 3.1 and 3.2 we get the value of 24.8 ns for the recharge time constant and a 90% to 10% recovery time of 54.64 ns.

For the J-series 30035 photodetector

$$C_{\mu\text{cell}} = \frac{1070 \text{ pF}}{5676} = \sim 188 \text{ fF}$$

$$R_Q = 220 \text{ k}\Omega$$

$$N = 5676$$

$$R_L = 50\Omega$$

Using the above values in equation 3.1 and 3.2 we get the value of 94.71ns for the recharge time constant and a 90% to 10% recovery time of 208.37 ns.

### 3.4 Transmitter end device design

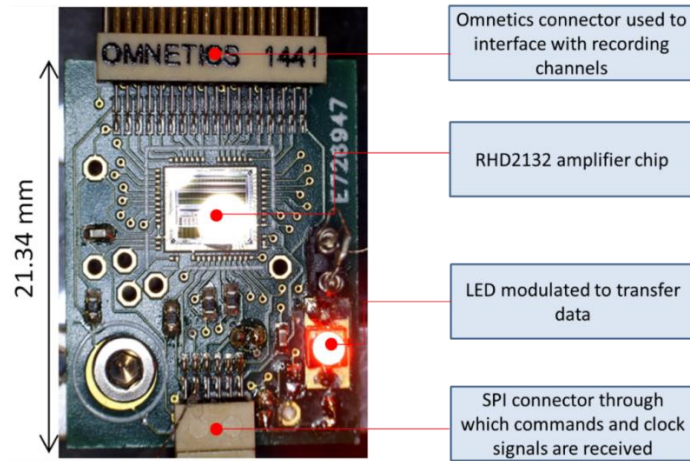


FIGURE 3.14: Plan view of the device showing the main components

The front end of the device incorporated a custom made PCB to accommodate an RHD2132 Intan chip which had its output connected to an LED to transmit the neural data. Several designs were tested, with the initial design incorporating a bare die chip. The exact chip dimensions, can be seen in Appendix 3.3a. The bare die chip was placed and glued on the large central pad using a conductive epoxy (CircuitWorks CW2400), and wire bonded to the appropriate pads on the PCB as shown in Appendix 3.4. The overall layout of the device is highlighted in Figure 3.14. The

dimensions of the device are 1.55 x 17.02 x 21.31 mm. The Omnetics connector at the top is used to interface with the electrodes used to detect neural activity, while the Intan amplifier chip is placed slightly towards the top from the centre of the device. The data transmitting LED is placed in the bottom right corner while the SPI connector (Omnetics PZN-12-VV) is at the bottom, and is used to interface with the evaluation board. A grounded screw hole was placed in the bottom left corner to fix the device in position. Pins for an optional jumper to allow the disconnection of the LED was placed right above it. Complimentary surface mount components required for the amplifier chip were implemented at values and ratings specified in the Intan data sheet. A 10 nF capacitor (Wurtz, 0402, X7R) was placed between ADC\_ref and ground near the bottom of the chip required for the ADC supply independent reference. A decoupling capacitor of 200 nF (Wurtz, 0402, X7R) was placed near the left side of the chip to enable voltage smoothing in case any spikes are propagated across VDD.

### 3.5 Data Acquisition (DAQ) using an oscilloscope

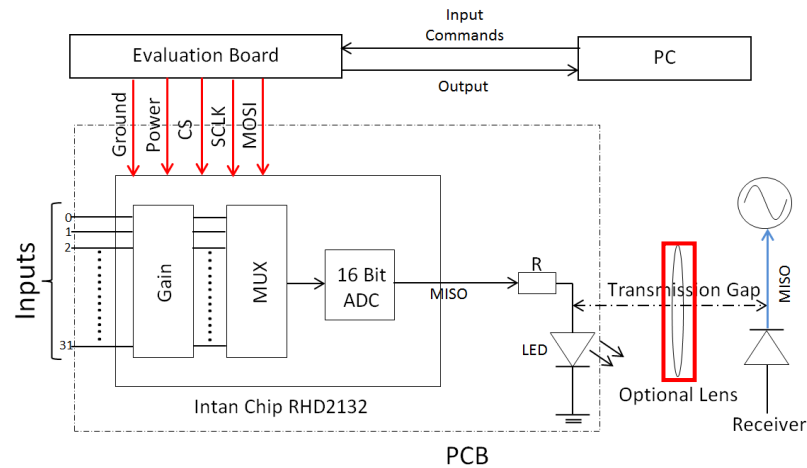


FIGURE 3.15: Block diagram showing the initial VLC setup that was used. The serial clock in (SCLK), reference electric MISO, and optically transmitted data were recorded using voltage probes, and then analysed post recording using a Matlab script. An optional optical lens (highlighted with the red rectangle) was also used to focus light onto the detector and improve SNR performance.

The first version of the modified system is shown in Figure 3.15, highlighting the differences from the original configuration (Fig. 3.1). The main changes include the incorporation of a data transmitting LED, which's output is limited by a 200 Ohm Resistor to limit current consumption and comply to the chips safety ratings. The LED transmitted the data to either a SensL C-series photodetector or a First Sense APD. At distances where the irradiance reaching the photodetector was insufficient an optical lens was used to focus light onto the detector to improve SNR. Using an oscilloscope, traces from SCLK and MISO are recorded by probing the PCB along with the optical signals detected by the photodetector, each made up of  $5 \times 10^6$  samples, and totalling record lengths of 0.1s. A thresholding Matlab algorithm (Appendix 3.5) checks that data points at each time stamp, and depending on its position relative to the threshold determines it to be a 1 or 0. The data is plotted in Matlab where the SCLK rising edges give the point at which the digitized output should be sampled. The rising edges are detected by using a script that differentiates the SCLK trace to locate the rising edges, points where the derived gradient will be at the maximum and limiting towards 1. These positions are then used to detect the bit values of the optical data, and compared to the bit values detected from the probed reference electrical MISO stream. Differences are categorized as errors and tallied up to calculate the bit error ratio (BER). Before the script is run the user has the option to set the threshold value, and other parameters, and introduce time shifts to properly align SCLK traces with the optical data. For post processing purposes this was sufficient, however for freely moving experiments, multi threshold protocols that are more adaptable to varying input signals would likely be more feasible. Figure 3.16 details the above, regarding how the recorded bit stream and clock signal can be used to reconstruct the neural data. The transmitting device was interfaced with a 61-channel array (Figure 3.17b), which had electrodes positioned in its centre in a hexagonal fashion (Figure 3.17c), and terminating on the edges of the glass substrate. A black circular aperture is placed on top of the array provided a compartment in which saline solution and neural tissue may be placed. A platinum wire was also

integrated, which served as reference electrode for the connected device, and was connected through a crocodile clip attached to the PCB. The PCB (Figure 3.17a) was fabricated with its pads aligning with the connections of the array.

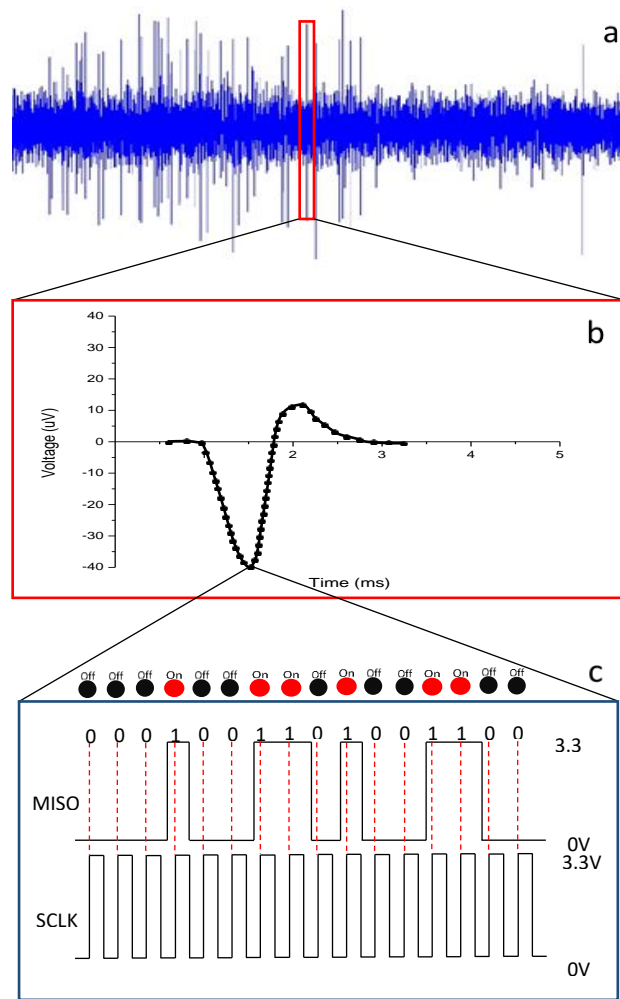


FIGURE 3.16: Illustration of how the data is being processed on the bit level. Starting from the top of the image (a), an arbitrary neural spike train is shown that was reconstructed from the bit stream that was recorded using an oscilloscope. In (b) a random neural spike from the spike train is magnified in the following section, with each dot indicating a sample at a given point in time, roughly correlating to 20 KS/s, enough to clearly reconstruct faster neural spikes as well. In (c) it is shown how each sample is made up of 16-bit values that are sampled on the rising edge of the SCLK clock signal indicated by the red dashed line. The LED states correlating to each bit are also indicated (On Red – Off Black). Depending on the state of the MISO at the given moment, a digital 0 or 1 is registered at the instance. A value is created once all 16 digits are read, to create a subsequent voltage reading at the associated time stamp of the sample. The channels are cycled through in a round robin fashion to read all 32 channels, followed by the readings from the three auxiliary inputs.

The PCB routed the detected electrical signals to a male Omnetics connector (NPD-36-AA-GS), which interfaced with a female Omnetics connector (NSD-36-AA-GS) on the VLC device. To test the system, saline solution was inserted into the compartment of the array, and random noise was initially analysed. Once established that a sufficiently low BER ( $<10^{-3}$ ) could be achieved, animal experiments were carried out using standard protocols. Mice were placed into a low light environment to facilitate dark adaption. After 20 minutes, cervical dislocation was carried out and the eyes were enucleated. The dissection was carried out in oxygenated Ames' solution (Sigma). The vitreous and the anterior portion of the eye were removed directly after enucleation. A dissected piece of retina approximately  $1-3 \text{ mm}^2$  was removed from the dorsal or nasal part of the eye with the retinal ganglion cell (RGC) side placed flat on an extracellular micro-electrode array (MEA). The retinal dissection and eye removal were performed under dim red light. Retinas were perfused with Ames' solution ( $34 \pm 2^\circ\text{C}$ ) bubbled with 95%  $\text{O}_2$ , 5%  $\text{CO}_2$ , pH 7.4, while recording. A MEA consisting of 61 electrodes with  $60 \mu\text{m}$  was

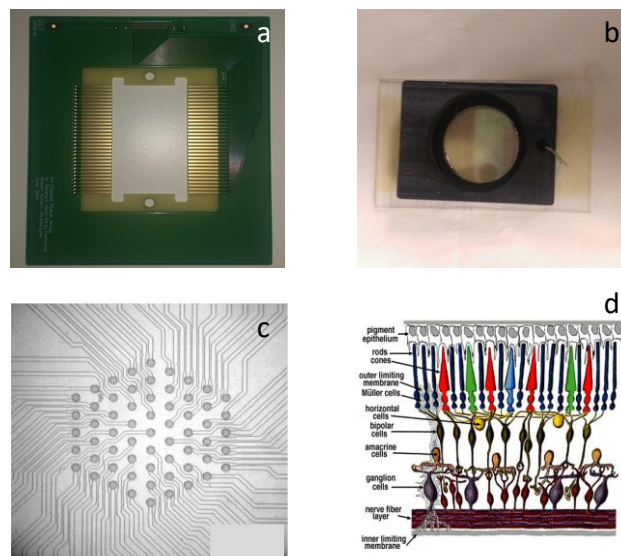


FIGURE 3.17: (a) The PCB with the central aperture into which the 61-channel array is inserted into. (b) The 61-channel array with tracks leading to the edge of the glass substrate. (c) Electrode layout of the array arranged in a hexagonal fashion with a 60-micron pitch. (d) Illustration of the cross section of retinal tissue that was placed on the MEA. Image from [22].

used for the recordings. The electrodes, arranged in an isosceles triangular lattice, covered a hexagonal region of 300  $\mu\text{m}$  on a side. The BER at various configurations is summarized in the table 3.1. More in-depth analysis, with respect to data rates vs distance and angles is carried out chapter IV with a more final iteration of the device.

### 3.6 DAQ with live streaming using Intan GUI

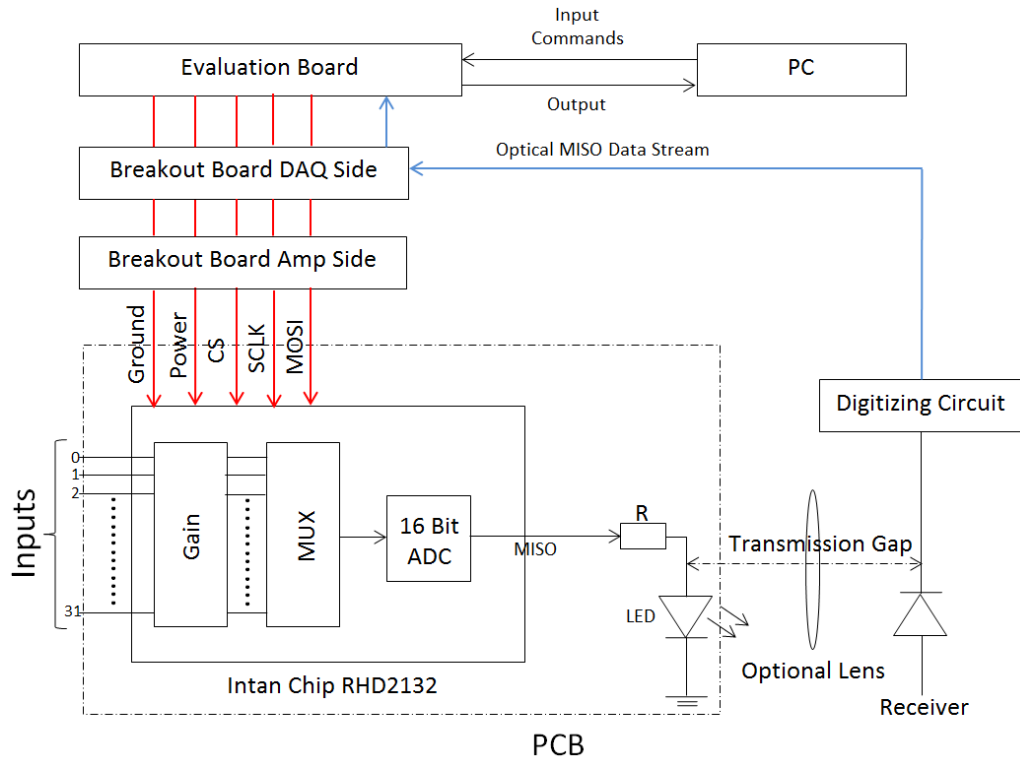


FIGURE 3.18: The block diagram of the final setup with the digitizing boards and the break-out boards present. These were used to introduce the optically transmitted signal to the evaluation board, which then allowed the neural data to be displayed in real time.

The final configuration for the *in vitro* setup is shown in figure 3.18. Figure 3.19a shows the array and PCB placed in a Faraday Cage with VLC device connected to (Figure 3.19b). In Figure 3.20 the photodetector is placed above it to receive the incoming data. It is similar to the setup shown in Figure 3.15 with the crucial difference being the inclusion of the break out boards (Figure 3.21) and digitizing circuit (Fig. 3.22), allowing the introduction of the optically transmitted MISO data stream to the evaluation board. This enabled live viewing of the investigated signals

as opposed to relying on post processing, and verified the feasibility of the system for in vivo experiments where real-time feedback is essential. Due to the delays arising from the processing of the optical signal through the digital circuitry, the reintroduced data was occasionally out of sync with the clock signals that were still derived from the evaluation board source. In these instances, the manual delay was set through the Intan GUI to enable proper alignment between the digital lines, which allowed fine tuning down to the bit level. There were also slight improvements made to the device itself as the bare die chip was replaced with a (Quad Flat No-Leads) QFN package, which allowed easier assembly. Additionally, the Avago LED was replaced by the Kingbright LED, which had roughly six times the radiant intensity (0.25 mW/sr vs 1.9 mW/sr) for the same current draw, and was also later implemented on the fully wireless device. Lastly the connectors were reinforced with a UV curable adhesive (Norland NOA68) to increase robustness, and test points were also introduced for the digital lines to provide easier access.

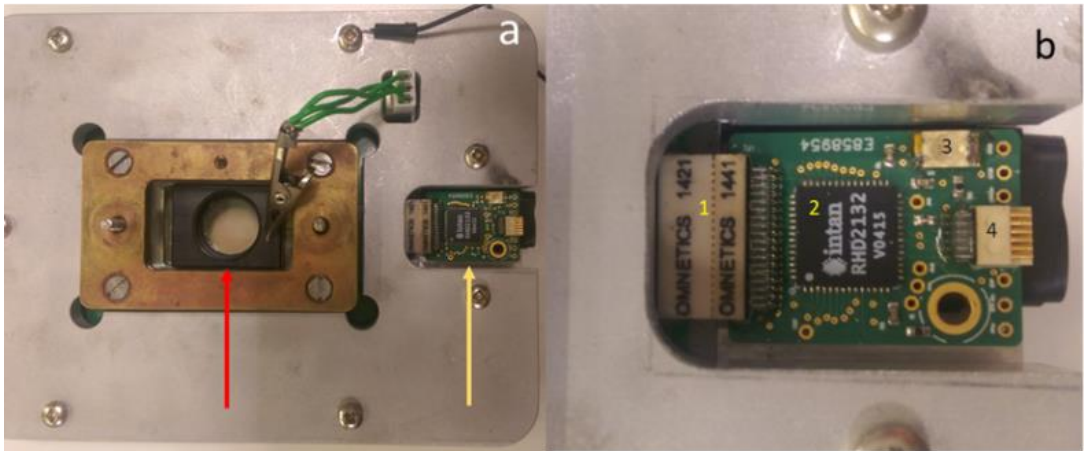


FIGURE 3.19: (a) Top down view of the 61-channel array (red arrow) and device (yellow arrow) in its Faraday cage. (b) The updated device and its main components (1) the Omnetics connector used to interface with the array (2) the Intan RHD2132 amplifier chip in a QFN package (3) data transmitting Kingbright LED connected to the MISO line (4) SPI connector reinforced with Norland adhesive connecting to the evaluation board.



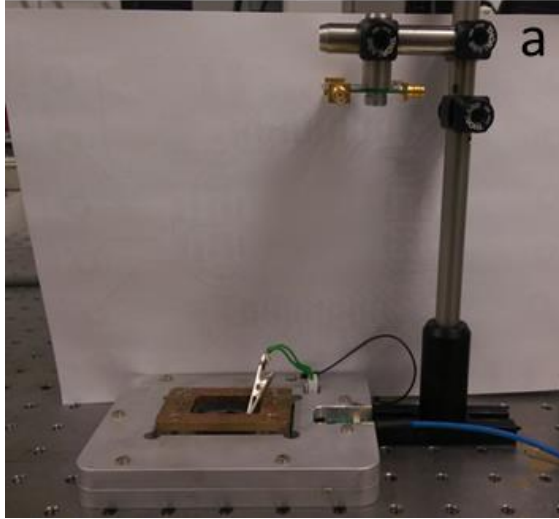


FIGURE 3.20: The front end of the setup showing the device interfacing with the 61-channel array and the PCB (not visible but shown in Figure 3.17a), while inserted into its Faraday cage. The photodetector is positioned above it to receive the data.

### 3.6.1 Break-out boards

Two break-out boards shown in Figure 3.22 were created in order to create a break in the SPI line, and to allow the option to introduce the optically received signal to the evaluation board. Each digital line arriving from the evaluation board was connected to an (Subminiature Version A) SMA termination on the break-out board that allowed robust interfacing with the required lines. The PCBs were made using standard fabrication techniques by Eurocircuits, and had a thickness of 1.55 mm. The PCBs, similarly to the device where made from four layers with a ground plane and power plane present to improve noise characteristics. An Omnetics PZN-12-VV connector was placed on each board to allow interfacing with the evaluation board ports and the device. A large plated hole was also drilled in the bottom right corner to allow the mounting of the PCBs. The matching signals (GND, VDD, CS, SCLK, MOSI) were connected from the appropriate SMA connector from one board to the other. The MISO line was left unconnected allowing the optically received signal that is digitized to be introduced instead.

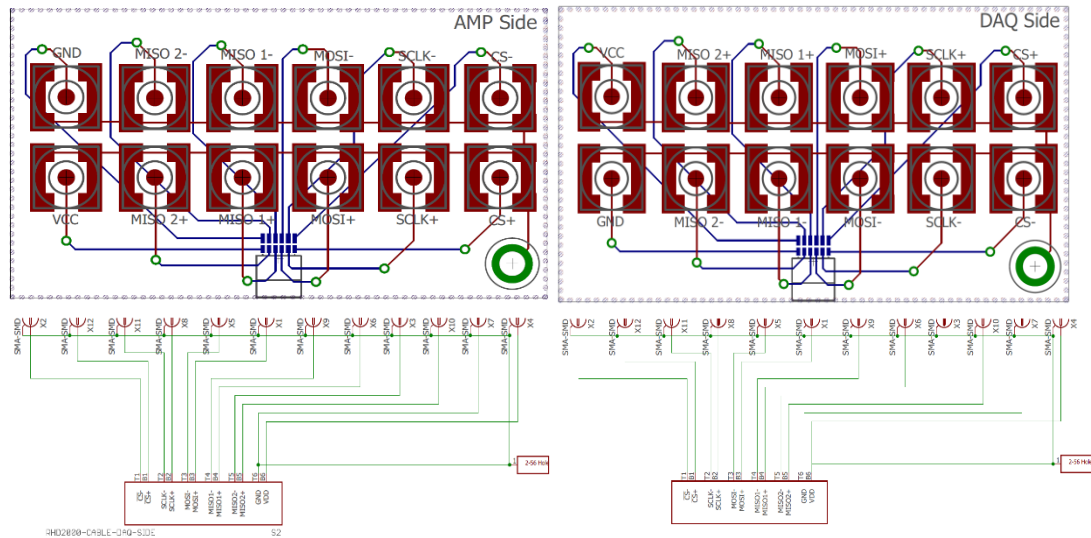


FIGURE 3.21: The break-out boards which were used to break the digital lines normally going through the SPI cable, and allow the introduction of the optical signal to the evaluation board. Two nearly identical versions with mirrored pin-out arrangements were created, one to interface with the front-end amplifying side and other with the evaluation board (DAQ) side.

### 3.6.2 Digitizing circuitry

A digitizing circuit was constructed as shown in Figure 3.22. The incoming optical signal is initially passed through and processed using a low pass filter, where a threshold is set as a function of RC values in the circuit, and the average amplitude and frequency of the incoming signal. A comparator (Linear Technologies LTC6752) was used to then digitize the signal where any value below the threshold was output as a 0, while any value over it as 1. SMA connections provided the inputs for the input and the output, while 100 nF and 2.2  $\mu$ F capacitor were used to decouple the comparator from the  $\pm 5$ V power source.

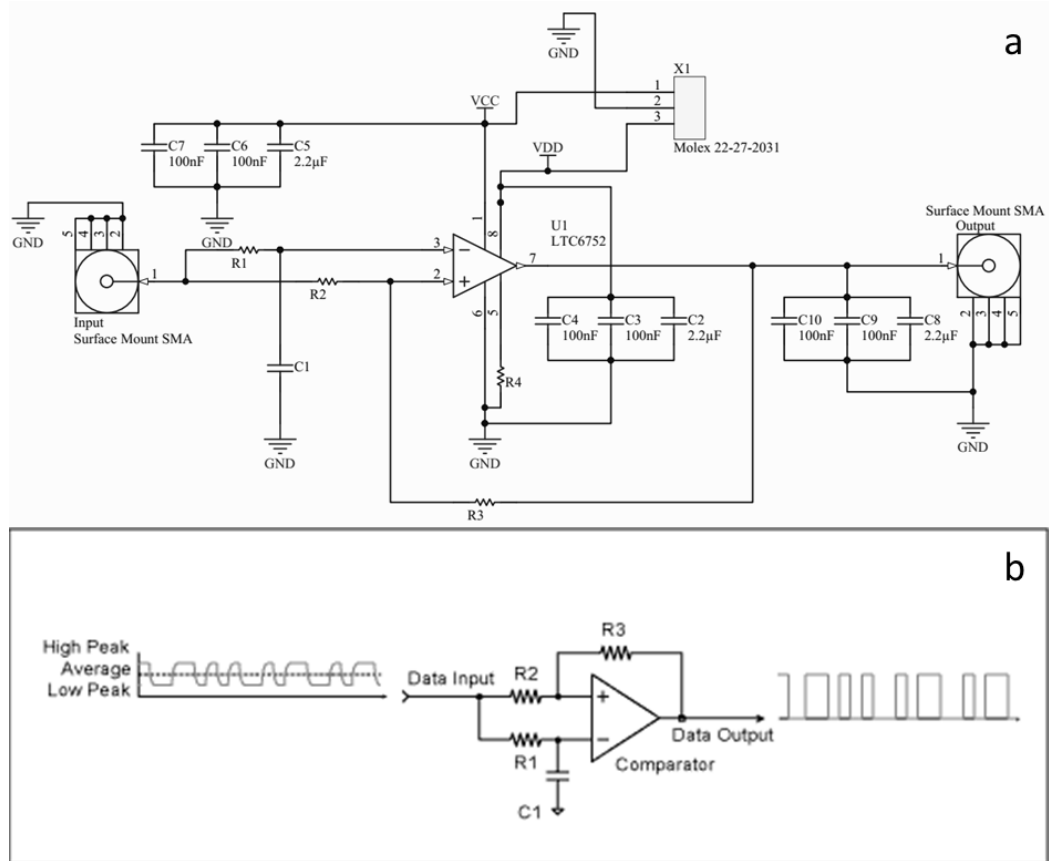


FIGURE 3.22: (a) Schematic outlining the digitising circuit, showing the input source, low pass filter (C1, R2), comparator, and output. 100 nF and 2.2 μF capacitors are also present to decouple the comparator from the power source. The comparator uses the low-pass filter placed before it to create a threshold based on average incoming signal. (b) Diagram of a typical low pass-filter, showing how an incoming analogue signal may be digitized. The threshold is set based on the RC ( $R_1$ ,  $R_2$ ,  $R_3$ ,  $C_1$ ) values in the circuit, and the average characteristics of the incoming signal. This is then used by the comparator to digitize the data. Image from Maxim Integrated website[23]

### 3.6.3 Results

The following sections summarize the results after introducing an artificial signal. Both regular wired recording and optically transmitted were compared to observe signal retention. Table 3.1 shows the BER of the optically transmitted signal using different arrangements. Due to the limited response time of the Avago LED ( $\tau_s = 45$  ns, 10%-90% rise time and fall time = ~99 ns) the increased data rate resulted in single bit pulses being too rapid for the LEDs to fully turn on and reach full

brightness, leading to lower SNR ratios at further distances, which proved increasingly difficult to effectively threshold. Using an optical lens as shown in figure 3.15, the SNR ratio was improved allowing error free data transmission with the APD. With the SiPM, at 30 kS/s the system struggled to keep up with the increased data rate. Due to its increased sensitivity however, it operated at 20 kS/s without the aid of optical lenses at distances (30 cm) where the APD couldn't. The actual neural data transmitted at a sampling rate of 30 kS/s is 15.24 Mbps, with single bit lengths being 41.6 ns, which are shorter than the recovery time of the detector (54.64 ns). This combined with decreased SNR at larger distances as observed with the APD as well, along with the limited response time of the transmitting LED, further reduced performance as demonstrated by the high BER.

To ensure a spike of known magnitude and timing is being transmitted, a platinum wire was connected to a Yokogawa GS610 power supply with the desired settings dialled in. This was then inserted into the compartment of the 61-channel array containing saline solution, which connected to the transmitting device and the system. A signal of 0.1 mV at 5 Hz was introduced. By using a slower signal than typical of neural spikes, the performance of the system could be assessed under more relaxed conditions, before moving on to faster signals. Data was then observed live and recorded through Intan's GUI, first using the regular wired method with the SPI cable (Fig. 3.23a), and then using the optically transmitted data that was digitized and reintroduced to the evaluation board through the break-out board (Fig 3.23b). Figure 3.24 shows strong temporal and amplitude correlation between the dummy data optically transmitted and acquired through wired methods. Figure 3.25a shows a train of neural spiking activity recorded from a single channel likely due to a single unit, which summed in Figure 3.25b demonstrated clear action potential characteristics.

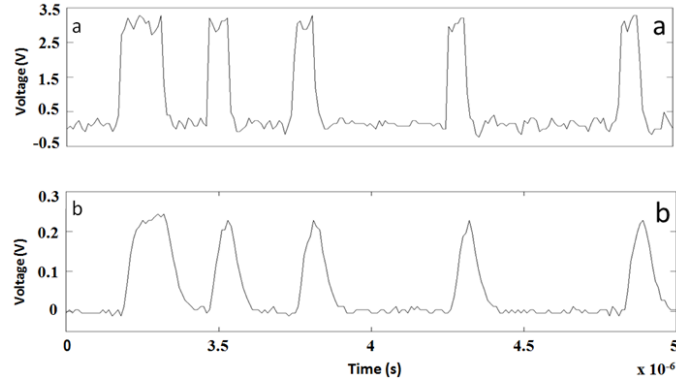


FIGURE 3.23: a) Electrical trace from the digital output of the Intan ASIC while recording neural data from retinal tissue. b) Received optical trace corresponding to trace in a)

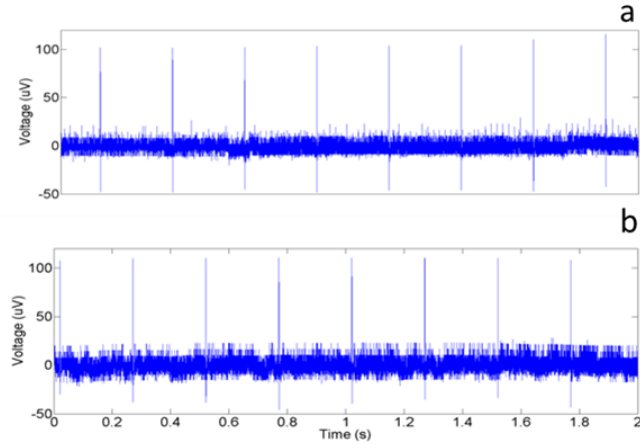


FIGURE 3.24: (a) Pseudo-neural signals recorded using the Intan software through the SPI cable while the system was running live (b) through optical link displayed using the Intan GUI. The two traces weren't recorded simultaneously as the evaluation board could only communicate with the chip either regularly, or using the optical method.

TABLE 3.1  
LED PERFORMANCE

BER	Transmission Gap (cm)	Sampling Rate (kS/s)	Photo Detector	Lens used
$2.26 \times 10^{-1}$	35	30	APD	No
0	35	30	APD	Yes
0	30	20	SiPM	No
$1.24 \times 10^{-1}$	30	30	SiPM	No

TABLE 3.1: Summary of results for random noise that was transmitted optically. The SiPM shows increased sensitivity with voltage peaks being nearly twice as high as with the APD at similar distances, with noise levels also being significantly lower. For sampling rates in excess of 20 kS/s, however the SiPM/LED combination reaches its bandwidth limit and is unable to keep up with the data rate resulting in a sharp increase in the number of errors. Bit rate at 20 KS/s is: (32 channels x 20000 samples/s x 16 bit per sample = 10.24 Mbps of neural data). At 30 KS/s this equals 15.36 Mbps.

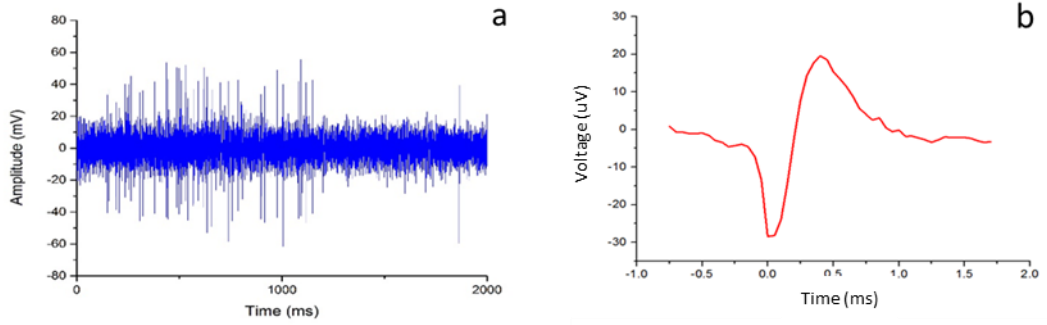


FIGURE 3.25: (a) Results from an *in vitro* experiment of a mouse retina. The neural spike train is reconstructed from 20, 0.1s oscilloscope recordings processed post recording in Matlab. (b) Averaged neural spike from (a) received and reconstructed from bit stream detected by the photo detector at 10.24 Mbps (20 KS/s/channel) and 20 cm distance.

### 3.7 Conclusion

The *in vitro* setup served as a valuable starting point to verify the feasibility of a system based around transmitting neural data using VLC. A device was fabricated that interfaced with a 61-channel array containing neural tissue, and was capable of sending neural data at distances up to 20 cm at a rate of  $\sim 10.24$  Mbps without any lens, and with BER rates being within acceptable limits ( $< 10^{-3}$ ). The received neural data was initially reconstructed from the recorded oscilloscope traces. The setup was then further modified to allow the reintroduction of the optical signal to the evaluation board, which made it possible for the system to display the data in real-time. For sampling rates in excess of 20 kS/s, however, the SiPM/off-the shelf LED (Avago Q156) link reaches its bandwidth limit and is unable to keep up with the data rate resulting in a sharp increase in the number of errors. A potential solution to solve this limitation could be the implementation of a lower value load resistor to increase timing characteristics of the SiPM as described by the response time equation earlier in this chapter. The APD on the other hand due to its fast rise time (1 ns) comfortably handles these rates as long as sufficient SNR achieved with the help of an optical lens. With the maximum power draw for the different components typically

desired to be as low as possible, the 6.6 mW (2 mA x 3.3V) requirement for the VLC module was low enough to allow operation on the scale of several hours using a 50 mAh battery. The data transmitted by the 32 channels of the amplifier chip at 30 kS/s corresponds to a rate of 15.24 Mbps of neural data and is currently limited by the Intan chip rather than the VLC link. The spatial performance and data rates reached can in principle be scaled up to handle more than the 32 channels shown here by, using larger area photodetectors (e.g. J-series 30020), reducing the load resistor value to improve response time of SiPMs, modulation schemes such as Pulse-Amplitude Modulation (PAM), and wavelength division multiplexing (WDM), and using chips with higher channel counts or several chips in parallel.

## References

- [1] D. Tsonev *et al.*, “A 3-Gb / s Single-LED OFDM-Based Wireless VLC Link Using a Gallium Nitride  $\mu$  LED,” vol. 26, no. 7, pp. 637–640, 2014.
- [2] H. Chun *et al.*, “LED based wavelength division multiplexed 10 Gb/s visible light communications,” *J. Light. Technol.*, vol. 34, no. 13, pp. 3047–3052, 2016.
- [3] M. S. Islam *et al.*, “Towards 10 Gb/s orthogonal frequency division multiplexing-based visible light communication using a GaN violet micro-LED,” *Photonics Res.*, vol. 5, no. 2, p. A35, 2017.
- [4] S. Rajbhandari *et al.*, “A review of gallium nitride LEDs for multi-gigabit-per-second visible light data communications,” *Semicond. Sci. Technol.*, vol. 32, no. 2, p. 023001, 2017.
- [5] Intan Technologies, “RHD2000 Evaluation System,” RHD2000-EVAL datasheet, March. 2013 [revised May. 2019].
- [6] Intan Technologies, “RHD2000 USB/FPGA Interface: Rhythm,” RHD 2000 datasheet, May. 2016.

- [7] Intan Technologies, "RHD2000 Series Digital Electrophysiology Interface Chips," RHD2216 RHD2132 datasheet, Dec. 2012. [Revised Sept. 2013].
- [8] G. H. Jacobs, G. A. Williams, H. Cahill, and J. Nathans, "Emergence of Novel Color," *Science (80-. )*, vol. 315, no. March, pp. 1723–25, 2007.
- [9] S. N. Peirson, L. A. Brown, C. A. Pothecary, L. A. Benson, and A. S. Fisk, "Light and the laboratory mouse," *J. Neurosci. Methods*, vol. 300, pp. 26–36, 2018.
- [10] M. P. Butler and R. Silver, "Divergent photic thresholds in the non-image-forming visual system: Entrainment, masking and pupillary light reflex," *Proc. R. Soc. B Biol. Sci.*, vol. 278, no. 1706, pp. 745–750, 2011.
- [11] Broadcom, "Subminiature High-Performance Red LED Lamps," HLMP-P106/P156 HLMP-Q102/Q152/Q106/Q156 datasheet, May. 2018.
- [12] Thorlabs, "Radiometric vs . Photometric Units," 2007.
- [13] J. A. Shaw, "Converting LED photometric to radiometric values Light," *EELE 482 Electro-Optical Syst. course notes, Mont. State Univ.*
- [14] Kingbright, "APETD3528SEC/J3-PRV,"datasheet, May. 2011.
- [15] First Sensor AG, " First Sensor APD" AD800-11 datasheet, June. 2011.
- [16] "MicroFC-SMA-100XX – SensL." [Online]. Available: <http://sensl.com/estore/microfc-sma-100xx/>. [Accessed: 18-Nov-2017].
- [17] On Semiconductor, SensL, "Reference Designs for the SMA and SMTPA MLP-Packaged SiPM Evaluation Boards" AND9809/D datasheet, Sept. 2018 [Rev 2].
- [18] On Semiconductor, SensL, "Silicon Photomultipliers (SiPM), Low-Noise, Blue-Sensitive," C-Series SiPM Sensors datasheet, Nov. 2018 [Rev 6].
- [19] On Semiconductor, SensL, "Introduction to SiPM An Introduction to the Silicon Photomultiplier Introduction to SiPM," July. 2018.



- [20] On Semiconductor, SensL, “J-Series High PDE and Timing Resolution, TSV Package,” datasheet, Dec. 2017 [Rev 3.1].
- [21] On Semiconductor, SensL, “Biasing & Readout,” *Tech. Note*, pp. 1–11, 2018.
- [22] H. Kolb, “Simple Anatomy of the Retina – Webvision,” 2011. [Online]. Available: <https://webvision.med.utah.edu/book/part-i-foundations/simple-anatomy-of-the-retina/>. [Accessed: 27-Sep-2018].
- [23] “Manchester Data Encoding for Radio Communications - Application Note - Maxim.” [Online]. Available: <https://www.maximintegrated.com/en/app-notes/index.mvp/id/3435#>. [Accessed: 18-Nov-2017].

## Chapter IV – *In vivo* device setup

### 4.1 Introduction

The following section describes a fully wireless system that builds on the *in vitro* system described in the previous chapter. Figure 4.1 outlines the overall signal chain, while different views of the head mountable neural data transmitting device are shown in Figure 4.2. To make the device completely tetherless, modifications had to be made to wirelessly replace the functions that the SPI cable provided in the *in vitro* system (commands, clock signals and power). A 50 mAh Ares Lithium Polymer (LiPo) battery was implemented as a power source and placed between two four-layer PCBs containing the required components. A low power STMicroelectronics STM32L432KC MCU was used to generate the required clock and command signals for the amplifier chip. The RHD2132's digital output interfaced with a Kingbright APETD3528SEC/J3-PRV 625nm LED, which transmitted the data to a SensL C-series 10020 photodetector. The clock signal CS from the MCU was tied to an OSRAM OSOLON® Black SFH 4715AS 850 nm IR LED, and was sent to a SensL J-series 30035 photodetector. The clock signal was required to allow the separation and synchronization of the received neural data samples. To avoid crosstalk between the optical streams a low pass 700 nm filter was placed in front of the C-series photodetector, and a high pass 700 nm filter before the J-series photodetector. The optical signals corresponding to the MISO data stream and CS were then digitized to logic levels of 0-3.3V, and sent to an Opal Kelly board containing a Spartan-6 FPGA

for further processing. The 16-bit samples were converted to voltage readings with associated time stamps, and relayed to a

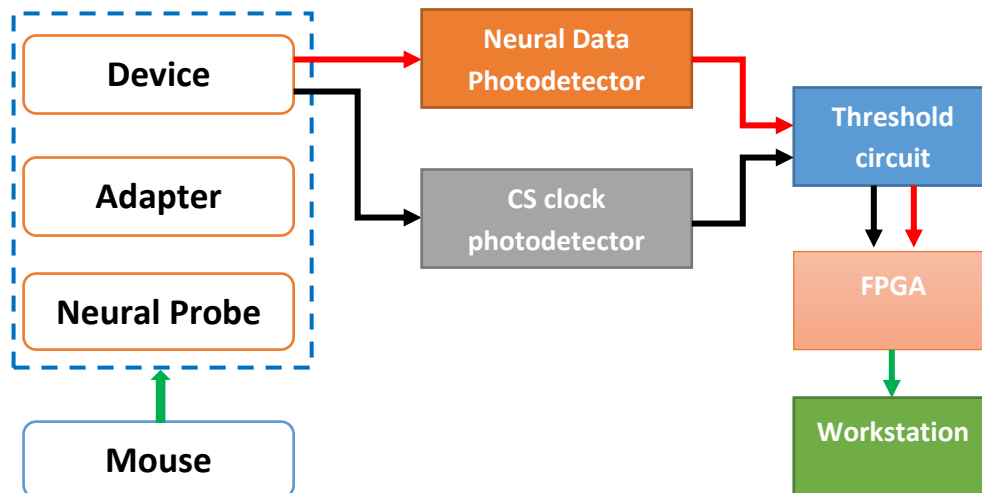


Figure 4.1 The above block diagram shows the simplified schematic of the system for the *in vivo* head-fixed experiments. The device interfaced with an adapter and off-the shelf neural probe which was inserted into the auditory cortex of a head fixed mouse. The clock signal and neural data were transmitted using two different wavelength LEDs, which were sent to two photodetectors with filters in front of them to separate the signals. The raw optical signals were digitized using a thresholding circuit and sent to an FPGA, which converted the data to voltage readings which were then visualized in real-time using a LabView virtual instrument on a workstation.

workstation with a LabVIEW Virtual Instrument (VI), enabling the live viewing of the received data. A test setup was created where the device was mounted on a platform allowing the angles and distances to be adjusted with respect to the photo detectors, and bit error ratio (BER) measurements to be taken. An adapter combined with an A32 Neuronexus probe, was attached to the device and placed into saline solution. A platinum wire connected to a NIDAQ USB-6259 device generated a dummy neural spikes into the solution. Finally, *in vivo* experiments were carried out by implanting into a head fixed mouse, located 20 cm from the photodetectors.

## 4.2 Head mountable device

### 4.2.1 Device Overview

A stacked two PCB was implemented to reduce the length and width of the device and make it more compact, with an 50 mAh Ares LiPo battery placed between them. The two PCBs interfaced with each other through header pins connecting the appropriate lines from one to the other. The total weight without a probe is 5.045g, while the dimensions are 10.7 x 14.6 x 22.05 mm. An overview of the device can be seen in Figure 4.3 showing all the main components. The further subsections (4.2.2-4.2.7) detail the purpose and specifications of all these parts. Different configurations and weight reduction strategies are explored in more detail in Chapter V. A block diagram showing how the different sections are connected is shown in Figure 4.4.

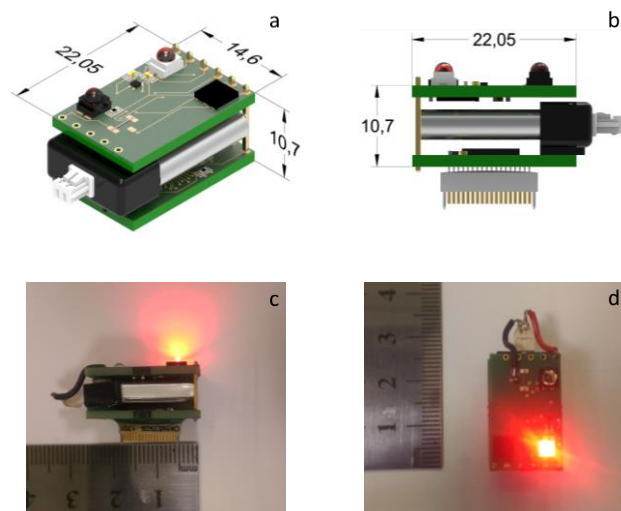


FIGURE 4.2: (a) Isometric schematic of the device showing the principal dimensions. All dimensions in mm. (b) Side schematic of the device. (c) The realized device in active mode with the data transmitting (LEDs turned on). Only the neural data transmitting LED is visible as the clock signal is transmitted with an IR LED. (d) Top view of the device in active mode.

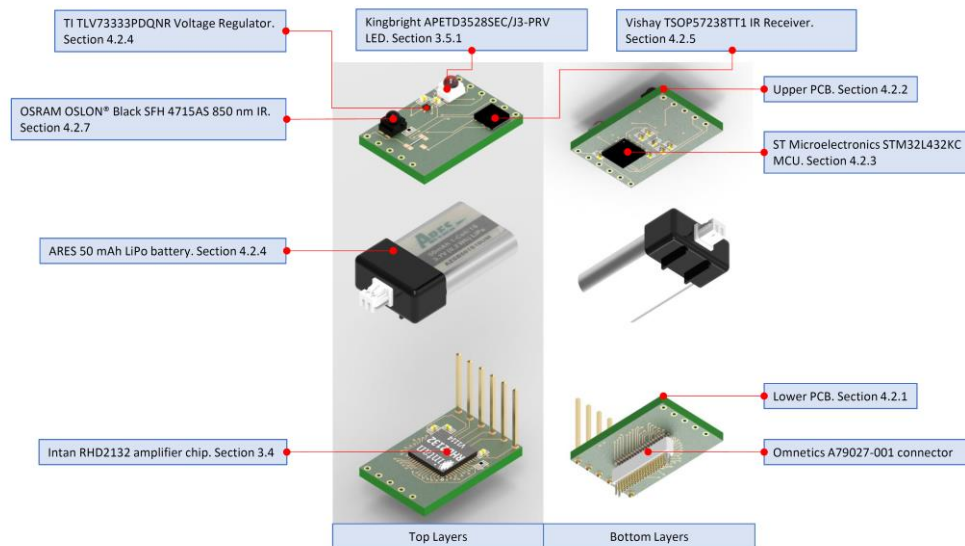


FIGURE 4.3: An exploded view of the device showing all the sub components. The left image shows the top layers of the PCBs while the right shows the bottom. The device consists of three main layers, a bottom PCB containing an Omnetics connector to interface with neural probes, and an Intan amplifier chip with the associated SMD components. It interfaces with the top PCB through six header pins soldered into the appropriate data and power lines. The middle layer is an Ares 50 mAh LiPo battery, that has its terminals connected to the top layer. The top layer contains a voltage regulator to convert the battery voltage to 3.3V, the neural data and clock transmitting LEDs, an IR receiver to capture the incoming commands, and an MCU to send the appropriate commands and clock signals to the Intan Amplifier chip.

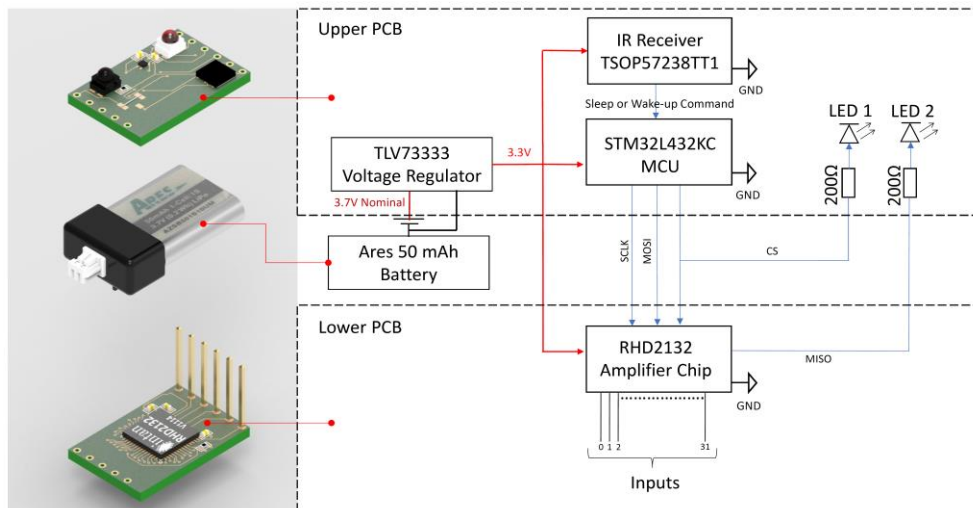


FIGURE 4.4: Exploded view of the device coupled with the schematic for the different layers. The data transmitting LEDs have resistors placed in front of them to reduce power consumption and limit the current draw to 2 mA. This is also needed to avoid possible damage to the chip

### 4.2.1 The PCBs – lower module

The schematics and board layout files of the PCBs were created using EAGLE, and sent to Eurocircuits for manufacturing. Both the lower and upper PCBs consisted of four layers, with the inner two being ground and power planes respectively. The lower PCB's bottom layer contained an Omnetics A79027-001 connector that is used to interface with neural probes (Figure 4.5a). The top layer contained the Intan RHD2132 amplifier chip with all its associated surface mount components (Figure 4.5b). This included two 100 nF voltage smoothing capacitors, a 10 nF voltage capacitor for the ADC reference pin, and a  $0\Omega$  resistor connecting ground to ADC reference. The dimensions of the PCBs are 1.55 x 14.6 x 22.05 mm, with a weight of 1.1g.

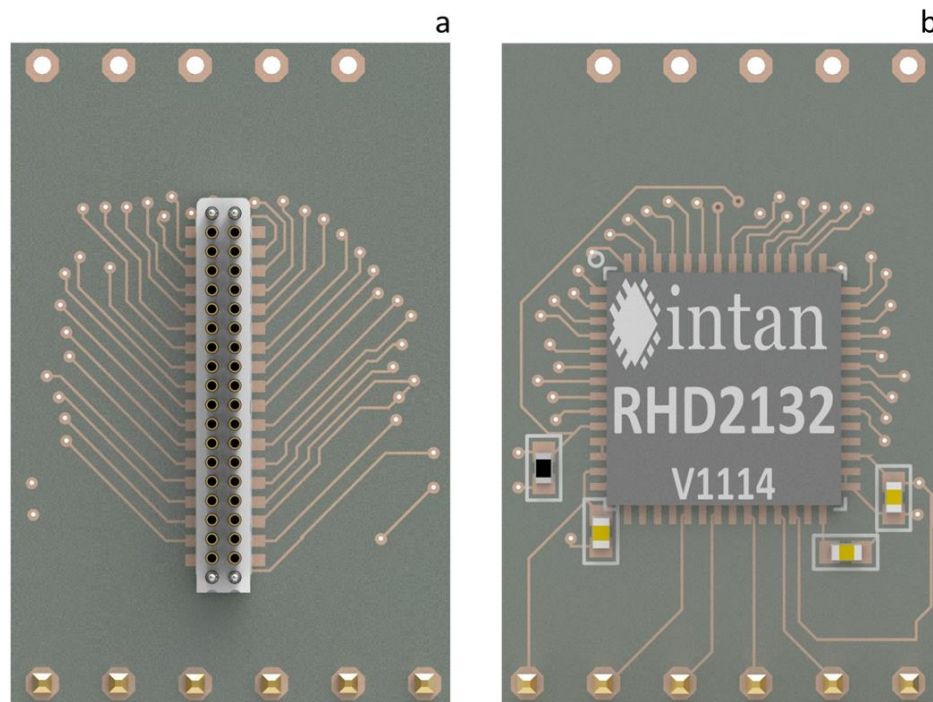


FIGURE 4.5: (a) The bottom layer of the bottom PCB only contains the Omnetics connector. For initial experiments this interfaces with an adapter that allows connection to the A32 Neuronexus probe. Along with the soldering, Norrland UV curable epoxy 68 was used to fix the connector in place. For future experiments involving freely moving animals, the adapter can be omitted in favour of the smaller lower weight Neuronexus CM32 probe, which can attach directly. (b) The top layer of the bottom PCB containing the Intan RHD2132 amplifier chip along with the required surface mount components.

### 4.2.2 The PCBs – top module

The top PCB module (Figure 4.6) has the same dimensions and weight as the lower module outlined in the previous section. It contains an MCU, IR receiver, transmitting LEDs, and a voltage regulator, along with additional passive components required for the ICs. The MCU (section 4.2.3) was placed on the bottom side of the PCB, and essentially takes the role of the evaluation board in the *in vitro* setup outlined in chapter III. Its main purpose was to send the appropriate clock signals (CS, SCLK), and commands. On the top layer an IR receiver was placed to receive commands from an IR transmitting device to control the standby state of the device. Two LEDs were placed on the top side to send the neural data and the CS clock signal to the appropriate photodetectors. To provide the necessary voltages for the components, a voltage regulator was used to down step the 3.7V nominal output voltage of the LiPo battery to 3.3V. Pads for an optional physical switch to completely disconnect the device from its power source were also placed on the top, which was eventually not implemented. The tactile force required activate even the smallest of switches was deemed too great, and thought of as something that may potentially cause further harm to the animal during an experiment or cause damage to the implanted probe. A small wire was used to solder the pads the switch would have connected together, thus permanently linking them. Low power mode could be entered using the IR receiver, while complete disconnection of the battery connector would only be carried out once the device was removed from the animal.

### 4.2.3 MCU

To control the device, an IC was required that could provide the necessary clock and command signals to the Intan RHD2132 amplifier chip while also having the capability to go into sleep mode when no data transmission is required. To carry out these tasks, a low power STMicroelectronics STM32L432KC microcontroller was used. The MCU is based on the ARM® Cortex®-M4 32-bit core and is capable of running

at clock frequencies up to 80 MHz, with its power consumption and impact on overall budget outlined in table 4.2. A 3-wire SPI protocol similar to the one used by the

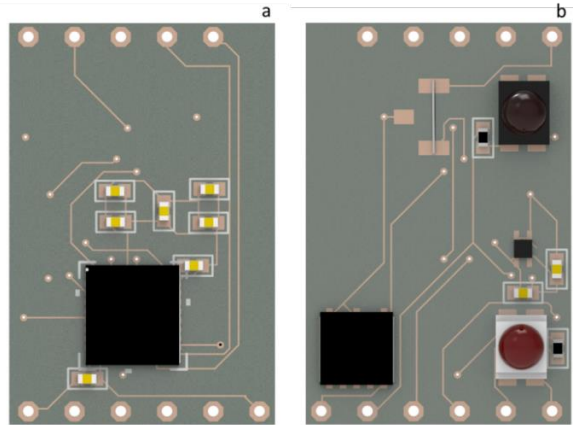


FIGURE 4.6: (a) The bottom layer of the top PCB containing the MCU which sends the clock and commands signals to the amplifier chip. It also contains 7 capacitors for noise reduction and voltage smoothing purposes. (b) The top layer of the top PCB containing the data transmitting LEDs, voltage regulator and IR receiver,

evaluation board was adapted, and implemented through the SPI peripheral of the MCU. The SPI peripheral is controlled by the advanced peripheral bus which runs at half the frequency of the core clock, enabling a maximum transmission rate of 40 Mbit/s. For a sampling rate of 20 kS/s, 16 MHz is required for the SCLK output of the SPI peripheral. The MCU architecture defines that the core clock has to run twice as fast as the advanced peripheral bus controlling the SPI. To enable a 16 MHz SCLK the core clock therefore had to be set to 32 MHz.

Standard MCU operating methods such as polling, can severely slow data processing down, as the MCU core is continuously kept busy by the large amounts of data required for high sampling rates. This manifests itself as large gaps in between each sequential sample ( $\sim 5 \mu\text{s}$ , or 4 full samples at 20 kS/s). To prevent this, direct memory access (DMA) was implemented (Figure 4.7), a method minimizing the involvement of the MCU core. This way the memory was directly linked to the SPI peripheral allowing commands to be streamed at a much faster rate. However, this led to another issue, where the gaps between each successive sample became too short,



which subsequently led to the hardware generated CS pulses becoming insufficient in length as well. This caused issues as there would be inadequate time to process the samples, which would merge into each other and create unreliable results. To solve this problem, another peripheral timer was implemented. The timer was programmed to have similar timing characteristics as the CS clock signal coming from the evaluation board and was set to generate an output through one of the general-purpose input output (GPIO) pins of the MCU. The rising edge of the timer pulse was then used to trigger a DMA transfer, thus ensuring the appropriate timing breaks. In normal operation, the commands to sample each channel were then transmitted sequentially in a circular fashion, until a stop command was received. STMicroelectronics's Cube MX, a GUI and software for configuring the generic parameters of the MCU was used to set up the clock frequencies and necessary pins.

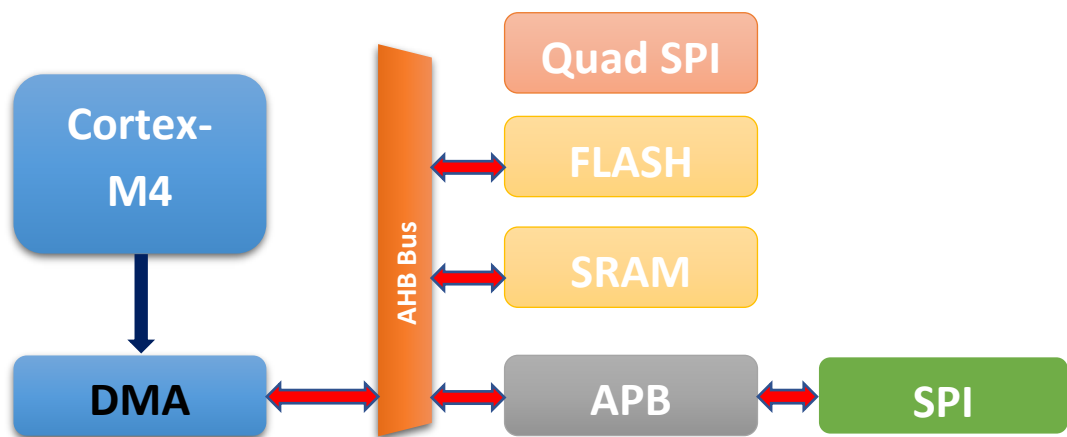


Figure 4.7: Diagram showing data being streamed straight from the memory to the SPI peripheral. The core sends a command to the DMA controller (blue arrow) which then streams the data directly from the memory (red arrow) to the peripheral through the advanced high-performance (AHB) and advanced peripheral bus (APB) to control the SPI peripheral, freeing up the core to do other tasks.

It was also applied to setup the relation between the memory and peripherals, and to implement the DMA protocol. Once all settings were complete, it generated the desired settings and represented them in C code, using STMicroelectronics's Low Layer (LL) Application Programming Interface (API). The LL is required to have direct access to settings of the MCU on the hardware and register level for correct

initiation. This was created along with all the essential drivers and system files required for the microcontroller. The STMicroelectronics STLink/V2 programmer was used to compile the C code into machine code so that the microcontroller can understand. The programmer uses a Serial Wire Debug (SWD) protocol to access the MCU, requiring only two lines; Serial Wire Clock (SWCLK) and Serial Wire Data In Out (SWDIO) to flash the MCU. In addition to the digital lines, ground and power lines are also needed to be connected to ensure proper operation. The top layer of the upper PCB had access points through which the required connections could be made (Appendix 4.3).

The code that was used to flash the MCU is shown in Appendix 4.1. It started by defining all the register values that are required for the Intan chip's desired operation. This is outlined in more detail in Chapter III section 3.2.2. When the device powers up, the MCU sends the appropriate commands to write and setup the required chip register banks. This was transmitted in normal DMA mode, that is the commands were sent once without jumping back to the first value and restarting the cycle. Following the initial setup, the MCU then enters the circular DMA mode and begin cycling through the commands for the sampling of the 32 channels. In default mode, the Intan system sends 3 random instructions after a full sequence is complete. This leaves the user with the option to replace these words with commands to sample the three auxiliary channels if required. Since these were not used, the command "read register 60" was sent in these slots, which reads the version of the chip and always returns the value of one. The three ones received in a row were useful for indicating when a full cycle of sampling 32 channels was completed, while debugging the system.

Once programmed the MCU generated the required digital lines to activate and control the RHD2132 amplifier chip. The two ICs communicated through three digital lines, with the MCU operating in "Transmit Only Master" mode. The CS, controlled by the timer, was also connected to an LED to transmit the status. This was required to mark where each 16-bit word making up a sample began and ended. It was also

needed to derive the SCLK rising edges (section 4.3), which were essential for determining the values of each bit making up a sample. The MOSI line, sending the commands, and SCLK were generated by the SPI peripheral and connected directly into the appropriate inputs of the amplifier chip.

Additionally, the MCU interfaced with an IR receiver, which obtained instructions to enter or wake up the device from standby mode. This was achieved by enabling the input capture for one of the pins of the MCU connected to the output of the IR receiver. When it received a signal that sets the output to logic low, the MCU enters a low power state where it stops sending commands and reduces the core clock frequency thus decreasing power consumption. If a logic low was received again, the system would reset and restart the chip setup and data acquisition procedure as outlined in preceding sections. Since both entering and waking from sleep mode was triggered by the same logic low command coming from the IR transmitter, care had to be taken with the timing to not sequentially activate them at the same time. This was ensured by inserting appropriate delays after the execution of each task, which were longer than the amount of time the MCU pin would detect a logic low state for from the IR receiver. Bypass capacitors were arranged around the MCU as shown in its data sheet (Appendix 4.7), to make it robust against a wide range of potential voltage fluctuations. The architecture of the MCU is shown in Appendix 4.8.

#### **4.2.4 Battery, Charging and Voltage Regulation**

A crucial factor contributing to the overall weight of the device is the type and the capacity of the battery used. Because of this, careful consideration was taken to find the optimum type of power source. The solution had to provide enough energy to allow the device to run for sufficient amount of time to record meaningful amount of data (>1 hour, 32 channels, 20 KS/s), while also being light weight enough to be carried by a mouse. Eventually an Ares 50 mAh LiPo battery (Figure 4.8a) was used to power the device, and was fused to the lower PCB using a flowable silicon rubber

(Dow Corning 3140 RTV coating). The total weight of it was 1.8g, including the protective cap. When fully charged the battery had a voltage of 4.2V, while the nominal voltage was 3.7V. The battery interfaced with a 1.25 mm pitch micro female JST connector, which had two pins connecting to the power and ground lines. UV curable Norland NOA68 epoxy was used to strengthen the solder joint around the connector. A MikroElektronika VOLT battery charger (Figure 4.8b) was used to recharge the device, which linked with a laptop through a USB mini type-B connector to receive the power required to charge the battery. As the nominal voltage was above the required voltage for most components (3.3V), a TI TLV73333PDQNR low-dropout regulator was used to set the voltage of the power plane, from which all components received power. As recommended by the data sheet, two optional 0402 0.1 $\mu$ F (Würth) capacitors were also soldered in proximity to the voltage regulator to assist with voltage smoothing.

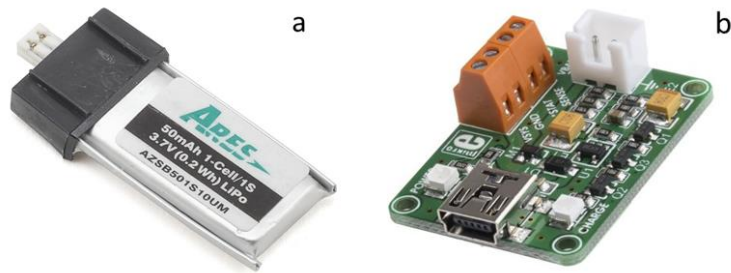


FIGURE 4.8: (a) Ares 50 mAh LiPo battery used to power the device. (b) USB based battery charger used to charge the battery.

#### 4.2.5 IR receiver

To control the device, a Vishay TSOP57238TT1 38 kHz IR receiver was used to take instructions from the IR transmitter of a mobile phone with IR transmitter (android HTC M8). The app IR Remote® was installed on it, giving users the options to create custom user commands. The pronto protocol was used to program the instructions into the phone. The procedure involved defining a carrier frequency and a series of on and off burst pairs to define each directive. The receiver filters out any IR sources that are not at its carrier frequency, enabling interference free operation. The

following code was used for the entering and leaving of the low power mode for the device: 0000 006d 0000 0001 0000 FFFF where the numbers indicate the following:

Word 1 is always 0000, and designates that the IR code is raw data.

Word 2 006d, which is 109 in decimal determines the carrier frequency the command is transmitted with. This value was picked in order to set it to 38000 Hz, the frequency the receiver was attuned to. The following equation [1] was used to determine it:

$$\frac{4145146}{109} = 38.028 \text{ Khz} \quad (4.1)$$

Word 3: 0000, is the length of the onetime burst present at the beginning of a sequence. In this case there is no one time burst.

Word 4: 0001, is the length of the repeat burst. There are two bits or a single burst pair in this code. A code length of one burst was enough, as only a single logic low of sufficient length was required to trigger the MCU as described in section 4.2.3.

Word 5: 0000 on time length = 0 s. As the protocol requires values to be defined in pairs, a place holder number 0 was entered for the on-time length.

Word 6: FFFF off time length  $FFFF = 65536 * 1/38028 = \sim 1.72s$

#### 4.2.6 Adapter board and probes

To reduce the cost for prototyping purposes, a Plexon HST/32V Neuronexus adapter (Figure 4.9) was used to attach to a larger, and more economical Neuronexus A32 neural probe (Figure 4.9) with 32 electrodes. The freely moving version of the device is planned to be used with the smaller CM32 probe pictured in figure 4.9. The adapter's main purpose was to allow interfacing between the probe and the device, which had different connectors. The probe itself also had a reference electrode, which was connected to the system ground and inserted into the medium; saline solution in

the case of the initial testing of the device (section 4.4), neural tissue of a head fixed mouse during *in vivo* experiments (section 4.5).

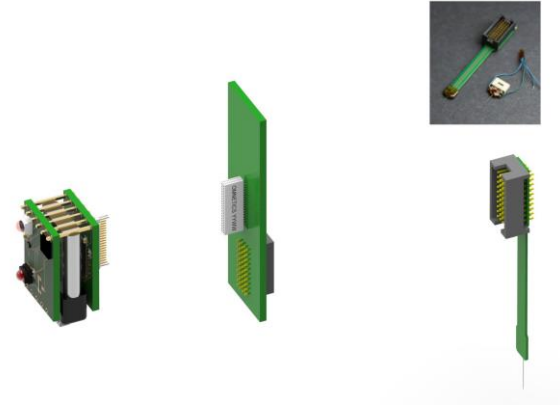


FIGURE 4.9: Exploded view of the device connecting to an adapter board required to interface with the 32 channel A32 Neuronexus recording probe. The top right image shows a photo of the probe, along with the smaller CM32 probe which can be used to directly interface with the device without the use of an adapter.

#### 4.2.7 LEDs

As the reference clock was generated on the device, as opposed to off-board, a second LED was incorporated to relay the signal for synchronization purposes. While not the most efficient method, it was the simplest, allowing rapid prototyping of the system. Other methods such as clock recovery and Manchester encoding protocols (section 5.7), require more involved circuitry and coding, but will also be explored in the future. The clock was used to break up the received continuous raw neural data stream into samples, correlated to the voltage readings of the observed biopotentials. This was sent using an OSRAM OSOLON® Black SFH 4715AS 850 nm IR LED (Figure 4.10), which was connected to the chip select output of the MCU (section 4.2.3). The neural data was still transmitted with the 625 nm Kingbright APETD3528SEC/J3-PRV LED described in Chapter III. Different wavelengths (625nm vs 850 nm) were used for the two lines, enabling them to operate simultaneously with the use of suitable filters, described in more detail in section 4.3.1. The emission profile of the LEDs used is shown in Figure 4.11. Comparison of the LED spectra and receiver PDE ranges are shown in Figure 4.12, with a more

detailed description outlined previously in section 3.3.2. Performance decreased with higher incidence angles and is further explored in section 4.5.2.

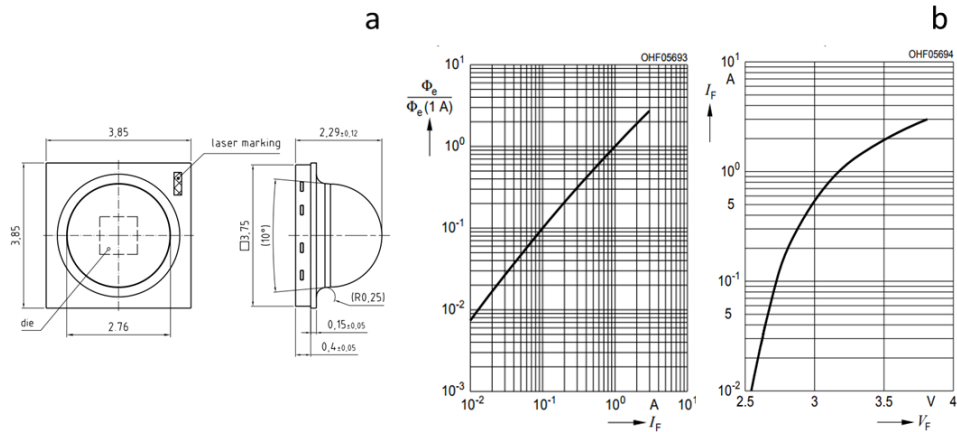


FIGURE 4.10: (a) The physical dimensions of the OSRAM OSOLON® Black SFH 4715AS 850 nm IR LED that was used to transmit the CS clock signal. (b) The left graph shows the relative total radiant flux with respect to current draw of the LED. This relationship is linear similarly to the Kingbright LED used to transmit data, but is only plotted down till 10 mA. The right graph shows the IV curve of the LED, from which it can be seen that the regulated voltage of 3.3V supplied is more than enough to draw the supplied current (~2 mA). Images from OSRAM data sheet [2]

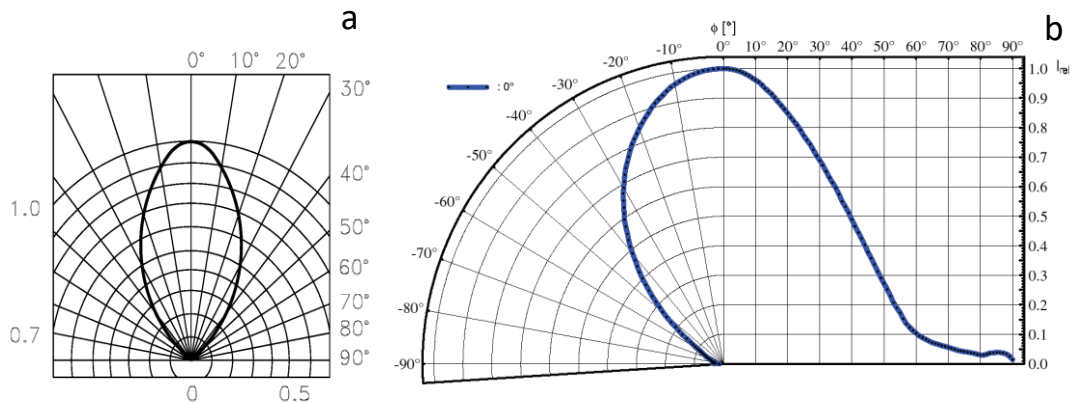


Figure 4.11: The associated emission profile with respect to angle for the LEDs that were implemented on the device. (a) The radiation characteristic for the data transmitting Kingbright LED shows transmitted relative power to decrease to 0.5 at 30°, the half angle. After 10° deviation from the centre line, the relative power starts to decrease rapidly by 20% for each 10° decreasing to 0.3 by 40°. Image from [3] (b) The relative intensity graph for the clock transmitting Osram LED shows that it has a larger half angle at 45°. From its datasheet however, it can also be inferred that it has a lower radiant intensity of ~1.56 mW/sr. Image from [2].

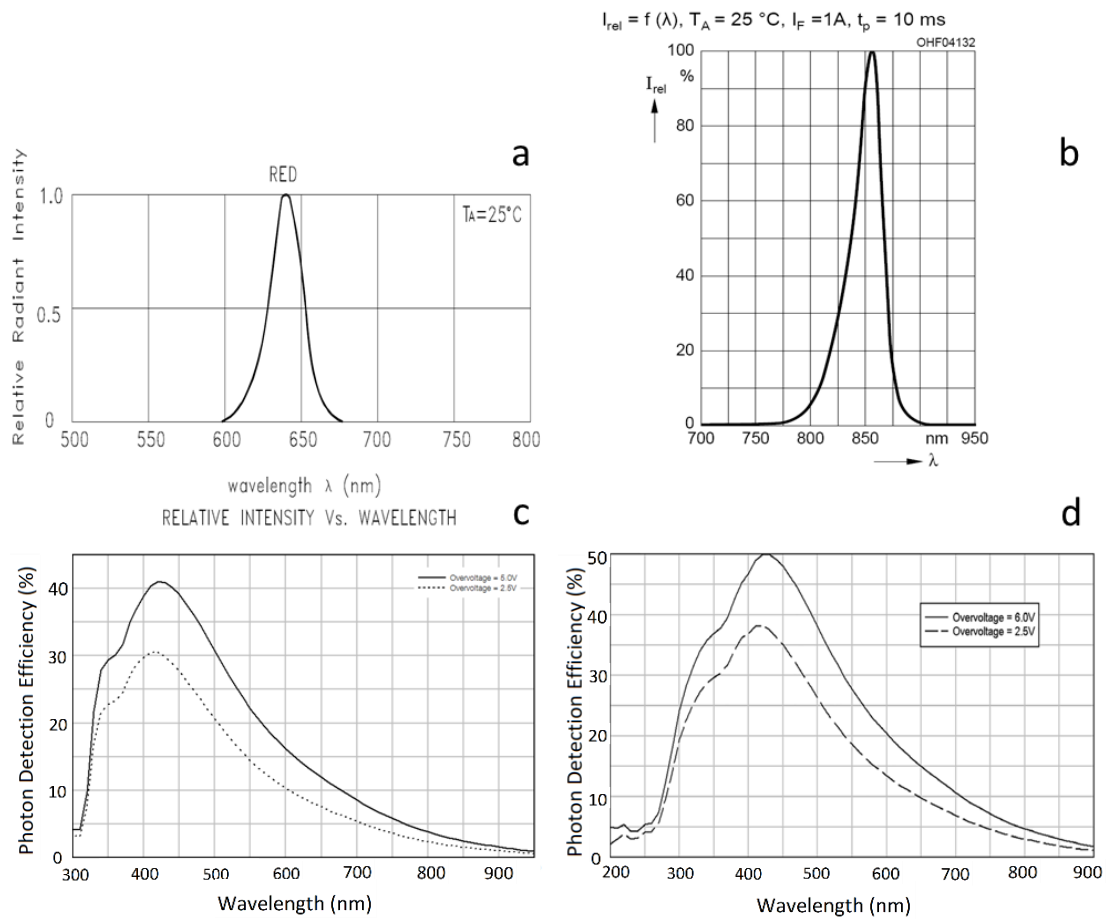


FIGURE 4.12: (a) The spectrum of the neural data transmitting Kingbright APETD3528SEC/J3-PRV 625 nm LED (Image from [3]), with the spectral range of the receiving SensL C-series 10020 photodetector shown below in panel (c). Image adapted from [4]. The dotted line indicates an overvoltage of 2.5V, while the solid line corresponds to 5V. (b) The spectrum of the synchronizing clock transmitting OSRAM OSOLON® Black SFH 4715AS 850 nm LED (Image from [2]), with the spectral range of the receiving SensL J-series 30035 photodetector shown below in panel d. Image adapted from [5]. The dashed line indicates an overvoltage of 2.5V, while the solid line corresponds to 6V.



### 4.2.8 Device Summary

Tables 4.1-4.4 summarize the key performance characteristics of the device. The weight of the different parts constituting the device are shown in table 4.1, while the current consumption of the major components are detailed in table 4.2. A more in depth look at the consumption of the Intan amplifier chip and its sub modules is shown in Table 4.3. Several parts such as the LEDs, MCU and the amplifier chip have sampling rate specific current requirements, which were measured at the sampling rate required for *in vivo* experiments (20 KS/s).

TABLE 4.1  
DEVICE COMPONENT WEIGHTS

<b>Part</b>	<b>Weight (g)</b>	<b>*Additional Components</b>
Top PCB	1.1	Osram LED
Bottom PCB	1.1	Kingbright LED
Battery 50 mAh	1.6	STM32 MCU
Battery Plastic Cap	0.2	Vishay TSOP IR Receiver
Omnetrics Connector	0.24	TI TLV7333 Voltage Regulator
Intan QFN	0.168	6 x Pins
CM32 Probe and PCB	0.29	Battery Connector and Wires
Additional Components*	0.637	Nordic Adhesive
<b>Total Weight</b>	<b>5.045</b>	Solder

TABLE 4.1: The weight of the different components making up the device. Additional components, which individually had negligible weights or were difficult to weigh are listed separately in the right table.

TABLE 4.2  
DEVICE CURRENT CONSUMPTION

<b>Part</b>	<b>Current Draw (mA)</b>
Intan Chip (20 KS/s)*	4.851
MCU (20 KS/s)*	2.688
Kingbright LED (20 KS/s)*	~2
Osram LED (20 KS/s)*	~2
IR Receiver	0.75
Voltage Regulator	0.034
<b>Total</b>	<b>12.323</b>

TABLE 4.2: The current draw of the different components. Calculations for the Intan chip are outlined in more detail in table 4.3. The STML432KC datasheet lists the MCU current consumption as 84 uA/MHz in run mode. Since it's running at 32 MHz the total current consumption is  $32 \times 84 \text{ uA} = 2.688 \text{ mA}$ . \*These components have sampling rate dependent current consumption. For typical current consumption a sampling rate of 20 kS/s was assumed.

TABLE 4.3  
INTAN AMPLIFIER CHIP CURRENT CONSUMPTION

Chip Module	Current Draw ( $\mu\text{A}$ )
Baseline amplifier array current	200
Amplifiers = $32 \times 7.6 \mu\text{A}/\text{kHz} \times \text{fh}^*$	Variable, Parameter Dependant
Baseline ADC current	510
ADC/MUX = $2.14 \mu\text{A}/(\text{kS/s}) \times \text{sample rate}^{**}$	Variable, Parameter Dependant
LVDS I/O	5700†
Impedance measurement	120
Temperature sensor	70
Supply voltage, auxiliary inputs = $4 \times 10 \mu\text{A}$	40

TABLE 4.3: The current draw of the different parts of the amplifier chip as listed in the Intan datasheet [6]. As described in Chapter II, LVDS was to reduce power consumption by 5.6 mA. As the device was set to have an upper cut-off frequency of 10 kHz, the current draw of the amplifiers was calculated as follows:  $32 \times 7.6 \times 10000 = 2.432 \text{ mA}$ . Since the sampling rate used was 20 kS/s the ADC/MUX current draw was calculated as follows:  $2.14 \times 35 \times 20000 = 1.498 \text{ mA}$

TABLE 4.4  
DEVICE PERFORMANCE

Transmission Distance (cm)	20
Transmission Angle (degrees)	60
Operating Time (hrs)	3.5
Channel Number	32 + 3 aux
Data Rate (Mbps)	10.24
Dimensions (mm)	10.7 x 14.6 x 22.05
ADC Resolution	16
Sampling Rate (KS/s/channel)	20
Transmission Wavelengths (nm)	625 and 850

TABLE 4.4: A summary of the fundamental characteristics of the device.

## 4.3 The receivers

### 4.3.1 SensL photodetectors

Two photodetectors were used to receive the incoming signals. For the neural data stream the SensL C-series 10020 (described in chapter III section 3.3.2) continued to be used. For the CS clock, the SensL J-series 30035 was utilized, biased at 5V above its break down voltage of 24.5V with an RS IPS 4303S power supply. While the larger 35-micron SPAD cell resulted in a slower response (37 ns microcell recharge time constant), this was not an issue, as the clock signal transmitted to it was uniform, and at a much lower frequency than the MISO output of the chip. To avoid crosstalk between the two LEDs, filters were implemented. A 700 nm a 25.4mm diameter low pass filter was placed in front of the C-series photodetector (Figure 4.13b), while a 25.4mm 700 nm high pass filter was placed in front of the J-series (Figure 4.13a). Since the detectable radiation intensity with respect to wavelength spectrum of the LEDs was outside of this cut-off (580-700 nm for the Avago, and 750-900 nm for the Osram), sufficient separation without virtually any cross talk was achieved.

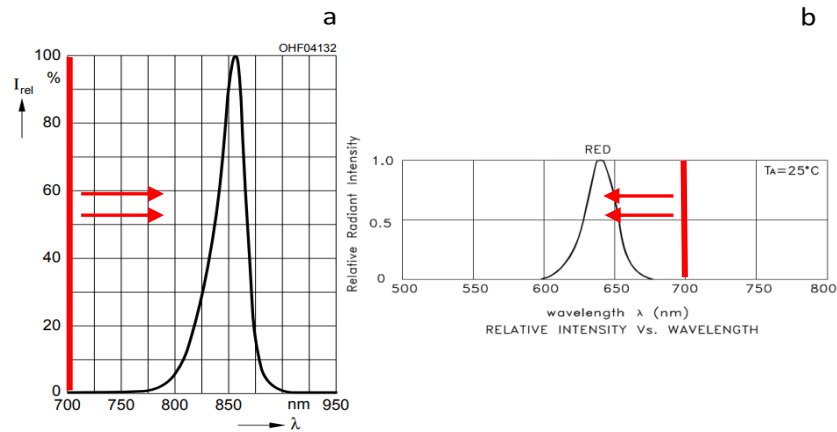


FIGURE 4.13: (a) The emission spectra of the OSRAM IR LED with red line indicating the high pass filter cut-off point, while the arrows show the direction in which the filter lets light pass. Adapted from [2] (b) Emission spectra for the Kingbright LED, with the red line indicating the low pass filter cut off point, and the arrows indicating which way the filter lets light pass. Adapted from [3]

### 4.3.2 Digitizing circuitry

The incoming analogue optical signals had to be digitized to logic levels of 0-3.3V for the FPGA to operate properly. Digitizing circuitry was implemented after each optical line (Figure 4.14), which integrated to the photodetectors through SMA cables with 50  $\Omega$  termination. Following the input stage, the signal passed through a diode and charged a capacitor. The diode prevented the current from flowing backwards, while the capacitor was selected to have a time constant large enough to avoid rapid discharge and keep it saturated. A voltage divider consisting of a resistor and a trimmer potentiometer were placed after it to set a threshold depending on the potential across the capacitor, and the value set on the trimpot. The circuit effectively operated by charging up the capacitor to the average peak value of the incoming optical pulses, which set a baseline threshold that was further adjusted depending on the values of the voltage divider resistances, and were dictated by the equation:

$$V_{\text{threshold}} = \frac{R_4}{R_4 + R_3}$$

(4.1)

The threshold and raw optical signal were then input into a comparator (Linear Technologies LTC6752-3), which digitized the optical signal to the required logic low or high depending on its relation with respect to the threshold. An RS IPS 4303S power supply was used to provide the 5V required for the IC to operate.

### 4.3.3 Pulse Digitization

Figures 4.15 a-d, demonstrate how the raw optical signals, threshold and digitized logic converted signal vary with distance. The threshold controlling potentiometer was left unadjusted, to show how the system behaves when no manual tuning is implemented.

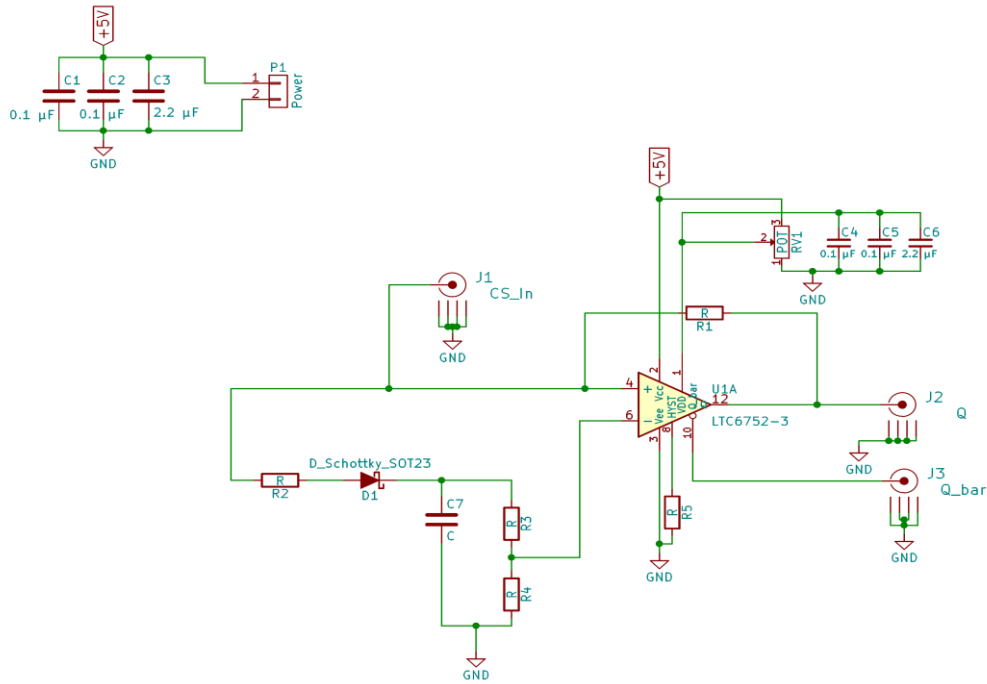


FIGURE 4.14: Schematic for the digitizing circuit. The optical signal enters at J1 and is split into two paths. One line enters the positive input of comparator, as a reference to be digitized. The second line passes through a Schottky diode and charges a capacitor C7 to a near peak value of the ingoing signal. A voltage divider made up from R<sub>3</sub> and R<sub>4</sub> pot trimmers is the used to set a threshold and is input into the negative input of the comparator. The output through J2 is then connected to the FPGA board (section 4.3.4).

#### 4.3.4 FPGA

A Spartan-3 based FPGA board (Opal Kelly XEM3010) shown in figure 4.16, was used to convert the 16-bit samples into time-stamped voltage readings. The Opal Kelly board interfaced with a larger, custom made base board, containing a series of inputs. The FPGA firmware was programmed in Verilog, and a MATLAB script written to specify the decoding parameters of the FPGA. The incoming signals were oversampled at 100 MHz to capture all the relevant logic changes. Rising and falling edges were determined by observing bit state transitions, and time stamped accordingly. A 32 Mbyte SDRAM

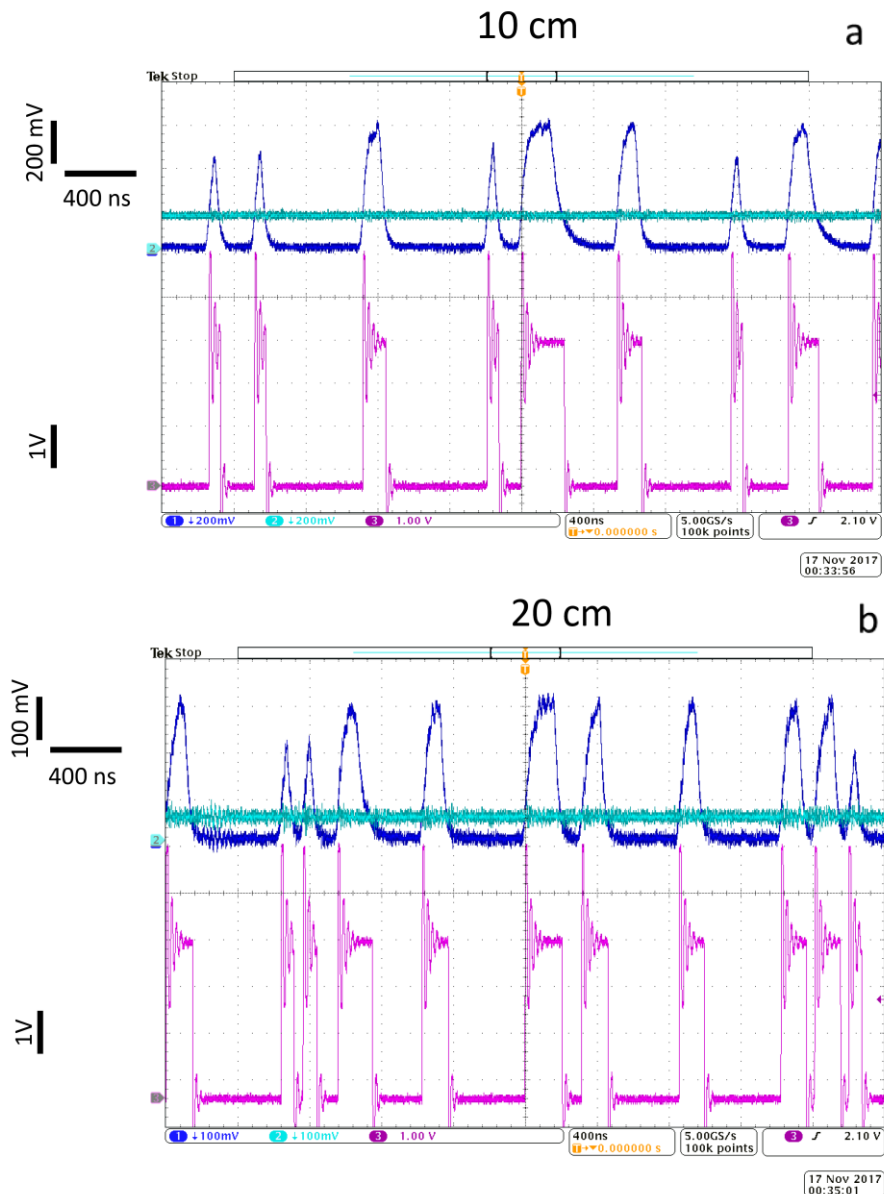


FIGURE 4.15: (a) The dark blue trace (top) shows the optical signal pulses received by the photodetector 10 cm away from the device, while the light blue horizontal trace (top) shows the threshold created, as outlined in section 4.3.2. The magenta trace (bottom) shows the digitized 3.3V signal output by the comparator. Ringing can be seen on them, likely caused by the impedance mismatch between the output of the comparator and measuring probe (b) When increasing the distance to 20 cm, digitization is still properly maintained despite the optical signal nearly halving in magnitude. This also causes the threshold to decrease more in relation to the peaks of the ingoing signals, a direct result of the voltage drop across the Schottky diode.

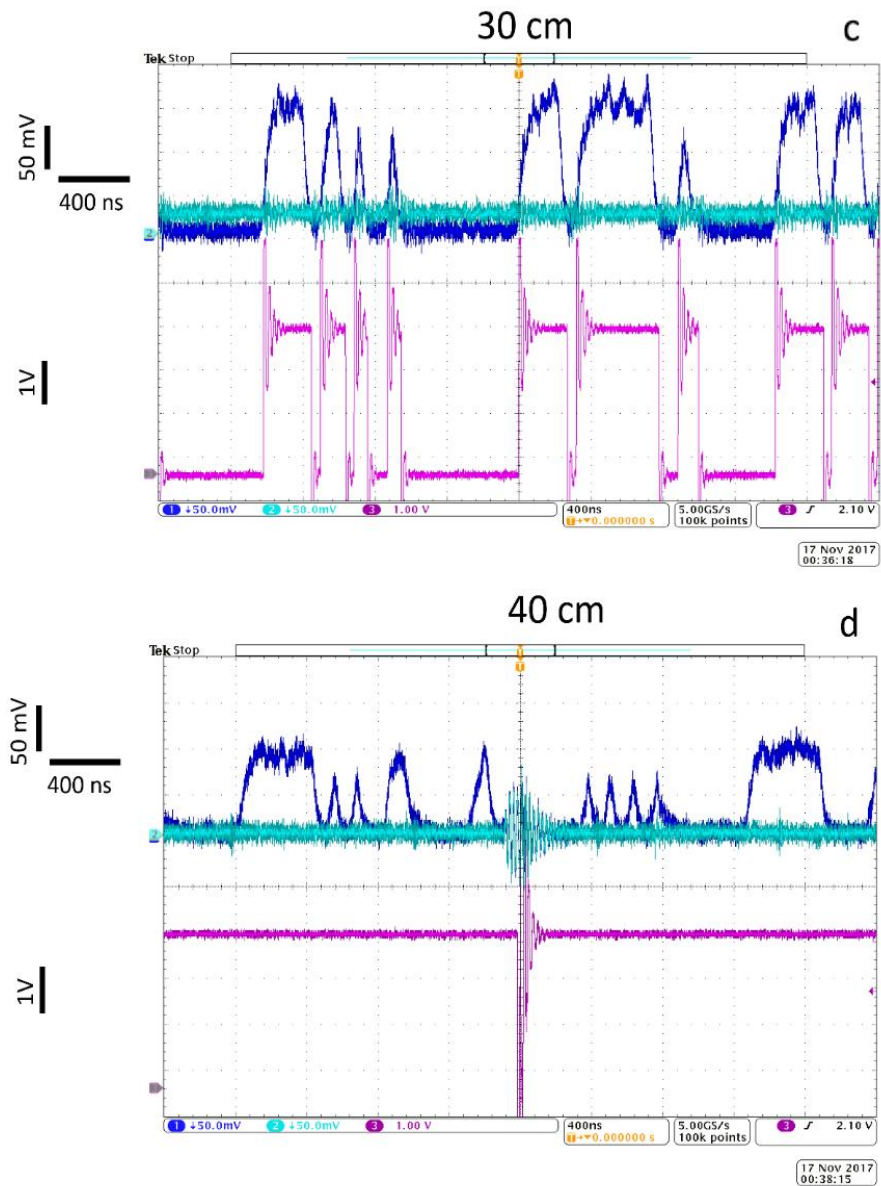


FIGURE 4.15: (c) The reduction in optical trace amplitude is more pronounced as the distance increases to 30 cm, along with the further decrease of the threshold. Nonetheless digitized pulses are still largely similar to the raw optical trace. (d) At 40 cm the threshold has sunk to a level too low to produce the required logic levels. Using threshold readjustment and amplification can however improve data retention at these distances as well (Section 4.5.1)

module at 133 MHz was used as buffer memory for the live streaming of the data from the FPGA to the computer. The MATLAB script was also used to start the recording and begin data processing. The incoming falling edge of the CS pulse was then used as a reference from which the 16 SCLK rising edges were derived to reconstruct the 16-bit samples. Timing between the falling edge of the optical clock signal CS and the first SCLK rising edge; was adjusted in the MATLAB script to synchronize the digital lines. The temporal value between the successive SCLK rising edges was also set here, and adjusted to 62.5 ns, the value correlating to a sampling rate of 20 kS/s. The FPGA then determined the bit states at each virtual SCLK rising edge and tallied the values between consecutive CS pulses. The 16-bit data word was then converted to a time-stamped voltage value and saved to a hard disk.



FIGURE 4.16: The FPGA used to convert the processed digital signals to actual voltage readings. The neural data was introduced through XBUS2 (yellow arrow), while the clock signal CS was input through XBUS0 (red arrow).

#### 4.3.5 LabVIEW VI

A LabVIEW VI was used to live stream and visualize the voltage values processed by the FPGA. It operated by initializing the MATLAB code controlling the FPGA to regulate the start and stopping of recording. A file and folder structure was then simultaneously created and named based on the date and time of the recording. Once the MATLAB script was running, the Labview VI waited a second for the FPGA to



generate data. The files created by the FPGA would then be read, while separating the data into individual streams correlating to the 32 channels. The 3 additional auxiliary channels would also be removed as they showed no relevant information to the observer. The data was then saved as a bin file in the folder previously created. The VI also concurrently checks the amount of backlogged data, and displays it in the form of a time value on the screen. This gives the user feedback regarding how much delay there is between the recorded and displayed data. Once completed the code reverts back to checking and displaying the data followed by the backlog check until a stop command is received. Currently, there is also a place-holder block in the VI that could be used as a filtering module to get rid of unwanted noise, and erroneous readings due to bit errors. This is not fully implemented, and will be discussed in more detail in chapter V. Several options were incorporated to adjust scaling of the displayed information (Appendix 4.6). A time scale of a 100 ms to a 1000 ms can be selected. At the moment a master voltage scale is used by all the channels, with the option to set a separation defined in  $\mu\text{V}$  between them. This can be used to avoid all the signals being superimposed on one another. A spike scope is also present, which can be used to focus in on an individual channel. A threshold can be defined in  $\mu\text{V}$  to keep readings on the screen that were above it. This is useful for overlaying spikes to determine the average firing characteristics for a specific neuron. A layout of the VI can be seen in Appendix 4.6, showing all the key settings that can be adjusted.

#### **4.3.6 Saleae Matlab code**

To carry out BER measurements, a Saleae Logic Pro 8 was used to record the necessary logic signals (Figure 4.17) at a 100 MHz sampling rate. The MISO coming from the amplifier chip, CS and SCLK clock signals from the MCU, and the digitized optical signals (CS and MISO) on the receiving end, were observed. A MATLAB script was written (Appendix 4.2) that created a reference bit stream from the reference MISO straight from the RHD2132 chip and the SCLK from the MCU. Initially a second stream was created from the optical MISO and SCLK. Since SCLK

was never sent, but derived from the CS pulse, this only gave a partial summary of the system performance. Nonetheless, it was useful for looking at how well the neural data line performed independently of the transmitted clock. A more accurate representation of the actual received data involved using the received CS only (Appendix 4.3). In a similarly way to the FPGA, the BER Matlab script derived virtual SCLK rising edges from the CS clock. This was then used to determine the bit values of the optically received MISO to create a second bit stream. The data arrays were then compared and differences tallied to determine the bit error ratio.

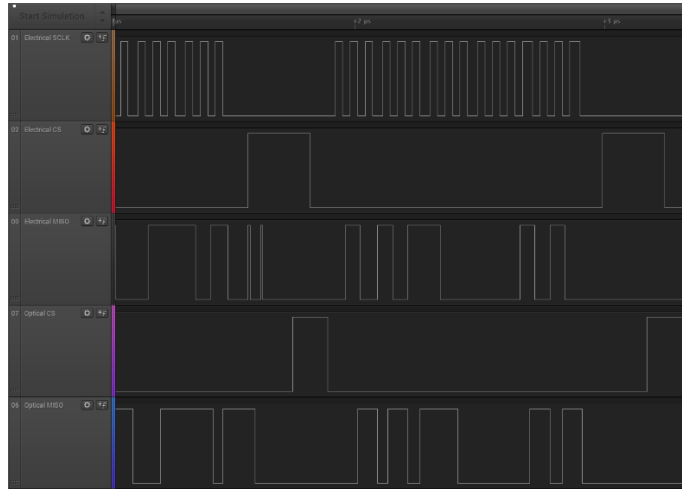


FIGURE 4.17: Data traces recorded using the Saleae logic analyser with the detectors placed 10 cm and turned 10 degrees away from the device. From top to bottom the traces show: Reference SCLK provided by the MCU, CS provided by MCU Timer, MISO output of Intan chip, optically received and digitized CS, optically received and digitized MISO

## 4.4 The experimental setups

### 4.4.1 The dummy data setup

Before testing the system in a live animal, preliminary runs involving dummy spikes were carried out. The complete assembled system (Figure 4.19 and 4.20), including a linear A32 Neuronexus probe with a reference pad (Figure 4.18), adapter board and the VLC device was mounted using Thorlabs optical components. This allowed angles

and distances to be readily adjusted with respect to the photodetectors. A small plastic container containing saline solution was inserted below the device, into which the tip of the probe was immersed. A NIDAQ USB-6259 system was then used to generate a dummy spike with a  $150\mu\text{V}$  undershoot,  $50\mu\text{V}$  overshoot and length of 1 ms (Figure 4.20a). A roughly 2 cm long platinum wire was then clasped was connected to the NIDAQ system. The ground from the NIDAQ system was connected to the ground of the device, which was also coupled to the reference input of the amplifier chip through a zero Ohm resistor. This provided a suitable baseline and grounding for the device from which the dummy spikes could be measured. The signal was introduced at a repetition rate of 2 Hz, and measured by all the electrodes in the saline solution (Figure 4.21 and section 4.5).

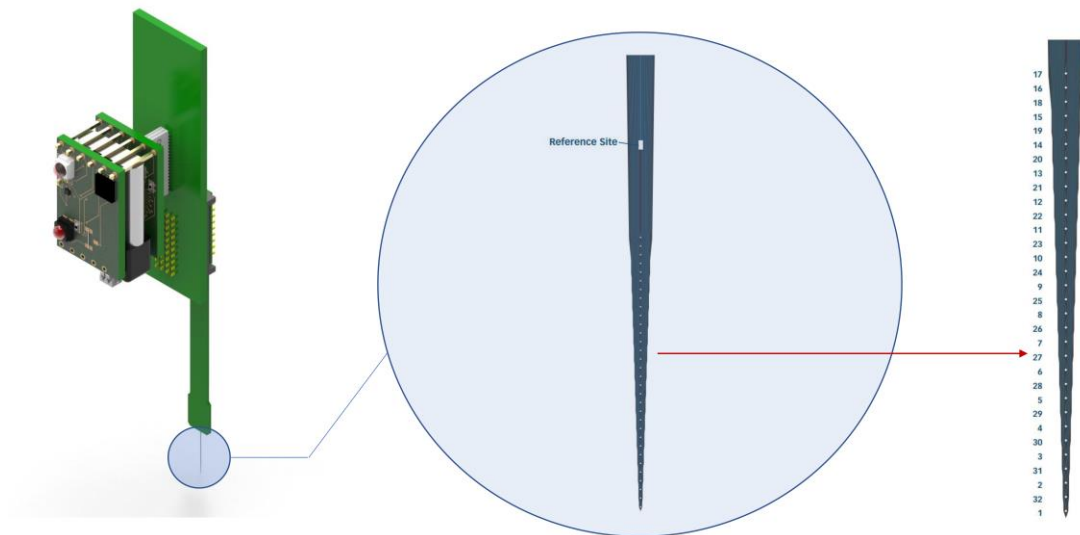


FIGURE 4.18: A zoomed in view of the probe being inserted into the saline solution and brain of the animal. A linear 32 channel Neuronexus A32 probe was used with large reference pad situated on the shank behind the recording electrodes.

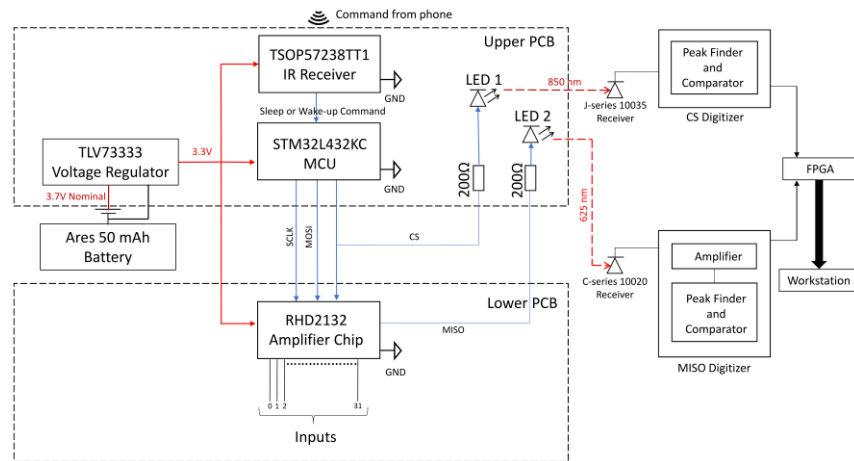


FIGURE 4.19: A schematic of the system used for the experiments. Inputs in the either the form of artificial dummy spikes or neural data from *in vivo* experiments were introduced to the amplifier end of the device, which then relayed the neural information to LED 2 to transmit the data. An MCU was used to provide the commands and clock signals to the Intan chip, of which CS was sent to LED 1, and relayed for synchronization purposes. Two photodetectors received the separate clock and data streams by using a combination of high and low pass filters. The data was digitized and sent to an FPGA, which converted the binary values to voltage readings, which were then displayed live using a Labview VI.

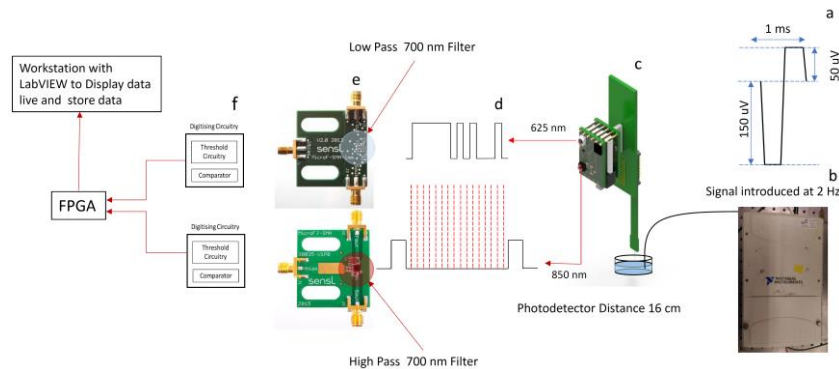


FIGURE 4.20: (a) The artificial dummy spikes introduced had an upward spike of 50  $\mu\text{V}$ , and downward spike of 150  $\mu\text{V}$ . (b) A NIDAQ device along with Labview VI was used to generate and set the characteristics of the dummy spike. (c) The artificial spikes were propagated through a platinum wire dipped into the saline solution in contact with the probe end of the device. (d) The neural data and CS clock were transmitted using two different LEDs at different wavelengths. CS was used to derive SCLK rising edges (red dashed lines) to sample the data line. (e) The two photodetectors with filters in front of them to separate the two streams (f) The digitizing circuit and DAQ part of the system used to live display the streaming data.

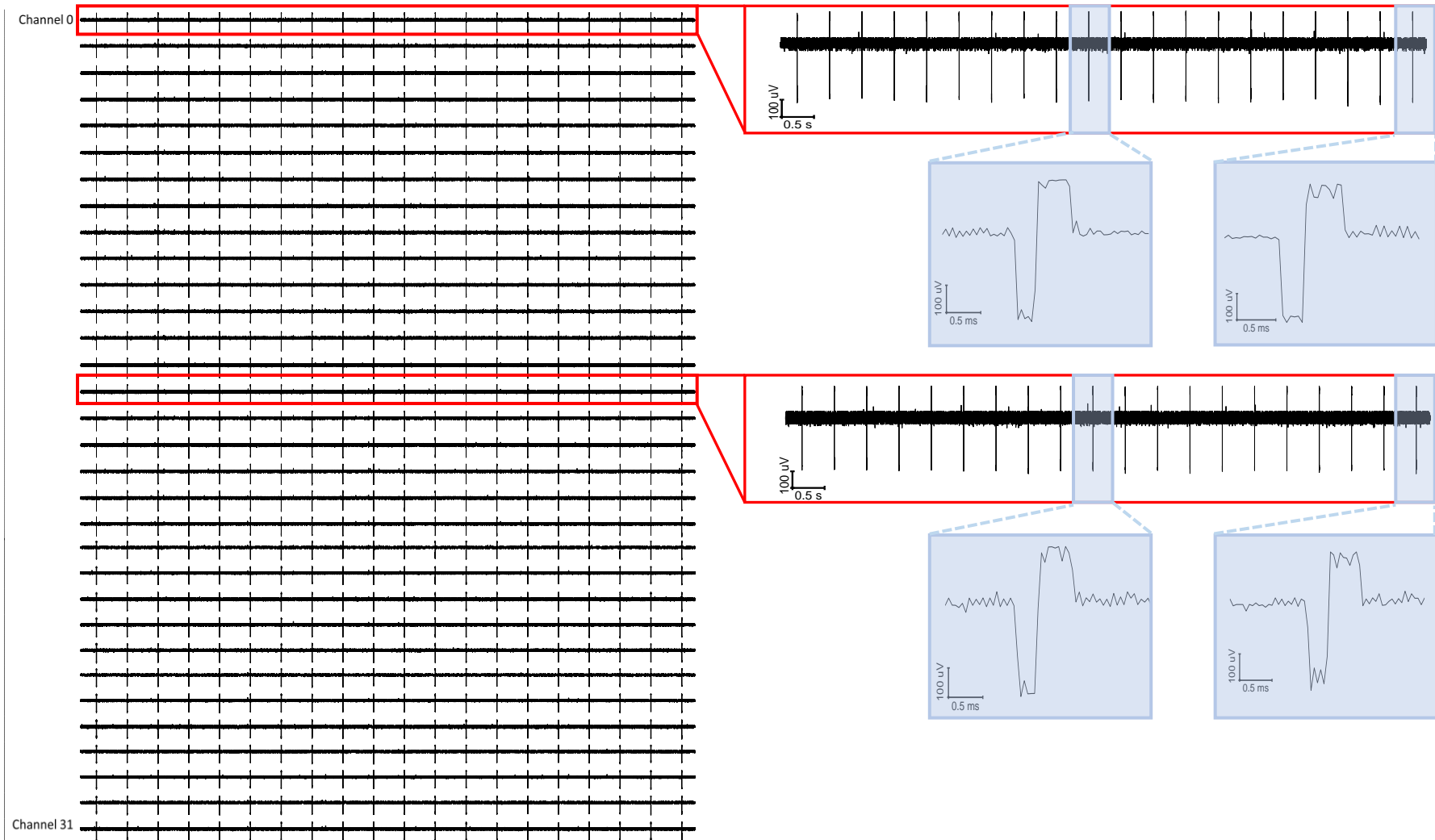


FIGURE 4.21: A snapshot of 32 channels worth of dummy neural data being transmitted from a distance of 10 cm. The spike shape and timing is maintained across all channels.

#### 4.4.2 The *in vivo* setup

4.4.2 Sections A-E, and section 4.5.5 are described by Dr. Shuzo Sakata and Dr. Daniel Lyngholm. They detail the exact type of animals used, along with the necessary surgical preparations required for *in vivo* testing. The recording and stimulating methods are also described along with the data analysis techniques implemented. A brief evaluation of the *in vivo* recordings is also described in section 4.5.5.

##### A. Animals

Two mice (one SOM-IRES-Cre::Ai32 mouse, C57BL/6-CBA/Ca F1 background, female, 19.1 g, 25 week old; one PV-IRES-Cre::Ai32 mouse, C57BL/6-CBA/Ca F1 background, male, 41.1 g, 65 week old) were used in this study. These mice were produced by crossing Ai32 mice (JAX012569) on CBA/Ca background with SOM-IRES-Cre (JAX013044) or PV-IRES-Cre mice (JAX008069) on C57BL/6J background to express channelrhodopsin2 (ChR2) in somatostatin-(SOM-) or parvalbumin-(PV-) positive neurons. All animal experiments were performed in accordance with the UK Animals (Scientific Procedures) Act of 1986 Home Office regulations and approved by the Home Office (PPL 70/8883).

##### B. Surgery

All procedures have been described elsewhere[7]. Briefly, animals were anesthetized with isoflurane (1 – 1.5%). Lidocaine (2%, 0.1–0.3 mg) was also administered subcutaneously at the site of incision. To provide analgesia after the surgery, Carprofen (Rimadyl, 5 mg/kg) was administered intraperitoneally. A head-post was attached on the skull by implanting two frontal bone screws (AP +3 mm, ML 2 mm from bregma) one of them used for EEG recording. Another two screws were implanted on the cerebellum, one of them used as a ground and a reference. Fixtures were attached to the screws with dental cement as a head-post. After the surgery the animals were left to recover for at least 5 days. During the acclimation period, the

animals were placed in a head-fixed apparatus (SR-8N-S, Narishige), by securing the head-post and placing the animal into an acrylic tube. This procedure was continued for at least 5 days, throughout which the head-fixed duration was gradually extended from 15 to 60 min. A day after this acclimation period, the animals were anesthetized with isoflurane and a craniotomy was performed to expose the auditory cortex (AC). During the following day, the animals were placed in the head-fixed condition to carry out the electrophysiological recording.

### C. In vivo electrophysiology

Detailed recording procedures are essentially the same as previous works[7]–[9]. All electrophysiological recordings were performed in a single-walled acoustic chamber (MAC-3, IAC Acoustics) with the interior covered by 3 inches of acoustic absorption foam. After placing an animal in the head-fixed condition, a 32-channel silicon probe (A1×32–10 mm–25s–177-A32, NeuroNexus Technologies) was inserted (Figure 4.22a) using a manual micromanipulator (SM-25A, Narishige) 1200 – 1400  $\mu\text{m}$  from the cortical surface so that the center of the probe shank could be in cortical layer 5. The probe was inserted perpendicularly with respect to the cortical surface. The location of the electrode in the AC was assessed by evaluating the local field potential (LFP) and multiunit activities (MUA) in response to white noise stimulation.

### D. Optical Stimulation

Blue light (450 nm, PlexBright, Plexon) was delivered through a fiber optic close to the silicon probe above the cortical surface (Figure 4.22b). The light output at tip of the fiber optic (200  $\mu\text{m}$  core diameter) was measured with a constant long ( $> 1$  sec) light pulse before probe insertion and was 28.5 – 29.0  $\text{mW}/\text{mm}^2$ . Optical stimulation consisted of 100 ms pulses.

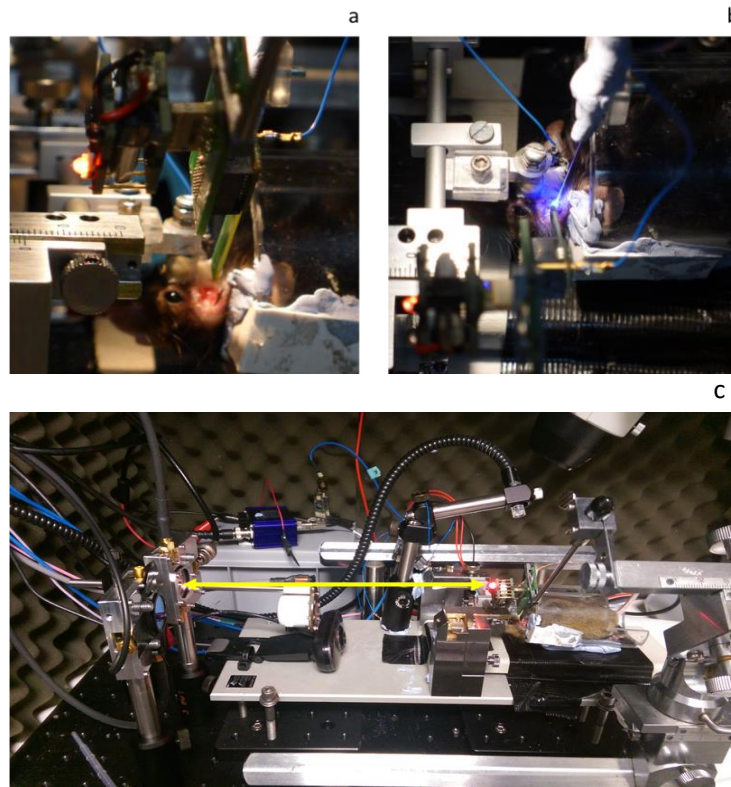


FIGURE 4.22: (a) Zoomed in views of the device inserted into the brain of the animal (b) Optogenetic stimulation used to activate neurons in the auditory cortex of an in vivo awake mouse. (c) In vivo experiment with the device inserted into the brain of a mouse. The distance between the photodetector and device was 20 cm (yellow arrow).

#### E. Data Analysis

Data analysis was performed offline. For spike sorting, Kilosort[10] was used with a GPU (Quadro M5000, NVIDIA) followed by a manual process with phy (<https://github.com/kwikteam/phy>). Other spike analyses were performed using MATLAB.

## 4.5 Results

To characterize how the system operates at different orientations, BERs were measured at a variety of different angles and distances. With the use of a MATLAB script (Appendix 4.2) the reference bit stream from the amplifier chip was compared to the optically received logic converted signal provided to the FPGA. This provided



insight into what sort of performance maybe expected if the device is mounted on a freely moving animal.

#### 4.5.1 Distance measurements

The two photodetectors were placed as close to each other as possible. The device was then placed on an angular platform midway between them, with the data transmitting LEDs facing the receivers at 0 degrees with respect to the centre line. Two long sections of thin guide posts originating from behind the photodetectors were then used to form a horizontal rail, essentially forming a barrier within which the platform could be moved. Distances were measured every 10 cm until signal retention degraded to below acceptable levels (BER of  $>2 \times 10^{-3}$ ). Tables 4.5 and 4.6 show how the system performed independently of the transmitted CS clock.

TABLE 4.5  
BER DISTANCE RELATIONSHIP

BER	Distance (cm)	Angle	Number of bits transmitted	Errors
0	10	0	1124427	0
0	20	0	1123844	0
0	30	0	1124348	0
0	40	0	1124480	0
5.33E-06	50	0	1125135	6
0.10072	60	0	1124133	113223

TABLE 4.5: BER measurements at distances from 0 to 60 cm. The bit stream was recorded directly at the amplifier chip output and compared to the digitized optical stream using the SCLK rising edges.

#### 4.5.2 Angle measurements

The platform had angular markings on the bottom to measure rotations with respect to the centre line of the detectors. Angles were measured at various distances at increments of 10 degrees. Since the viewing angle of the neural data transmitting LED was 60 degrees, a deflection of 30 degrees or more from the centre line would result in significantly reduced irradiance reaching the photodetector. Because of this, angles only up to this point were measured as beyond that the BER deteriorated significantly.

TABLE 4.6  
BER ANGLE RELATIONSHIP

BER	Distance (cm)	Angle	Number of bit transmitted	Errors
0	10	10	1124401	0
0	10	20	1124358	0
0	10	30	1124463	0
0.22844	10	40	1124352	256848
8.90E-07	20	10	1124132	1
0	20	20	1123904	0
0	20	30	1124277	0
†	20	40	†	†

TABLE 4.6: BER measurements at various distances and angles. The bit stream was recorded directly at the amplifier chip output and compared to the digitized optical stream using the SCLK rising edges. † At this distance and angle, the optical signal attenuates to such low levels that thresholding becomes impossible, with the received bitstream being unreliable (Appendix 4.9).

### 4.5.3 Eye Diagrams

As expected, SNR degrades with increasing angles and distances as shown in the eye diagrams (Figure 4.23 and 4.24), and reaches levels unfeasible beyond the half angle ( $30^\circ$ ) even at close distances. Combining table 4.5 and 4.6 with the eye diagrams gives insight into what characteristics are associated with successful error-free transmissions. Panel *u* shows the eye diagram for a scenario at which the system cannot perform efficiently anymore ( $\text{BER} > 10^{-3}$ ). Observing the eye opening width and height, it is shown that data transmission breaks down when the vertical height drops to  $\sim 5$  mV, and width to  $\sim 40$  ns. The distortion on the 0 and 1 levels is also significant at this point, with its ratio to the maximum eye opening being  $\sim 1:1$ . Figure 4.24 shows the system response with respect to different data rates. For *in vitro* and *in vivo* experiments the data was transmitted at bit rates equivalent to 16 Mbps (Figure 4.23 and 4.24g). Due to the timing gaps required between successive samples however, the actual data rate correlating to neural information was 10.24 Mbps. At faster rates the system reaches its limit demonstrated by the lack of clear eye openings for the diagrams. In panel *h* and *i* It can also be seen that lower peak pulses start to dominate, due to limitations of the LED rise and fall times. The short burst single bits

only have time to roughly reach 50% and 25% of the total level respectively, presenting thresholding challenges for the different bit levels.

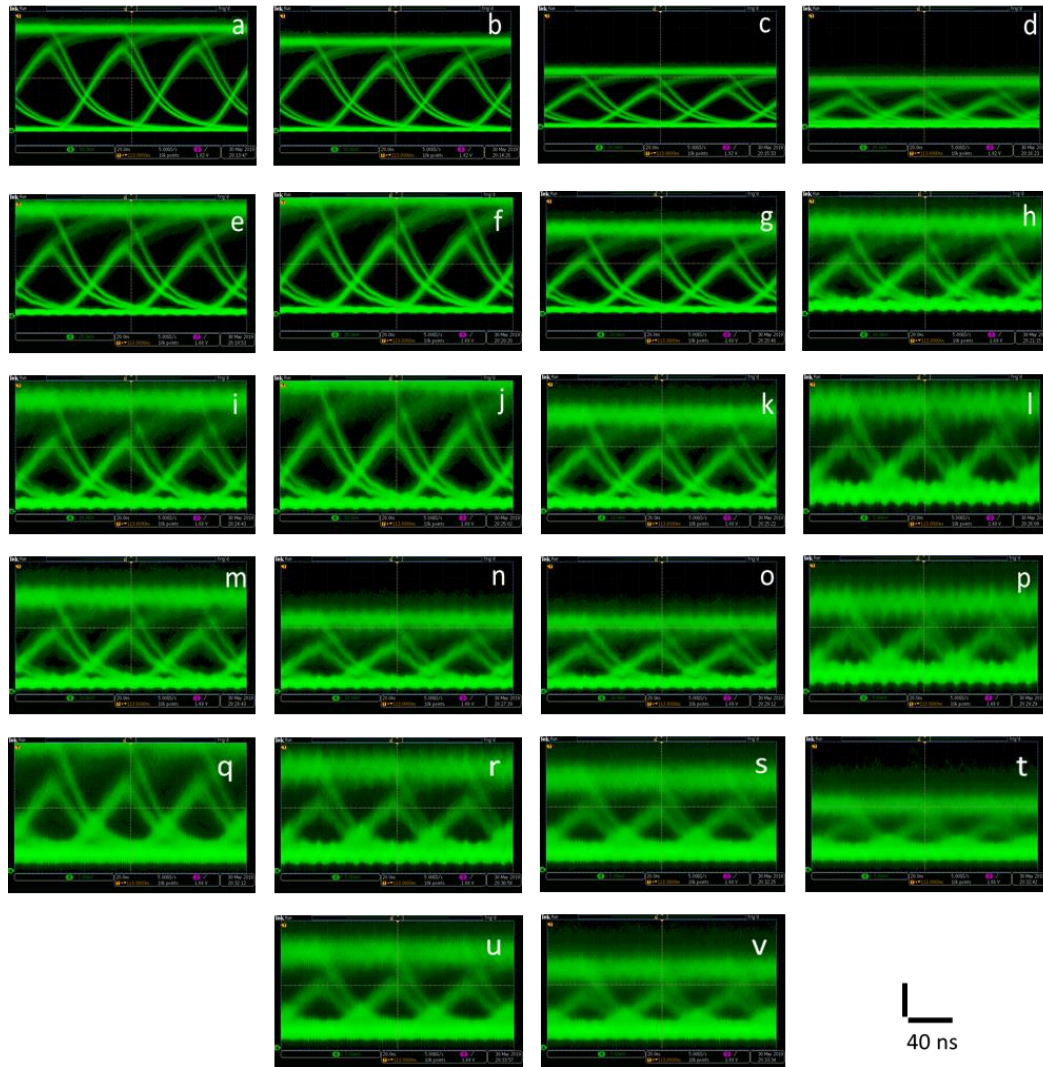


FIGURE 4.23: shows the eye diagrams for various angles ( $0^\circ - 30^\circ$ ) and distances (0 – 60 cm). The horizontal scale bars in the bottom right corner is constant for all figures at 40 ns, while the vertical bar is 20 mV for figures a-g, 10 mV for figures h,i,j,k,m,n,o and 5 mV for figures l,p,q,r,s,t,u and v. Columns a-q, b-r, c-s, and d-t are for angles  $0^\circ$ ,  $10^\circ$ ,  $20^\circ$ ,  $30^\circ$  respectively, while rows starting with a,e,i,m,q and u are for distances 0, 10, 20, 30, 40, 50 and 60 cm respectively. Panel u and v are for angles  $0^\circ$  and  $10^\circ$ .

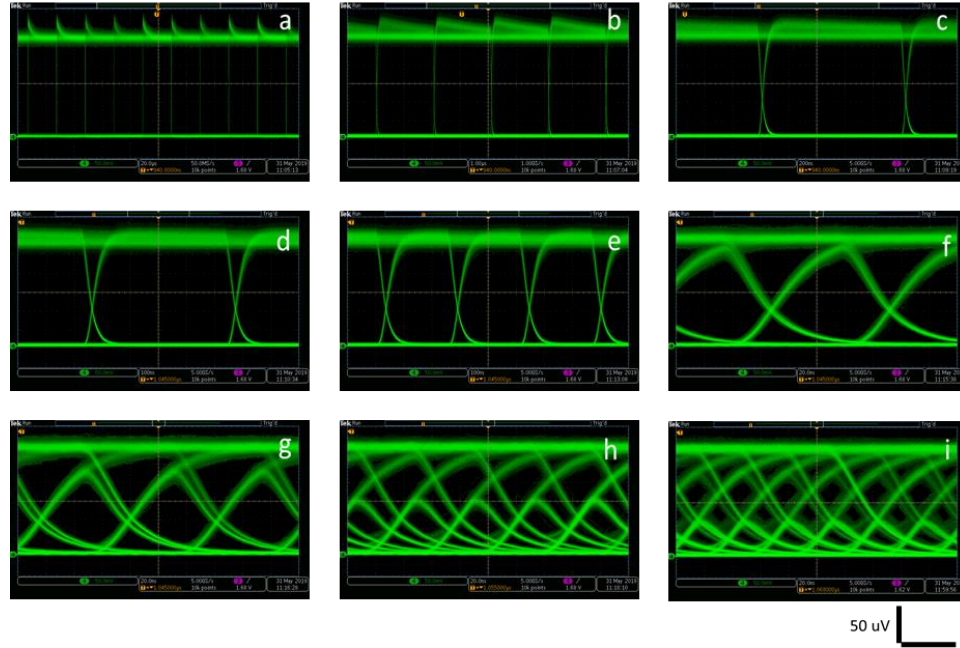


FIGURE 4.24: shows how the eye diagrams change with different data rates, all recorded from a distance of 10 cm at an angle of deflection of  $0^\circ$ . From panel *a-i* the data rates are, 0.05, 1, 2, 5, 12.5, 16, 24 and 40 Mbps, with the horizontal scale bar being 40  $\mu$ s, 2  $\mu$ s, 400 ns, 200 ns for *d* and *e*, and 40 ns for the remaining panels respectively.

#### 4.5.4 Performance modelling comparison

Hamza [11] and Khalighi [12] derive equations for the performance of SensL SiPM photodetectors under ideal conditions (no ambient light), as a function of received power, distance, Poisson based photon detection probability and photodetector characteristics. Theoretical modelled estimations for the data rate used throughout the experiments (Figure 4.25), were compared to the experimental results to see how much they correlate. A script was written as shown in Appendix 4.10, with the performance due to Poisson based shot noise being isolated by setting the other sources of noise to zero. The experimental data (Table 4.5, and 4.6) closely matches the modelled data up to 50 cm, and similarly shows a very low number of errors ( $< \text{BER}$  of  $10^{-5}$ ). Beyond this distance however, the probability of error seems increased by two magnitudes compared to the simulated data ( $\text{BER}$  of  $10^{-1}$  vs  $10^{-3}$ ). This sharp increase of errors is likely due to the effect of the real-world ambient light dominating SNR ratios at these distances.

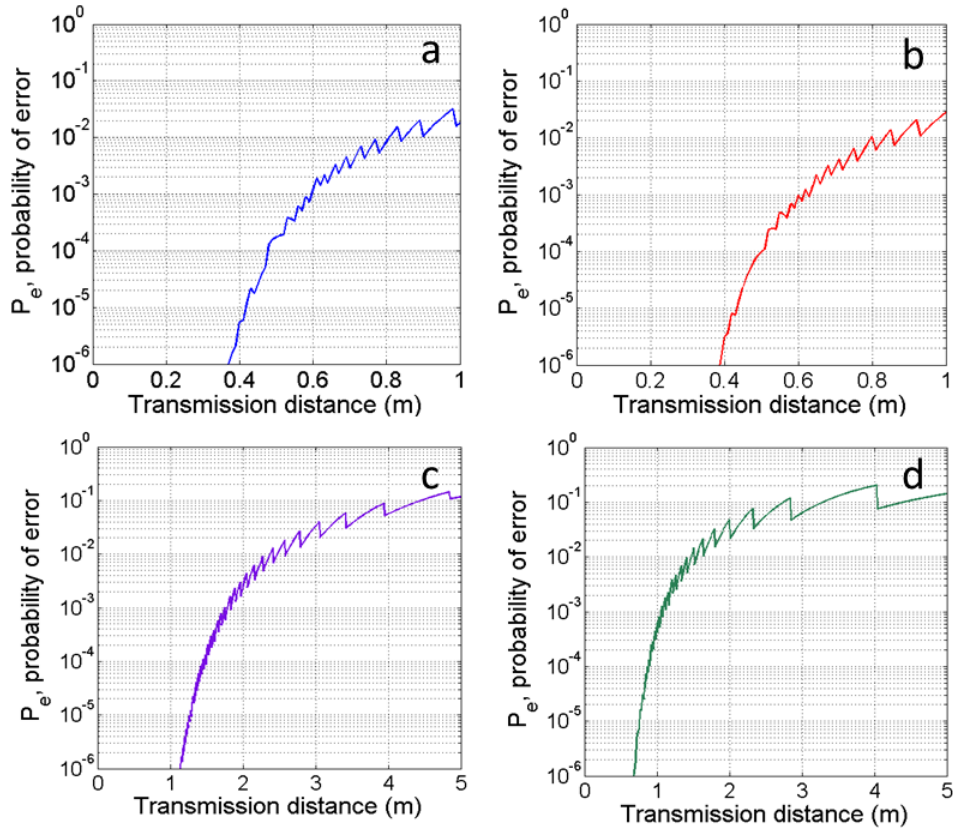


FIGURE 4.25: (a) Shows the modelled response of the system under ideal conditions (no ambient light, dark current/thermal noise, after pulsing or cross talk) with only shot noise present. (b) Introducing all other sources of noise except ambient light seems to make minimal difference compared to panel a, where other sources of noise were omitted. (c) A hypothetical scenario with a larger photodetector (9 mm<sup>2</sup>) but with other noise parameters left the same. The distance at which BER increases above 10<sup>-3</sup> more than doubles from 0.6m to 1.6m, showing a strong effect on performance. (d) A theoretical projection assuming the transmitted optical power from the transmitting LED is increased from the 3.2 mW/sr used to 10 mW/sr. The increase in performance is not as impactful as increasing the photodetector area, it is however still substantial. The distance at which the threshold BER of 10<sup>-3</sup> is reached, increases from 0.6m to 1.2m.

#### 4.5.5 Power measurements

To measure the actual consumption of the device as opposed to relying on the power consumptions listed in the data sheets for the different components, the device was left running until the battery was depleted. The device was first fully charged and switched on, after which voltage readings from the battery were taken every half an hour (Figure 4.26). As the voltage required for the Intan chip to properly operate without entering derated mode is 3.3V, readings below this value were considered as

points where the device did not have enough power to properly work. While not used throughout the experiments, power consumptions for different sampling rates were also calculated and shown in Figure 4.27.

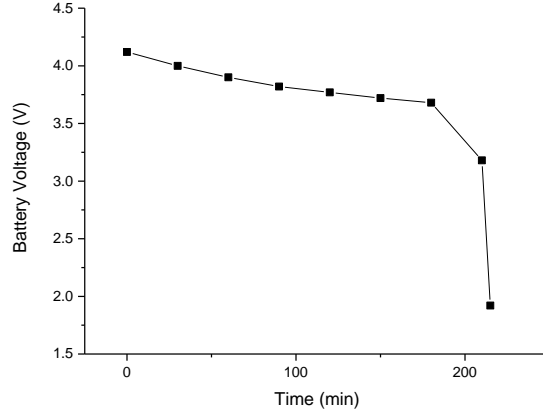


FIGURE 4.26: Graph showing how the battery voltage changes with respect to time as the device is running. A sharp fall from 3.12V can be noticeable after 215 minutes, indicating the maximum time the device can run on a single charge.

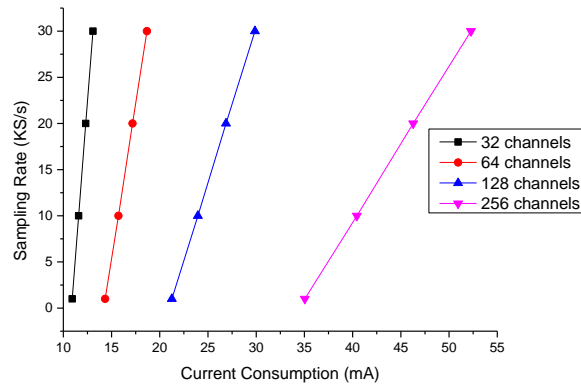


FIGURE 4.27: The power consumption for the device at various sampling rates and theoretically scaled up channel counts. Increasing the sampling rate and channel counts linearly increased the power consumption. It was assumed that the power required for the LEDs to transmit increased data rate is negligible compared to current draw of the amplifying chips. For future devices with up to 256 channels, an operating time of roughly 1 hour is possible with the currently implemented 50 mAh battery. Scaling up to longer operation times will require higher capacity batteries, which will likely weigh more. To retain the compactness for mice, either alternative powering (Section 5.4) solutions or lower power ADC (Application Specific Integrated Circuit) ASICS will be required (Chapter II, Table 2.5).

#### 4.5.4 Noise measurements

Dummy spikes were introduced as outlined in section 4.4.1 to ensure that signal transmission was working properly. Care was taken to ensure that the device and the surrounding environment was properly grounded. Once established, the artificial spikes were switched off so only the noise was transmitted. The recorded data was then analyzed using MATLAB's RMS function to determine the noise. Figure 4.28 shows a typical noise trace with the associated RMS noise, while table 4.7 shows the RMS noise for the different channels. The average noise across all channels was 9.18  $\mu\text{V}$ .

TABLE 4.7  
CHANNEL RMS NOISE

Channel Number	Noise RMS ( $\mu\text{V}$ )	Channel Number	Noise RMS ( $\mu\text{V}$ )
0	8.47	16	9.42
1	8.05	17	8.03
2	7.69	18	10.37
3	7.5	19	9.92
4	8.34	20	8.07
5	8.02	21	9.88
6	10.11	22	10.76
7	9.99	23	8.09
8	9.16	24	9.44
9	7.97	25	7.68
10	10.32	26	7.03
11	9.79	27	10.73
12	8.64	28	7.97
13	8.59	29	10.12
14	9.25	30	7.76
15	7.03	31	10.53

TABLE 4.7: The RMS noise for each channel.

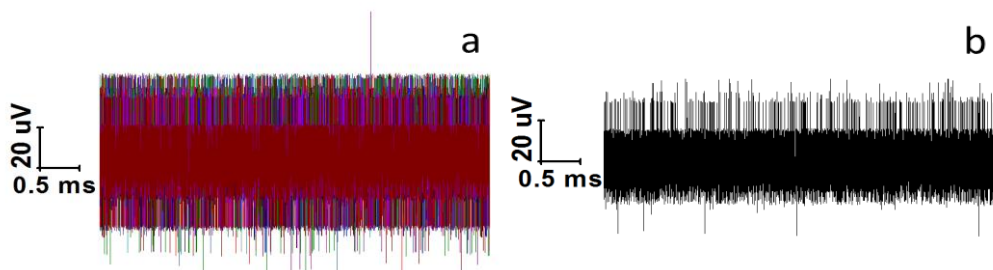


FIGURE 4.28: (a) Noise from all channels superimposed on one another. (b) Noise recorded from a single channel



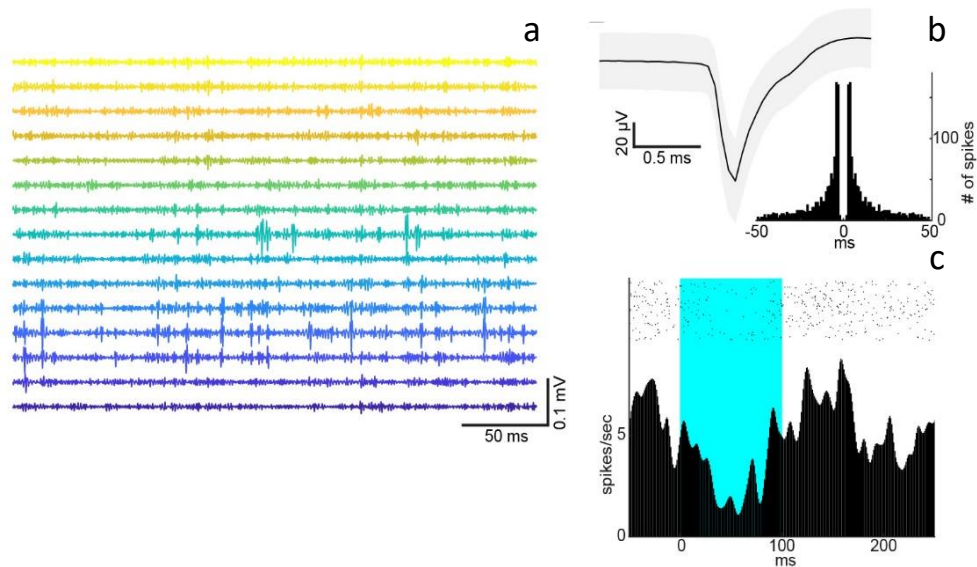
4.5.5 *In Vivo* Results

Fig 4.29. *in vivo* experiments with LED-based wireless data transmission system (A) Example traces of high frequency (500-1500 Hz bandpass filtered, 20 kHz sampling) signals. (B) An average spike waveform of an isolated single unit. Standard deviation of spike waveforms is also shown (shaded area). Inset, autocorrelogram of this single unit. (C) An example of optically modulated multiunit activity. 100 ms optical pulses (14 mW/mm<sup>2</sup> at the tip) were applied in an awake head-fixed PV-IRES-Cre::Ai32 mouse.

To demonstrate the capability of the device *in vivo*, neural spiking activity was monitored in the AC of awake head-fixed mice ( $n = 3$ ; one session from SOM-IRES-Cre::Ai32 mouse; two sessions from PV-IRES-Cre::Ai32 mouse) by using a 32 channel silicon probe (Figure 4.18). We confirmed that high frequency signals can be transmitted from the sender to the receiver by observing clear spiking activities across channels (Figure 4.29a). To isolate these spiking activities, we performed spike sorting offline. From three recordings, 12 single units were isolated (range: 1-7 single units per experiment). An example average spike waveform was shown in Figure 4.29b. The autocorrelogram of this isolated cell showed a bursting behaviour with a clear refractory period. Finally, to demonstrate the compatibility of the system with optogenetic experiments, we also applied optical stimulations to activate cortical inhibitory neurons to inhibit neural activity in awake head-fixed mice ( $n = 3$ ). Weak inhibitory effects were confirmed from the optical stimulation (Fig. 4.22c). Together,



the system can be utilized for *in vivo* electrophysiological and optogenetic experiments.

## 4.6 Conclusion

A fully wireless VLC based system was created and tested. The device was initially verified by introducing dummy spikes into a saline solution, and transmitting it at various angles and distances. The BER results show that acceptable levels can be reached at distances up to 50 cm (5.33E-06), with further improvements likely with simple changes made to the apparatus on the receiving end. The shape and temporal characteristics of the simulated spikes were maintained, with no visible corruption. With respect to angular performance, the results were limited by the viewing angle of the particular LED used (60°). Using different LEDs larger deviations from the photodetector could readily be achieved, and will be discussed in more detail in chapter V. The device had a total weight of 5.045g, which at the moment is too heavy for freely moving mice but suitable for rats and larger animals. Various strategies to decrease this will also be discussed in the next chapter, where approaches detailing the use of thinner PCBs and different power sources will also be explored. Lastly, the device was tested *in vivo* in a head fixed mouse from distance of 20 cm, with high frequency neural spikes being clearly observable and recorded.

## References

- [1] “RC: The Pronto’s IR Code Format (2).” [Online]. Available: <http://www.remotecentral.com/features/irdisp2.htm>. [Accessed: 07-Feb-2018].
- [2] Osram, “OSLON Black Series (850 nm).” SFH 4715AS Datasheet, Aug. 2016.
- [3] Kingbright, “APETD3528SEC/J3-PRV,”datasheet, May. 2011.

- [4] On Semiconductor, SensL, “Silicon Photomultipliers (SiPM), Low-Noise, Blue-Sensitive,” C-Series SiPM Sensors datasheet, Nov. 2018 [Rev 6].
- [5] On Semiconductor, SensL, “J-Series High PDE and Timing Resolution, TSV Package,” datasheet, Dec. 2017 [Rev 3.1].
- [6] Intan Technologies, “RHD2000 Series Digital Electrophysiology Interface Chips,” RHD2216 RHD2132 datasheet, Dec. 2012. [Revised Sept. 2013].
- [7] J. G. Yague, T. Tsunematsu, and S. Sakata, “Distinct Temporal Coordination of Spontaneous Population Activity between Basal Forebrain and Auditory Cortex,” *Front. Neural Circuits*, vol. 11, no. September, pp. 1–14, 2017.
- [8] N. McAlinden, E. Gu, M. D. Dawson, S. Sakata, and K. Mathieson, “Optogenetic activation of neocortical neurons in vivo with a sapphire-based micro-scale LED probe,” *Front. Neural Circuits*, vol. 9, no. May, p. 25, 2015.
- [9] R. Scharf, T. Tsunematsu, N. McAlinden, M. D. Dawson, S. Sakata, and K. Mathieson, “Depth-specific optogenetic control in vivo with a scalable, high-density  $\mu$ LED neural probe,” *Sci. Rep.*, vol. 6, no. 1, p. 28381, 2016.
- [10] M. Pachitariu, N. Steinmetz, S. Kadir, M. Carandini, and K. D. Harris, “Kilosort: realtime spike-sorting for extracellular electrophysiology with hundreds of channels,” *bioRxiv*, p. 061481, 2016.
- [11] T. Hamza, M. A. Khalighi, S. Bourennane, P. Leon, and J. Opderbecke, “On the suitability of employing silicon photomultipliers for underwater wireless optical communication links,” *2016 10th Int. Symp. Commun. Syst. Networks Digit. Signal Process. CSNDSP 2016*, no. 1, 2016.
- [12] M.-A. Khalighi, T. Hamza, S. Bourennane, P. Leon, and J. Opderbecke, “Underwater Wireless Optical Communications Using Silicon Photomultipliers,” *IEEE Photonics J.*, vol. 9, no. 4, pp. 1–10, 2017.

## Chapter V – Conclusion and future work

### 5.1 Overall summary

A VLC based head mountable device for small animals has been successfully designed and assembled. It was tested in both *in vitro* and *in vivo* experiments. Neural data was successfully transmitted at distances up to 20 cm (likely to improve), with BERs being within acceptable limits ( $<2e-3$ ). The 50 mAh battery provided enough operating time (3.5-4 hours) for experiments to be carried out, and to collect significant amount of neural data. Power consumption is mostly dominated by the amplifier chip, with the current draw being linear with the number of channels being sampled. This is added on top of the constant base usage of the control circuit and data transmitting LEDs. Higher electrode counts, up to 128 channels, would result in energy requirements that would still be practical using the current setup at the expense of reduced operating time ( $\sim 1$  hour). With alternative powering strategies discussed in Section 5.5 this could be further increased. Using off the shelf LEDs, a data rate of 10.24 Mbit/s was achieved, enough to sample 32 channels of neural data at 20 kS/s. This is roughly 3-10 times the data rate as similarly classed ( $<5g$ ) devices [1][2]. The bandwidth limitation was mainly due to the slow rise and fall time of the commercial LEDs used, which are predominantly designed for indicator purposes as opposed to fast data transmission. Using custom made LEDs [3], [4], data rates that are orders of magnitudes higher than this can be achieved at the expense of relatively minimal power consumption. Currently, the commercial market and research is dominated by RF based wireless devices. Compared to these devices, which are

limited by fundamental physical principles (Shannon Hartley, Chu-Harrington equations outlined in Chapter II), the simultaneous wireless observation of significantly higher channels is possible for small animals using the outlined optical methods. There are, however, a new set of challenges that need to be addressed before the technique can be used with freely moving animals. The angle relation between the LEDs and photodetectors is continuously changing, thus creating uneven and unpredictable light flux densities between the two components. The currently used light sources had viewing angle characteristics dictated by the manufacturer provided optics on them ( $60^\circ$  for Kingbright and  $90^\circ$  for Osram), and are too small to create a feasible enclosure without using a large number of photodetectors. This is apparent from the BER results, which show significantly reduced performance beyond the viewing angles of the LEDs. Using LEDs with larger viewing angles could significantly improve spatial performance and the orientations the device operate in, and are discussed in more detail in Section 5.6. Other approaches such as using photodetectors with larger areas and optical collectors are discussed in Section 5.2. The digitizing circuitry successfully converted the optical signals at a wide range of angles and distances, but is constrained by the passive components with respect to the ranges it can operate in. Distance variations of up to 10 cm are still acceptable to maintain operation at a sufficiently low BER with a given set of capacitance and resistance values in the circuit. This uneven operation is due to the continuously changing optical signal and threshold relations at different configurations.

The weight for the complete device is currently 5.045g and is too heavy to be used with mice. However, several strategies such as using thinner PCBs and different power sources may be implemented to alleviate this problem. Specific calculations and methods are outlined in Section 5.5.

Since the data is sent on two separate streams as opposed to one, the corresponding apparatus on the receiving end is consequently more complicated than if a single channel was used. By using techniques such as Manchester encoding the two streams

on the device could merged into a single one, thus creating a more streamlined solution with only one LED and simpler photodetector arrangements. The idea is further explored in section 5.7.

The electrical noise characteristics of the device are within an acceptable range with an RMS of  $9.18 \mu\text{V}$ , which produce SNR ratios of  $5 <$  even for small  $50 \mu\text{V}$  spikes, and allow straightforward spike identification. The dummy spikes were clearly displayed at distances of 20 cm (likely to increase), while maintaining the physiological features of the artificial signal. Typically spikes had a spike amplitude size of a  $150 \mu\text{v}$ .

The data was transmitted using regular OOK, which yields lower rates than more complex techniques. Other methods such as PAM and OFDM could be used to achieve bandwidths well in excess of the achieved data rates and are expanded on in section 5.8.

The device was interfaced with a recording only probe with 32 electrodes. Technologies for increasing the number of recording sites is continuously being improved by a number of research groups [5]–[8]. Integrating such devices would greatly increase the recording capacity of the device. Further advances such as optogenetic probes simultaneously capable of recording and stimulating could also be introduced to allow increased resolution and accuracy with respect to mapping the correlation between stimulation and behaviour. Different probes and various approaches to interface with the device are explored in section 5.9.

The device was activated by connecting to the power and ground lines of the device, and then setting it to low power mode, then waking it up remotely. Since a base power draw is still present, even when low power mode is activated, a solution to completely disconnect the power supply is needed. Since physical contact after implantation is ideally minimized, a completely wireless and fully detaching solution of the battery is required. Possible approaches are discussed in section 5.9.

Further improving the MCU code is also an aspect that is planned to be further developed. Currently the system starts sampling at 20 kS/s with adjustments only possible rates and filter cut-offs by reflashing the MCU. A protocol could be set up where different commands are sent to the MCU through the IR receiver, with each command restarting the device at a specified frequency. Additional commands controlling stimulating probes in future devices could also be sent.

Other novel methods such as transfer printing LEDs could be used to even further miniaturize the device, and use micro LEDs directly implanted on a bare chip to reach even smaller sizes and weight. A brief description of transfer printing is detailed in section 5.11, along with how it may be implemented on the device.

Finally, *in vivo* results clearly show that live neural data was transmitted while maintaining the physiological and temporal characteristics of neural activity. Audio and optogenetic stimulation was also carried out, and demonstrated the expected response from the excitation. The stimulating blue fiber (450 nm) did not interfere with the data transmission, and allowed modulation to be carried out at intensities towards the upper limit of what is required for standard neural activation.

## 5.2 Detector placement

From the results presented in the previous chapter (Table 4.5), it was shown that data with low error rates may be transmitted at distances up to 50 cm using the current configuration, if appropriate alignment and optimum thresholding of the incoming optical signal is carried out. To create an observational area for freely moving animals, where full coverage is achieved, the previously demonstrated radiant intensities need to reach the photodetectors in all orientations the device on the animal's head may be in. One approach may be the implementation of a multi detector system consisting of 5 pairs, which would be placed along the cardinal planes

of the cage (Figure 5.1-5.7). The electrical output from the total received optical energy is then summed by either connecting them together, or using a dedicated IC to combine the incoming signals. These would then be sent to the digitizing circuitry and FPGA, as has been outlined in chapter IV. Figure 5.1 shows how one such setup might look. Given the viewing angle ( $60^\circ$ ) of the currently used LEDs, insufficient coverage would be achieved if the detectors are placed right at the barrier of the observational area. One method to alleviate this problem is to place the detectors further back to allow the photons from the LED to hit them even from extreme cases, such as coordinates originating from the corner of the area.

Another method to improve performance would be to use reflective surfaces such as mirrors, which could be placed along the inner side of the cage. This way, even if the transmitting light sources are not incident with respect to the photodetectors, light may be reflected from one of the orthogonal surfaces, and directed towards a photodetector.

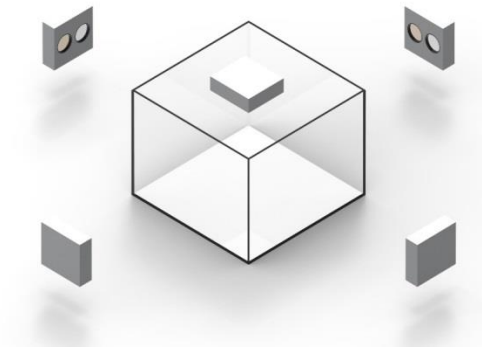


FIGURE 5.1: A possible photodetector placement strategy, with them positioned opposite the face of 20 cm x 20 cm cage. Each unit contains two photodetectors and appropriate filters to separate the different digital lines. Using techniques such as Manchester encoding may allow both streams to be sent using one LED, thus halving the required photodetectors.

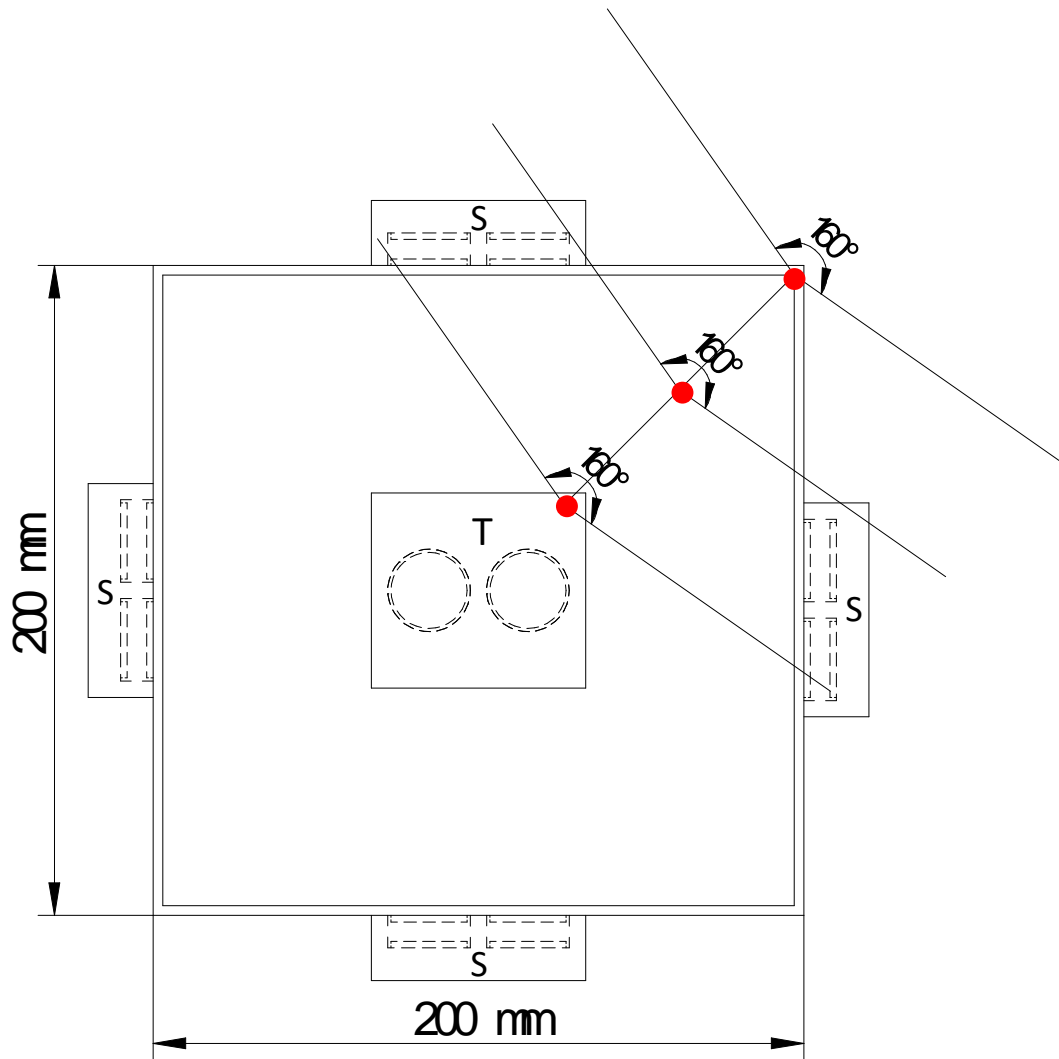


FIGURE 5.2: The figure shows a top down view of the setup, where the photodetectors would be flush with the edge of the walls of a 20 cm x 20 cm cage. (S) indicates detectors placed at the side of the observed area, while (T) indicates the detector placed at the top or above the enclosure. The height is 15 cm. This is less than ideal, as the angle required to hit the detectors in extreme scenarios is extremely large (the mouse might be in the corner standing on hind legs with the head mount pointing away, and impossible to reach with even wide ( $>120^\circ$ ) viewing angle LEDs). The origins of these hypothetical points is indicated by the red dots on the diagram (distance between them is 50 mm). A more suitable approach is to place them further back as show in Figure 5.1 and 5.3. The nomenclature described in this figure applies to figures 5.3-5.7 as well.



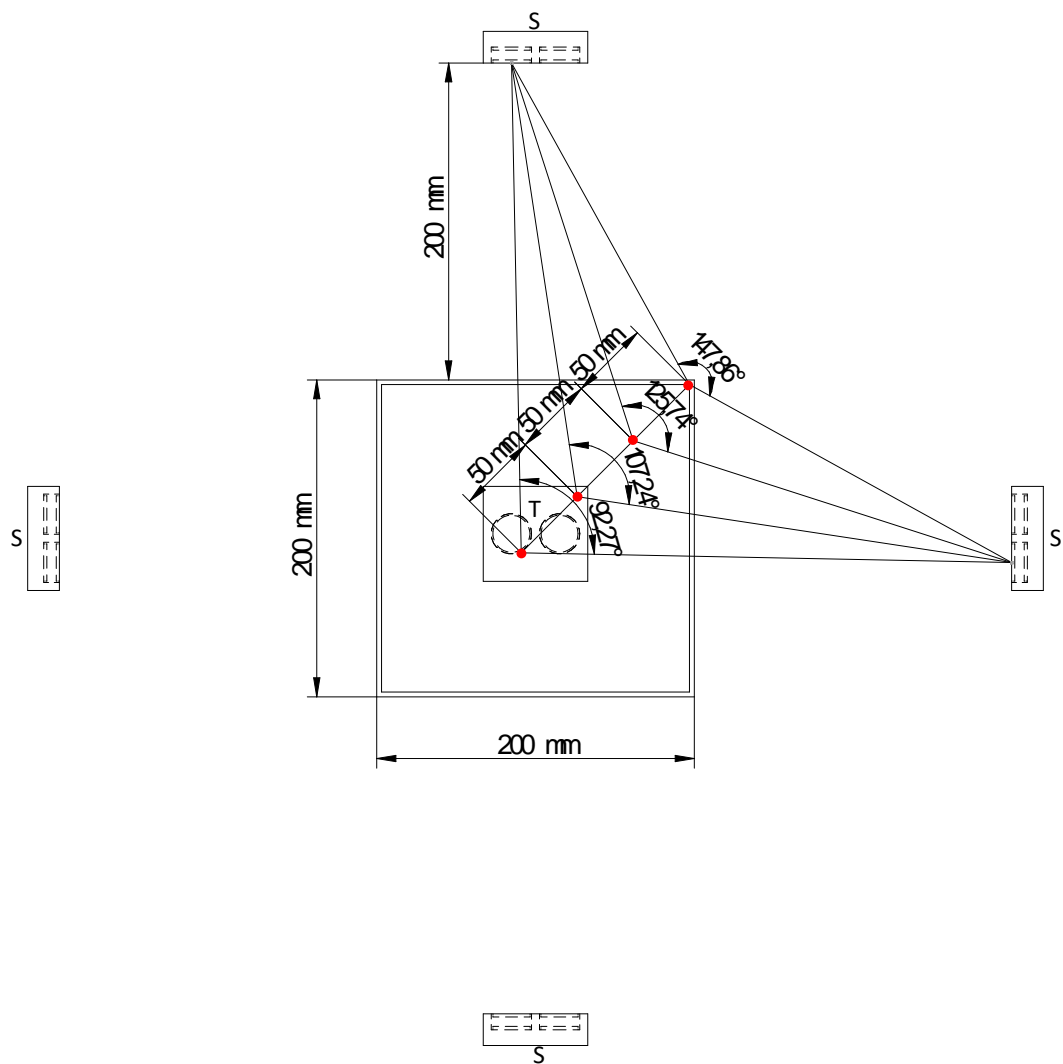


FIGURE 5.3: The figure shows a top down view of the setup. By placing the detectors further back 20 cm, it can be seen that for the same scenario as outlined in Figure 5.2, a much smaller viewing angle is sufficient to reach the photodetectors. A variety of different positions are explored at increments of 5 cm apart, from the corner of the enclosure to the centre. In the most extreme case, with the mouse being in the corner exactly (maximum separation) a viewing angle of  $147.86^\circ$  is enough to hit the detectors (if the centreline of the transmitting LED is exactly at the midpoint between the two detectors). While this is larger than the LEDs that were used in the prototype device, off the shelf LEDs are available with wider viewing angles and similar irradiances (section 5.6). This is a very unlikely orientation to occur in a live experiment, especially for a prolonged time. Furthermore, light is still transmitted outside of the viewing angle as well, along with the reflections from the different surfaces that may also be picked up by the multi detector system proposed.

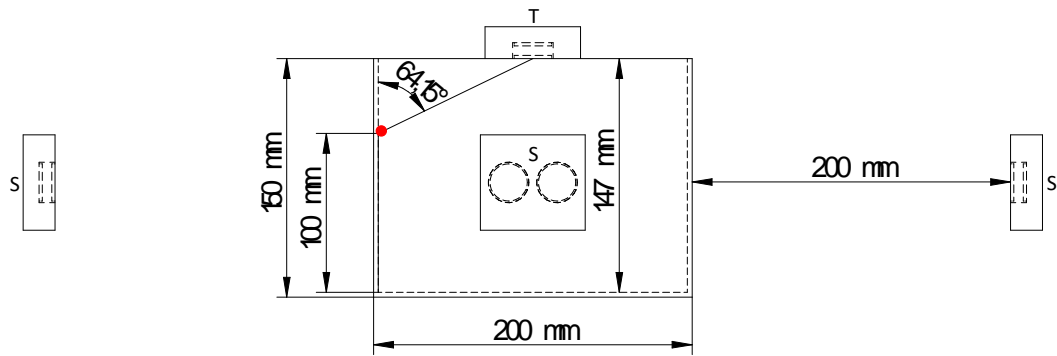


FIGURE 5.4: Side view of the proposed detector system. Another extreme case scenario is examined where the mouse may be standing on its hind legs with the device's LEDs pointing upwards. In this case the angle between origin of the light and the detector would be  $64.75^\circ$  at most. Using this arrangement the largest distance from a given photodetector will be  $\sim 18$  cm.

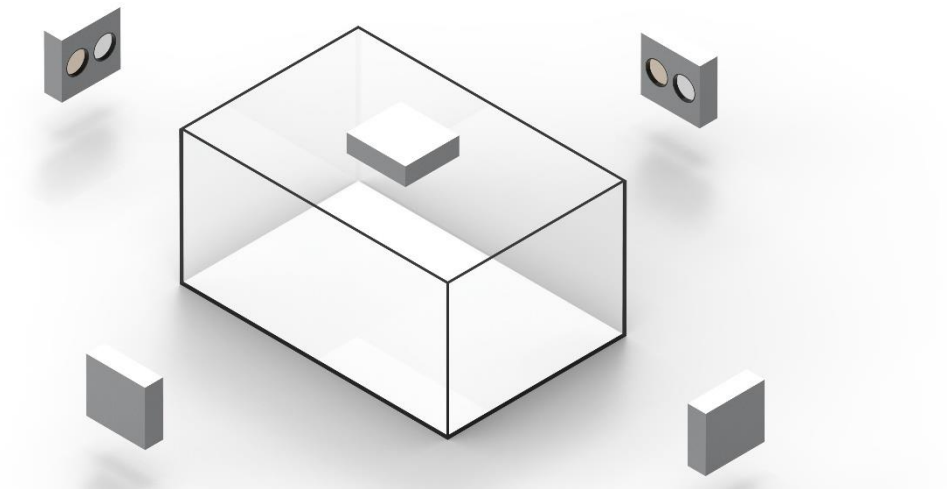


FIGURE 5.5: A different cage geometry that may be used. In this case the base is a longer rectangle with the dimensions 20 cm x 30 cm. The height is the same as before at 15 cm.

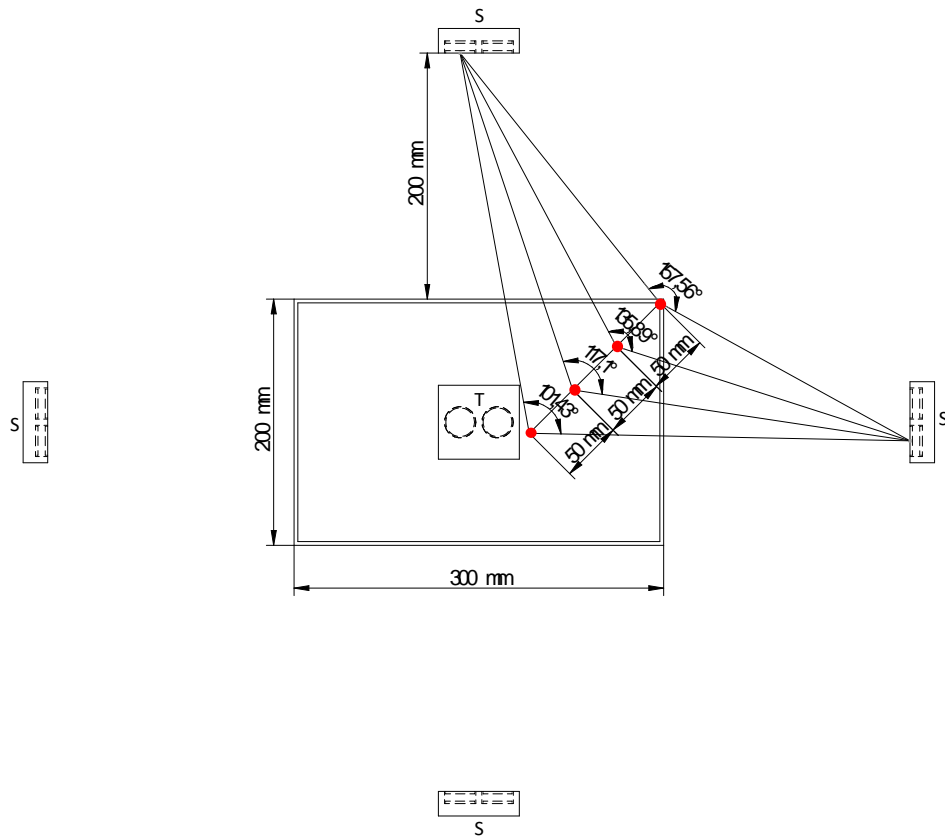


FIGURE 5.6: Observing the angles required to hit the detectors from different coordinates, it can be seen that larger angles ( $157.56^\circ$ ) are required than for the smaller cage, increasing the likelihood of instances occurring where not enough light reaches the detectors.

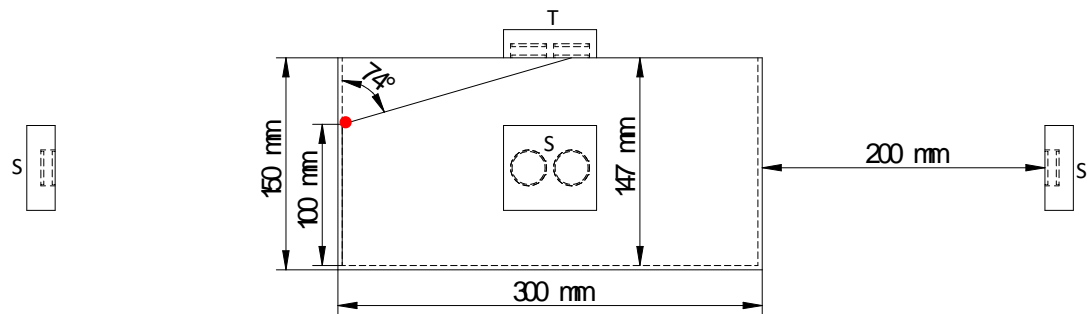


FIGURE 5.7: Side of the 20 cm x 30 cm cage, with the extreme case scenario outlined again. In this case  $74^\circ$  is the separation between the LEDs and the top detector. Using this arrangement the largest distance from a given photodetector will be  $\sim 21.21$  cm.

The characteristics of the photodetectors are crucial for system performance. Vital factors such as the recharge time constant, photon detection efficiency (PDE) at the transmitting wavelengths, detector size, dark current amount, and gain all influence that maximum receivable data rates possible. To ensure optimum operation, detectors that are sensitive yet still fast enough to transmit at the required data rates are needed. The SiPMs that were implemented were very sensitive, but struggled to keep up with higher data rates. This was especially prominent with the larger area but slower J-series detector, which could not cope with the neural data stream, but was still sufficient for the lower frequency CS clock. The bandwidth is proportional to the microcell size, while sensitivity is mainly dominated by the sensor size. An ideal detector would have the largest sensor made up from the smallest microcells possible. There is a limit to how far this can go, however, as each microcell has an associated “dead area” which adds up significantly below a certain size. From the SensL datasheet the most suitable units to upgrade to would be the J-series 30020 (3 x 3 mm detector area made up from 20 micron cells). This is the same microcell size that was used in the C-series neural data receiving photodetector, however, with 9 times the detector area, a faster recharge time constant (15 ns vs 23 ns) and a better PDE (38% vs 31%) . This would allow increased sensitivity while maintaining the first response. Smaller cell sizes (10 $\mu$  with 5 ns recharge time constant) are also available, but only up to 1 mm x 1 mm detector areas. This is the same as used for the neural data, so should provide enough sensitivity to operate at the irradiances used during the experiments, and allow much faster speeds. Red sensitive (R-series) detectors are also available providing better photon detection efficiencies and responsivities in the desired spectrum (<800 nm), but are only available 1 mm x 1mm sizes. The smallest available cell size is the same at 10 $\mu$ , but the recharge time constants are higher at 13 ns vs 5ns. Given that the sensitivity provided by the J-series seemed sufficient to detect the neural data, it is likely more suitable to stay with the larger area J-series. Lastly, other type of photodetectors may also be suitable such as APDs and SPADs that generally provide increased response times but less sensitivity. Optical collectors

may also be used that could collect and focus the detected light onto the photosensitive area [9].

One possible solution to ensure complete coverage is to create a detector system array that completely envelops the surrounding area. While this would guarantee light hitting detectors in all orientations, it comes at the price of increased complexity and cost. Depending on the density of deployed photodetectors, setting up such a system would likely require additional setup time for the connection and placement of each additional photodetector. Contingent on the price of cheaper photodetectors this might be an economically viable solution; however more sensitive and faster detectors typically incur a higher cost. The associated complexity could be potentially overcome by connecting the detectors in an array to a fixed frame to accommodate a typical mouse cage, with all outputs connected to a common output. This more complicated setup would likely increase assembly and manufacturing costs however.

### 5.3 Receiving end circuitry modifications

The thresholding method that was currently used required manual setting with respect to larger distance and rotation changes. While the threshold did alter and scale as the device moved away from the detectors, it was not consistent enough to maintain the strict requirements for timing relations (Figure 4.11). The clock pulse was especially subject to distortion as it was transmitted to the slower but larger detector. While the recharge time constant of the detector was 45 ns, it still seems to have affected the shape of the transmitted pulse, increasing the rise and (especially) the fall time. Transmission to the faster C-series detector did not seem to create this problem. The combination of increased detector size/sensitivity and slower speeds meant that the CS pulses had different shaping characteristics, requiring different thresholding requirements than the neural data stream. Furthermore, the slower out of sync property of the clock data link had to be compensated in the FPGA to ensure

that the timing between the clock and data allow sampling without missing any significant bits. By incorporating the same photodetectors for both links this could be mostly avoided leaving any timing differences down to the characteristics of the transmitting LEDs (negligible at the data rates and for LEDs used on the device). To make the system more robust against orientation changes different methods such as dual thresholding could allow the pulse width to be defined by a lower and upper bound, giving more control over what the size of the digitized pulse should be. With respect to noise interference the comparator hysteresis, which was not utilized, could provide further stability against fluctuations.

## 5.4 Alternative powering solutions

A large percentage of the device weight was due to the contributions from the power source, the LiPo battery. Using alternative powering solutions, smaller total weights may be achieved. For example methods such as inductive powering would not only allow devices to perpetually operate, given the right conditions, but could reduce the mass of the receiver as well. A currently available device on the market is the Ferro Solutions[10] inductive coupling system. It consists of a large base station incorporated into the base of a maze cage coupling into smaller 3D receiver coils, weighing 1g (Figure 5.8). This is a significant reduction in weight, given the currently implemented battery weight of 1.8g. Furthermore, this would allow the device to be used perpetually without the need for recharging, thus allowing long term experiments, such as the observation of sleep wake cycles to be carried out. The data sheet states that the base transmitter can provide 500mW (277mA @ 1.8V) power from 25.4 mm and 200mW (111mA @ 1.8V) from 76.2 mm. Since most of the components operate at 3V, step up transformer will be required. Assuming a transformer step up efficiency of 90% this would translate to 450 mW (136.36 mA @ 3.3V) at 25.4 mm and 180 mW (54.54 mA @3.3V) at 76.2 mm . Given that a typical

mouse is 7.5-10 cm in length, this would cover the maximum separation the receiver would be from the base transmitting coil in instances when a mouse may be standing on its hind legs. The default 3D coil has its wires rated for currents up to 17.5 mA in the X and Y directions, but only 13.7 mA in the Z direction. To allow the flow of higher currents of ~66.0-71.6 mA required, 3D coils with thicker wires will have to be used. A custom made 3-D printed frame may be created to accommodate the larger gauge wires. The load bearing capacity of wires of 0.018mm thickness is 72 mA [11], and more than capable of carrying the current required for the device. RF harvesting based methods generally offer low returns with respect to transmitter output and receiver antenna size[12], making them generally unsuitable for devices digitizing >10 channels. The omnidirectional propagated RF waves do not scale efficiently with distance, as the section that transects the receiving antenna is inversely proportional with square distance [13].

Other powering methods that may prove useful include novel approaches as those offered by Energous[14] and Ossia[15]. The redirective RF based methods employ a transmitting base consisting of thousands of miniature antennas that are tuned on the fly depending on the receiver position (Figure 5.9).

The main current sink in the current device is the amplifier IC. Decreasing this would yield significant reduction in total power consumption and allow smaller batteries to be used, which consequently reduce weight. Custom made low power chips have been made and demonstrated in numerous works [16]–[19]. These often use smaller transistor technology thus using lower voltages as well (1.8 vs 3.3V). The commercially available 16 channel TaiNi [20] device has roughly a quarter of the power consumption of the Intan chip as it operates at half the voltage and has half the current consumption.

Additionally, further reductions could be made by decreasing the ADC resolution to 12-bits from 16. Several groups have demonstrated that the reduced resolution is still sufficient enough to accurately reconstruct neural information[21]–[24] This would not

only decrease the power required for digitizing and multiplexing, but would also reduce the number of bits that need to be transmitted encoding the neural data by quarter.

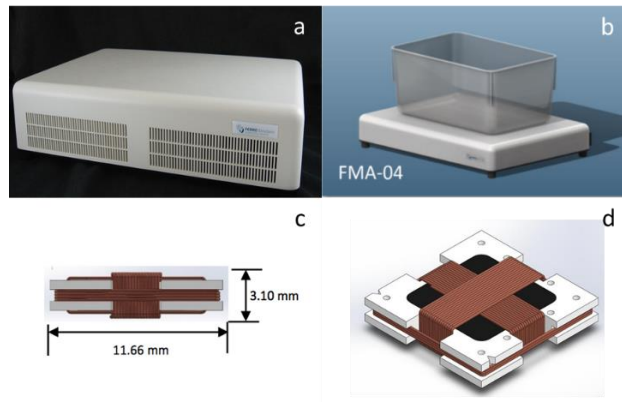


FIGURE 5.8: (a) The base station containing the large transmitting coil with dimensions  $298 \text{ mm} \times 381 \text{ mm} \times 64 \text{ mm}$  ( $L \times w \times h$ ). The provided power is  $500 \text{ mW}$  ( $277 \text{ mA} @ 1.8 \text{ V}$ ) from 1 inch and  $200 \text{ mW}$  ( $111 \text{ mA} @ 1.8 \text{ V}$ ) from 3 inches. (b) A standard plastic container that may be placed on top of the transmitter in which the animal may be contained. (c) The receiving 3D coil with a weight of  $1 \text{ g}$ . (d) Isometric view of the 3D coil. The wires in the  $x$  and  $y$  plane are rated up to  $17.5 \text{ mA}$  while in the  $z$  plane it is rated up till  $13.7 \text{ mA}$ . Using thicker wires could increase this.

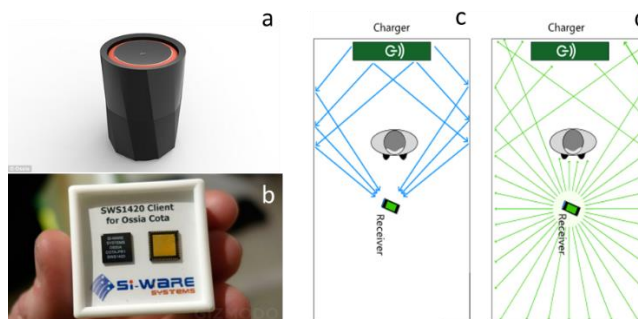


FIGURE 5.9: (a) A power transmitting antenna array designed by Ossia, using its COTA technology. The module contains thousands of miniature antennas that are tuned on the fly to transmit in the directions of the receiver. (b) The receiver ICs that are incorporated into wireless devices. They send a beacon signal at a hundred times a second to the transmitter based station containing the micro antennas. (c) Calculating the difference between the incoming beacon pulses received by the antennas allows the locations of the device to be determined and the coordinates to which the RF power should be sent. (d) The receiver transmits the beacon signal omnidirectionally, which can also bounce off surfaces and around obstacles.



## 5.5 Weight reduction

The current PCBs weigh 1.1g each or 2.2g in total, and so amount to ~43% of the total weight. By reducing this a significant decrease in weight can be achieved. Several PCB manufacturers offer thin PCB options which could be used to address the weight issue. Eurocircuits[25] offers rigid PCB thicknesses down to 200 microns, however, due to the manufacturing capabilities, keeping the four layer structure would limit the minimum thickness to 360 microns. Other manufacturers PW Circuits[26] offer flexible 4 layer PCBs down to 200 microns at an increased cost. The predicted total PCB weight using the thin type is estimated to be:

$$2.2 \times 0.2 / 1.55 = 0.28\text{g}$$

Or a reduction of ~1.92 grams. Another approach may involve increasing the number of layers in the PCB from 4 to 6. This could potentially allow both top and bottom PCBs to be incorporated into a single PCB. An additional 0.2 grams may be further reduced by removing the plastic cap from the LiPo battery, which is not necessary. Using bare dies and epoxy to protect the wirebonds, instead of QFN package would yield a further 0.15g decrease. Smaller LiPo batteries may also be implemented at the expense of reduced operational time. Zinc air batteries were also considered by stepping up their voltages (typically 1.35-1.4V) to the 3.3V required for the transmitting device. Due to their limited current supply capabilities at these potentials however, they were incapable of proving the required power levels. Additionally, an inductive 3D coil may also be implemented as outlined in section 5.4. With a weight of 1g this would cut the weight by a further 0.8g. Incorporating all these modifications could comfortably create a device adhering to the weight limitations, and results in a total weight of ~2.615g as shown in Table 5.2. Currently a large adapter combined with an A32 probe was used (~5g) for the head-fixed studies. For freely moving experiments the lighter 0.29g CM[26] series probe could be used instead (Figure 5.10).

TABLE 5.1  
DEFAULT WEIGHT CONFIGURATION

Battery Weight (g)	1.8 (50 mAh)
PCB Weight (g)	2.2
Probe PCB + Omnetics connector (g)	0.53
Other components (g)	0.805
Operating Hours (hrs)	4
Total Weight (g)	5.335

Table 5.1: The weight of the main components in the default configuration and the associated max operating time

TABLE 5.2  
THIN PCB NO BATTERY

Battery Weight (g)	1.6 (50 mAh)
PCB Weight (g)	0.511
Probe PCB + Omnetics connector (g)	0.53
Other components (g)	0.805
Operating Hours (hrs)	4
Total Weight (g)	3.446

Table 5.2: The weight of the main components using thin PCBs and the associated max operating time

TABLE 5.3  
FELXIBLE THIN PCB SMALLER BATTERY

Battery Weight (g)	1.2 (30 mAh)
PCB Weight (g)	0.28
Probe PCB + Omnetics connector (g)	0.53
Other components (g)	0.805
Operating Hours (hrs)	2.5
Total Weight (g)	2.815

Table 5.3: The weight of the main components using thin flexible PCBs, lower weight smaller capacity batteries, and the associated max operating time

TABLE 5.4  
FLEXIBLE THIN PCB 3D COIL

Battery Weight (g)	1
PCB Weight (g)	0.28
Probe PCB + Omnetics connector (g)	0.53
Other components (g)	0.805
Operating Hours (hrs)	Perpetual
Total Weight (g)	2.615

Table 5.4: The weight of the main components using thin flexible PCBs, and the inductively powered 3D coil provided by Ferro Solutions.

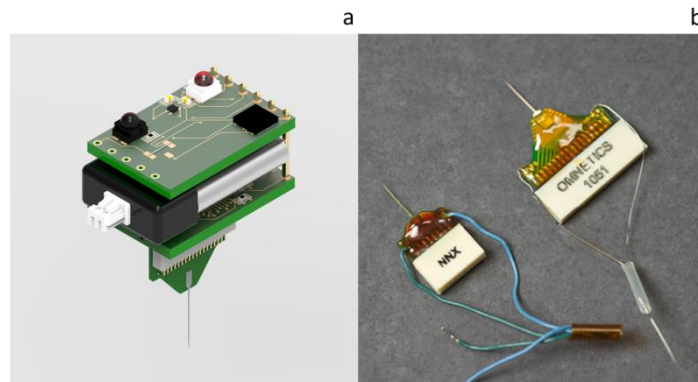


FIGURE 5.10: (a) Device interfacing with the Neuronexus CM32 probe (b) CM32 Neuronexus probe (top right)

## 5.6 Alternative LED solutions

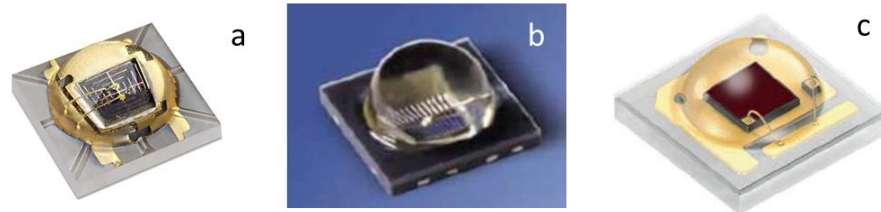


FIGURE 5.11: Three different LEDs proposed to replace the currently used ones. (a) Lumileds L110-0940150000000[27] (b) Lite-On LTE-R38386A-ZF-U[28] (c) Osram LH CPDP-3T4T-1-0-350-R18[29]

Other off the shelf LEDs with more desirable characteristics are also available, shown in Figure 5.11 and Appendix 5.1. While they might not have the concentrated radiant intensity of the LEDs used in the reported device, they have over double the viewing angle ( $90^\circ$ ) and faster rise (11 ns) and fall times (14 ns). The reduced intensity may be counter balanced by: larger more sensitive photodetector, using a higher number of detectors, or simply driving the LEDs at higher currents at the expense of reduced operating time. By replacing the limiting resistor and doubling the drive current from 2 mA to 4 mA, similar irradiances may be reached ( $\sim 1.4$  mW/sr) while maintaining the benefits with the Lumiled or Lite-On LEDs. The extra 4 mA power consumption would approximately reduce the operating time by an hour, leaving it at a total of  $\sim 3$  hours, still enough to acquire meaningful amounts of neural data.

Custom made LEDs could also open avenues for increased data rates. The devices presented in [4], [30] have reached speeds of 3 Gbit/s and 10 Gbit/s using gallium nitride (GaN) based LEDs. In both cases OFDM was implemented, which significantly increases the bandwidth compared to standard OOK implemented on the device. By breaking the transmitted signal into smaller sub-carrier frequencies, and sending them in parallel, higher data rates can be achieved. Setting the carrier spacing to be the same as the bit rate, reduces cross-talk between the bands, allowing many to be sent simultaneously [31]. Implementing this, however, would require additional circuitry and power consumption on the head stage. Often these high-speed LEDs are made at wavelengths that the mouse retina is sensitive to (eg. 470 nm, blue). In these cases colour conversion schemes would need to be implemented, such as quantum dots [32]. This comes at the expense of reduced efficiency but irradiance levels are still high enough to transmit >100 channels. Additionally, several light sources in parallel could be used to further increase data rates. Using WDM, multiple optical carrier signals could be sent with different wavelengths to increase data rates[33]–[35]. This would relax the maximum speed and timing requirement for a single source LED, as several slower streams could be used to transmit higher data rates concurrently. Implementing this would again require additional circuitry and power consumption, but could also significantly increase the bandwidth to >100 Gbit/s[36].

Lastly, Resonant cavity LEDs could also be an alternative, which can provide high data rates (250 Mbps)[37], at the desired wavelengths, while infrared based methods have also been demonstrated to reach 1 Gbit/s [38].

In section 3.3, the effect of light sources triggering visual stimulus in mice was introduced. Due to the structure of the device used *in vivo* (Chapter IV), the transmitting LEDs are directed upwards and away from the eye of the animal. Because of the large angle (>180°) between the eyes and the light sources (which are at wavelengths mice are not sensitive to >600 nm), the viewing angle of most commercially available LEDs (<180°) are too small to produce radiant intensities

large enough to stimulate the photoreceptors. Additionally, the PCB of the device acts as a barrier that blocks a significant amount of the light that may arrive from above. Placing a Thorlabs PM100A light power meter under the device where the head of the animal would normally be, produced readings too low for the instrument to detect. Unless significant reflection occurs from the environment, unintended visual stimulation should be negligible. The option also remains to use even longer wavelength LEDs to completely eradicate any possibility of behavioural effects they might have.

## 5.7 Manchester encoding

The clock and data signals are currently sent on separate streams to separate photodetectors. This results in double the amount of receiving circuitry and photodetectors needed for it to properly operate. Using Manchester encoding would allow the two data lines to be merged into one, thus significantly simplifying the setup. Manchester encoding works by combining the two data streams into one through an (exclusive or) XOR gate (table 5.5). Since the data line would essentially be self-clocking, both MISO and CS could be included in a single digital line. Alternatively SCLK could be included instead of CS to achieve more accurate clocking edges. The shortfall of transmitting CS is that a shift in it can cause an entire sample to be corrupted, as the 16 virtual SCLK edges are derived from it. By transmitting SCLK a single falling edge shift would only corrupt one bit in a sample, which is less likely to create a large error especially if it is towards the least significant bit side. The trade-off is, however, that faster LEDs and photodetectors are needed, since SCLK is twice as fast. Another potential approach would be to simply combine the two signals. This, however, could lead to difficulties from separating CS from a bit stream of similar length, and some sort of additional marker would have to be transmitted with well.

Data value	bit	Clock value	Manchester value
0		0	0
		1	1
1		0	1
		1	0

Table 5.5: Manchester values tabulated depending on the data input bit and clock values going through an XOR gate. The Manchester value can then be deconstructed to determine what the clock value and data bit value was at a given point in time.

Using the values originally shown for the sample in the diagram in Chapter III, Figure 3.15 we would get the output shown in Figure 5.12 if CS is incorporated or Figure 5.13 if SCLK is used.

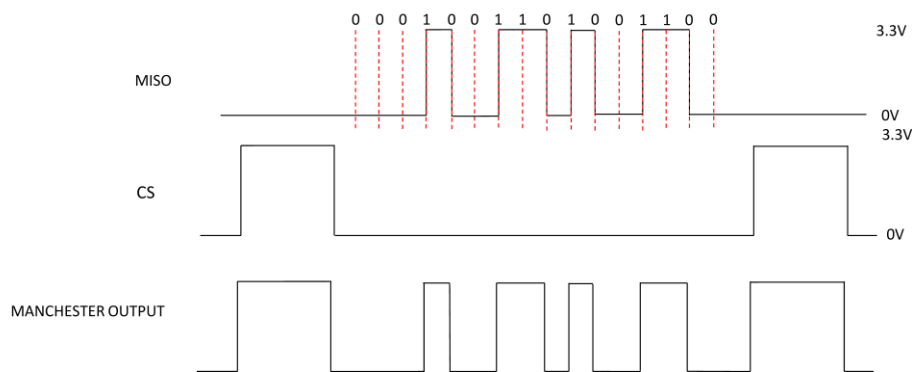


FIGURE 5.12: Combining the CS clock and neural data stream, a digital line incorporating both is created. Separating them on the receiving end would then allow data processing to be carried out the same way as demonstrated before.

## 5.8 Further data encoding techniques

The device uses the simplest form of optical communication, OOK. In section 2.7 and 3.7 alternative encoding techniques that could potentially increase efficiency were briefly mentioned as a substitute, which will be expanded in this section. Methods such as PAM[39], [40] operate by encoding the information into the amplitude size of transmitted uniform pulses, where different levels can correspond to different values.

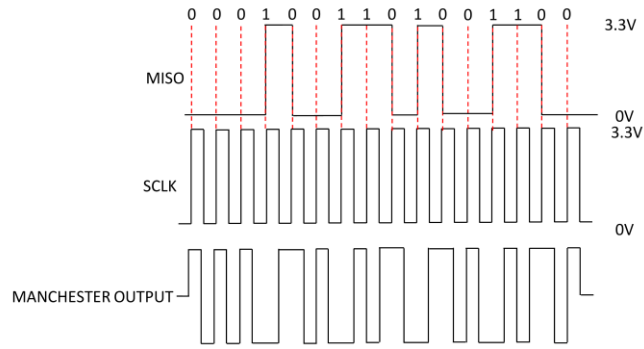


FIGURE 5.13: Combining the neural bit stream with SCLK instead of CS would allow more precise transmissions with reduced errors. This would however come at the price of twice the required bandwidth.

The key advantage is the increase in spectral efficiency, however trade-offs include this approach more sensitivity to noise, and lower power efficiency compared to other modulations techniques. Pulse-Position Modulation (PPM)[41], [42] involves short pulses of equal length and amplitude that define bit values based on the time shift between them. These characteristics translate to minimal noise interference, allowing more effective separation of noise from signal. It is also more power efficient than other techniques such as PAM, but involves increased system complexity and higher bandwidth requirements to be efficiently implemented.

Lastly, FEC could be used to reduce the number errors by including on overhead of extra bits that are cross checked on the receiver end. An additional 7% of the total data transmitted is enough to reach 0 errors with a typical BER of  $2 \times 10^{-3}$ [30].

To summarize, a number of different modulations techniques exist that could be explored to replace the currently employed mode of transmission. The exact trade-off between power requirement, data rate, complexity is yet to be determined and is something that will have to be investigated in more detail, to verify the suitability of other techniques as a replacement for the current method.

## 5.9 Multiple chip systems

To scale up to higher channel counts more amplifier chips will be required to process the increased number of inputs. A straightforward approach would be to simply multiply the number of amplifier chips proportionally with the electrode sites desired to be observed. For example, a 256-channel system could be created by multiplexing four of the highest channel count (64 channel) Intan chips [35]. While using several of these chips may be applicable for reduced scaling, it becomes quickly impractical for larger channel counts. The increased footprint to record a thousand channels (~15 chips) would be too big, while also imposing large power requirements. Probes have been developed that incorporate the CMOS circuitry required for multiplexing and digitization [5], [7], [43]. Using these devices, scaling up to thousands of channels is possible while maintaining the small form factor. Combining with the VLC based data transmission that has been demonstrated in the earlier chapters, low weight wireless head stages capable of transmitting >1000 channels may be created.

While it is generally desirable to transmit all the neural information, sometimes it is acceptable to only observe spiking activity while ignoring LFPs. Devices incorporating FPGAs that employ spike sorting algorithms have been created that detect the action potentials while ignoring other information. Using this type of approach reduces the bandwidth requirement, at the expense of lossy compression. As demonstrated by Turcotte[2], using a 1 Mbps RF transmission protocol, 32 channels worth of compressed data was relayed. Applying the same technique to the developed VLC based device may make it possible to send ~320 channels worth of data across its optical link. This would of course come at the expense of increased power consumption required for the FPGA.



## 5.10 Bidirectional probes and stimulating

Incorporating two-way optogenetic probes [44] would allow large scale neural data transmission to be combined with the precision of light-based stimulation. However, this comes at the cost of additional circuitry to activate the LEDs on the probe, increasing the total weight and size of the device. Commercially available stimulating ASICs are already available from Intan technologies[45], capable of stimulating up to 16 sources. The increased complexity of such a system mainly arises from the additional power required for the extra ASIC, and increased voltage requirements for the stimulating circuitry. The extra voltage is needed to turn on the blue LEDs, which typically need 5V at least to produce the required output required to activate optogenetically transfected neurons.

## 5.11 Auxiliary improvements

As long as the amplifier chip is connected to a power source, it draws current, even when it is not running. Additionally, the IR detector also needs a small amount of base current to continuously monitor the potential incoming IR commands. While putting the system to sleep mode does reduce the power consumption, it still draws a significant amount. Currently the only way to fully reduce power consumption is to physically disconnect the battery by uncoupling the connector. This is inconvenient, and may cause disruptions during longer experiments. One potential solution might entail using a latching reed switch on the power line. The switch could be controlled by placing a magnetic wand into close proximity to cycle its state. Another approach may involve using a latching Hall-Effect switch, which can similarly be controlled by magnetic fields[46].

The amplifier and comparator were also on different boards, essentially creating 4 units that need to be connected. Once a circuitry has been finalized that is more robust with respect to transmitter displacements, all the components should be incorporated onto a single board.

The code the MCU is flashed with could also be improved. Currently once the device is powered it starts sampling at 20 kS/s with no option to change it. Incorporating a protocol where depending on the IR command received the MCU clock reconfigures itself to accommodate a different sampling rate, would allow users to optimize the device for lower frequency signals (EEG, EMG).

## 5.12 Transfer printing

Transfer printing has allowed micro scale LEDs to be placed on a wide range of substrates, by exploiting the Van Der Waals forces dominating at such small scales[47]. This allows miniature light sources to be placed at virtually any coordinate as long as the appropriate footprint for the LED is provided on the base material. An outline of the technique is shown in Figure 5.14. LEDs capable of fast data rates have been produced using such methods and are demonstrated [47]. This could enable the device to be further miniaturized, and also improve the data rates over the currently used off the shelf LEDs. By using amplifier bare dies, micro LEDs could be directly placed on the chip enabling a very high data rate, compact system.

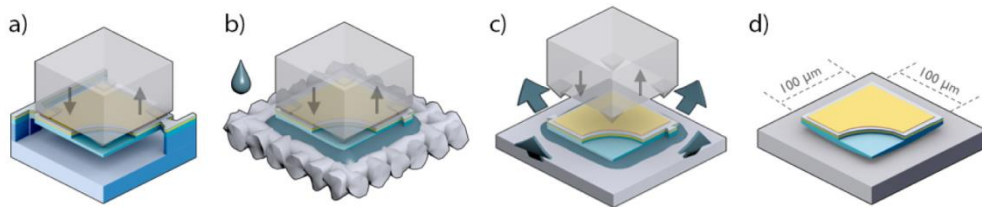


FIGURE 5.14: The process required to transfer print LEDs. Image from[47]. (a) An LED is fabricated, which is then selectively under etched using a strong alkaline solution such as potassium hydroxide KOH, leaving it to be suspended by anchors that do not react with the chemicals used. An elastomeric stamp is then used to apply pressure and break the LED from the anchors, and to pick it up. (c) The LED adheres to the stamp and is removed from fabrication substrate. (d) The LED is then placed on the desired surface, i.e. the surface of a bare die amplifier chip. It stays in position due to Van der Waals forces present in the liquid as it is transferred and placed with. If stronger adhesion is required other types of bonding chemicals may be used. Once in position a combination of wire bonding, and predeposited conductive tracks connect the LED to the desired output pads of the IC.

## 5.12 Concluding remarks

The transmission of large scale neural information from freely moving animals remains one of the central challenges of neuroscience. A device was presented in the thesis that may be used as a platform to scale up to a large number of channels, while maintaining a low weight. By implementing visible light communication to relay the recorded neural information, data rates far surpassing current RF solutions should be feasible. A number of simple improvements such as using thinner PCBs and lower weight batteries could allow the device to exceed the weight/data rate performance in other wireless neural recording devices available. Some refinements still have to be made however before the system can be used with freely moving animals. A photodetector system covering a typical observation area is outlined.

## References

- [1] Triangle Biosystems International, “TBSI W16 System Manual,” datasheet, July. 2015.
- [2] G. Gagnon-Turcotte, Y. LeChasseur, C. Bories, Y. Messaddeq, Y. De Koninck, and B. Gosselin, “A Wireless Headstage for Combined Optogenetics and Multichannel Electrophysiological Recording,” *IEEE Trans. Biomed. Circuits Syst.*, pp. 1–14, 2016.
- [3] R. X. G. Ferreira *et al.*, “High bandwidth GaN-based micro-LEDs for multi-Gbps visible light communications,” *IEEE Photonics Technol. Lett.*, vol. 28, no. 19, pp. 2023–2026, 2016.
- [4] M. S. Islim *et al.*, “Towards 10 Gb/s orthogonal frequency division multiplexing-based visible light communication using a GaN violet micro-LED,” *Photonics Res.*, vol. 5, no. 2, p. A35, 2017.

- [5] B. C. Raducanu *et al.*, “Time multiplexed active neural probe with 678 parallel recording sites,” *Eur. Solid-State Device Res. Conf.*, vol. 2016-October, pp. 385–388, 2016.
- [6] C. M. Lopez *et al.*, “22.7 A 966-electrode neural probe with 384 configurable channels in 0.13 $\mu$ m SOI CMOS,” *Dig. Tech. Pap. - IEEE Int. Solid-State Circuits Conf.*, vol. 59, pp. 392–393, 2016.
- [7] C. M. Lopez *et al.*, “An implantable 455-active-electrode 52-channel CMOS neural probe,” *IEEE J. Solid-State Circuits*, vol. 49, no. 1, pp. 248–261, 2014.
- [8] C. Mora Lopez *et al.*, “A Neural Probe With Up to 966 Electrodes and Up to 384 Configurable Channels in 0.13  $\mu$ m SOI CMOS,” *IEEE Trans. Biomed. Circuits Syst.*, no. April, 2017.
- [9] J. Garcia-Marquez, J. C. Valencia, H. Perez, and S. Topsu, “Catadioptric lenses in visible light communications,” *J. Phys. Conf. Ser.*, vol. 605, no. 1, 2015.
- [10] “Ferro Solutions Transmitter Manual.” [Online]. Available: [http://www.ferrosi.com/pdf/FS\\_WPT-05\\_data\\_sheet.pdf](http://www.ferrosi.com/pdf/FS_WPT-05_data_sheet.pdf). [Accessed: 01-Jun-2017].
- [11] “American Wire Gauge Chart and AWG Electrical Current Load Limits table with skin depth frequencies and wire breaking strength.” [Online]. Available: [https://www.powerstream.com/Wire\\_Size.htm](https://www.powerstream.com/Wire_Size.htm). [Accessed: 03-Apr-2018].
- [12] S. Mattigiri and C. Warty, “A study of fundamental limitations of small antennas: MIMO approach,” *IEEE Aerosp. Conf. Proc.*, 2013.
- [13] C. R. Paul, “The Remarkable Inverse Distance-Squared Law,” *IEEE Newsletter*, pp. 65–68, 2011.
- [14] “Energous – WattUp® Wire-Free Charging Technology.” [Online]. Available: <http://energous.com/>. [Accessed: 03-Apr-2018].

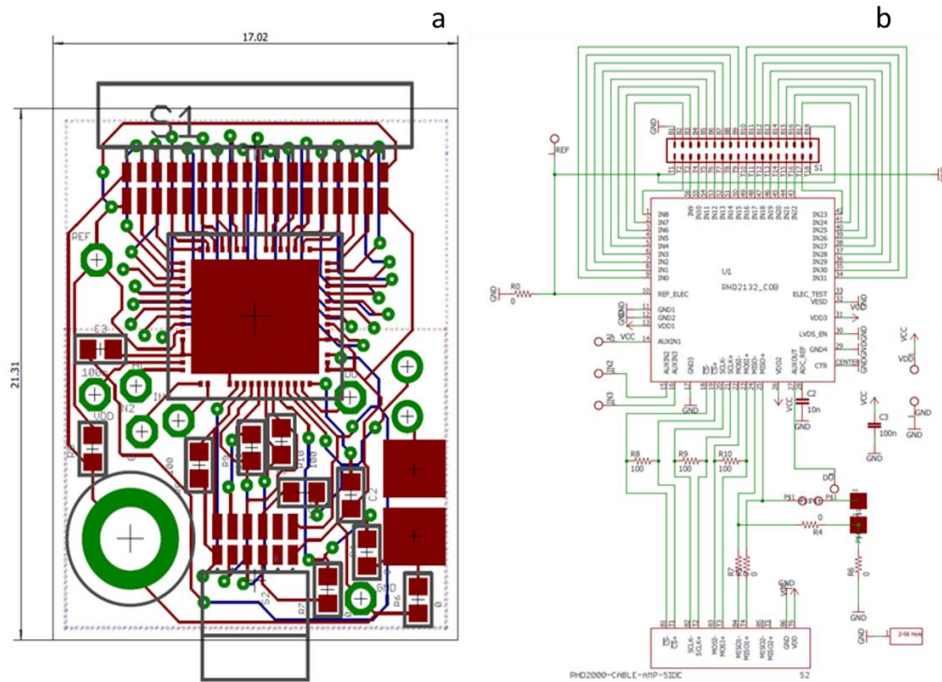
- [15] “Cota: Real Wireless Power.” [Online]. Available: <http://www.ossia.com/cota/>. [Accessed: 03-Apr-2018].
- [16] A. De Marcellis, E. Palange, M. Faccio, G. Di, P. Stanchieri, and T. G. Constandinou, “A 250Mbps 24pJ / bit UWB-inspired Optical Communication System for Bioimplants.”
- [17] R. M. Walker *et al.*, “A 96-channel full data rate direct neural interface in 0.13 $\mu$ m CMOS,” *VLSI Circuits (VLSIC), 2011 Symp.*, vol. 4, no. 3, pp. 144–145, 2011.
- [18] M. Chae, Z. Yang, M. R. Yuce, L. Hoang, and W. Liu, “A {128-Channel} 6 {mW} Wireless Neural Recording {IC} With Spike Feature Extraction and {UWB} Transmitter,” vol. 17, no. 4, pp. 312–321, 2009.
- [19] M. Ballini *et al.*, “A 1024-Channel CMOS Microelectrode Array With 26 , 400 Electrodes for Recording and Stimulation of Electrogenic Cells In Vitro,” vol. 49, no. 11, pp. 2705–2719, 2014.
- [20] Z. Jiang *et al.*, “TaiNi: Maximizing research output whilst improving animals ’ welfare in neurophysiology experiments,” pp. 1–12, 2017.
- [21] Y.-K. Song *et al.*, “Active microelectronic neurosensor arrays for implantable brain communication interfaces.,” *IEEE Trans. Neural Syst. Rehabil. Eng.*, vol. 17, no. 4, pp. 339–45, 2009.
- [22] H. Ando, K. Takizawa, T. Yoshida, K. Matsushita, M. Hirata, and T. Suzuki, “Wireless Multichannel Neural Recording With a 128-Mbps UWB Transmitter for an Implantable Brain-Machine Interfaces,” *IEEE Trans. Biomed. Circuits Syst.*, pp. 4097–4100, 2016.
- [23] K. Abdelhalim, L. Kokarovtseva, J. L. Perez Velazquez, and R. Genov, “915-MHz FSK/OOK wireless neural recording soc with 64 mixed-signal fir filters,” *IEEE J. Solid-State Circuits*, vol. 48, no. 10, pp. 2478–2493, 2013.

- [24] D. A. Schwarz *et al.*, “Chronic, wireless recordings of large-scale brain activity in freely moving rhesus monkeys,” *Nat. Methods*, vol. 11, no. 6, pp. 670–676, 2014.
- [25] “Eurocircuits – Online PCB Prototype and small series specialist.” [Online]. Available: <https://www.eurocircuits.com/>. [Accessed: 03-Apr-2018].
- [26] “P.W. Circuits Ltd.” [Online]. Available: <http://www.pwcircuits.co.uk/>. [Accessed: 03-Apr-2018].
- [27] Lumileds, “LUXEON IR Domed Line,” L1I0-0940150000000 datasheet, 2018.
- [28] Lite-On, “IR Emitter and Detector," LTE-R38386A-ZF-U datasheet.
- [29] Osram, “OSLON SSL 150," LH CPDP-3T4T-1-0-350-R18 datasheet, Jan. 2015.
- [30] D. Tsonev *et al.*, “A 3-Gb / s Single-LED OFDM-Based Wireless VLC Link Using a Gallium Nitride  $\mu$  LED,” vol. 26, no. 7, pp. 637–640, 2014.
- [31] S. B. Weinstein, “The history of orthogonal frequency-division multiplexing,” *IEEE Commun. Mag.*, vol. 47, no. 11, pp. 26–35, 2009.
- [32] K. Rae *et al.*, “InGaN micro-LEDs integrated onto an ultra-thin , colloidal quantum dot functionalized glass platform,” *Opt. Express*, vol. 25, no. 16, pp. 19179–19184, 2017.
- [33] L. Cui, Y. Tang, H. Jia, J. Luo, and B. Gnade, “Analysis of the Multichannel WDM-VLC Communication System,” *J. Light. Technol.*, vol. 34, no. 24, pp. 5627–5634, 2016.
- [34] Y. Wang, X. Huang, L. Tao, J. Shi, and N. Chi, “4.5-Gb/s RGB-LED based WDM visible light communication system employing CAP modulation and RLS based adaptive equalization,” *Opt. Express*, vol. 23, no. 10, p. 13626, 2015.
- [35] S. Rajbhandari *et al.*, “A review of gallium nitride LEDs for multi-gigabit-per-second visible light data communications,” *Semicond. Sci. Technol.*, vol. 32, no. 2, p. 023001, 2017.

- [36] D. Tsonev, S. Videv, and H. Haas, "Towards a 100 Gb/s visible light wireless access network," *Opt. Express*, vol. 23, no. 2, p. 1627, 2015.
- [37] Firecomms, "250 Mbps Fiber Optic LC Transceiver" FB2M5LVR datasheet, Rev. E.
- [38] "Wireless data at top speed - Research News October 2012 - Topic 3." [Online]. Available: <https://www.fraunhofer.de/en/press/research-news/2012/october/wireless-data-at-top-speed.html>. [Accessed: 03-Apr-2018].
- [39] N. Chi, M. Zhang, J. Shi, and Y. Zhao, "Spectrally efficient multi-band visible light communication system based on Nyquist PAM-8 modulation," *Photonics Res.*, vol. 5, no. 6, pp. 588–597, 2017.
- [40] X. Li *et al.*, "Wireless visible light communications employing feed-forward pre-equalization and PAM-4 modulation," *J. Light. Technol.*, vol. 34, no. 8, pp. 2049–2055, 2016.
- [41] J. H. Yoo and S. Y. Jung, "Multi-coded variable PPM with level cutting for high data rate visible light communications," *APCC 2012 - 18th Asia-Pacific Conf. Commun. "Green Smart Commun. IT Innov.*, vol. 16, no. 2, pp. 703–708, 2012.
- [42] M. Biagi and A. M. Vegni, "Enabling high data rate VLC via MIMO-LEDs PPM," *2013 IEEE Globecom Work. GC Wkshps 2013*, no. 1, pp. 1058–1063, 2013.
- [43] C. M. Lopez *et al.*, "A Neural Probe With Up to 966 Electrodes and Up to 384 Configurable Channels in 0.13  $\mu$  m SOI CMOS," vol. 11, no. 3, pp. 510–522, 2017.
- [44] F. Wu, E. Stark, and P. Ku, "Monolithically Integrated m LEDs on Silicon Neural Probes for High-Resolution Optogenetic Studies in NeuroResource Monolithically Integrated m LEDs on Silicon Neural Probes for High-Resolution Optogenetic Studies in Behaving Animals," pp. 1–13, 2015.

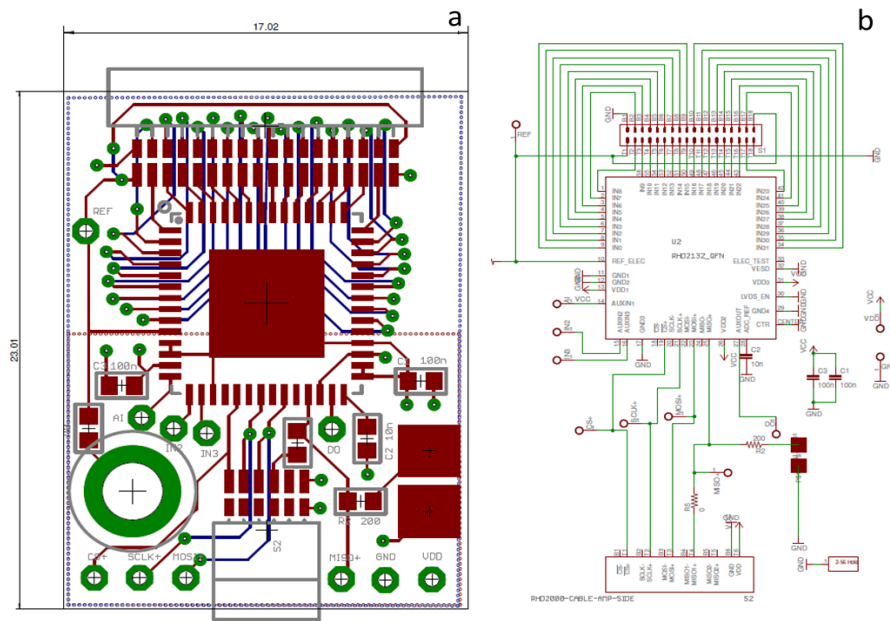
- [45] Intan Technologies, “Digital Electrophysiology Stimulator/Amplifier Chip,” RHS2116 datasheet, Jan. 2016. [Revised March. 2017].
- [46] “Allegro Microsystems - A3211 and A3212: Micropower, Ultrasensitive Hall-Effect Switches.” [Online]. Available: <https://www.allegromicro.com/en/Products/Magnetic-Digital-Position-Sensor-ICs/Micropower-Switches-Latches/A3211-2.aspx>. [Accessed: 03-Apr-2018].
- [47] A. J. Trindade *et al.*, “Heterogeneous integration of gallium nitride light-emitting diodes on diamond and silica by transfer printing,” *Opt. Express*, vol. 23, no. 7, pp. 9329–9338, 2015.

## Appendix – Chapter III

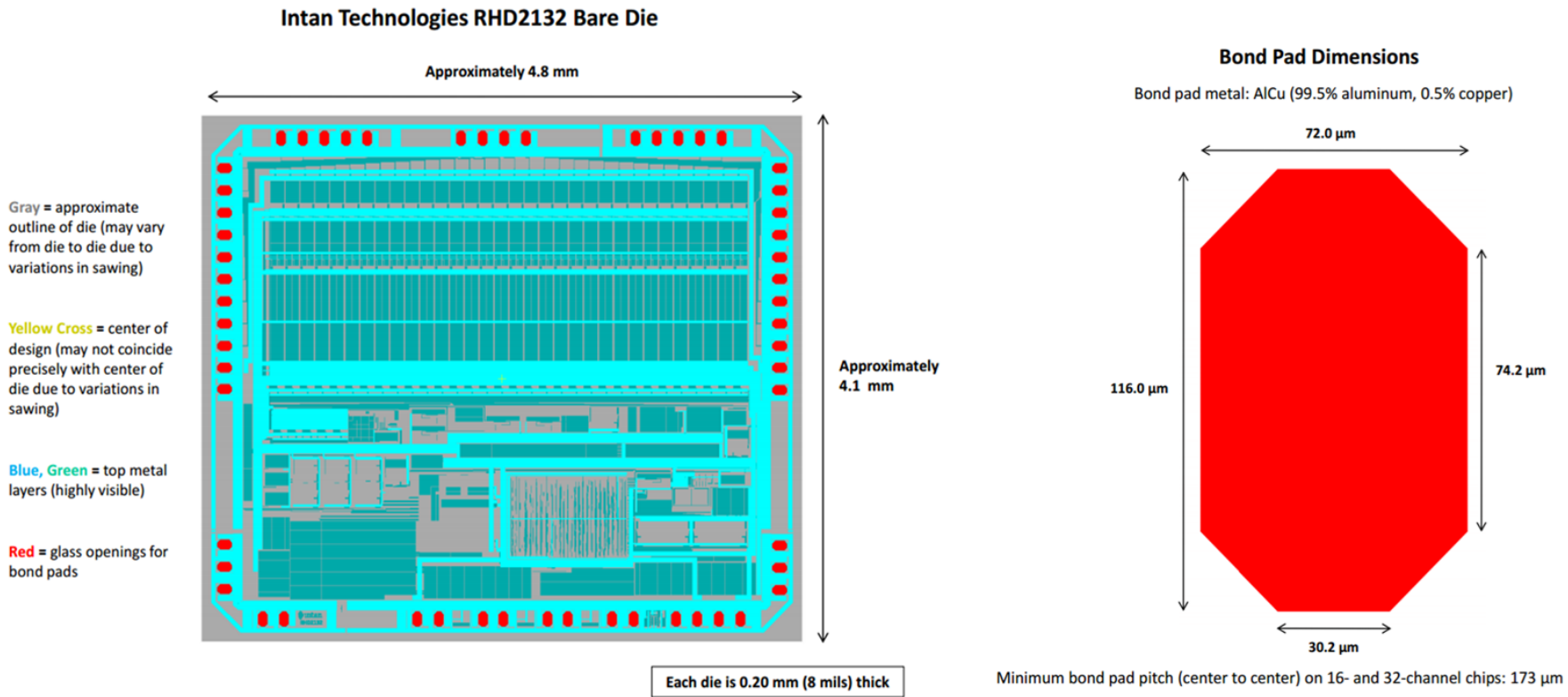


APPENDIX 3.1: (a) Board layout of the first version of the neural VLC board with a bare die chip (b) Schematic of the same board

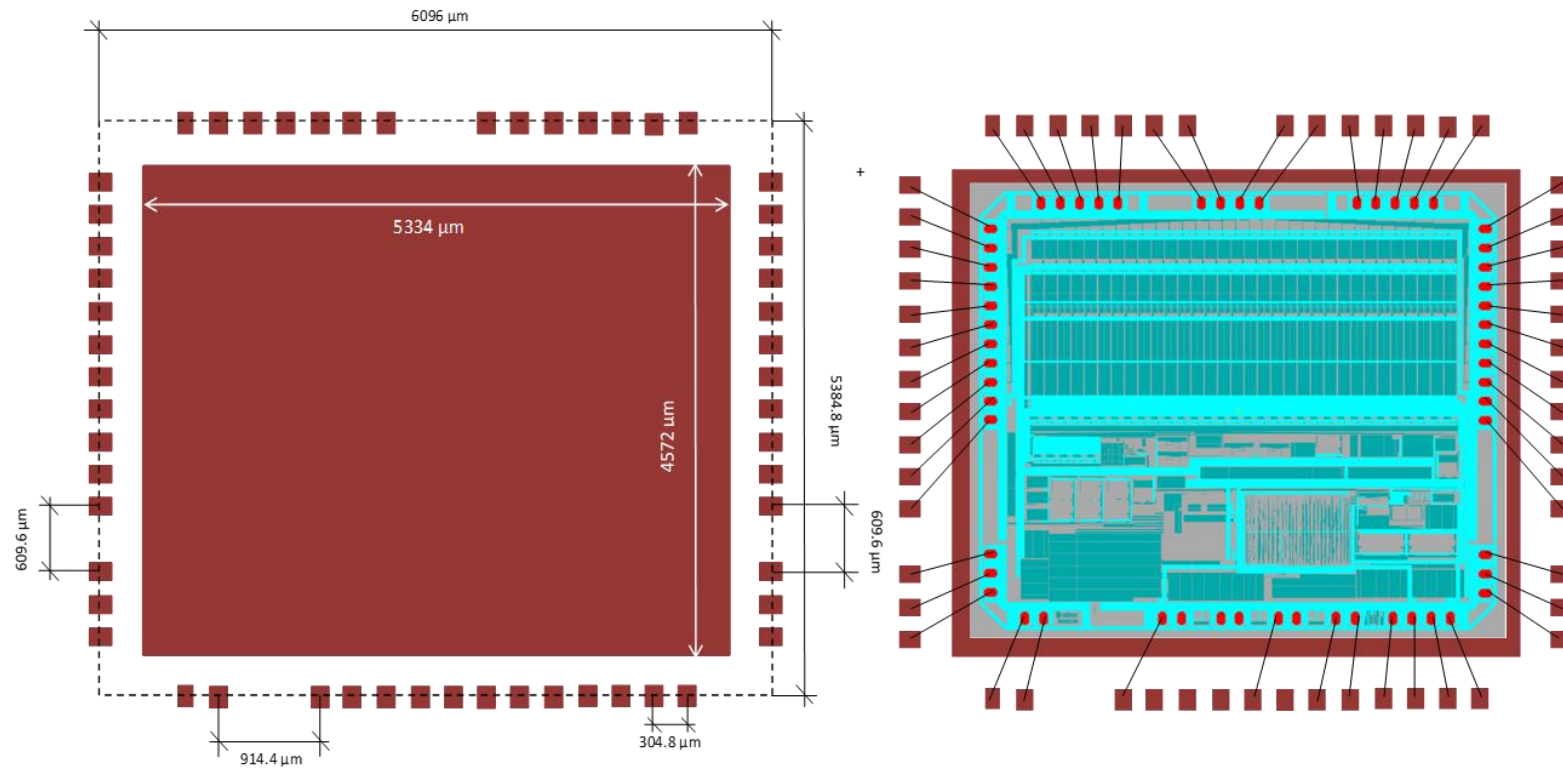




APPENDIX 3.2: (a) Board layout of the second version of the neural VLC board with QFN package, connectors are epoxied to make the device more robust, and test points are introduced to access the digital lines (b) Schematic of the same board



APPENDIX 3.3: (a) Intan RHD2132 bare chip dimensions, and pad layout (b) Pad dimensions and pad material description. Image from Intan manual[16]



APPENDIX 3.4: (a) PCB chip ground pad to which the bare chip was glued. The surrounding small pads are for the wire bonds coming from the chip and are covered in nickel gold (b) Chip to PCB wire bond map. The black lines indicate which pad of the chip was wire-bonded to which pad of the PCB

## Appendix 3.5 Jonathan J.D. McKendry's – BER Matlab Script

```

%%% Intan BER analysis 1.0
%-----
% This script uses the SCLK signal from the Intan chip as a
reference clock
% for sampling the MISO electrical and optical signals (nominally on
the
% rising edge of SCLK). The calculated BER, number of errors and
processed
% signals may be saved to a text file once complete.

%%%%%%%%%%%%%%%%%%%%%%%%%%%%%%%%%%%%%%%%%%%%%%%%%%%%%%%%%%%%%%%%%%%%%%%%
% 1) Process the SCLK signal
%%%%%%%%%%%%%%%%%%%%%%%%%%%%%%%%%%%%%%%%%%%%%%%%%%%%%%%%%%%%%%%%%%%%%%%%

%%% Threshold SCLK signal %%%

SCLK_prompt = 'Please enter a value for the SCLK threshold voltage:
';
th_SCLK = input(SCLK_prompt);

SCLK_thresh = SCLK; %SCLK_thresh is the thresholded SCLK signal
SCLK_thresh(SCLK_thresh<th_SCLK) = 0; % Set all values below thresh
to 0
SCLK_thresh(SCLK_thresh>th_SCLK) = 1; % Set all values above thresh
to 1
SCLK_thresh(SCLK_thresh==th_SCLK) = 1; % Set all values equal to
thresh to 1

%%% Find the SCLK rising edges %%%

dSCLK = gradient(SCLK_thresh, mean(diff(t))); % Take derivative of
SCLK_th w.r.t time
[dypks,sample_times] = findpeaks(dSCLK); % Find the derivative peaks
(rising edges)

%%% Analyse SCLK %%%

Intan_fs = roundn(length(sample_times) / (16*35*(max(t)-min(t))),3);
% Intan sampling rate (Hz)
scope_ps = (max(t)-min(t)) / length(t); % Oscilloscope sampling
period (s)
nsamp = round((t(sample_times(2,:)) - t(sample_times(1,:))) /
scope_ps); % Approx # samples per bit

%%% If there is an incompletely-sampled bit at the end of MISO_Rx,
%%% truncate it (remove it).

if (length(t) - sample_times(end)) < nsamp
    sample_times = sample_times(1:end-1);
end

%%% Display information to the user %%%
disp(' ');
disp('The estimated Intan sampling rate (S/s) is ');

```

```

disp(Intan_fs);
disp('The estimated total number of bits is ');
disp(length(sample_times));
disp('The estimated number of samples per bit is ');
disp(nsamp);

%%%%%%%%%%%%%%%%%%%%%%%%%%%%%%%%%%%%%%%%%%%%%%%%%%%%%%%%%%%%%%%%%%%%%%%%
% 2) Process the electrical MISO signal
%%%%%%%%%%%%%%%%%%%%%%%%%%%%%%%%%%%%%%%%%%%%%%%%%%%%%%%%%%%%%%%%%%%%%%%%

%% Threshold the electrical MISO signal %%

MISO_elec_prompt = 'Please enter a value for the electrical MISO
signal threshold voltage: ';
th_MISO_elec = input(MISO_elec_prompt);

MISO_elec_thresh = MISO; %SCLK_thresh is the thresholded SCLK signal
MISO_elec_thresh(MISO_elec_thresh<th_MISO_elec) = 0; % Set all
values below thresh to 0
MISO_elec_thresh(MISO_elec_thresh>th_MISO_elec) = 1; % Set all
values above thresh to 1
MISO_elec_thresh(MISO_elec_thresh==th_MISO_elec) = 1; % Set all
values equal to thresh to 1

%% Sample the thresholded MISO signal %%

MISO_elec_sample_offset_prompt = 'Please enter an offset for the
electrical MISO sampling (# of samples): ';
elec_sample_offset = input(MISO_elec_sample_offset_prompt);

OOK = MISO_elec_thresh(sample_times+elec_sample_offset); % The input
data to the LED

%%%%%%%%%%%%%%%%%%%%%%%%%%%%%%%%%%%%%%%%%%%%%%%%%%%%%%%%%%%%%%%%%%%%%%%%
% 3) Process the electrical MISO signal
%%%%%%%%%%%%%%%%%%%%%%%%%%%%%%%%%%%%%%%%%%%%%%%%%%%%%%%%%%%%%%%%%%%%%%%%

%% Theshold the optical MISO signal %%
%-----%
MISO_opt_prompt = 'Please enter an estimated value for the optical
MISO signal threshold voltage: ';
x0(1,1) = input(MISO_opt_prompt);

%% Sample the thresholded MISO optical signal %%
%-----%
MISO_Rx_sample_offset_prompt = 'Please enter an estimated offset for
the optical MISO sampling (# of samples): ';
x0(1,2) = input(MISO_Rx_sample_offset_prompt);

%%%%%%%%%%%%%%%%%%%%%%%%%%%%%%%%%%%%%%%%%%%%%%%%%%%%%%%%%%%%%%%%%%%%%%%%
% 4) Estimate the BER and optimum parameters
%%%%%%%%%%%%%%%%%%%%%%%%%%%%%%%%%%%%%%%%%%%%%%%%%%%%%%%%%%%%%%%%%%%%%%%%

options = optimset('Display','final','TolFun',1e-6,'TolX',1e-6);

```

```

output = fminsearchbnd(@(prms) BER_optimise(prms(1), prms(2)),x0,[-
inf 0],[+inf nsamp-1],options);

BER = horzcat('Bit-error-ratio is ',num2str(ber));
NERR = horzcat('Total number of errors is ',num2str(nerr));
disp(' ');
disp('=====');
disp('***BER results***');
disp('=====');
disp(BER);
disp(NERR);
disp(' ');
params = horzcat('Using a MISO threshold value of
',num2str(output(1,1)), ' and a MISO sampling offset of
',num2str(round(output(1,2))));
disp(params);
disp('=====');
disp(' ');

```

## Appendix – Chapter IV

### Appendix 4.1 MCU code

```

/* Includes -----
-----*/
#include "main.h"

/* USER CODE BEGIN Includes */

/* USER CODE END Includes */

/* Private variables -----
-----*/

/* USER CODE BEGIN PV */
/* Private variables -----
-----*/

/* USER CODE END PV */

/* Private function prototypes -----
-----*/
static void LL_Init(void);
void SystemClock_Config(void);
static void MX_GPIO_Init(void);
static void MX_DMA_Init(void);
static void MX_SPI1_Init(void);
static void MX_TIM2_Init(void);
static void MX_TIM2_Init2(void);

/* USER CODE BEGIN PFP */

```

```

/* Private function prototypes -----
-----*/

/* USER CODE END PFP */

/* USER CODE BEGIN 0 */
uint8_t dataTx4 [] = {0,0,0,1,0,2,0,3,0,4,0,5,0,6,0,7,0,8,
0,9,0,10,0,11,0,12,0,13,0,14,0,15,
0,16,0,17,0,18,0,19,0,20,0,21,0,22,0,
23,0,24,0,25,0,26,0,27,0,28,0,29,0,
30,0,31,0,255,0,255,0,255};

uint8_t dataTx8 [] =
{0x00,0x00,0x00,0x00,0x00,0x00,0x00,0x00,0x00,0x00,0xFC,0x00,0xFF,0xDE,0x
80,0x42,0x81,0x04,0x82,0x00,0x83,
0x9C,0x84,0x40,0x85,0x00,0x86,0x00,0x87,0x11,0x88,0x80,0x89,
0x10,0x8A,0x80,0x8B,0x22,0x8C,0x80,0x8D,0xFF,0x8E,0xFF,0x8F,
0xFF,0x90,0xFF,0x91,0,0,0,0,0,0,0,0,0,0,0,0,0,0,0,0,0x00,0x55,
0x00,0xFF,0x00,0xFF,0x00,0xFF,0x00,0xFF,0x00,0xFF,0x00,0xFF,0x00,0xFF,
0x00,0xFF,0x00,0xFF,0x00,0xFF};

uint8_t dataTx9 [] = {0,28};

//Send 2 dummy commands

//          1111110000000000 (0xFC, 0x00)
//          1111111000000000 (0xFF, 0x00)

//Setup Registers

//Register 0          100000011011110 (0x80, 0xDE)
//Register 1          100000101000010 (0x81, 0x42)
//Register 2          1000001000000100 (0x82, 0x04)
//Register 3          1000001100000000 (0x83, 0x00)
//Register 4          1000010010011100 (0x84, 0x9C)
//Register 5          1000010101000000 (0x85, 0x40)
//Register 6          1000011000000000 (0x86, 0x00)
//Register 7          1000011100000000 (0x87, 0x00)
//Register 8          1000100000010001 (0x88, 0x11)
//Register 9          1000100110000000 (0x89, 0x80)
//Register 10         1000101000010000 (0x8A, 0x10)
//Register 11         1000101110000000 (0x8B, 0x80)
//Register 12         1000110000101100 (0x8C, 0x2C) 1 Hz,
1000110000100010 (0x8C, 0x22) 50 Hz, 1000110000001111 (0x8C, 0x0F)
300 Hz
//Register 13         1000110110000110 (0x8D, 0x86) 1 Hz,
1000110110000000 (0x8D, 0x80) 50 Hz, 1000110110000000 (0x8D, 0x80)
300 Hz
//Register 14         1000111011111111 (0x8E, 0xFF)
//Register 15         1000111111111111 (0x8F, 0xFF)
//Register 16         1001000011111111 (0x90, 0xFF)
//Register 17         1001000111111111 (0x91, 0xFF)

```





```
/* USER CODE END SysInit */

/* Initialize all configured peripherals */
MX_GPIO_Init();
MX_DMA_Init();
MX_SPI1_Init();
MX_TIM2_Init();

/* USER CODE BEGIN 2 */
LL_mDelay(8);
LL_TIM_CC_EnableChannel(TIM2, LL_TIM_CHANNEL_CH1);
LL_TIM_EnableDMAReq_UPDATE(TIM2);
LL_TIM_EnableAllOutputs(TIM2);
LL_TIM_EnableCounter(TIM2);
LL_TIM_GenerateEvent_UPDATE(TIM2);
LL_SPI_Enable(SPI1);
LL_DMA_EnableChannel(DMA1, LL_DMA_CHANNEL_2);

LL_mDelay(1);

LL_DMA_DisableChannel(DMA1, LL_DMA_CHANNEL_2);

MX_TIM2_Init2();
LL_TIM_CC_EnableChannel(TIM2, LL_TIM_CHANNEL_CH1);
LL_TIM_EnableDMAReq_UPDATE(TIM2);
LL_TIM_EnableAllOutputs(TIM2);
LL_TIM_EnableCounter(TIM2);
LL_TIM_GenerateEvent_UPDATE(TIM2);
LL_SPI_Enable(SPI1);
LL_DMA_EnableChannel(DMA1, LL_DMA_CHANNEL_2);

/* USER CODE END 2 */

/* Infinite loop */
/* USER CODE BEGIN WHILE */
while (1)
{
/* USER CODE END WHILE */

/* USER CODE BEGIN 3 */

}
/* USER CODE END 3 */

}

static void LL_Init(void)
{
```

```
LL_APB2_GRP1_EnableClock(LL_APB2_GRP1_PERIPH_SYSCFG);
LL_APB1_GRP1_EnableClock(LL_APB1_GRP1_PERIPH_PWR);

NVIC_SetPriorityGrouping(NVIC_PRIORITYGROUP_4);

/* System interrupt init*/
/* MemoryManagement_IRQn interrupt configuration */
NVIC_SetPriority(MemoryManagement_IRQn,
NVIC_EncodePriority(NVIC_GetPriorityGrouping(),0, 0));
/* BusFault_IRQn interrupt configuration */
NVIC_SetPriority(BusFault_IRQn,
NVIC_EncodePriority(NVIC_GetPriorityGrouping(),0, 0));
/* UsageFault_IRQn interrupt configuration */
NVIC_SetPriority(UsageFault_IRQn,
NVIC_EncodePriority(NVIC_GetPriorityGrouping(),0, 0));
/* SVCall_IRQn interrupt configuration */
NVIC_SetPriority(SVCall_IRQn,
NVIC_EncodePriority(NVIC_GetPriorityGrouping(),0, 0));
/* DebugMonitor_IRQn interrupt configuration */
NVIC_SetPriority(DebugMonitor_IRQn,
NVIC_EncodePriority(NVIC_GetPriorityGrouping(),0, 0));
/* PendSV_IRQn interrupt configuration */
NVIC_SetPriority(PendSV_IRQn,
NVIC_EncodePriority(NVIC_GetPriorityGrouping(),0, 0));
/* SysTick_IRQn interrupt configuration */
NVIC_SetPriority(SysTick_IRQn,
NVIC_EncodePriority(NVIC_GetPriorityGrouping(),0, 0));

}

/** System Clock Configuration
*/
void SystemClock_Config(void)
{

LL_FLASH_SetLatency(LL_FLASH_LATENCY_1);

if(LL_FLASH_GetLatency() != LL_FLASH_LATENCY_1)
{
Error_Handler();
}
LL_PWR_SetRegulVoltageScaling(LL_PWR_REGU_VOLTAGE_SCALE1);

LL_RCC_MSI_Enable();

/* Wait till MSI is ready */
while(LL_RCC_MSI_IsReady() != 1)
{

}
LL_RCC_MSI_EnableRangeSelection();

LL_RCC_MSI_SetRange(LL_RCC_MSIRANGE_10);

LL_RCC_MSI_SetCalibTrimming(0);
```

```
LL_RCC_SetAHBPrescaler(LL_RCC_SYSCLK_DIV_1);

LL_RCC_SetAPB1Prescaler(LL_RCC_APB1_DIV_1);

LL_RCC_SetAPB2Prescaler(LL_RCC_APB2_DIV_1);

LL_RCC_SetSysClkSource(LL_RCC_SYS_CLKSOURCE_MSI);

/* Wait till System clock is ready */
while(LL_RCC_GetSysClkSource() != LL_RCC_SYS_CLKSOURCE_STATUS_MSI)
{
}
LL_Init1msTick(32000000);

LL_SYSTICK_SetClkSource(LL_SYSTICK_CLKSOURCE_HCLK);

LL_SetSystemCoreClock(32000000);

/* SysTick_IRQn interrupt configuration */
NVIC_SetPriority(SysTick_IRQn,
NVIC_EncodePriority(NVIC_GetPriorityGrouping(),0, 0));
}

/* SPI1 init function */
static void MX_SPI1_Init(void)
{
LL_SPI_InitTypeDef SPI_InitStruct;

LL_GPIO_InitTypeDef GPIO_InitStruct;

/* Peripheral clock enable */
LL_APB2_GRP1_EnableClock(LL_APB2_GRP1_PERIPH_SPI1);

/**SPI1 GPIO Configuration
PA1  -----> SPI1_SCK
PA7  -----> SPI1_MOSI
*/
GPIO_InitStruct.Pin = LL_GPIO_PIN_1|LL_GPIO_PIN_7;
GPIO_InitStruct.Mode = LL_GPIO_MODE_ALTERNATE;
GPIO_InitStruct.Speed = LL_GPIO_SPEED_FREQ_VERY_HIGH;
GPIO_InitStruct.OutputType = LL_GPIO_OUTPUT_PUSHPULL;
GPIO_InitStruct.Pull = LL_GPIO_PULL_NO;
GPIO_InitStruct.Alternate = LL_GPIO_AF_5;
LL_GPIO_Init(GPIOA, &GPIO_InitStruct);

SPI_InitStruct.TransferDirection = LL_SPI_FULL_DUPLEX;
SPI_InitStruct.Mode = LL_SPI_MODE_MASTER;
SPI_InitStruct.DataWidth = LL_SPI_DATAWIDTH_16BIT;
SPI_InitStruct.ClockPolarity = LL_SPI_POLARITY_LOW;
SPI_InitStruct.ClockPhase = LL_SPI_PHASE_1EDGE;
SPI_InitStruct.NSS = LL_SPI_NSS_SOFT;
SPI_InitStruct.BaudRate = LL_SPI_BAUDRATEPRESCALER_DIV2;
SPI_InitStruct.BitOrder = LL_SPI_MSB_FIRST;
SPI_InitStruct.CRCCalculation = LL_SPI_CRCCALCULATION_DISABLE;
```

```
SPI_InitStruct.CRCPoly = 7;
LL_SPI_Init(SPI1, &SPI_InitStruct);

LL_SPI_SetStandard(SPI1, LL_SPI_PROTOCOL_MOTOROLA);

LL_SPI_EnableNSSPulseMgt(SPI1);

}

/* TIM2 init function */
static void MX_TIM2_Init(void)
{

LL_TIM_InitTypeDef TIM_InitStruct;
LL_TIM_OC_InitTypeDef TIM_OC_InitStruct;

LL_GPIO_InitTypeDef GPIO_InitStruct;

/* Peripheral clock enable */
LL_APB1_GRP1_EnableClock(LL_APB1_GRP1_PERIPH_TIM2);

/* Peripheral DMA init*/

LL_DMA_SetPeriphRequest(DMA1, LL_DMA_CHANNEL_2, LL_DMA_REQUEST_4);

LL_DMA_SetDataTransferDirection(DMA1, LL_DMA_CHANNEL_2,
LL_DMA_DIRECTION_MEMORY_TO_PERIPH);

LL_DMA_SetChannelPriorityLevel(DMA1, LL_DMA_CHANNEL_2,
LL_DMA_PRIORITY_LOW);

LL_DMA_SetMode(DMA1, LL_DMA_CHANNEL_2, LL_DMA_MODE_NORMAL);

LL_DMA_SetPeriphIncMode(DMA1, LL_DMA_CHANNEL_2,
LL_DMA_PERIPH_NOINCREMENT);

LL_DMA_SetMemoryIncMode(DMA1, LL_DMA_CHANNEL_2,
LL_DMA_MEMORY_INCREMENT);

LL_DMA_SetPeriphSize(DMA1, LL_DMA_CHANNEL_2,
LL_DMA_PDATAALIGN_HALFWORD);

LL_DMA_SetMemorySize(DMA1, LL_DMA_CHANNEL_2,
LL_DMA_MDATAALIGN_HALFWORD);

LL_DMA_ConfigAddresses(DMA1, LL_DMA_CHANNEL_2,
(uint32_t)dataTx8, LL_SPI_DMA_GetRegAddr(SPI1),
LL_DMA_DIRECTION_MEMORY_TO_PERIPH);

LL_DMA_SetDataLength(DMA1, LL_DMA_CHANNEL_2, 43);

DMA1->IFCR = 0x00;

TIM_InitStruct.Prescaler = 0;
```

```
TIM_InitStruct.CounterMode = LL_TIM_COUNTERMODE_UP;
TIM_InitStruct.Autoreload = 44;
TIM_InitStruct.ClockDivision = LL_TIM_CLOCKDIVISION_DIV1;
LL_TIM_Init(TIM2, &TIM_InitStruct);

LL_TIM_SetClockSource(TIM2, LL_TIM_CLOCKSOURCE_INTERNAL);

LL_TIM_OC_EnablePreload(TIM2, LL_TIM_CHANNEL_CH1);

TIM_OC_InitStruct.OCMode = LL_TIM_OCMODE_PWM1;
TIM_OC_InitStruct.OCState = LL_TIM_OCSTATE_DISABLE;
TIM_OC_InitStruct.OCNState = LL_TIM_OCSTATE_DISABLE;
TIM_OC_InitStruct.CompareValue = 8;
TIM_OC_InitStruct.OCPolarity = LL_TIM_OCPOLARITY_HIGH;
LL_TIM_OC_Init(TIM2, LL_TIM_CHANNEL_CH1, &TIM_OC_InitStruct);

LL_TIM_OC_DisableFast(TIM2, LL_TIM_CHANNEL_CH1);

LL_TIM_SetOCRefClearInputSource(TIM2, LL_TIM_OCREF_CLR_INT_NC);

LL_TIM_DisableExternalClock(TIM2);

LL_TIM_ConfigETR(TIM2, LL_TIM_ETR_POLARITY_NONINVERTED,
LL_TIM_ETR_PRESCALER_DIV1, LL_TIM_ETR_FILTER_FDIV1);

LL_TIM_SetTriggerOutput(TIM2, LL_TIM_TRGO_RESET);

LL_TIM_DisableMasterSlaveMode(TIM2);

/**TIM2 GPIO Configuration
PA5  -----> TIM2_CH1
*/
GPIO_InitStruct.Pin = LL_GPIO_PIN_5;
GPIO_InitStruct.Mode = LL_GPIO_MODE_ALTERNATE;
GPIO_InitStruct.Speed = LL_GPIO_SPEED_FREQ_LOW;
GPIO_InitStruct.OutputType = LL_GPIO_OUTPUT_PUSHPULL;
GPIO_InitStruct.Pull = LL_GPIO_PULL_NO;
GPIO_InitStruct.Alternate = LL_GPIO_AF_1;
LL_GPIO_Init(GPIOA, &GPIO_InitStruct);

}

static void MX_TIM2_Init2(void)
{

LL_TIM_InitTypeDef TIM_InitStruct;
LL_TIM_OC_InitTypeDef TIM_OC_InitStruct;

LL_GPIO_InitTypeDef GPIO_InitStruct;

/* Peripheral clock enable */
LL_APB1_GRP1_EnableClock(LL_APB1_GRP1_PERIPH_TIM2);

/* Peripheral DMA init*/
```

```
LL_DMA_SetPeriphRequest(DMA1, LL_DMA_CHANNEL_2, LL_DMA_REQUEST_4);

LL_DMA_SetDataTransferDirection(DMA1, LL_DMA_CHANNEL_2,
LL_DMA_DIRECTION_MEMORY_TO_PERIPH);

LL_DMA_SetChannelPriorityLevel(DMA1, LL_DMA_CHANNEL_2,
LL_DMA_PRIORITY_LOW);

LL_DMA_SetMode(DMA1, LL_DMA_CHANNEL_2, LL_DMA_MODE_CIRCULAR);

LL_DMA_SetPeriphIncMode(DMA1, LL_DMA_CHANNEL_2,
LL_DMA_PERIPH_NOINCREMENT);

LL_DMA_SetMemoryIncMode(DMA1, LL_DMA_CHANNEL_2,
LL_DMA_MEMORY_INCREMENT);

    LL_DMA_SetPeriphSize(DMA1, LL_DMA_CHANNEL_2,
LL_DMA_PDATAALIGN_HALFWORD);

    LL_DMA_SetMemorySize(DMA1, LL_DMA_CHANNEL_2,
LL_DMA_MDATAALIGN_HALFWORD);

LL_DMA_ConfigAddresses(DMA1, LL_DMA_CHANNEL_2,
(uint32_t)dataTx4, LL_SPI_DMA_GetRegAddr(SPI1),
LL_DMA_DIRECTION_MEMORY_TO_PERIPH);

LL_DMA_SetDataLength(DMA1, LL_DMA_CHANNEL_2, 35);

DMA1->IFCR = 0x00;

TIM_InitStruct.Prescaler = 0;
TIM_InitStruct.CounterMode = LL_TIM_COUNTERMODE_UP;
TIM_InitStruct.Autoreload = 44;
TIM_InitStruct.ClockDivision = LL_TIM_CLOCKDIVISION_DIV1;
LL_TIM_Init(TIM2, &TIM_InitStruct);

LL_TIM_SetClockSource(TIM2, LL_TIM_CLOCKSOURCE_INTERNAL);

LL_TIM_OC_EnablePreload(TIM2, LL_TIM_CHANNEL_CH1);

TIM_OC_InitStruct.OCMode = LL_TIM_OCMODE_PWM1;
TIM_OC_InitStruct.OCState = LL_TIM_OCSTATE_DISABLE;
TIM_OC_InitStruct.OCNState = LL_TIM_OCSTATE_DISABLE;
TIM_OC_InitStruct.CompareValue = 8;
TIM_OC_InitStruct.OCPolarity = LL_TIM_OCPOLARITY_HIGH;
LL_TIM_OC_Init(TIM2, LL_TIM_CHANNEL_CH1, &TIM_OC_InitStruct);

LL_TIM_OC_DisableFast(TIM2, LL_TIM_CHANNEL_CH1);

LL_TIM_SetOCRefClearInputSource(TIM2, LL_TIM_OCREF_CLR_INT_NC);

LL_TIM_DisableExternalClock(TIM2);

LL_TIM_ConfigETR(TIM2, LL_TIM_ETR_POLARITY_NONINVERTED,
LL_TIM_ETR_PRESCALER_DIV1, LL_TIM_ETR_FILTER_FDIV1);
```

```
LL_TIM_SetTriggerOutput(TIM2, LL_TIM_TRGO_RESET);

LL_TIM_DisableMasterSlaveMode(TIM2);

/**TIM2 GPIO Configuration
PA5  -----> TIM2_CH1
*/
GPIO_InitStruct.Pin = LL_GPIO_PIN_5;
GPIO_InitStruct.Mode = LL_GPIO_MODE_ALTERNATE;
GPIO_InitStruct.Speed = LL_GPIO_SPEED_FREQ_VERY_HIGH;
GPIO_InitStruct.OutputType = LL_GPIO_OUTPUT_PUSHPULL;
GPIO_InitStruct.Pull = LL_GPIO_PULL_NO;
GPIO_InitStruct.Alternate = LL_GPIO_AF_1;
LL_GPIO_Init(GPIOA, &GPIO_InitStruct);

}

/**
 * Enable DMA controller clock
 */
static void MX_DMA_Init(void)
{
    /* Init with LL driver */
    /* DMA controller clock enable */
    LL_AHB1_GRP1_EnableClock(LL_AHB1_GRP1_PERIPH_DMA1);

    /* DMA interrupt init */
    /* DMA1_Channel2_IRQn interrupt configuration */
    NVIC_SetPriority(DMA1_Channel2_IRQn,
    NVIC_EncodePriority(NVIC_GetPriorityGrouping(),0, 0));
    NVIC_EnableIRQ(DMA1_Channel2_IRQn);
}

/** Configure pins as
 * Analog
 * Input
 * Output
 * EVENT_OUT
 * EXTI
 */
static void MX_GPIO_Init(void)
{
    GPIO_InitTypeDef GPIO_InitStruct;

    /* GPIO Ports Clock Enable */
    __HAL_RCC_GPIOA_CLK_ENABLE();

    /*Configure GPIO pin : PA8 */
    GPIO_InitStruct.Pin = GPIO_PIN_8;
    GPIO_InitStruct.Mode = GPIO_MODE_IT_FALLING;
    GPIO_InitStruct.Pull = GPIO_PULLUP;
    HAL_GPIO_Init(GPIOA, &GPIO_InitStruct);
}
```

```
/* EXTI interrupt init*/
HAL_NVIC_SetPriority(EXTI9_5_IRQn, 0, 0);
HAL_NVIC_EnableIRQ(EXTI9_5_IRQn);

}

/* USER CODE BEGIN 4 */

/* USER CODE END 4 */

/**
 * @brief This function is executed in case of error occurrence.
 * @param None
 * @retval None
 */
void _Error_Handler(char * file, int line)
{
    /* USER CODE BEGIN Error_Handler_Debug */
    /* User can add his own implementation to report the HAL error
return state */
    while(1)
    {
    }
    /* USER CODE END Error_Handler_Debug */
}

#ifdef USE_FULL_ASSERT

/**
 * @brief Reports the name of the source file and the source line
number
 * where the assert_param error has occurred.
 * @param file: pointer to the source file name
 * @param line: assert_param error line source number
 * @retval None
 */
void assert_failed(uint8_t* file, uint32_t line)
{
    /* USER CODE BEGIN 6 */
    /* User can add his own implementation to report the file name and
line number,
ex: printf("Wrong parameters value: file %s on line %d\r\n",
file, line) */
    /* USER CODE END 6 */

}

#endif

/**
 * @}
 */

/**
 * @}
 */
```



```

/***** (C) COPYRIGHT STMicroelectronics *****/
OF FILE*****/

```

**Appendix 4.2** Joanthan McKendry's BER analysis script used to compare optically transmitted MISO and chip reference MISO, based on SCLK (not transmitted).

```

% Using the script %
%%%%%%%%%%%%%%%%%%%%%%%%%%%%%%%%%%%%%%%%%%%%%%%%%%%%%%%%%%%%%%%%%%%%%%%%

% Data required to be imported:
% - Time stamps: import as "Times"
% SCLK: import as SCLK
% Electrical MISO: import as MISO_elec
% Optical MISO: import as MISO_opt

% You will also need to adjust the value of "sample_offset" in the
script
% below. This can be estimated by manually observing the electrical
and
% optical MISO signals.

% OUTPUTS:
%-----

% nerr: total number of errors
% BER: bit-error ratio
% individual_errors: the location of each error is marked as a "1"
in this
% array

%%%%%%%%%%%%%%%%%%%%%%%%%%%%%%%%%%%%%%%%%%%%%%%%%%%%%%%%%%%%%%%%%%%%%%%%
% Find SCLK rising edges %
%%%%%%%%%%%%%%%%%%%%%%%%%%%%%%%%%%%%%%%%%%%%%%%%%%%%%%%%%%%%%%%%%%%%%%%%
i = 1;
j = 1;

while i < length(SCLK)
    if (SCLK(i) == 0) && (SCLK(i+1) == 1); % If you find a rising edge
        edges(j,:) = (i+1); % Then record the sample number for the
rising edge
        edge_times(j,:) = Times(i,:); % And the corresponding time
value
        j = j + 1; % Increment j counter
        i = i + 1; % Increment i counter
    else
        i = i + 1; % Increment i counter
    end
end

%%%%%%%%%%%%%%%%%%%%%%%%%%%%%%%%%%%%%%%%%%%%%%%%%%%%%%%%%%%%%%%%%%%%%%%%
% Find places to sample the electrical and optical signals %
%%%%%%%%%%%%%%%%%%%%%%%%%%%%%%%%%%%%%%%%%%%%%%%%%%%%%%%%%%%%%%%%%%%%%%%%

```

---

```

sample_offset = 7; % Sample offset between electrical and optical
signals

elec_test = MISO_elec(edges,:); % Electrical samples to BER test
opt_test = MISO_opt(edges+sample_offset,:); % Optical samples to
BER test

[nerr,BER,individual_errors] = biterr(elec_test,opt_test); % BER
test

BER_print = horzcat('Bit-error-ratio is ',num2str(BER));
NERR_print = horzcat('Total number of ',num2str(nerr),' errors out
of ',num2str(length(edges)),' transmitted bits.');
```

```

% Print results to command window
disp(' ');
disp('=====');
disp('***BER results***');
disp('=====');
disp(BER_print);
disp(NERR_print);
disp('=====');
disp('=====');
```

### 4.3 Jonathan McKendry's BER analysis script used based on the transmitted clock signal, chip select (CS)

```

% Using the script %
%%%%%%%%%%%%%%%%%%%%%%%%%%%%%%%%%%%%%%%%%%%%%%%%%%%%%%%%%%%%%%%%%%%%%%%%

% Data required to be imported:
% - Time stamps: import as "Times"
% Electrical SCLK: import as SCLK
% Electrical MISO: import as MISO_elec
% Optical MISO: import as MISO_opt
% Optical CS: import as CS_opt

% You will also need to adjust the value of "sample_offset" in the
script
% below. This can be estimated by manually observing the electrical
and
% optical MISO signals.

% OUTPUTS:
%-----

% nerr: total number of errors
% BER: bit-error ratio
% individual_errors: the location of each error is marked as a "1"
in this
% array
```

```

%%%%%%%%%%%%%%%%%%%%%%%%%%%%%%%%%%%%%%%%%%%%%%%%%%%%%%%%%%%%%%%%%%%%%%%%
% 1) Find SCLK rising edges %
%%%%%%%%%%%%%%%%%%%%%%%%%%%%%%%%%%%%%%%%%%%%%%%%%%%%%%%%%%%%%%%%%%%%%%%%
i = 1;
j = 1;

while i < length(SCLK)
    if (SCLK(i) == 0) && (SCLK(i+1) == 1); % If you find a rising edge
        SCLK_edges(j,:) = (i+1); % Then record the sample number for
the rising edge
        SCLK_edge_times(j,:) = Times(i+1,:); % And the corresponding
time value
        j = j + 1; % Increment j counter
        i = i + 1; % Increment i counter
    else
        i = i + 1; % Increment i counter
    end
end

%%%%%%%%%%%%%%%%%%%%%%%%%%%%%%%%%%%%%%%%%%%%%%%%%%%%%%%%%%%%%%%%%%%%%%%%
% 2) Find places to sample the electrical MISO signal %
%%%%%%%%%%%%%%%%%%%%%%%%%%%%%%%%%%%%%%%%%%%%%%%%%%%%%%%%%%%%%%%%%%%%%%%%

%sample_offset = 2; % Sample offset between electrical and optical
signals

elec_test = MISO_elec(SCLK_edges,:); % Electrical samples to BER
test

%%%%%%%%%%%%%%%%%%%%%%%%%%%%%%%%%%%%%%%%%%%%%%%%%%%%%%%%%%%%%%%%%%%%%%%%
% 3) Find CS (optical) rising edges %
%%%%%%%%%%%%%%%%%%%%%%%%%%%%%%%%%%%%%%%%%%%%%%%%%%%%%%%%%%%%%%%%%%%%%%%%
i = 1;
j = 1;

while i < length(CS_opt)
    if (CS_opt(i) == 0) && (CS_opt(i+1) == 1); % If you find a rising
edge
        CS_edges(j,:) = (i+1); % Then record the sample number for the
rising edge
        CS_edge_times(j,:) = Times(i+1,:); % And the corresponding time
value
        j = j + 1; % Increment j counter
        i = i + 1; % Increment i counter
    else
        i = i + 1; % Increment i counter
    end
end

%%%%%%%%%%%%%%%%%%%%%%%%%%%%%%%%%%%%%%%%%%%%%%%%%%%%%%%%%%%%%%%%%%%%%%%%
% 4) Determine the times at which to sample optical MISO %
%%%%%%%%%%%%%%%%%%%%%%%%%%%%%%%%%%%%%%%%%%%%%%%%%%%%%%%%%%%%%%%%%%%%%%%%
Bitlprompt = 'Please specify the time offset between each rising
edge of Optical CS signal and the first bit (s): ';
Bloffset = input(Bitlprompt);

Bitprompt = 'Please specify the bit period (s): ';

```

```

Bitoffset = input(Bitprompt);

offset_matrix =
[Bloffset;Bloffset+Bitoffset;Bloffset+(2*Bitoffset);Bloffset+(3*Bitoffset);Bloffset+(4*Bitoffset);Bloffset+(5*Bitoffset);Bloffset+(6*Bitoffset);Bloffset+(7*Bitoffset);Bloffset+(8*Bitoffset);Bloffset+(9*Bitoffset);Bloffset+(10*Bitoffset);Bloffset+(11*Bitoffset);Bloffset+(12*Bitoffset);Bloffset+(13*Bitoffset);Bloffset+(14*Bitoffset);Bloffset+(15*Bitoffset)];

Opt_sample_times = zeros(16*length(CS_edge_times),1);
i = 1;
j = 1;

while i < length(CS_edge_times)+1
Opt_sample_times(j:j+15,1) = offset_matrix + CS_edge_times(i,1);
i = i + 1;
j = j + 16;
end

%%%%%%%%%%%%%%%%%%%%%%%%%%%%%%%%%%%%%%%%%%%%%%%%%%%%%%%%%%%%%%%%%%%%%%%%
%%
% 5) Determine the logic levels of optical MISO at these sample
times %
%%%%%%%%%%%%%%%%%%%%%%%%%%%%%%%%%%%%%%%%%%%%%%%%%%%%%%%%%%%%%%%%%%%%%%%%
%%
i = 1;
j = 1;

%Opt_MISO_output = zeros((length(Opt_sample_times)),1);
%(Times(i) <= Opt_sample_times(j,1)) && (Times(i+1) >=
Opt_sample_times(j,1));

while i < length(Times)-1;
if Times(i,1) >= Opt_sample_times(j,1);
Opt_MISO_output(j,1) = MISO_opt(i-1,1);
i = i + 1;
j = j + 1;
else
i = i + 1; % Increment i counter
end
end

%%%%%%%%%%%%%%%%%%%%%%%%%%%%%%%%%%%%%%%%%%%%%%%%%%%%%%%%%%%%%%%%%%%%%%%%
% 6) Test BER %
%%%%%%%%%%%%%%%%%%%%%%%%%%%%%%%%%%%%%%%%%%%%%%%%%%%%%%%%%%%%%%%%%%%%%%%%

Discard_prompt = 'Please specify the number of bits to skip: ';
discard = input(Discard_prompt);

ELEC_TEST = elec_test((discard+1):end,1);
OPT_TEST = Opt_MISO_output(1:length(ELEC_TEST),1);

[nerr,BER,individual_errors] = biterr(ELEC_TEST,OPT_TEST); % BER
test

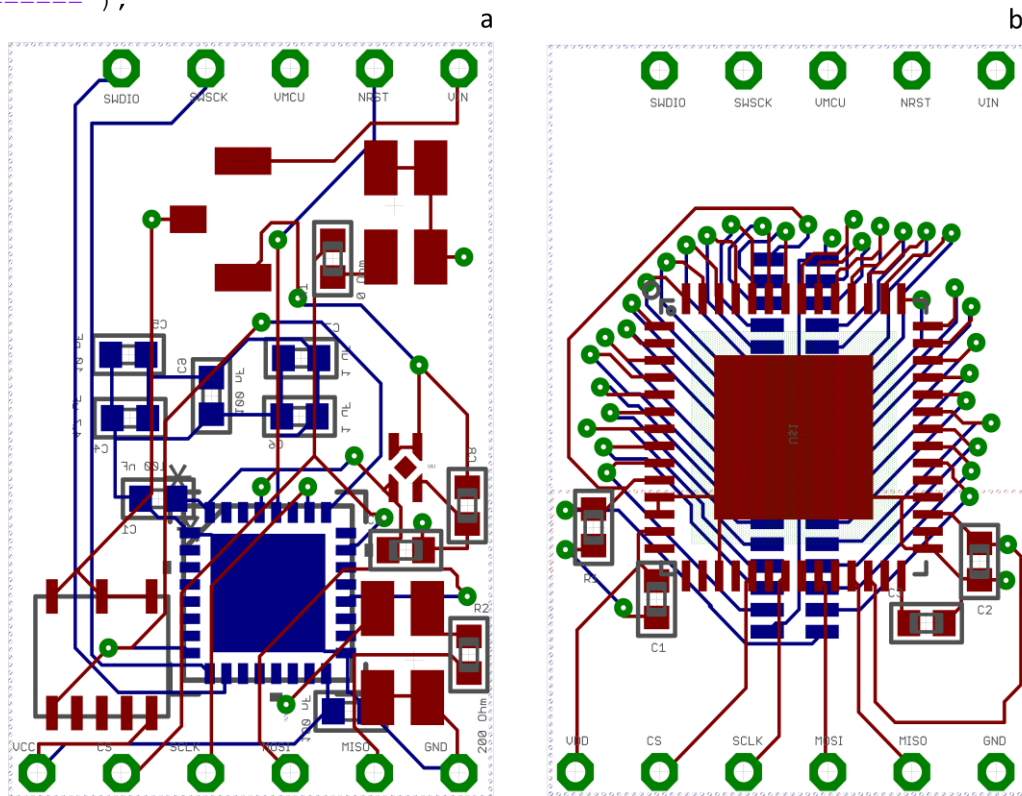
```

```

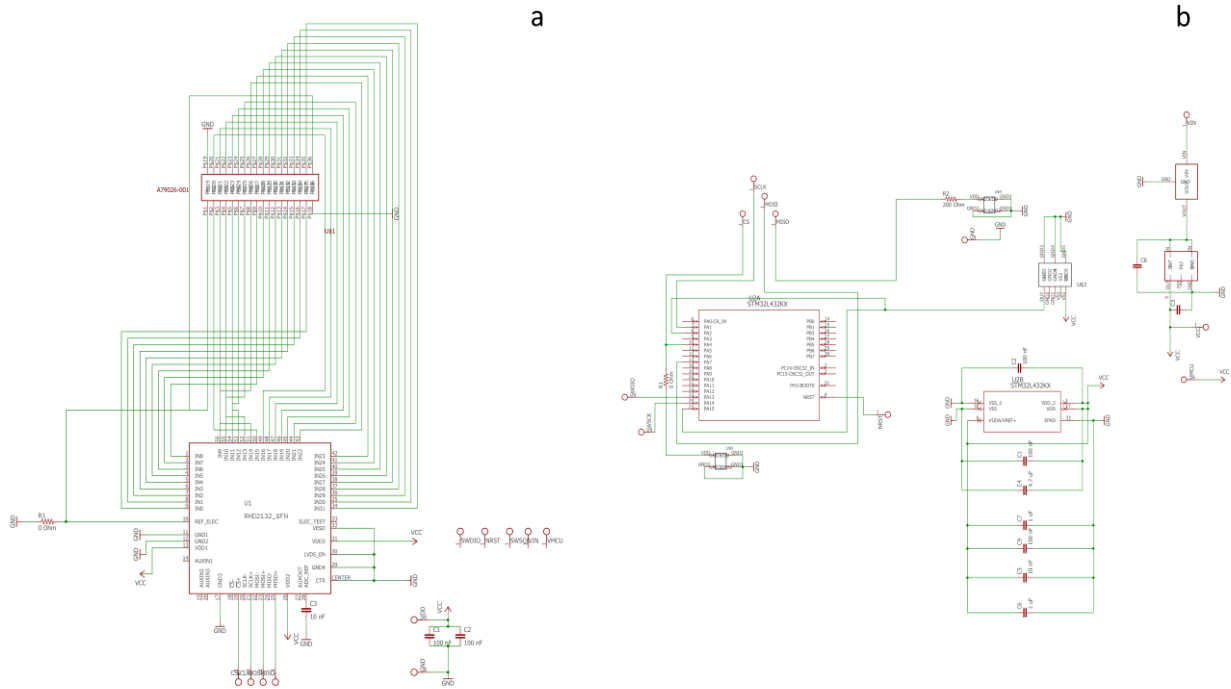
BER_print = horzcat('Bit-error-ratio is ', num2str(BER));
NERR_print = horzcat('Total number of ', num2str(nerr), ' errors out
of ', num2str(length(SCLK_edges)), ' transmitted bits. ');

% Print results to command window
disp(' ');
disp('=====');
disp('***BER results***');
disp('=====');
disp(BER_print);
disp(NERR_print);
disp('=====');
disp(' ');

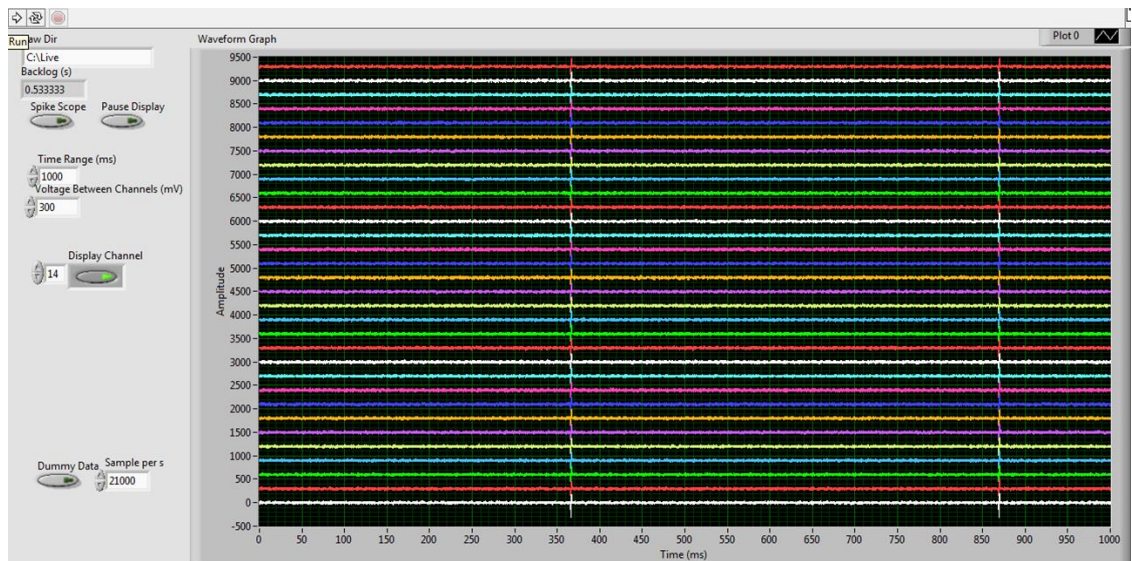
```



Appendix 4.4: (a) Board layout of the top PCB, with blue indicating the features on the bottom layer, while red indicates them being on the top. It incorporated the MCU, two data transmitting LEDs, IR receiver and voltage regulator. (b) The bottom PCB containing an Omnetics connector on the bottom layer, which is used to interface with neural probes. The top layer contained the Intan amplifier chip along with the associated surface mount components. There are two rows of holes on the PCBs, the lower one connects the bottom PCB to the top PCB through header pins, and ensures that the appropriate ground, power and signal lines (GND, VDD, CS, SCLK, MOSI, MISO) reach the appropriate components. The top row of holes (SWDIO, SWCLK, VMCU, NRST) is only connected on the top PCB, and is used to interface with MCU for debugging and programming purposes.

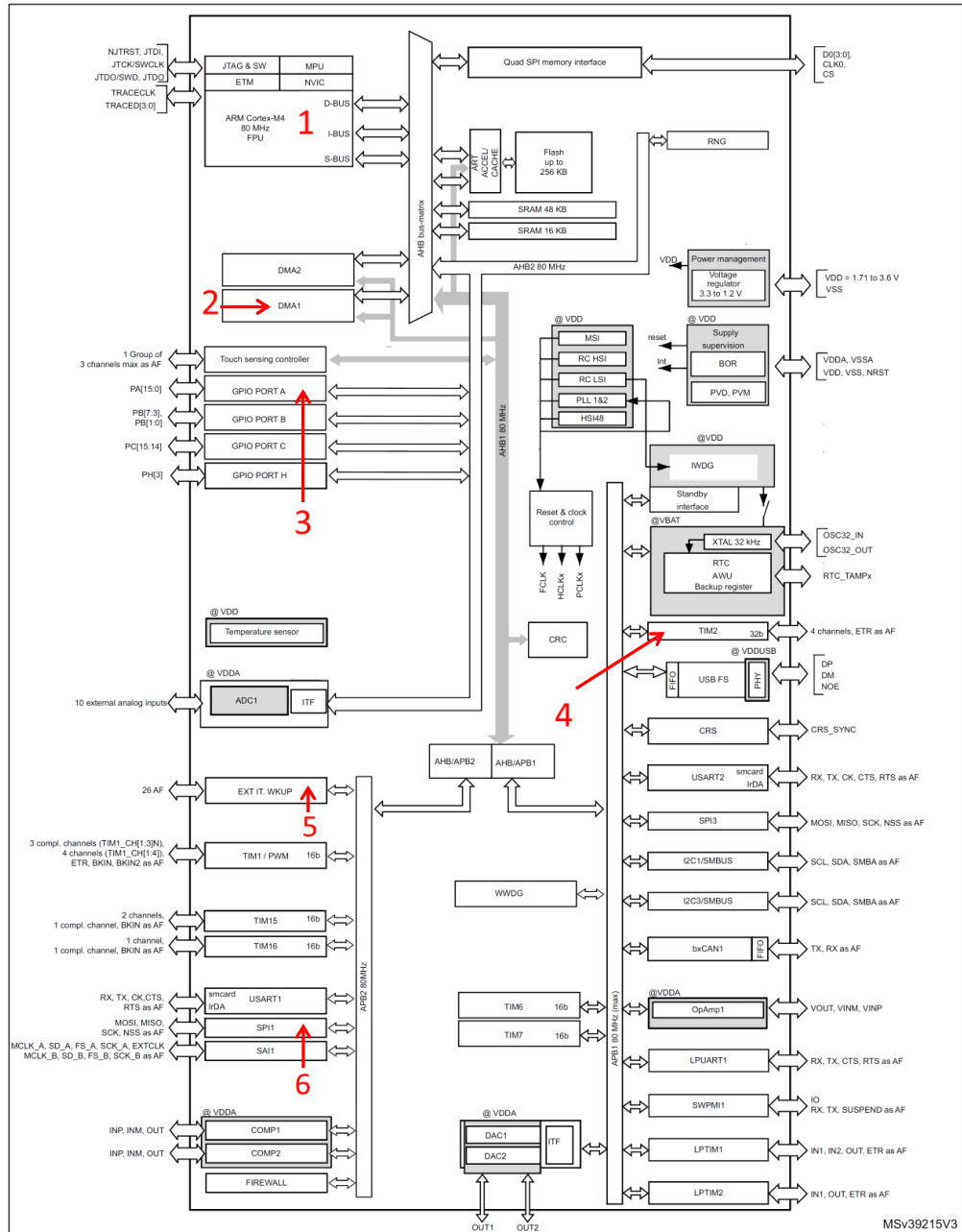


Appendix 4.5: (a) Schematic of the top PCB (b) Schematic of the bottom PCB



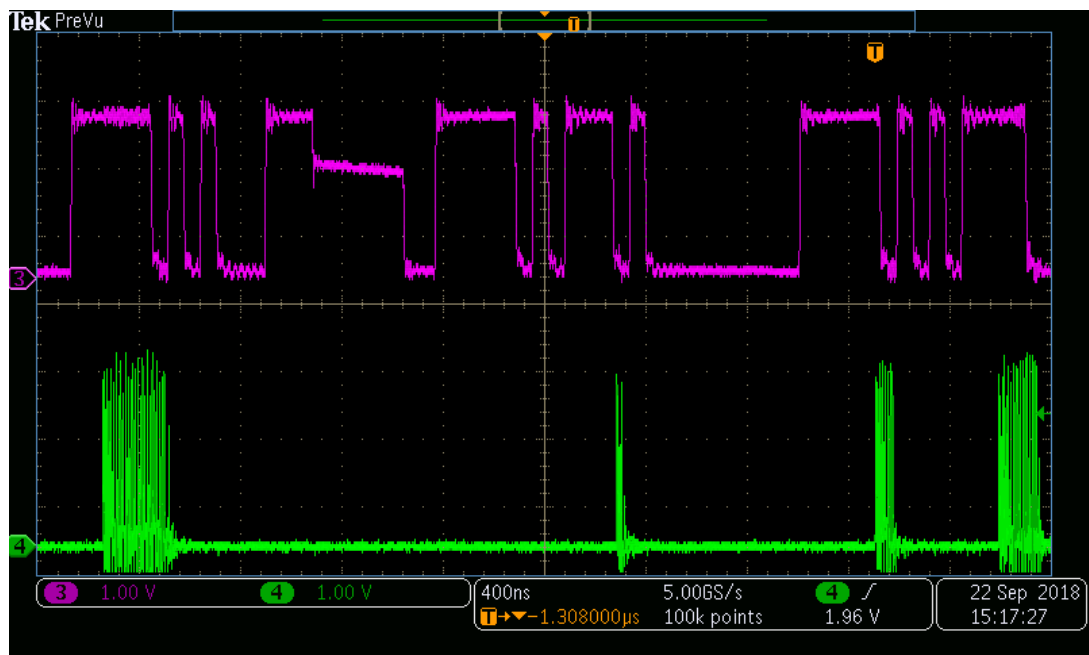
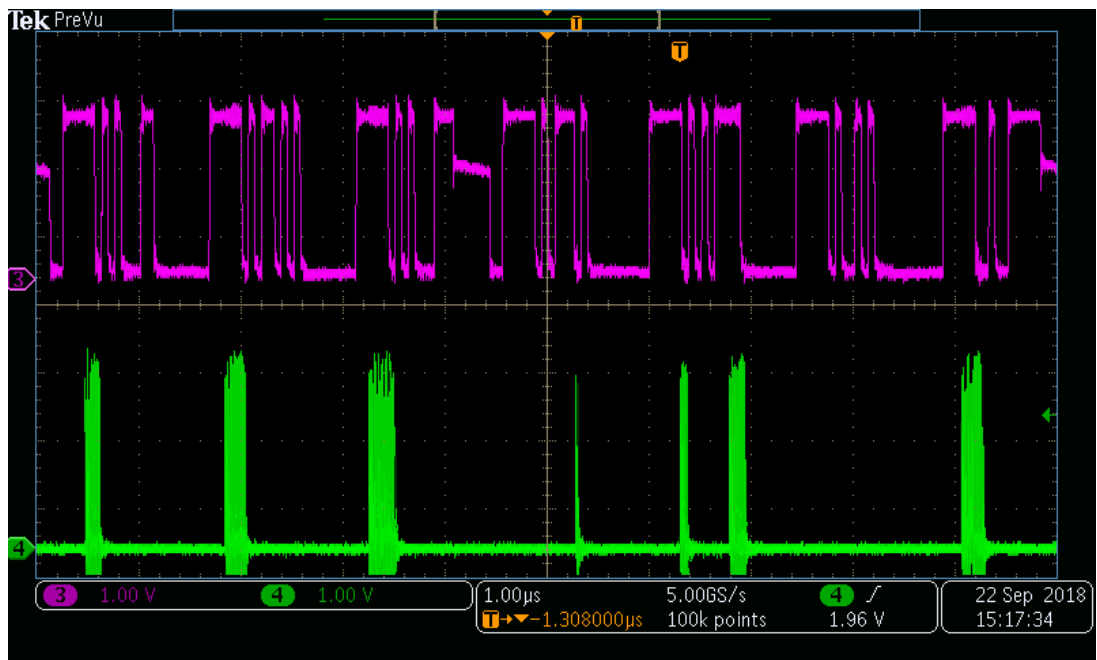
Appendix 4.6: The display of the Labview VI showing 32 channels of live data, with the artificially introduced dummy spikes clearly visible. The VI allowed the turning on and off of different channels, changing the time range and the separation between the different channels. It also incorporated a spike scope, which enabled a threshold to set for the isolation of neural spikes.





Appendix 4.8: Block diagram of the STM32L432KC MCU, showing the key features that were used. Adapted from [5]. (1) The core of the MCU used to initiate commands and communicate with the appropriate peripherals. (2) The DMA module used to minimize involvement from the core, and creating a direct bridge between memory and the peripherals. (3) The GPIO block used to activate and control the GPIO pins that were required. (4) The Timer block used to generate the CS clock. (5) The Wake Up module that controlled the device waking up or going to sleep if a command was received from the IR receiver. (6) The SPI block generating the necessary command clock (SCLK) and command (MOSI) signals.





Appendix 4.9: The magenta pulse (top) compared to the green digitized pulses (bottom) at 20 cm distance and 40° deflection. A near complete lack of signal retention can be observed.

#### 4.10 Jonathan McKendry's code for modelling BER performance vs distance based on the calculation in Hamza et. al. and Khalighi et. al. 2017

```

%%% SiPM OOK BER calculator %%%
%%% See Hamza 2016 and - Khalighi et al., IEEE Photonics
Journal, 9 (2017). %%%
%%%%%%%%%%%%%%%%%%%%%%%%%%%%%%%%%%%%%%%%%%%%%%%%%%%%%%%%%%%%%%%%%%%%%%%%

%%% Parameter specifications %%%
%%%%%%%%%%%%%%%%%%%%%%%%%%%%%%%%%%%%%%%%%%%%%%%%%%%%%%%%%%%%%%%%%%%%%%%%
%a = 0.0516; % Absorption coefficient
%b = 0.0872; % Scattering coefficient
C = 0;%a + b; % Overall attenuation coefficient (estimate from
quarry)

% Constants %
%-----%
h = 6.626e-34; % Planck's constant
c = 3e8; % Speed of light
z = 0:0.01:5; % Distance between Tx & Rx;

% SiPM %
%-----%
% Data for C series 10020 %

PDE = 0.0967; % PDE of SiPM at wavelength of interest (0.45 @ 450nm)
A = (1e-6); % Area of SiPM (m^2)
fDCR = 0 % (1e6)*(96e3)*(A); % SiPM dark count rate (Hz)
td = 23e-9; % SiPM cell dead time (s)
NSPAD = 1296; % # of cells in the SiPM
PCT = 0; % Probability of cross talk
PAP = 0; % Probability of after-pulsing

% Tx %
%-----%
P1 = 10e-3; % Total power transmitted for bit = 1;
P0 = 0e-3; % Total power received for bit = 0;
theta = deg2rad(60); % LED half angle
m = -log(2) / log(cos(theta));
Pt1 = P1 * ((m+1)/(2*pi)) * (cos(theta)^m); % Useful power
transmitted for bit = 1;
Pt0 = P0 * ((m+1)/(2*pi)) * (cos(theta)^m); % Useful power
transmitted for bit = 0;

lambda = 625e-9; % Tx wavelength (m)
Eph = (c*h)/lambda; % Photon energy (J)

f = 16e6; % Bit rate
T = 1/f; % Bit period

%%% Calculations %%%
%%%%%%%%%%%%%%%%%%%%%%%%%%%%%%%%%%%%%%%%%%%%%%%%%%%%%%%%%%%%%%%%%%%%%%%%
Pr1 = Pt1.*exp(-C*z).*(A./(z.^2)); % Received power versus distance
(W), logic 1 - Khalighi et al., IEEE Photonics Journal, 9 (2017).
Pr0 = Pt0.*exp(-C*z).*(A./(z.^2)); % Received power versus distance
(W), logic 0 - Khalighi et al., IEEE Photonics Journal, 9 (2017).

```

```
Pr_dBm = (20*log10(Pr1/1e-3)) / log10(10);

mu_1 = ((PDE*Pr1)/Eph + fDCR) * (1 + PAP + PCT)*T; % Average #
counts for bit = 1 - Khalighi et al., IEEE Photonics Journal, 9
(2017).
mu_0 = ((PDE*Pr0)/Eph + fDCR) * (1 + PAP + PCT)*T; % Average #
counts for bit = 0 - Khalighi et al., IEEE Photonics Journal, 9
(2017).

mu_th = (mu_1 + mu_0) / 2; % Threshold counts

Pe = 0.5*(1-
(cdf('Poisson',mu_th,mu_0))+(cdf('Poisson',mu_th,mu_1))); % -
Khalighi et al., IEEE Photonics Journal, 9 (2017).
LOGBER = -log10(Pe);

%%% Plot %%%
%%%%%%%%%%%%%%%%%%%%%%%%%%%%%%%%%%%%%%%%%%%%%%%%%%%%%%%%%%%%%%%%%%%%%%%%
semilogy(z,Pe);
xlabel('Transmission distance (m)');
ylabel('P_e, probability of error');
grid on;
axis([0 max(z) 1e-6 1]);
set(gca, 'FontSize', 16);
```

## Appendix – Chapter V

## APPENDIX 5.1

## LED COMPARISON

LED Model Number	Lumileds L110-0850150000000	Lumileds L110-0940150000000	Lite-On LTE-R38386A-ZF-U	Osram LH CPDP-3T4T-1-0-350-R18	Kingbright APETD3528SEC/J3-PRV	Osram
<b>Radiant Intensity at 1A (mW/sr)</b>	335	350	200	*Radiant Flux 355 mW at 350 mA	4200 mcd @ 20 mA	780
<b>Approximate Radiant Intensity at 2 mA (mW/sr)</b>	0.67	0.7	0.4	~1.1 mW	420 mcd	1.56
<b>Viewing Angle (Degrees)</b>	150	150	150	130	60	90
<b>Rise Time (ns) at 2 mA</b>	22	22	?	?	~40	? 11 @ 350 mA
<b>Fall Time (ns) at 2 mA</b>	36	36	?	?	~40	? 14 @ 350 mA
<b>Wavelength (nm)</b>	850	940	850	660	640(625)	860(850)

Appendix 5.1: A brief summary of the proposed replacement LEDs. The radiant intensity at 2 mA was deduced from the graphs in the datasheet which show that it is near linear with respect to input current.

## Publications and Projects Arising from This Work

### Conferences

[1] G. Varkonyi, J. J. D. McKendry, N. McAlinden, M. D. Dawson, and K. Mathieson, “Data transmission for high-bandwidth neural interfacing using visible light communication,” *2016 IEEE Photonics Conf. IPC 2016*, pp. 41–42, 2017. DOI: 10.1109/IPCon.2016.7830971, Oral Presentation

[2] G. Varkonyi, J. J. D. McKendry, N. McAlinden, S. Sakata, M. D. Dawson, and K. Mathieson, “Data transmission for high-bandwidth neural interfacing using visible light communication,” *2016 Photonex Conf.*, Poster Presentation

### Patent

Filed Patent: Published on 04/04/2019 under the International Publication Number: WO 2019/063964 A1

Inventors: Gábor Várkonyi, Jonathan J.D. McKendry, Martin D. Dawson, Keith Mathieson

### Other Work

Royal Society of Edinburgh Enterprise Fellowship Award – Further developing and exploring the commercial opportunities of the device presented in the thesis. Commencing 01/10/2018, Awardee: Gábor Várkonyi

BBSRC Pathfinder Award – Working with IP Pragmatics to carry out an in-depth market assessment for the device. Commencing: 15/10/2018, Awardee: Shuzo Sakata, with support for Gábor Várkonyi to complement the Royal Society of Edinburgh Enterprise Fellowship Award

ESPRC Impact Acceleration Account Award – Further developing and exploring the commercial opportunities of the device presented in the thesis. 05/03/2018 – 30/06/2018

Awardee: Gábor Várkonyi